Oil & Natural Gas Technology

DOE Award No.: DE-FC26-06NT42955

Final Report

Design and Implementation of Energized Fracture Treatment in Tight Gas Sands

Submitted by:
Mukul M. Sharma
Kyle Friehauf
The University of Texas at Austin
1 University Station C0300
Austin, Texas 78712

Prepared for:
United States Department of Energy
National Energy Technology Laboratory

December 31, 2009

Office of Fossil Energy

Design and Implementation of Energized Fracture Treatment in Tight Gas Sands

Final Report

October 1, 2006 – December 31, 2009

By

Mukul M. Sharma

December 31, 2009

Work Performed under Contract No. DE-FC26-06NT42955

William Gwilliam
Project Officer
U. S. Department of Energy
National Energy Technology Laboratory
Morgantown, WV

Prepared by
The University of Texas at Austin

DISCLAIMER

This report was prepared as an account of work sponsored by an agency of the United States Government. Neither the United States Government nor any agency thereof, nor any of their employees, makes any warranty, express or implied, or assumes any legal liability or responsibility for the accuracy, completeness, or usefulness of any information, apparatus, product, or process disclosed, or represents that its use would not infringe privately owned rights. Reference herein to any specific commercial product, process, or service by trade name, trademark, manufacturer, or otherwise does not necessarily constitute or imply its endorsement, recommendation, or favoring by the United States Government or any agency thereof. The views and opinions of authors expressed herein do not necessarily state or reflect those of the United States Government or any agency thereof.

ABSTRACT

Hydraulic fracturing is essential for producing gas and oil at an economic rate from low permeability sands. Most fracturing treatments use water and polymers with a gelling agent as a fracturing fluid. The water is held in the small pore spaces by capillary pressure and is not recovered when drawdown pressures are low. The un-recovered water leaves a water saturated zone around the fracture face that stops the flow of gas into the fracture. This is a particularly acute problem in low permeability formations where capillary pressures are high. Depletion (lower reservoir pressures) causes a limitation on the drawdown pressure that can be applied.

A hydraulic fracturing process can be energized by the addition of a compressible, sometimes soluble, gas phase into the treatment fluid. When the well is produced, the energized fluid expands and gas comes out of solution. Energizing the fluid creates high gas saturation in the invaded zone, thereby facilitating gas flowback.

A new compositional hydraulic fracturing model has been created (EFRAC). This is the first model to include changes in composition, temperature, and phase behavior of the fluid inside the fracture. An equation of state is used to evaluate the phase behavior of the fluid. These compositional effects are coupled with the fluid rheology, proppant transport, and mechanics of fracture growth to create a general model for fracture creation when energized fluids are used.

In addition to the fracture propagation model, we have also introduced another new model for hydraulically fractured well productivity. This is the first and only model that takes into account both finite fracture conductivity and damage in the invaded zone in a simple analytical way.

EFRAC was successfully used to simulate several fracture treatments in a gas field in South Texas. Based on production estimates, energized fluids may be required when drawdown pressures are smaller than the capillary forces in the formation. For this field, the minimum CO_2 gas quality (volume % of gas) recommended is 30% for moderate differences between fracture and reservoir pressures (2900 psi reservoir, 5300

psi fracture). The minimum quality is reduced to 20% when the difference between pressures is larger, resulting in additional gas expansion in the invaded zone. Inlet fluid temperature, flow rate, and base viscosity did not have a large impact on fracture production. Finally, every stage of the fracturing treatment should be energized with a gas component to ensure high gas saturation in the invaded zone.

A second, more general, sensitivity study was conducted. Simulations show that CO_2 outperforms N_2 as a fluid component because it has higher solubility in water at fracturing temperatures and pressures. In fact, all gas components with higher solubility in water will increase the fluid's ability to reduce damage in the invaded zone. Adding methanol to the fracturing solution can increase the solubility of CO_2. N_2 should only be used if the gas leaks-off either during the creation of the fracture or during closure, resulting in gas going into the invaded zone. Experimental data is needed to determine if the gas phase leaks-off during the creation of the fracture. Simulations show that the bubbles in a fluid traveling across the face of a porous medium are not likely to attach to the surface of the rock, the filter cake, or penetrate far into the porous medium.

In summary, this research has created the first compositional fracturing simulator, a useful tool to aid in energized fracture design. We have made several important and original conclusions about the best practices when using energized fluids in tight gas sands. The models and tools presented here may be used in the future to predict behavior of any multi-phase or multi-component fracturing fluid system.

Table of Contents

List of Tables

List of Figures

EXECUTIVE SUMMARY

A hydraulic fracturing process can be energized by the addition of a compressible, sometimes soluble, gas phase into the treatment fluid. When the well is produced, the energized fluid expands and gas comes out of solution. This, coupled with the high mobility of the fluid in the fracture, results in a rapid cleanup of the fracturing fluid as it is blown out of the well by the liberated gas phase[3].

Energized fluids can use CO_2[4,6], N_2[7,8], methanol[9], or any combination of gases[10]. They can be pumped solely as an energized fluid[5,11] or can be mixed with an external phase, such as a cross-linked gel or hydrocarbons[12]. The addition of CO_2 and N_2 to a traditional, aqueous based fluid is common and can be beneficial at high volume fractions because foam is created. Foam has all the same advantages as other energized fluids with similar composition, but has higher viscosities than single-phase fluids.

In traditional hydraulic fracture modeling, fracture dimensions are estimated and propagated over time by coupling rheological fluid flow models and fracture mechanics. Volume conservation is assumed because the fluid is incompressible. Traditional fracturing fluids are single-phase and do not require that compositional effects be taken into account. The process is also assumed to be isothermal; the fluid properties are evaluated at reservoir temperatures. The reader is referred to Nordgren[13] for an example of a model with these assumptions.

In the case of energized fluids, however, these assumptions cannot be made. The conservation equations can no longer be approximated on a volume basis, but need to be preserved in a mass basis. The presence of multiple fluid phases causes each component to leak-off at a different rate, resulting in compositional changes throughout the fracture. The process is no longer isothermal since the injected fluid may be at a temperature that is 200 ^{o}F lower than the reservoir.

Unlike traditional fracturing fluids, energized fluid systems involve the injection of multiple components. Several mechanisms (phase behavior, leak-off, multi-phase flow) can cause compositional changes of the fluid during fracturing. In addition, phase changes can occur as a result of changes in temperature and pressure. Fracture dimensions, as well as proppant carrying ability, depend both on the overall composition and the phase properties of the fracturing fluid. Changes in composition are tracked using component balances and incorporated into a fracture model, a feature that no existing fracturing model has. The results are analyzed to determine the effect that composition has on fracture performance.

It is not uncommon for energized fluids to be pumped at low temperatures (0-70^{o} F)[4]. The temperature difference between the fluid and the earth causes an increase in fluid temperature as it flows down the wellbore. Heat transfer continues in the fracture because the fracture face is exposed to the high reservoir temperature (< 350^{o} F). Temperature variations cause significant differences in the phase behavior, as well as changes in other fluid properties, affecting fracture performance. Energy balances are implemented in the fracture model to track temperature changes in the fluid. This allows us, for the first time, to quantify the effect that heat transfer has on hydraulic fracturing.

Changes in solubility and compressibility are predicted by the implementation of an equation of state (EOS). The input to the equation of state is the fluid composition (tracked by the component balance), the fluid temperature (tracked by the energy balance), and the fluid pressure (tracked by an overall mass balance). The output is updated density, phase composition, and phase fraction. The Peng-Robinson equation of state was used in this research and implemented in the fracturing model.

Energized fluids have very efficient fracture fluid recovery because of the creation of a high gas saturation in and around the fracture. The rate of fluid recovery depends on the amount of leak-off, composition of leak-off, placement of proppant, relative mobility of each phase in the reservoir and the fracture, and the amount of gas that comes out of solution when the well is put back on production. The amount of leak-off, composition of leak-off, and placement of proppant are determined from the fracture

model with compositional effects. The relative mobility of the fluid phases is a property of the porous medium and the fluids. The amount of gas that comes out of solution is determined by the phase behavior calculated by an equation of state. Published models do not include a mechanism for flowback, or do so in a simplistic way. A model has been created that predicts steady state flow from a fractured reservoir. Damage around the fracture face is included so that the difference in production from energized and non-energized systems can be compared.

Results from the new simulator (EFRAC) are compared to field results. Engineers from Anadarko provided data on a pre-existing energized fluid treatment on a South Texas gas well. The data includes recorded pressures during fracturing and fluid recovery during flowback. Comparing the modeled results contributes to better understanding of the capabilities and limitations of the model. Once the pumping schedule that was actually pumped is accurately modeled, the design can be optimized by variation of controllable engineering parameters determined by the fracture engineer. Possible recommendations for future energized fracture jobs on similar wells are included.

The parameters that dominate energized fracture performance have been determined. The following questions have been asked in energized fracture design, and answered with this research:

1. When should we use energized instead of traditional fluids?
2. Which gas component works best, and when?
3. How does leak-off and closure affect energized fracture performance?
4. What quality (volume fraction of gas) works best?
5. What permeability rocks are more suitable for energized fractures?
6. What other factors are important?

Each of the parameters is varied over a broad range of values to answer each question.

By adding thermal and compositional capabilities to hydraulic fracture models, operators will be able to design and optimize energized fracture stimulation treatments in a systematic way. Such improvements will help operators better develop under-pressurized reservoirs, many of which are water-sensitive and will require energized treatments to be effectively produced. The resulting improvement in the development approach will require fewer wells and fewer completion or re-completion attempts to achieve a satisfactory level of natural gas production. It will also reduce costs.

CHAPTER 1: INTRODUCTION

Hydraulic fracturing is an effective stimulation technique for oil and gas wells. In this process, fluid is pumped into a well at a pressure high enough to overcome the in-situ stresses and the strength of the rock, forming a tensile crack or fracture. Sand or bauxite, referred to as proppant, is added in later stages of pumping to keep the fracture open during flowback. The proppant pack in the fracture provides a conductive channel for fluid to flow because it has a much higher permeability than the formation. This results in a higher production rate from the well. In low permeability rocks, hydraulic fracturing is essential in order to achieve profitable flowrates in a well. It is estimated that over 80% of all oil and gas wells are hydraulically fractured.

Although the effect of creating a hydraulic fracture is mostly beneficial, some adverse consequences may develop. For example, water pumped during fracture creation can reduce the permeability to hydrocarbons because the water is held in the porous medium by capillary forces. If clays are present, the water will be absorbed by the clay, causing swelling and creating permeability damage. The effect is amplified because of polymer additives added to the water. Polymer residue can plug the pore space and restrict flow. In ideal situations, about 40% of the water that is pumped during fracturing is recovered when the well is put back on production. This is not the case in low permeability and depleted formations. In these cases, very little of the water is recovered and alternatives to traditional fracturing fluids are needed. One way to reduce damage by water is to "energize" the fluid by the use of gases. Understanding what happens when a fracture is energized is the main goal of this research.

When a fracture is energized, the amount of water pumped during fracturing is reduced or eliminated by adding a gas component to the fracturing fluid. The less water that is pumped, the less damage it will create. In addition, the gas component stimulates the area around the face of the fracture that has been exposed to fluid leak-off. Gas, unlike water, changes density by variations in pressure. The gas expands when fracturing

is stopped and the well is put on production because it will go from high to low pressure. Expansion of the gas phase increases the saturation of the gas phase, reducing gas relative permeability damage. Gas comes out of solution from the water phase when the pressure is reduced, further increasing gas saturation. The term "energized" is used because of the above properties.

A tight gas reservoir may be defined as a gas reservoir that can only be produced at economic flow rates by stimulating the well by hydraulic fracture treatments or by use of horizontal or multilateral wellbores[2]. This definition implies that the vast majority of gas wells in tight gas fields need to be stimulated using a fracturing treatment. Conventional fracturing technology uses a viscosified aqueous fluid for fracture propagation and placement of proppant. As the need to produce unconventional reservoirs grows, alternative fracturing fluids are required. One alternative to conventional fracturing is energized fluids.

Energized fluid fracturing has many uses, but its common applications are in natural gas reservoirs that have a low fluid pressure[3], or in water sensitive formations[4,5]. When the reservoir pressure is low, the viscous forces applied to the trapped liquid phase (usually water) may not be sufficient to overcome the capillary pressure of the fracturing fluid in the formation; this results in little or no flowback. With energized fluids, the creation of a free gas phase in the rock matrix allows the gas relative permeability to increase as soon as the pressure is reduced. Energized fluids also minimize or eliminate the use of water which is beneficial because water causes fines migration or clay swelling problems in the formation.

Energized fractures are used in almost all hydraulic fracturing treatments in depleted tight gas sand formations of North America. They are used worldwide on water sensitive formations where non-conventional fluids are incompatible. In the future, it is expected that a higher percentage of hydraulic fractures are energized because current fields will be depleted and new plays will be in tighter formations.

As the popularity of energized fractures grows, so does the need to understand the process. A hydraulic fracture uses thousands of gallons of fluids, thousands of pounds of

proppant, and costs hundreds of thousands of dollars. Every engineering decision is valuable because of significant increases in production or decreases in cost. The complexity of the problem is increased because the engineer cannot measure fracture growth in the field. Models that predict fracture growth have been used in the design of hydraulic fractures to make up for the lack of known information.

Several hydraulic fracturing models have been implemented where traditional (water-based) fluids have been used. Many of the assumptions made while creating these models cannot be applied to the gas used in energized fluids. This research aims to create a fracture propagation model that can be used for energized fracturing fluids. The model can be used by operators to design and optimize energized fracture stimulation treatments in a systematic way. The simulator aids in identifying the important parameters for energized fracturing leading to improvements in fracture design and perhaps an increased use of energized fracturing fluids.

1.1 Review of Chapters

The research discussed here forms the basis for creating the first model for energized fracture treatments. The research is divided into the following chapters:

Chapter 2 discusses past fracture models. The theory and assumptions of each model are included. Many of the theories behind these models can be kept and applied to the new model. This chapter places an emphasis on what can and cannot be included in an energized fracture model.

Chapter 3 presents the theories and equations behind the new fracture model (EFRAC). The compositional balances, an energy balance, and phase behavior are included in a fracture model for the first time. Other equations (fracture mechanics, proppant transport, wellbore behavior) incorporates the work of past authors.

Chapter 4 reviews energized fluid behavior. The chapter opens with a discussion of fluid types and their differences. The chapter discusses the different gas components that are used as energizers. For the model to work, the phase behavior, rheology, and

leak-off behavior must be correctly characterized. The chapter concentrates on common fluids and fluid types that are shown as case studies for this research.

Chapter 5 is a compilation of example runs that show how the model can be run and shows an example of the output. The chapter serves as an introduction to preliminary issues that are included in energized fractures. It also confirms the model can predict some of the same behavior as past models discussed in Chapter 2.

Chapter 6 shows the assumptions, theory, equations, and formulation of a new model to predicted steady state production from a fractured reservoir. It includes a comparison to past models with common assumptions. It is the first time a model incorporates a damaged zone around the fracture and includes the behavior of energized fluids.

Chapter 7 discusses the first application of the energized fluid model to actual field treatments. The model is used to optimize fracturing treatments in a South Texas tight gas field operated by Anadarko Petroleum. We use data from 3 previously performed treatments in the area to verify that the model can correctly predict fracture growth. Once the model is confirmed, it can be used instead of costly field trial-and-error procedures to optimize fracture performance. The conclusions discuss the optimum conditions to apply energized fracturing fluids in this field.

Chapter 8 discusses mechanisms for dynamic leak-off of energized fluids. Theory and assumptions of 4 possible mechanisms are discussed. The effect each mechanism has on field performance and laboratory leak-off experiments is shown. The conclusions of this chapter should be confirmed with experimental data in the future.

Chapter 9 is a sensitivity study on fracturing parameters. The chapter shows which parameters are important in energized fracturing and why. This includes a comparison between different energizing components and the effect of a range of reservoir properties. Neither of theses issues is covered in Chapter 7 because that chapter is only applied to a specific tight gas field.

Chapter 10 is a summary of conclusions from each chapter. The chapter also gives the author's ideas on future work involving this subject.

References

1. Friehauf, K.E. and Sharma, M.M. 2008. A New Compositional Model for Hydraulic Fracturing With Energized Fluids. Paper SPE 115750 presented at the 2008 SPE Annual Technical Conference and Exhibition held in Denver, CO, 21-24 September.
2. Holditch, S.A. 2006. Tight Gas Sands. *Journal of Petroleum Technology*, June: 86-93. SPE 103356.
3. Wendorff, C.L. and Ainley, B.R. 1981. Massive Hydraulic Fracturing of High-Temperature Wells with Stable Frac Foams. Paper SPE 10257 presented at the Fall Technical Conference and Exhibition, San Antonio, Texas, 5-7 October.
4. Gabris S.J. and Taylor J.L. III. 1986. The Utility of CO2 as an Energizing Component for Fracturing Fluids. *SPE Production Engineering*. September: 351-358. SPE 13794.
5. Mazza, R.L. 2001. Liquid-Free CO2/Sand Stimulations: An Overlooked Technology – Production Update. Paper SPE 72383 presented at the SPE Eastern Regional Meeting held in Canton, Ohio, 17-19 October.
6. Rodvelt, G, Dials, G.A. and Monte, H. 1999. Case History: Carbon Dioxide Foam Stimulates Rome in Eastern Kentucky. Paper SPE 57430 presented at the SPE Eastern Regional Conference and Exhibition, Charleston, W.Virginia, 21-22 October.
7. King, G.E. 1986. Foam and Nitrified Fluid Treatments-Stimulation Techniques and More. This paper is based on a speech presented as a Distinguished Lecture during the 1985-1986 season. SPE 14477.
8. Blauer, R.E. and Kohlhaas, C.A. 1974. Formation Fracturing with Foam. Paper SPE 5003 presented at the 49th SPE-AIME Annual Fall Meeting, Houston, Texas, October.
9. Antoci, J.C, Briggiler, N.J. and Chadwick, J.A. 2001. Crosslinked Methanol: Analysis of a Successful Experience in Fracturing Gas Wells. Paper SPE 69585 presented at the SPE Latin America and Caribbean Petroleum Engineering Conference, Buenos Aires, Argentina, 25-28 March.
10. Gupta, D.V.S. 2003. Field Application of Unconventional Foam Technology: Extension of Liquid CO2 Technology. Paper SPE 84119 presented at SPE Annual Technical Conference and Exhibition, Denver, Colorado, 5-8 October.
11. Cambell, S.M, Fairchild, N.R. Jr., and Arnold, D.L. 2000. Liquid CO2 and Sand Stimulations in the Lewis Shale, San Juan Basin, New Mexico: A Case Study. Paper SPE 60317 presented at the SPE Rocky Mountain Regional/Low-Permeability Reservoirs Symposium and Exhibition, Denver, Colorado, 12-15 March.
12. Taylor, R, Khallad, A, Cheng, A, Barree, B, Byrnes, J, Kelly, K, Conway, M, Caufield, R, and Tourigny, S. 2002. Optimized Gas-Well Stimulating using CO2-Miscible, Viscosified Hydrocarbon Fracturing Fluids. Paper SPE 75666 presented at the SPE Gas Technology Symposium, Calgary, Alberta, Canada, 30 April – 2 May.
13. Nordgren, R.P. 1972. Propagation of a Vertical Hydraulic Fracture. *Society of Petroleum Engineers Journal*, August: 306-314.

CHAPTER 2: REVIEW OF TRADITIONAL FRACTURE MODELING*

Tight gas sands consist of geological formations that have different petrophysical and mechanical properties. Geoscientists and engineers decide which layers can be targeted to produce economical volumes of oil or gas. Once the target layers are identified, the engineer decides whether the zone needs stimulation, and if a fracture is necessary. The design of the fracture is based on predictive fracture propagation models, in order to optimize the fracture geometry and maximize hydrocarbon recovery.

Most fracture models make some preliminary assumptions about the fracture geometry and fluid mechanics. The fracturing model typically consists of three fundamental equations that are solved simultaneously:

- The injected fluid mass balance.
- The fracture mechanics equation that relates the pressure to the fracture width.
- A fluid flow equation that relates the pressure to the fluid flow in the fracture.

Other features such as proppant transport and fluid leak-off are included in these equations. All current fracture models (including those discussed in this chapter) do not include compositional, thermal, or phase behavior effects, so they are not applicable to energized fluids.

This chapter discusses two fracture propagation models. The first is a model developed by Nordgren[2]. It is a simple, one-dimensional model for vertical fractures. The second is a 3D model developed at The University of Texas at Austin and referred to as UTFRAC-3D. The UTFRAC-3D model has many more capabilities than Nordgren's model, including non-Newtonian flow, height propagation, and proppant transport. Many

* Many of the ideas expressed in this chapter were first written for SPE 115750 by Friehauf and Sharma[1].

of the ideas and theories used in these two models form the basis for developing the new model for energized fluids.

In Nordgren's model, UTFRAC-3D, and the new model for energized fluids presented in Chapter 3, it is assumed that a fracture is present when the fluid pressure is larger than the minimum horizontal stress in the formation. The fluid pressure causes a displacement (width) in the rock, which behaves elastically. The minimum horizontal stress signifies the minimum fluid pressure in the fracture because any lower pressure will cause the fracture to close. The fracture will grow perpendicular to the direction of minimum horizontal stress. Symmetry allows us to assume that the fluid injection creates two equal planar fractures. Each wing accepts half of the total injected flowrate. Only one wing is modeled.

2.1 Nordgren's Model for Vertical Fracture Propagation

Nordgren[2] considers a fracture that is vertical, and of constant height, propagating away from the wellbore. The cross-section of the fracture is elliptical, a result of assuming plane-strain in the vertical direction. This combination of assumptions comprises the Perkins-Kern-Nordgren or PKN fracture geometry, shown in Figure 2.1.

At least three items are coupled to create a complete hydraulic fracture propagation model: fluid mass balances, fracture mechanics, and flow behavior through the given geometry. Nordgren accomplished this for fractures with a PKN geometry.

Equation 2.1 is the continuity equation, or mass balance, for an incompressible fluid with one-dimensional flow:

$$h\frac{dq}{dx} + q_l + \frac{dA_c}{dt} = 0 \qquad (2.1)$$

q is the flowrate per unit height, q_l is the leak-off rate per unit length, and A_c is the cross-sectional area of the fracture.

Fracture mechanics defines the relationship between the fluid pressure in the fracture and the fracture width. Nordgren uses a simple expression, Equation 2.2, which shows that the fracture width is directly proportional to the difference between the fluid pressure and the stress in the layer:

$$w[x,z] = \frac{(1-\nu)}{G}(h^2 - 4z^2)^{1/2}(P[x] - \sigma); \quad -\frac{h}{2} < z < \frac{h}{2} \tag{2.2}$$

For an elliptical cross section, the average and maximum widths are related by a factor of $\pi/4$; therefore

$$A_c = \frac{\pi}{4} h w_{\max}. \tag{2.3}$$

A Newtonian fluid flowing through an ellipse has the following relationship between the flowrate and pressure drop in the fracture:

$$q = \frac{\pi {w_{\max}}^3}{64\mu}\frac{dP}{dx} \tag{2.4}$$

Where μ is the Newtonian viscosity of the fluid. The fluid loss per unit length has been shown to follow the following relationship:

$$q_l = \frac{2Ch}{\sqrt{t-\tau}} \tag{2.5}$$

Where C is the leak-off coefficient, t is pumping time, and τ is the time where the fracture is first opened at a given position. If we combine Equations 2.1-2.5, we derive the following differential equation:

$$\frac{G}{64(1-\nu)\mu h}\frac{d^2 {w_{\max}}^4}{dx^2} = \frac{8C}{\pi\sqrt{t-\tau}} + \frac{dw_{\max}}{dt} \tag{2.6}$$

Where G is the shear modulus of the formation:

$$G = \frac{E}{2(1+\nu)} \tag{2.7}$$

Equation 2.6 has the following boundary and initial conditions:

$$w_{\max}[x,0]=0 \tag{2.8.a}$$

$$w_{\max}[L(t),t]=0 \tag{2.8.b}$$

$$\frac{dw_{\max}{}^{4}[0,t]}{dx}=\frac{-256(1-\nu)\mu}{\pi G}q_{inj}h \tag{2.8.c}$$

Time, length, and width are made non-dimensional by Equations 2.9-2.11:

$$t_D=\frac{1}{\pi^2}[\frac{(1-\nu)\mu h q_{inj}{}^{2}}{32C^5G}]^{-2/3}t \tag{2.9}$$

$$L_D=\frac{1}{\pi}[\frac{(1-\nu)\mu h q_{inj}{}^{5}}{256C^8G}]^{-1/3}L \tag{2.10}$$

$$w_D=[\frac{16(1-\nu)\mu h q_{inj}{}^{2}}{C^2G}]^{-1/3}w \tag{2.11}$$

Nordgren solved this problem numerically, but analytical solutions can be obtained for the following cases:

$$L_D=1.32t_D{}^{4/5} \quad \& \quad w_D=t_D{}^{1/5} \text{ For 0 leak-off} \tag{2.12}$$

$$L_D=\frac{2}{\pi}t_D{}^{1/2} \quad \& \quad w_D=0.798t_D{}^{1/8} \text{ For high leak-off} \tag{2.13}$$

Equations 2.12 and 2.13 are plotted with the numerical results in Figures 2.2 and 2.3. Nordgren's results (Figures 2.2 and 2.3) are compared to the new model's results in Chapter 5.

2.2 Theory of Traditional 3D Fracture Propagation Model (UTFRAC-3D)

UTFRAC-3D is a simulator capable of modeling 3-D hydraulic fracture growth and proppant transport. This particular simulator solves the material balance, fracture width, and proppant concentration equations using a moving boundary element solver. The model assumes non-Newtonian, incompressible flow through a narrow slit. Fluid loss is modeled as a sink term in the 2-dimensional balance equation to represent flow in the third dimension. The fluid pressure determines the magnitude of the fracture width. Equations 2.14 and 2.17 show the fracture mechanics and fluid balance equations. These two equations are solved simultaneously in UTFRAC-3D. The technical nature of the program is discussed in Dr. Cheng Yew's book, *Hydraulic Fracture Mechanics*[3].

In UTFRAC-3D, the domain of the entire fracture face (2-dimensional plane) is referred to with the symbol Ω. The edges of the domain are given the symbol dΩ. Specifically, $d\Omega_p$ refers to the inlet of the fracture, or x = 0 and $d\Omega_f$ refers to the other edges of the fracture.

The fracture mechanics is governed by Equation 2.14:

$$-P(x,z)+\sigma(x,z)=\frac{G}{4\pi(1-\nu)}\int_{\Omega}[\frac{\partial}{\partial x}(\frac{1}{r})\frac{\partial w}{\partial x'}+\frac{\partial}{\partial z}(\frac{1}{r})\frac{\partial w}{\partial z'}]dx'dz' \qquad (2.14)$$

Where:

$$r=\sqrt{(x-x')^2+(z-z')^2} \qquad (2.15)$$

The boundary condition along the fracture edges is

$$w(x,z,t)=0 \qquad (2.16)$$

Equation 2.17 is the continuity equation for flow in the fracture:

$$\frac{\partial(\rho w)}{\partial t}+\frac{\partial(\rho q_x)}{\partial x}+\frac{\partial(\rho q_z)}{\partial z}+\frac{\rho_f q_l}{h}=0 \qquad (2.17)$$

Boundary conditions for all the edges are listed in Equation 2.18 and 2.19:

$$q_x = q_{inj} \text{ on inlet edge} \tag{2.18}$$

$$q_x \text{ or } q_z = 0 \text{ on all other edges} \tag{2.19}$$

The flowrate per unit height and pressure gradient have the following relationship[3]:

$$q_x = -\frac{n}{2n+1} K^{-\frac{1}{n}} \frac{w^{\frac{2n+1}{n}}}{2^{\frac{n+1}{n}}} [(\frac{dP}{dx})^2 + (\frac{dP}{dz})^2]^{\frac{1-n}{2n}} \frac{dP}{dx} \tag{2.20}$$

UTFRAC-3D includes an additional resistance to fracture growth by the use of the stress intensity factor (K_I) along the fracture edges. The stress intensity factor is calculated on the nodes on the edges of the facture by Equation 2.21[3].

$$K_I = \frac{G}{2(1-\nu)} \left(\frac{2\pi}{r} \right)^{1/2} w \tag{2.21}$$

Where r is the distance from the fracture tip. The fracture will advance whenever the stress intensity factor exceeds a critical value, K_{IC}, a material property of the rock. An iterative solution is needed in UTFRAC-3D because of this additional criterion. The additional resistance results in shorter fractures and higher bottom-hole pressures than Nordgren's model.

2.3 Estimation of Leak-off Coefficients from Reservoir Properties

Leak-off represents a loss of fluid into the formation. The driving force for leak-off is the pressure difference between fracture and reservoir. Fracturing models assume that leak-off occurs perpendicular to the fracture face. The rate of leak-off is usually not represented by Darcy's law or other types of flow equations. All of the above models require an estimation of the leak-off coefficient, C, to determine the leak-off rate. In the field, leak-off is estimated by doing a mini-frac test where a small amount of fluid is injected and the pressure response gives an estimation of the leak-off[4]. In the absence of

such data, leak-off can be estimated from fluid and reservoir properties. This section covers how the estimation is done.

The velocity of leak-off, u_l, is used to define the overall leak-off coefficient, C:

$$u_l = \frac{C}{\sqrt{t-\tau}} \tag{2.22}$$

The square root of time dependence results from the use of wall-building fluids. The symbol τ in Equation 2.22 represents the time where the fracture is first opened at a given position. The delayed time allows the wall-building material of the fluid to have a larger effect near the wellbore. Conversely, leak-off is high in newly opened regions of the fracture where no wall-building material has accumulated.

Traditional, single-phase leak-off can be described by the combination of three mechanisms: compression of reservoir fluids, the invaded zone of the reservoir filled with the fracturing fluid, and the filter cake built up by wall-building materials found in the fracturing fluid. Each mechanism can be described by its own leak-off coefficient[5].

The compressibility leak-off coefficient is:

$$C_c = \sqrt{\frac{\phi \kappa_R k}{\pi \mu_R}} \Delta P \tag{2.23}$$

The invaded zone leak-off coefficient is:

$$C_v = \sqrt{\frac{\phi k}{2\mu}} (\Delta P)^{1/2} \tag{2.24}$$

The wall-building coefficient is:

$$C_w = \frac{m_w}{2} \propto \Delta P^{1/2} \tag{2.25}$$

where m_w is determined by a fluid loss experiment where the fracturing fluid is flowed through a core sample. m_w is equal to the slope of the graph of cumulative filtrate volume versus the square root of time. In all three mechanisms, ΔP represents the difference between the fluid and reservoir pressures. This pressure difference needs to be

constant in order for C to be constant. This is not intuitively true because fluid pressure changes through time and down the length of the fracture. Usually C is calculated using an average pressure difference so it remains constant. The three coefficients can be combined to determine the overall leak-off coefficient[5]:

$$C = \frac{-\frac{1}{C_c} + \sqrt{\frac{1}{C_c^2} + 4\left(\frac{1}{C_v^2} + \frac{1}{C_w^2}\right)}}{2\left(\frac{1}{C_v^2} + \frac{1}{C_w^2}\right)} \tag{2.26}$$

Nomenclature

A_c	Fracture cross-sectional area
C	Overall leak-off coefficient
C_c	Compressibility of reservoir leak-off coefficient
C_v	Invaded zone leak-off coefficient
C_w	Wall-building coefficient
E	Young's modulus
G	Shear modulus
h	Fracture height
k	Permeability
K	Fluid consistency index
K_I	Stress intensity factor
K_{IC}	Critical stress intensity factor
L	Fracture half length
L_D	Dimensionless length
m_w	Wall-building factor
n	Power law Index
P	Pressure
q_{inj}	Injection rate per unit height
q_x	Fluid rate per unit height, x –direction
q_z	Fluid rate per unit height, vertical direction
q_l	Fluid loss rate per unit length
t	Time
t_D	Dimensionless time
u_l	Fluid loss velocity
w	Fracture width
w_D	Dimensionless width
w_{max}	Maximum fracture width
x	Horizontal coordinate
z	Vertical coordinate
Greek Symbols	
ΔP	Pressure difference, fracture and reservoir
$d\Omega_f$	Un-perforated edges of fracture
$d\Omega_p$	Perforated edge of fracture
κ_R	Compressibility of reservoir, 1/psi
ρ	Density, slurry
ρ_f	Density, fluid
μ	Fluid viscosity
μ_R	Viscosity of reservoir fluid
σ	Stress
ϕ	Porosity
τ	Fracture opening time
ν	Poisson's ratio
Ω	Fracture flow domain

References

1. Friehauf, K.E. and Sharma, M.M. 2008. A New Compositional Model for Hydraulic Fracturing With Energized Fluids. Paper SPE 115750 presented at the 2008 SPE Annual Technical Conference and Exhibition held in Denver, CO, 21-24 September.
2. Nordgren, R.P. 1972. Propagation of a Vertical Hydraulic Fracture. *Society of Petroleum Engineers Journal*, August: 306-314.
3. Yew, C.H. 1997. *Mechanics of Hydraulic Fracturing.* Gulf Pub Co.
4. Nolte, K.G, Mack, M.G. and Lie, W.L. 1993. A Systematic Method for Applying Fracturing Pressure Decline. Paper SPE 25845 presented at the SPE Rocky Mountain Regional Low Permeability Symposium, Denver, Colorado, 12-14 April.
5. Schechter, R.S. 1992 .*Oil Well Stimulation.*Englewood Cliffs, N. Jersey:Prentice Hall.

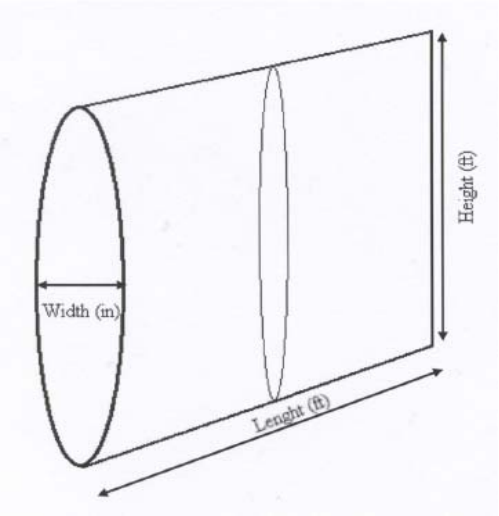

Figure 2.1. Drawing of Perkins-Kern-Nordgren[2] or PKN fracture geometry.

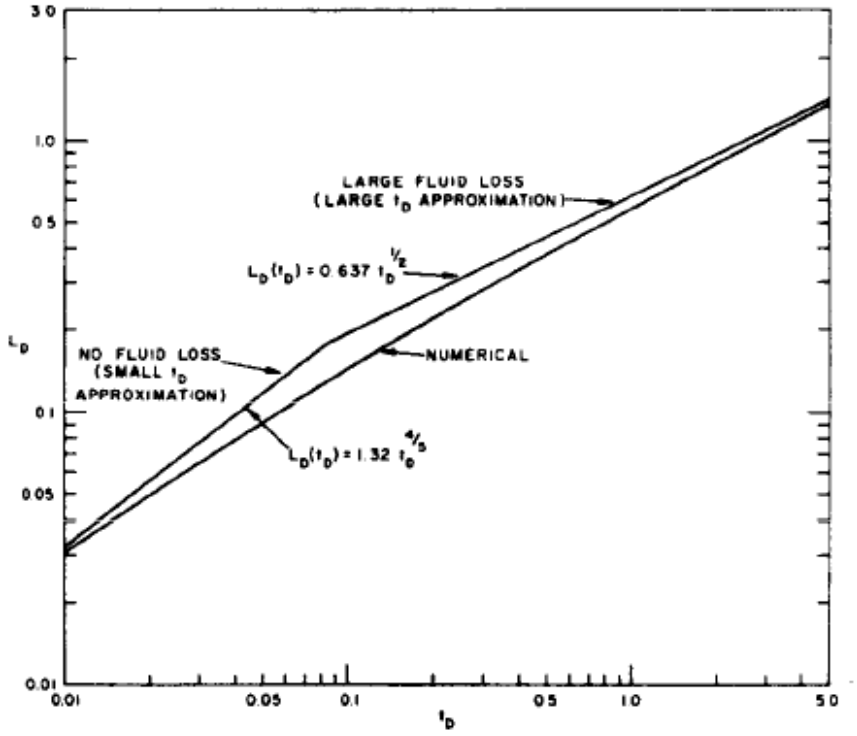

Figure 2.2. Nordgren's[2] results of dimensionless length versus dimensionless time for his fracture propagation model.

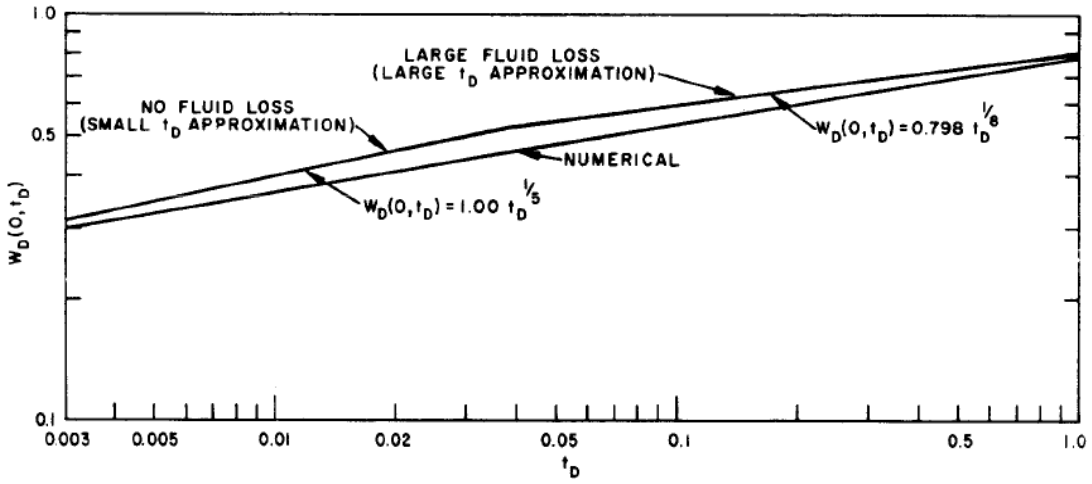

Figure 2.3. Nordgren's[2] results of dimensionless width versus dimensionless time for his fracture propagation model.

CHAPTER 3: FORMULATION OF ENERGIZED FRACTURE PROPAGATION MODEL

This chapter discusses the theories and equations that make up the fracture propagation model for energized fluids (EFRAC). The discussion is split into nine sections. The first seven of these cover the topics of fracture mechanics, component balances, proppant transport, overall mass balances, energy balances, phase behavior, and wellbore equations. Each section lists the assumptions and their justification as well as the limitations of the model. The model equations are coupled together in a modular fashion to create the complete model. The eighth section covers multiple fractures, and the last section draws connections between topics and describes the numerical methods used to solve the equations.

All equations were derived to be as general as possible. There are no specific assumptions that limit the fluid behavior. For example, the equations for a general number of components (NC) and fluid phases (NP) are shown. This way, the user is not limited regarding the choice of fluid. However, some assumptions are still needed in order to create an efficient and complete model. These assumptions are justified in their respective sections.

New theories are distinguished from those which have been established in the past. The ideas behind the component balance, energy balance, and phase behavior have never been applied to a fracture model, but there are several analogies that can be made to the world of compositional reservoir simulators. The ideas in the fracture mechanics, proppant transport, and wellbore model have been used in preceding fracture models.

3.1 Fracture Mechanics

In our model, it is assumed that the fractures are contained (constant height) and follow the shape prescribed by the Perkins-Kern and Nordgren (or PKN) fracture model[2]. The PKN geometry assumes that fractures are vertically oriented and are of a constant height. Vertically oriented fractures occur in formations where the overburden (vertical) stress is larger than in any other directions, making it easier for the fluid to part the rock, rather than lift it. Constant height fractures occur when the stress contrast between the sand and the bounding geologic layers is high. For example, in tight gas sands, overlying and underlying shale layers have high stress and maintain the fracture height in the sandstone layer.

All equations are solved in a rectangular domain, shown in Figure 3.1. The fracture width (in the third dimension) is included by mapping it on the 2D domain. In the PKN geometry, the cross-section of the fracture is elliptical. The width at each location is calculated by:

$$w[x,z]=\frac{(1-\nu)}{G}(h^2-4z^2)^{1/2}(P[x]-\sigma) \quad -\frac{h}{2}<z<\frac{h}{2} \tag{3.1}$$

The pressure in Equation 3.1 is one-dimensional and varies only in the x direction. In the model presented here, the pressure varies not only in the x direction, but in the z direction as well (2D). To calculate the fracture width, the fluid pressure in the fracture is averaged vertically (z direction), giving a pseudo one-dimensional pressure profile that can be used in Equation 3.1:

$$w=\frac{(1-\nu)}{G}(h^2-4z^2)^{1/2}\left(\sum_{jj}^{Numj}\frac{P[x,jj]}{Numj}-\sigma\right)=B\left(\sum_{jj}^{Numj}\frac{P[x,jj]}{Numj}-\sigma\right)=BP^{*net} \tag{3.2}$$

Equation 3.2 gives the definition of the parameter, B, which is the proportionality constant between the fracture width and the average vertical net pressure.

The fracture grows in length by a macroscopic mass balance on the fluid. The macroscopic balance tracks the mass of fluid pumped, leaked-off, and currently existing

in the fracture. Calculating the fracture length in this way is simple but does not include additional mechanical resistance to fracture growth at the tip.

3.2 Component Mass Conservation Equations

The mass of each component pumped into the fracture must be conserved; therefore, a component mass balance is derived. The mass balance of each component, i, is shown in Equation 3.3. There are NC number of components and therefore NC number of component balance equations. NP is the number of fluid phases. The solid phase (proppant) is not included as a phase or component. Proppant transport is covered by a separate mass balance, shown in the next section.

$$\frac{d[w(1-c)\sum_{j=1}^{NP} S_j \rho_j x_{ij}]}{dt} + \frac{d[(1-c)\sum_{j=1}^{NP} q_{x,j} \rho_j x_{ij}]}{dx} + \frac{d[(1-c)\sum_{j=1}^{NP} q_{z,j} \rho_j x_{ij}]}{dz} + \frac{2}{\sqrt{t-\tau}} \sum_{j=1}^{NP} S_j \rho_j x_{ij} C_j = 0 \tag{3.3}$$

Equation 3.3 includes no diffusive fluxes because it is assumed that convection dominates the process. The (1-c) in the terms of Equation 3.3 accounts for the space that is occupied by the proppant. Each of the variables is described in the nomenclature section.

The fourth term on the left-hand side of Equation 3.3 represents the mass lost because of fluid leak-off. Leak-off occurs perpendicular to the fracture face and is determined by the leak-off coefficient[3], C. Multi-phase leak-off is defined in the same way, with the leak-off coefficient defined for each phase, C_j. The inverse of the square root of time dependence for leak-off is associated with the wall-building characteristics of fracturing fluids.

We assume that the multi-phase leak-off is proportional to the phase saturation, S_j. This idea is not discussed in the traditional fluid leak-off literature because it does not

include multiple phases. As a result, the leak-off coefficient for phase j, C_j, represents the leak-off if the saturation of that given phase is one. As the saturation goes down, the leak-off decreases because the wall of the fracture is exposed to less of that phase. Clearly the leak-off will go to zero when the saturation goes to zero.

The definition of the overall mass fraction of component i is:

$$z_i = \frac{\sum_{j=1}^{NP} S_j \rho_j x_{ij}}{\sum_{j=1}^{NP} S_j \rho_j} \tag{3.4}$$

Equation 3.3 is altered so that z_i, the overall mass fraction, is the dependant variable.

$$\frac{d[z_i w(1-c)\sum_{j=1}^{NP} S_j \rho_j]}{dt} + \frac{d[(1-c)\sum_{j=1}^{NP} q_{x,j} \rho_j x_{ij}]}{dx} + \frac{d[(1-c)\sum_{j=1}^{NP} q_{z,j} \rho_j x_{ij}]}{dz} + \frac{2}{\sqrt{t-\tau}} \sum_{j=1}^{NP} S_j \rho_j x_{ij} C_j = 0 \tag{3.5}$$

$$z_i = z_{i,inj} \text{ on } \partial\Omega_P$$
$$q = 0 \text{ on } \partial\Omega_f \ \& \ \partial\Omega_L$$

The boundary conditions for the component mass conservation equations are shown in Equation 3.5. The upper and lower boundaries are no-flow boundaries. This condition is true for all equations pertaining to the flow inside the fracture. On the inlet edge of the fracture, composition of the fluid is known and constant during each stage of pumping.

Fluid additives such as foamer and breaker are assumed to partition into the fluid phases, but do not adsorb on the proppant or reservoir rock. Additives are generally not considered as a component. In cases where this assumption does not hold, the additive in question can become a traceable component by adding it to NC and taking the proper measures in evaluating its phase behavior.

3.3 Proppant Transport Equations

The proppant does not participate in phase behavior and may travel at a different velocity than the fluid phases because of gravity, wall, and concentration effects. As a result, proppant is tracked with a separate transport equation. Equation 3.6 shows the proppant transport equation based on the conservation of mass of solid. The UTFRAC-3D model discussed in Chapter 2 solves a similar equation.

$$\frac{\partial[\rho_p wc]}{\partial t}+\frac{\partial[\rho_p q_x k_{ret} c]}{\partial x}+\frac{\partial[\rho_p (q_z - V_{set} w)c]}{\partial z}=0 \qquad (3.6)$$

$$c = c_{in} \text{ on } \partial\Omega_p$$
$$q = 0 \text{ on } \partial\Omega_f \ \& \ \partial\Omega_L$$

V_{set} is the settling velocity of the proppant. V_{set} is calculated by Stokes Law and is corrected for inertial effects, proppant concentration, and fracture walls. Experiments show[4] that high proppant concentrations and small fracture widths retard the horizontal movement of the proppant. The parameter k_{ret} is a horizontal retardation factor, calculated by experimental correlations. The parameter corrects for the fact that the proppant may not be traveling at the same velocity as the fluid. The next two sections list the correction factors for proppant transport.

3.3.1 PROPPANT SETTLING

In addition to the velocity of the fluid, the proppant will experience an additional velocity in the direction of gravity because of the gravitational body force felt by the proppant particles. As a first approximation, the settling velocity is calculated using Stoke's Law.

$$V_{stokes}=\frac{(\rho_p-\rho_f)gd_p^2}{18\mu} \qquad (3.7)$$

Stoke's law is applicable to low Reynolds number flows in an unbounded fluid (no walls or additional spheres). We correct the settling velocity of the fluid by three correction factors.

- Inertial effects

- Effect of proppant concentration
- Effect of fracture walls

Each correction factor is applied to the Stoke's velocity. Equations 3.8-3.10 are correction factors for the inertial, proppant concentration, and fracture walls, respectively[4].

$$f(\mathrm{Re}_p) = \frac{0.3736\mu^{0.57}}{\rho_f^{0.29}(\rho_p - \rho_f)^{0.29} d_p^{0.86}} \tag{3.8}$$

$$f(c) = -5.9c^3 + 8.8c^2 - 4.8c + 1 \tag{3.9}$$

$$f(w) = 0.563\left(\frac{d_p}{w}\right)^2 - 1.563\left(\frac{d_p}{w}\right) + 1 \tag{3.10}$$

As Equation 3.11 shows, the correction factors are multiplicative and assumed to be independent of each other.

$$V_{set} = V_{stokes} f(\mathrm{Re}_p) f(c) f(w) \tag{3.11}$$

3.3.2 PROPPANT RETARDATION

While the settling velocity corrects for the proppant transport in the vertical direction, proppant particles also experience similar effects in the horizontal direction.

Two effects have been studied in regard to proppant retardation[4]: 1) effect of fracture walls and 2) effect of proppant concentration. Results from the fracture wall study are shown in Equation 3.12. The effect of proppant concentration is evaluated by calculating an effective fracture width, and using the new width (Equation 3.13) in Equation 3.12.

$$k_{ret} = 1 + \left(\frac{d_p}{w}\right) - 2.02\left(\frac{d_p}{w}\right)^2 \tag{3.12}$$

$$\frac{1}{w_c^2} = 1.411\left(\frac{1}{d_p{}^2} - \frac{1}{w^2}\right)c^{0.8} \tag{3.13}$$

3.4 Overall Mass Balance (Pressure Equation)

The previous two sections covered mass balances on all fluid components and proppant respectively. The sum of all the balances is converted into an overall mass balance equation. The overall mass balance is combined with the flow equations in the given geometry. An equation with the pressure as the dependant variable is the outcome. This section shows the derivation of this equation.

Summing all component mass balances and adding the proppant mass balance results in the equation shown below.

$$\frac{d[w(\sum_{i=1}^{NC}\sum_{j=1}^{NP}(1-c)S_j\rho_j x_{ij}+\rho_p c)]}{dt}+\frac{d[(\sum_{i=1}^{NC}\sum_{j=1}^{NP}q_{x,j}((1-c)\rho_j x_{ij}+\rho_p c)]}{dx}$$
$$+\frac{d[(\sum_{i=1}^{NC}\sum_{j=1}^{NP}q_{z,j}((1-c)\rho_j x_{ij}+\rho_p c)]}{dz}+\frac{2}{\sqrt{t-\tau}}\sum_{i=1}^{NC}\sum_{j=1}^{NP}S_j\rho_j x_{ij}C_j=0 \quad (3.14)$$

Equation 3.15 shows definitions of the proppant corrected density, ρ_j^*, and Equation 3.16 shows the definition of the fractional flow of each phase, F_j.

$$\rho_j^* = \rho_j(1-c)+\rho_p c \quad (3.15)$$

$$q_{x,j} = q_x F_j \quad (3.16)$$

Also note that the sum of all compositions, x_{ij}, in each phase is equal to one. Equation 3.14 is simplified to:

$$\frac{d[w(\sum_{j=1}^{NP}S_j\rho_j^*)]}{dt}+\frac{d[q_x(\sum_{j=1}^{NP}F_j\rho_j^*)]}{dx}$$
$$+\frac{d[q_z(\sum_{j=1}^{NP}F_j\rho_j^*)]}{dz}+\frac{2}{\sqrt{t-\tau}}\sum_{j=1}^{NP}S_j\rho_j C_j=0 \quad (3.17)$$

Next, the fluid flow term, q, is expanded. It is assumed that flow inside the fracture is laminar, and the fluid behaves with power law rheology. The presence of two

or more phases in the fracture can alter the flow behavior. This is because 1) each phase can have different power law parameters, and 2) a single phase does not occupy the entire width. The previously mentioned assumptions lead to:

$$q_{x,j} = -S_j^{m_j} \frac{n_j}{2n_j+1} K_j^{-\frac{1}{n_j}} \frac{w^{\frac{2n_j+1}{n_j}}}{2^{\frac{n_j+1}{n_j}}} [(\frac{dP}{dx})^2 + (\frac{dP}{dz})^2]^{\frac{1-n_j}{2n_j}} \frac{dP}{dx} \quad (3.18)$$

Where $q_{x,j}$ is the flowrate per unit height of each phase including proppant (flowrate of both the fluid and solid phases, not just the fluid phases). For single-phase fluids, Equation 3.18 reverts to the form used in traditional hydraulic fracture models[5]:

$$q_x = -\frac{n}{2n+1} K^{-\frac{1}{n}} \frac{w^{\frac{2n+1}{n}}}{2^{\frac{n+1}{n}}} [(\frac{dP}{dx})^2 + (\frac{dP}{dz})^2]^{\frac{1-n}{2n}} \frac{dP}{dx} \quad (3.19)$$

If the fluid is Newtonian (n = 1), Equation 3.19 is equivalent to flow in a slot with narrow width[3]:

$$q_x = -\frac{w^3}{12\mu} \frac{dP}{dx} \quad (3.20)$$

Equations 3.18-3.20 show the difference between flow equations for the three different models discussed. Each relates the flow per unit height of the slurry to the width, rheology, and pressure gradient applied. Equation 3.20 assumes Newtonian viscosity. Equation 3.19 introduces power law rheology. Finally, Equation 3.18 represents both multiple-phase flow and power law rheology. The parameters n, K, and m all have j subscripts in Equation 3.18, meaning that each phase can have a different value. This allows each phase to flow at different rates because of different rheology or saturation.

The power law values of n and K are known functions of polymer loading, temperature, proppant concentration, pH, shear history, surfactant conditions, and other factors[6-14]. This list is greatly extended for foams. However, Equation 3.18 still holds

because it is generally written for local or nodal values of n and K. As a result, any *a priori* model that describes changes in n and K can easily be incorporated into the fracture model.

Let's take foam for example; experiments involving foam showed that the continuous liquid phase and the bubbles of gas traveled at the same rate[8,11] (no slippage between phases). Therefore, we model all n_j's and K_j's as equal to each other and m_j's equal to one. The same references[8,11] report n and K values changing with different temperatures and foam qualities. At each node, the value of n and K is updated based on changes in those properties but n and K have the same value for each phase. Because the flow equations are for the slurry and not just the fluid phases, it is appropriate that n and K can change with proppant concentration too.

The parameter A can be defined for each phase or for the slurry so that:

$$q_{x,j} = A_j \frac{dP}{dx} = -\frac{S_j^{\,m_j} w^3}{12\mu_{eff,j}} \frac{dP}{dx} \tag{3.21}$$

$$q_x = A\frac{dP}{dx} = -\frac{w^3}{12}\sum_{j=1}^{NP} \frac{S_j^{\,m_j}}{\mu_{eff,j}} \frac{dP}{dx} \tag{3.22}$$

Similar equations can be written for the vertical direction. The term F_j, the fraction of the overall flowrate that is of the jth phase, is also defined in terms of another parameter, A, shown in Equation 3.23.

$$F_j = \frac{A_j}{\sum_{j=1}^{NP} A_j} = \frac{A_j}{A} \tag{3.23}$$

Equations 3.2 and 3.22 are plugged into the overall mass balance (Equation 3.17) to get a form of the overall mass balance where the pressure is the dependant variable (Equation 3.24). This is the form of the equation that is solved in the model. Note that pressure gradients and the net pressure gradients are equivalent because $P^{net} = P-\sigma$.

$$\frac{d[P^{*net}B(\sum_{j=1}^{NP}S_j\rho_j^{\ *})]}{dt}+\frac{d[(\sum_{j=1}^{NP}F_j\rho_j^{\ *})A\frac{dP}{dx}]}{dx}$$
$$+\frac{d[(\sum_{j=1}^{NP}F_j\rho_j^{\ *})A\frac{dP}{dz}]}{dz}+\frac{2}{\sqrt{t-\tau}}\sum_{j=1}^{NP}S_j\rho_jC_j=0 \quad (3.24)$$

$$q=q_{inj} \text{ on } \partial\Omega_P$$
$$q_z=0 \text{ on } \partial\Omega_f$$
$$P=\sigma \text{ on } \partial\Omega_L$$

It is important to take note of the boundary conditions in Equation 3.24. The upper and lower boundaries are no-flow boundaries, similar to the component mass balance. The right and left boundaries are different. The inlet edge of the fracture has a known injection rate. The far edge is set to a net pressure of zero or a pressure equal to the stress. The fracture width will also be zero at the tip.

3.5 Energy Conservation Equations

The following equation is the energy balance formulated for a multi-phase fluid in the fracture:

$$\frac{d((\sum_{j=1}^{NP}C^*_{p,j}S_j)wT)}{dt}+\frac{d(T\sum_{j=1}^{NP}C^*_{p,j}q_{x,j})}{dx}+\frac{d(T\sum_{j=1}^{NP}C^*_{p,j}q_{z,j})}{dz}$$
$$+\frac{2\sum_{j=1}^{NP}C_{p,j}\rho_jS_jC_jT}{\sqrt{t-\tau}}=Q_{cond} \quad (3.25)$$

$$T=T_{inj} \text{ on } \partial\Omega_P$$
$$q=0 \text{ on } \partial\Omega_f \ \& \ \partial\Omega_L$$

Equation 3.25 was derived assuming kinetic energy and Joule-Thompson effects are negligible. $C^*_{p,j}$ is the proppant corrected heat capacity of phase j shown by:

$$C^*_{p,j} = (1-c)C_{p,j}\rho_j + cC_{p,prop}\rho_p \tag{3.26}$$

Q_{cond} is the heat conduction from the reservoir to the fracturing fluid. The amount of heat conducted is derived from a transient energy balance on the reservoir[3].

$$Q_{cond} = 2\sqrt{\frac{K_R\rho_R C_{pR}}{\pi t}}(T_R - T) \tag{3.27}$$

Equation 3.27 does not take the effect of leak-off into account. Meyer[15] identified two correction factors that reduced the heat conduction due to fluid leak-off, which he calls "heat blockage." He applied them to one-dimensional energy balances. We use these correction factors in the same way in the equation:

$$Q_{cond} = 2\sqrt{\frac{K_R\rho_R C_{pR}}{\pi t}}(T_R - T)\psi(C)\Phi(C) \tag{3.28}$$

$\Psi(C)$ corrects for cooling of the reservoir because of fluid leak-off. $\Phi(C)$ corrects for the thermal resistance of the fluid that has leaked-off. Each value is defined as follows:

$$\psi(C) = \exp(-\lambda^2) - \sqrt{\pi}\lambda erfc(\lambda) \tag{3.29}$$

$$\lambda = \frac{C}{2\sqrt{\alpha_R}}\frac{(\rho Cp)_{fL}}{(\rho Cp)_R}\frac{\rho_f}{\rho_{fL}} \tag{3.30}$$

$$\Phi(C) = \sqrt{\pi}\beta\exp(\beta^2)erfc(\beta) \tag{3.31}$$

$$\beta = \frac{\beta_o\sqrt{1-\tau/t}}{w/w_{\max}} \tag{3.32}$$

$$\beta_o = \frac{Nuk_f\sqrt{\alpha_R t}}{wK_R\Psi(\lambda)} \tag{3.33}$$

3.6 Phase Behavior Equations

An equation of state (EOS) is used to predict the phase behavior of the fluid. We assume that all phases are in phase equilibrium at all times. The equation of state calculates the compressibility factor and, therefore, the density of each phase. An EOS also updates the saturation and weight fractions of each phase. Any EOS can be used with the model; however, the results presented in this study are for the Peng-Robinson EOS[16]. A simpler method is to solve the Ratchford-Rice equation for known equilibrium (K_{eq}) values. The equations are discussed here because they constitute a number of independent equations that have to be satisfied if phase equilibrium is assumed.

3.6.1 PENG-ROBINSON EOS

Equation 3.34 is the Peng-Robinson equation of state.

$$P = \frac{RT}{\bar{V} - b} - \frac{a(T)}{\bar{V}(\bar{V} - b) + b(\bar{V} - b)} \tag{3.34}$$

$$a(T) = \Omega_a \frac{\alpha (RT_c)^2}{P_c}$$

$$b = \Omega_b \frac{RT_c}{P_c}$$

$$\Omega_a = 0.45724$$

$$\Omega_b = 0.07780$$

$$\alpha = [1 + m(1 - \sqrt{\frac{T}{Tc}})]^2$$

$$m = 0.37464 + 1.54226\omega - 0.26992\omega^2$$

For multiple components:

$$a = \sum_i^{Nc} \sum_k^{Nc} \bar{x}_i \bar{x}_k \sqrt{a_i a_k} (1 - BIP_{ik}) \tag{3.35}$$

$$b = \sum_i^{Nc} \bar{x}_i b_i \tag{3.36}$$

In terms of the compressibility factor, Z, Peng-Robinson becomes:

$$Z^3-(1-B)Z^2+(A-3B^2-2B)Z-(AB-B^2-B^3)=0$$
$$A=\frac{aP}{(RT)^2} \tag{3.37}$$
$$B=\frac{bP}{RT}$$

The fugacity coefficient for component i is:

$$\ln\phi_i=\frac{b_i}{b}(Z-1)-\ln(Z-B)$$
$$-\frac{A}{2\sqrt{2}B}\left(\frac{2}{a}\sum_k^{Nc}\overline{x}_k a_k-\frac{b_i}{b}\right)\ln\left(\frac{Z+(1+\sqrt{2})B}{Z+(1-\sqrt{2})B}\right) \tag{3.38}$$

A requirement for phase equilibrium is equal fugacity of each component in each phase, therefore, Equation 3.38 represents NC*(NP-1) number of equations that must be satisfied to use the PREOS.

The Peng-Robinson EOS sometimes shows errors in the estimations of molar volume. To correct this, the volume shift parameter can be used:

$$\overline{V}=\overline{V}^*-\sum_i^{NC}\overline{c}_{vsi}\overline{x}_i \tag{3.39}$$

The star in Equation 3.39 represents the molar volume predicted using the EOS.

Peng-Robinson subroutines have been associated with compositional reservoir simulators for years. It is not necessary to write an original piece of code when the subroutines are available from that field of study. The model presented here uses a subroutine written by Ryosuke Okuno[17-19] of the University of Texas instead of code written by this author.

3.6.2 KNOWN EQUILIBRIUM VALUES

Solubility of two phase multi-component systems is estimated by Henry's Law constants as an alternative to the Peng-Robinson equation of state. Henry's law constants

are specified for each component. Equation 3.40 shows the relationship between Henry's Law constants, H_i, and $K_{eq,i}$.

$$K_{eq,i} = \bar{y}_i / \bar{x}_i = H_i / P \tag{3.40}$$

The Ratchford-Rice equation (Equation 3.41) can estimate the phase split, F_v, from the known K values.

$$\sum_{i}^{Nc} \frac{\bar{z}_i (K_{eq,i} - 1)}{1 + \bar{F}_v (K_{eq,i} - 1)} = 0 \tag{3.41}$$

3.7 Wellbore Model

In fracturing, it is difficult to know the conditions at the bottom of the well because most measurements are done at the surface. Down-hole measurements are usually not conducted due to cost constraints. Most of the time, calculations are done to relate the surface and bottom-hole properties of the fluid. For example, a fluid's temperature is measured at the surface, before the fluid flows down the well, but this temperature may change by the time the fluid enters the fracture. Also, pressure changes in the wellbore because of the weight of the fluid in the wellbore and because of friction against the pipe walls. This following section describes the theories and equations behind the pressure and temperature variations in the wellbore.

3.7.1 Temperature Variation in the Wellbore

The fracturing fluid temperature usually increases when it is pumped down the wellbore. The heat transfer is amplified when the temperature difference between the fluid and the earth is large. This condition occurs with energized fluids that are pumped at temperatures up to 90° F colder than traditional fluids.

An energy balance on the fluid in the wellbore can be written as[20]:

$$\frac{dT_f}{dz} = -L_R (T_f - T_{ei}) \tag{3.42}$$

We assume that kinetic energy (dv/dz) and Joule-Thompson effects are negligible. Equation 3.42 implies that driving force between the fluid and earth temperature is the main and only contributor to temperature increase of the fluid in the wellbore. T_{ei} is the temperature of the earth as a function of depth:

$$T_{ei} = T_{es} + g_G z \tag{3.43}$$

Where T_{es} is the earth's surface temperature and g_G is the geothermal gradient (F/ft). Equation 3.42 is solved for the fluid temperature, T_f, as a function of depth, z, so that

$$T_f = T_{ei}(z) + \frac{g_G}{L_R}(e^{-L_R z} - 1) + (T_{fi} - T_{es})e^{-L_R z}. \tag{3.44}$$

The parameter L_R in Equation 3.42 is a type of overall heat transfer coefficient. It depends on the thermal properties of the wellbore and formation. For simplicity, L_R is assumed constant. L_R can be estimated as[20]

$$L_R = \frac{2\pi}{C^*_p \dot{m}}\left(\frac{r_{to}U_{to}K_R}{K_R + r_{to}U_{to}T_D}\right). \tag{3.45}$$

Where T_D is the dimensionless temperature and is correlated with dimensionless time t_D.

$$T_D = \ln(e^{-.2t_D} + (1.5 - .3719e^{-t_D})\sqrt{t_D}) \tag{3.46}$$

$$t_D = \frac{4K_R t}{\rho_e C_{p,R} D_{wb}^{\ 2}} \tag{3.47}$$

U_{to} is a heat transfer coefficient involving all thermal resistances through a common completion. A common completion includes the thermal resistances of

1) Convection inside the tubing

2) Conduction through the tubing

3) Conduction through insulation outside the tubing

4) Natural convection through the annulus

5) Conduction through the casing

6) Conduction through the cement

If any part of the completion does not exist in a particular case, the thermal resistance of that part can be set to zero. The following equation shows how all the thermal resistances can be combined into the term U_{to}:

$$\frac{1}{U_{to}} = D_{to}\left(\frac{1}{D_{ti}h_t} + \frac{1}{2\ln(D_{to}/D_{ti})k_t} + \frac{1}{2\ln(D_{ins}/D_{to})k_{ins}} + \frac{1}{D_{ins}h_c} + \frac{1}{2\ln(D_{caso}/D_{casi})k_{cas}} + \frac{1}{2\ln(D_{wb}/D_{caso})k_{cem}}\right) \quad (3.48)$$

The heat transfer coefficients for the natural convection in the annulus, h_c, and convection inside the tubing, h_t, are calculated from correlations.

3.7.2 PRESSURE DROP IN THE WELLBORE

We assume there are two mechanisms for pressure change in the wellbore: 1) hydrostatic head caused by the weight of the fluid above it, and 2) the frictional pressure drop. All others are assumed negligible. The pressure gain by the hydrostatic head per unit of length is simply the density of the fluid multiplied by the gravitational constant. The frictional pressure drop is calculated using friction factors from correlations. Usually, the flowrates, viscosities, and tubing diameters used in fracturing results in turbulent flow. The following equation shows a common correlation for the friction factor for turbulent flow[21]:

$$f = \{-1.737\ln[.269\frac{\varepsilon}{D_{ti}} - \frac{2.185}{\mathrm{Re}}\ln(.269\frac{\varepsilon}{D_{ti}} + \frac{14.5}{\mathrm{Re}})]\}^{-2} \quad (3.49)$$

This correlation predicts unreasonably large pressure drops. Fracturing fluids usually contain high molecular weight, friction reducing, polymers which have been known to dampen the energy dissipation for turbulent flows causing a reduction in friction. The process is called drag reduction. A new friction factor correlation is used that predicts a much lower friction factor[21]:

$$\ln(f) = 28.135 + (-29.379 + (8.2405 - 0.86227x)x)x \tag{3.50}$$

$$x = \ln(\ln(\mathrm{Re}_w))$$

The wall Reynolds number, Re_w, is used so that the shear thinning of the fluid is taken into account. The wall Reynolds number is related to the general Reynolds number by

$$\mathrm{Re}_w = \left(\frac{1+3n}{4n}\right)\mathrm{Re} \tag{3.51}$$

.

With the friction factor known, the pressure gradient can be calculated by

$$\frac{dP}{dz} = -\frac{2f\rho v^2}{D_{ti}} + \rho g \tag{3.52}$$

.

The multi-phase aspect of the fluid flow is taken into account by averaging fluid properties across a vertical section of the wellbore. Flash calculations are done at intermediate locations in the wellbore. Fluid properties are updated so that changes in pressure drop and temperature are adjusted for the phase behavior of the fluid.

3.8 Multiple Fractures

The fracture model includes a feature that can calculate fracture dimensions for multiple fractures when multiple sets of perforations are open during one pumping schedule. The challenge of modeling this is to determine the fraction of the total flowrate that enters each set of perforations. To determine this fraction, the fracture model works in connection with the wellbore model in order to maintain consistent pressures in the wellbore. In a given time step, the flow is arbitrarily divided into each open fracture and the bottom-hole pressure is calculated. If the calculated pressures are not consistent, the flowrate is redistributed until convergence of pressure is achieved.

3.9 Model Design and Numerical Methods

The model is built in a modular fashion so that each element of the model can be easily updated or improved. There are five primary modules:

- Wellbore model that correlates the surface and bottom-hole conditions.
- Coupling of fluid pressure balances with fracture mechanics.
- Compositional balance that computes fluid composition, including proppant concentration
- Energy balance that computes temperature.
- Phase behavior

The equations above form a set of non-linear partial differential equations that are solved numerically. There are NC*NP + 3NP + 4 equations and unknowns at each nodal location inside the fracture. Table 3.1 outlines each unknown variable. Table 3.2 outlines the number of equations.

A central finite differencing scheme is used to solve the conservation equations for net pressure, composition, temperature, and proppant concentration. In a given time step, the pressure equation is solved implicitly first. The new pressures are used to update the fluid flow rates in the other conservation equations, which are solved for explicitly. After all equations are satisfied, phase behavior calculations are made in order to estimate the volume fraction and properties of each phase. Fluid properties, including rheological properties, are then updated. Figure 3.2 shows a flowchart of these ideas. The information loop shown in Figure 3.2 is repeated for every time step. The modules for equation of state, leak-off, and rheology can easily be upgraded without redoing the rest of the code. In Figure 3.2, i and j represent the nodal numbering in the horizontal and vertical direction respectively; capital "I" refers to the component, k, the phase, and n, the time step. The full list of finite difference equations is shown in Appendix A.

The equations shown in this chapter are compiled together into an executable program. The program is used to acquire the conclusions that are given in the following

chapters. Also, a user interface was created for future researchers to use. The full model, with user interface, is referred to as EFRAC.

Nomenclature

* Bar over value represent molar value

a,b,A,B	Peng-Robinsion Coefficients
A	Parameter relating flowrate per unit height to pressure gradient
B	Parameter relating net fluid pressure to fracture width
BIP	Binary interaction parameter
c	Proppant concentration (vol/vol)
c_{in}	Proppant concentration (inlet)
C	Overall leak-off coefficient
C_j	Phase leak-off coefficient
C_p	Heat capacity
C_{pj}	Phase heat capacity (without proppant)
C_{pj}^*	Proppant corrected phase heat capacity
C_{pfl}	Heat capacity of leaked-off fluid
$C_{p,prop}$	Heat capacity of proppant
C_{pR}	Heat capacity, reservoir
c_{vsi}	Volume shift parameter*
d_p	Proppant diameter
D	Diameter, subscripts: wb = wellbore, caso = casing, outside, casi = casing, inside, ins = insulation, cem = cement, to = tubing, outside, ti = tubing, inside
E	Young's modulus
f	Friction factor
F_j	Fractional flow of each phase
F_v	Molar fraction of "gas" phase*
g	Gravitation constant
G	Shear modulus
g_G	Geothermal gradient
h	Fracture height
hc	Convective heat transfer coefficient, natural convection in annulus
ht	Convective heat transfer coefficient, tubing
H_i	Henry's law constant
K	Fluid consistency index
k_{cas}	Thermal conductivity, casing
k_{cem}	Thermal conductivity, cement
k_f	Thermal conductivity, fluid
k_{ins}	Thermal conductivity, insulation
k_t	Thermal conductivity, tubing
$K_{eq,i}$	Component K factor, phase behavior = yi/xi
K_R	Thermal conductivity, reservoir
k_{ret}	Proppant retardation factor
L	Fracture half length
L_R	Heat transfer in wellbore coefficient
m(dot)	Mass flowrate
m_j	Exponent of multi-phase flow
n	Power law Index
NC	Number of components
NP	Number of phases
Nu	Nusselt number

Numj	Number of nodes in vertical (z) direction
P	Pressure
P^{*net}	Average vertical net pressure
P_c	Critical pressure
q_{inj}	Injection rate per unit height
q_x	Fluid flowrate, x –direction
q_z	Fluid flowrate, vertical direction
Q_{cond}	Heat conducted into fracture
R	Gas constant
Re	Reynolds number
Re_w	Wall Reynolds number
r_{to}	Outside tubing radius
r_{wb}	Wellbore radius
S_j	Phase saturation
t	Time
t_D	Dimensionless time
T	Temperature
T_c	Critical temperature
T_f	Temperature of fluid in wellbore
T_{ei}	Temperature of earth
T_{es}	Temperature of earth, surface
T_{inj}	Temperature (inlet)
T_D	Dimensionless temperature
T_R	Reservoir temperature
U_{to}	Overall heat transfer coefficient
v	Velocity of fluid
V	Volume*
V_{stokes}	Stoke's proppant settling velocity
V_{set}	Proppant settling velocity
w	Fracture width
w_c	Corrected fracture width for proppant concentration (k_{ret} calculations)
x	Horizontal coordinate
x_i	Fraction of component in liquid phase*
x_{ij}	Fraction of component i in phase j
y_i	Fraction of component i in "gas" phase*
z	Vertical coordinate
z_i	Overall fraction of component i*
$z_{i,inj}$	Overall fraction of component, i* (inlet)
Z	Compressibility factor

Greek Symbols

α_R	Thermal diffusivity, reservoir
Γ	Quality
$d\Omega_f$	Un-perforated edges of fracture
$d\Omega_L$	Tip of fracture (edge that grows)
$d\Omega_p$	Perforated edge of fracture
ε	Roughness of pipe
ρ	Density, slurry (with proppant; mass of fluid plus proppant / total volume)
ρ_f	Density, fluid
ρ_{fl}	Density, leaked-off fluid
ρ_j	Density, phase (without proppant; mass of fluid phase / volume of fluid phase)
ρ_j^*	Proppant corrected phase density
ρ_R	Density, reservior

ρ_p	Density, proppant
μ	Fluid viscosity
μ_{eff}	Power law fluid effective viscosity
μ_R	Viscosity of reservoir fluid
σ	Stress
ϕ_i	Fugacity coefficient
Φ	Heat blockage correction factor for thermal resistance of leaked-off fluid
Ψ	Heat blockage correction factor for cooling of reservoir by leak-off
τ	Fracture opening time
ν	Poisson's ratio
ω	Accentric factor
Ω	Fracture flow domain

References

1. Friehauf, K.E. and Sharma, M.M. 2008. A New Compositional Model for Hydraulic Fracturing With Energized Fluids. Paper SPE 115750 presented at the 2008 SPE Annual Technical Conference and Exhibition held in Denver, CO, 21-24 September.

2. Nordgren, R.P. 1972. Propagation of a Vertical Hydraulic Fracture. *Society of Petroleum Engineers Journal*, August: 306-314.

3. Schechter, R.S. 1992. *Oil Well Stimulation*. Englewood Cliffs, New Jersey: Prentice Hall.

4. Sharma M.M. 2004. Advanced Fracturing Technology for Tight Gas: An East Texas Field Demonstration. DOE report, The University of Texas, Austin, Texas, September.

5. Yew, C.H. 1997. *Mechanics of Hydraulic Fracturing*. Gulf Pub Co.

6. Kenyon, D.E. 1993. CO2 Foam Slurry Friction Correlations. Paper SPE 26152 presented at the SPE Gas Technology Symposium, Calgary, Alberta, Canada, 28-30 June.

7. Fred, C.N, Miller, M.J. and Quintero, B.W. 2004. Impact of Water-Based Polymer Fluid Characteristics on CO2 Foam Rheology. Paper SPE 86493 presented at the SPE International Symposium and Exhibition on Formation Damage Control, Lafayette, Louisiana, 18-20 February.

8. Khade K.D. and Shah, S.N. 2004. New Rheological Correlations for Guar Foam Fluids. *SPE Production & Facilities*, May: 77-85.

9. Valko, P. and Economides, M.J. 1992. Volume Equalized Constitutive Equations for Foamed Polymer Solutions. *Journal of Rheology*, August: 1033-1055.

10. Harris, P.C. and Reidenbach, V.G. 1987. High Temperature Rheological Study of Foam Fracturing Fluids. *Journal of Petroleum Technology*, May: 613-619. SPE 13177.

11. Reidenbach, V.G, Harris, P.C, Lee, Y.N. and Lord, D.L. 1986. Rheological Study of Foam Fracturing Fluids using Nitrogen and Carbon Dioxide. *SPE Production Engineering*, January : 31-41.

12. Ozbayoglu, E.M, Akin, S. and Eren, T. 2005. Foam Characterization using image Processing Techniques. Paper SPE 93860 presented at the SPE Western Regional meeting, Irvine, California, 30 March – 1 April.

13. Harris, P.C. and Heath, S.J. 1996. Rheology of Crosslinked Foams. *SPE Production and Facilities*, May: 113-116. SPE 28512.

14. Harris, P.C. 1995. A Comparison of Mixed-Gas Foams with N2 and CO2 Foamed Fracturing Fluids on a Flow-Loop Viscometer. *SPE Production and Facilities*, August: 197-202. SPE 20642.

15. Meyer, B.R. 1989. Heat Transfer in Hydraulic Fracturing. *SPE Production Engineering*, November: 423-429.

16. Sandler, S.I. 1999. *Chemical and Engineering Thermodynamics*. John Wiley & Sons Inc.

17. Okuno, R and Johns, R.T. 2008. Application of a Reduced Method in Compositional Simulations. Paper SPE 119657 accepted for journal publication in SPE Journal.

18. Okuno, R, Johns, R.T, and Sephrenoori, K. 2008. A New Algorithm for Rachford-Rice for Multiphase Compositional Simulation. Paper SPE 117752 presented at the SPE Eastern Regional / AAPG Eastern Section Joint Meeting, Pittsburgh, Pennsylvania, 11-15 October.

19. Okuno, R, Johns, R.T, and Sepehrnoori, K. 2009. Three-Phase Flash in Compositional Simulation Using a Reduced Method. Paper presented at the 15th European Symposium on Improved Oil Recovery, Paris, France, 27-29 April.

20. Hasan, A.R. and Kabir, C.S. 2002. *Fluid Flow and Heat Transfer in Wellbores*. Society of Petroleum Engineers.

21. Valko, P. and Economides, M.J. 1995. *Hydraulic Fracture Mechanics*. John Wiley & Sons Inc.

Table 3.1. Number and description of unknown variables at each node location.

Unknowns	Number of independent variables
F_j	NP
ρ_j	NP
x_{ij}	NC*NP
S_j	NP
P	1
w	1
c	1
T	1
Total	3*NP+NC*NP+4

Table 3.2. Number and description of independent equations.

Equation	Number of independent equations
Component Balances	NC
Equal Fugacity	NC*(NP-1)
EOS	NP
$\Sigma x_{ij}=1$	NP
$\Sigma S_j=1$	1
Multi-phase flow	NP
Fracture Mechanics	1
Proppant Transport	1
Energy Balance	1
Total	3*NP+NC*NP+4

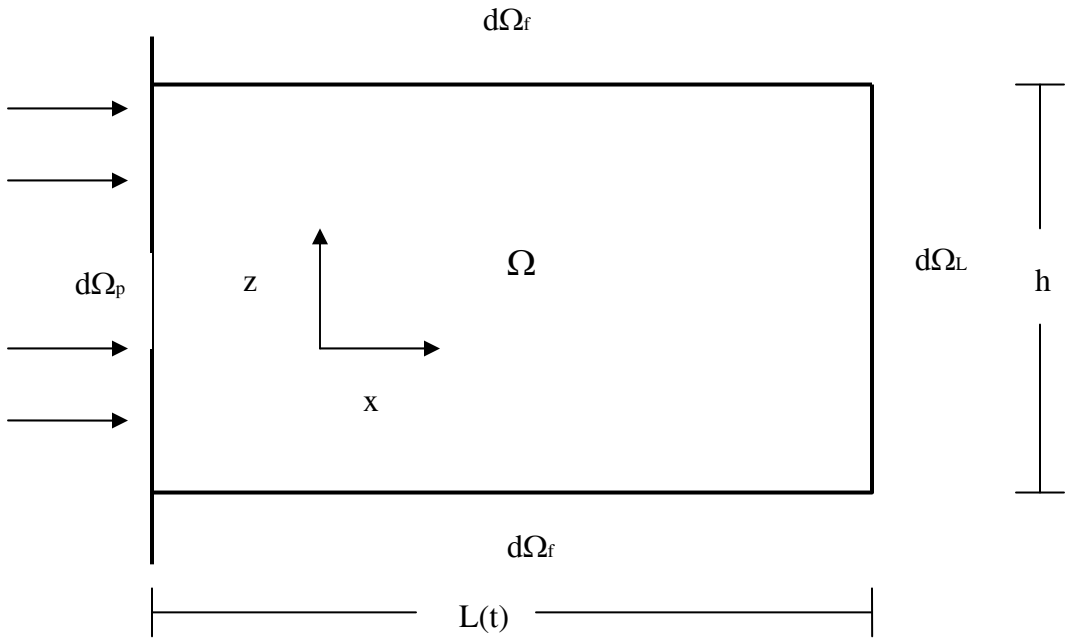

Figure 3.1. Drawing of the domain where equations are solved.

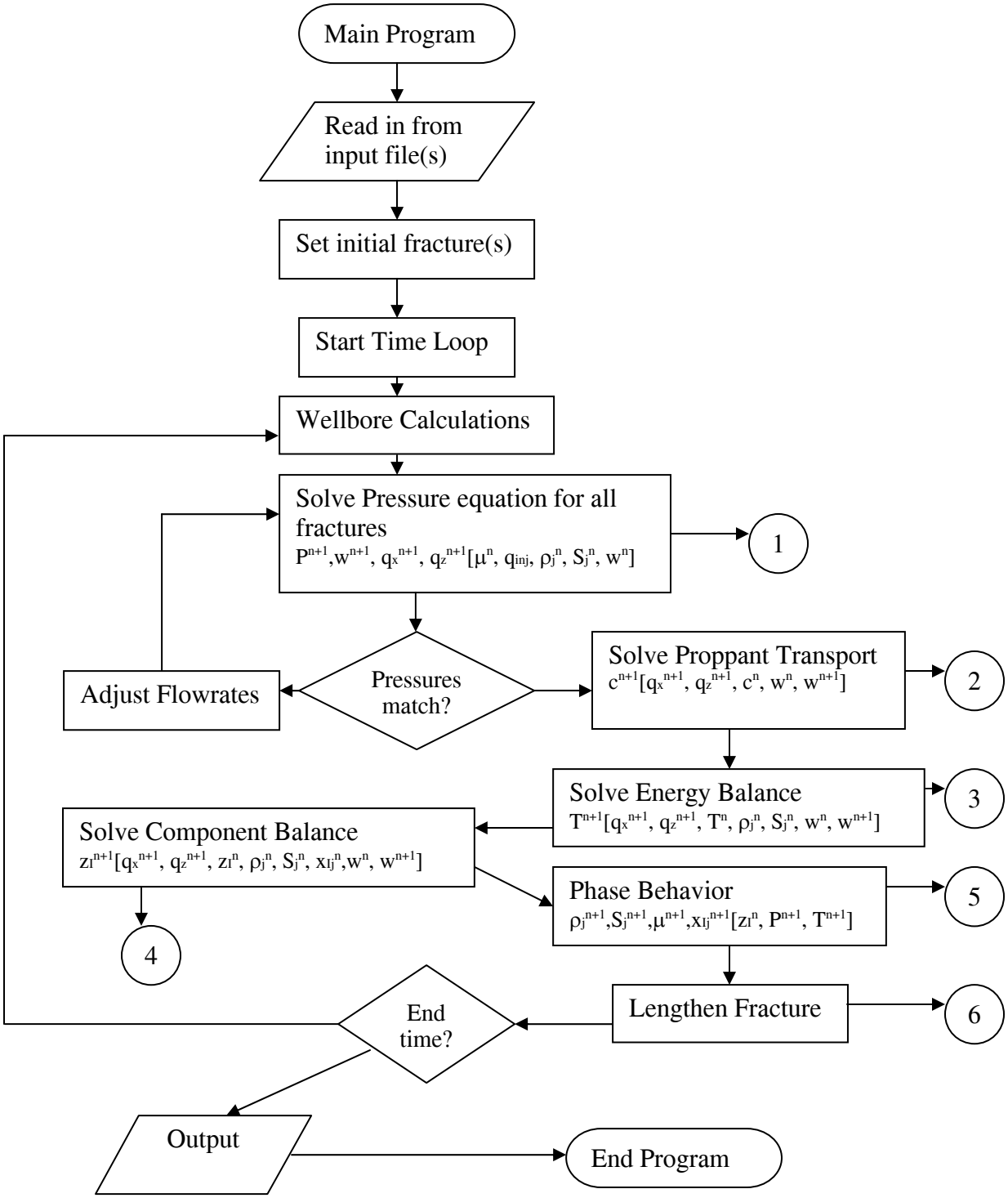

Figure 3.2. Flowchart for energized fracturing model (EFRAC).

1

Pressure equation:

1) Update rheology
   $K(i, j)$
   $n(i, j)$

2) Calculate intermediate nodal values, A and B.

3) Assemble Pressure matrix and RHS vector:
   $[AK]\{P^{n+1}\}=\{F\}$

4) Prescribe boundary conditions
   $P^{net,n+1}(i, Numj) = 0$
5) Solve system of equations for pressure
   P^{n+1}
6) Update width with new pressure
   w^{n+1}
7) Update intermediate nodal values, effectively updating fluxes with new pressure
   $A^{n+1}, q_x{}^{n+1}, q_z{}^{n+1}$

2

Proppant Transport:

1) Check to see if proppant has entered the fracture
2) Calculate settling velocity
   V_{set}
3) Calculate proppant retardation
   k_{ret}
4) Explicitly solve for proppant concentration
   c^{n+1}

3

Energy Balance:

1) Calculate Heat blockage
   ψ, Φ
2) Explicitly Solve for Temperature

T^{n+1}

3) Check that temperature doesn't go above reservoir temp or below lowest injected temperature

4

Component Balance:

1) Explicitly solve for overall composition of each component
   z_I^{n+1}
2) Normalize overall compositions

5

Phase Behavior:

1) Covert mass fraction to mol fraction
2) Perform Flash calculation (using K-values or Peng-Robinson)
3) Convert mol fractions back to mass
   $x_{Ik}^{n+1}(i,j) = EOS[z_I^{n+1}(i,j), T^{n+1}(i,j), P^{n+1}(i,j)]$
4) Update phase density
   $\rho_k^{n+1}(i,j) = EOS[z_I^{n+1}(i,j), T^{n+1}(i,j), P^{n+1}(i,j)]$
5) Update phase saturation
   $S_k^{n+1}(i,j) = EOS[z_I^{n+1}(i,j), T^{n+1}(i,j), P^{n+1}(i,j)]$

6

Lengthen Fracture:

1) Calculate un-accounted for mass of fluid by macroscopic mass balance
2) Calculate volume that mass occupies at fracture tip
3) Determine if un-accounted for volume is enough to propagate fracture
4) If so, increase the fracture length and update nodal values at tip

CHAPTER 4: BEHAVIOR OF ENERGIZED FLUIDS

The fracture propagation model presented in Chapter 3 requires certain properties of the fracturing fluid to be known as input to the model. Either a Newtonian viscosity or power law parameters (n and K) are specified that change the shape of the fracture. Phase behavior is another such important property. For non-energized fluids, the phase behavior is simple because it is always assumed that the fracturing fluid is single-phase and incompressible. With energized fluids we have to ask the questions: How many phases will there be? What is the composition of each phase? Leak-off is a third important parameter that needs to be specified. The leak-off coefficient is usually specified or calculated using reservoir properties. This chapter discusses these properties for some commonly used energized fluids.

Like all fluids, the properties of an energized fracturing fluid depend on the composition of the fluid and the range of conditions under which the fluid is applied. Common energized fluids add CO_2 or N_2 to a traditional water-based fluid. This chapter's main focus will be on these fluid systems because they are used most often and because their rheology has been studied to a great extent. Methanol is another possible component. This chapter discusses the behavior of fluid systems of carbon dioxide, water, and methanol as well.

In some instances, the properties of the fluid alone will be able to show the effectiveness of energized fluids. However, in most instances, the information in this chapter needs to be coupled with the fracture propagation model in order to get a complete picture of fracture performance. Changes in temperature, pressure, and composition create changes in phase behavior, which in turn affects the rheology and/or leak-off behavior of the fluid, which has a large influence on fracture dimensions. Also, the relationship between the fluids lost and the formation will play a role in whether

damage around the fracture can occur. These effects coupled together will allow a complete description of fracture performance.

4.1 Mixture Properties of CO_2-H_2O

Carbon dioxide's properties make it an ideal candidate as a gas additive. It is miscible with the methane gas being produced and it is soluble in an aqueous phase to some degree. The specific gravity can range from 0.8 to above 1 at fracturing pressure, which makes it suitable to reduce surface pressures because of the increased weight of the fluid in the well. Even though it causes damage, water is still used so that the various chemical additives can be used to increase the viscosity the fluid. Because CO_2 is only slightly soluble in water, it will usually form a second fluid phase. The degree of solubility and the compressibility of each of the phases are shown in Section 4.1.1. Multi-phase fluid properties must be taken into account, including their effect on the rheology of the system, as discussed in Section 4.1.2. Later sections show the comparison between CO_2-H_2O mixtures and N_2-H_2O, and CO_2-MeOH-H_2O mixtures.

4.1.1 Phase Behavior of CO_2-H_2O Mixtures

Before any specific energized fracturing cases can be studied, it is important that the phase behavior of the fluid be accurately accounted for. For example, a benefit of energized fluids is that the aqueous phase has a high solubility of gas at high pressures. The gas comes out of solution when the pressure drops during production. The released gas reduces the damage by increasing the gas relative permeability. Without an accurate calculation of the solubility, this effect cannot be quantified.

For this study, the binary system of CO_2 and H_2O was evaluated by the Peng-Robinson EOS (PREOS). Refer to Chapter 3, Section 3.6 for further information. This requires tuned binary interaction coefficients to match measured data (see Equation 3.35). Measured data for this binary system is available[1-3]. Figure 4.1 compares the predicted solubility of CO_2 in H_2O to the measured values. Good agreement with the PREOS is achieved with the following binary interaction parameter:

$$BIP_{H_2O-CO_2} = -0.0936 + 0.000486(T[^oF] - 113) \quad (4.1)$$

Solubility is just one aspect of phase behavior. It is also important that the phase behavior model be able to predict phase changes and phase compressibility. A phase diagram for the CO_2-H_2O system is shown in Figure 4.2. Figure 4.2 includes three curves. The first two are vapor-liquid equilibrium (VLE) lines of a 50/50 mol mixture of the two components, and of pure CO_2. The third curve is a possible path that a fracturing fluid could traverse during fracturing.

Consider a situation where CO_2 is pumped without water. Two-phase CO_2 (gas and liquid) will only coexist on the VLE line. The fracturing curve does not cross this line at any point. This means that when pure CO_2 is pumped, it will never go through a phase change where it goes from a liquid to a gas. However, this doesn't mean the fluid will not experience drastic changes in properties with changes in pressure and temperature (CO_2 will expand with higher temperature or lower pressures). Please take note that the fracturing pressures exceed the critical point of CO_2 very easily. The critical temperature is exceeded when the fluid is heated to reservoir conditions. We call the CO_2 component and the phase rich in CO_2 a "gas" even though critical conditions are reached.

Now consider a situation where a 50 mol% CO_2 and 50 mol% H_2O is pumped. The VLE curve is an envelope instead of a line because it is two components. The VLE curve for the 50/50 mixture is only one edge of the envelope. The other boundary is outside the domain of the figure. At all times, the fracturing curve is to the left of the VLE curve, inside the phase envelope, and in the two phase region. Under all fracturing conditions there will be two fluid phases present, a CO_2 rich phase, referred to as the "gas" phase, and the H_2O rich phase, referred to as the aqueous or liquid phase. Again, each phase is altered by changes in pressure and temperature.

Figure 4.3 shows a comparison between liquid phase density predicted by PREOS and experimental data[3]. The figure shows good agreement. The density varies by less than 0.1 lb/ft^3 in the temperature range shown, confirming that the liquid phase remains incompressible. The volume shift parameters (Equation 3.39) used to reach agreement between predicted and experimental data is shown in Equation 4.2.

$$\begin{aligned} \overline{c}_{vs,H_2O}[\text{ft}^3/\text{lb-mol}] &= 0.0303 + .000184T[^oF] \\ \overline{c}_{vs,CO_2}[\text{ft}^3/\text{lb-mol}] &= 0.01054 \end{aligned} \tag{4.2}$$

4.1.2 RHEOLOGY OF CO_2-H_2O MIXTURES

High viscosity fluids are used in hydraulic fracturing to increase bottom-hole pressure creating large enough fracture widths so that proppant may enter. The viscosity also supports the proppant so it doesn't settle too quickly under gravity as it is transported along the fracture. If the viscosity is too low, the proppant will bridge across the fracture causing an unwanted screen-out or settle to the bottom of the fracture causing inadequate vertical coverage. If the viscosity is too high the fracture lengths will be shorter, and the fracture will be wider and taller (depending on stress contrast).

Traditional fluids use soluble polymers in water to create viscosity. To increase the viscosity and achieve visco-elasticity, a chemical cross-linker is added that bonds strands of polymer together. The polymer creates shear thinning fluids. It is common practice to use the traditional un-crosslinked polymers as base fluids when gas components are added so that the same benefits of viscosity are utilized.

Section 4.1.1 showed that CO_2-H_2O mixtures form two phases under most compositions and ranges of fracturing temperature and pressure. The two phases can be pictured as gas bubbles in a continuous liquid. As more CO_2 is added to the system, the bubbles interact with each other in different ways, therefore, the volume fraction of the internal phase becomes an important parameter in the rheological study of these fluids. The volume fraction of the internal phase in referred to as "quality."

At high quality, the interactions between bubbles cause energy dissipation resulting in a higher effective viscosity, a property of foam[4]. The higher the quality, the higher the increase in viscosity. The internal phase is stable until very high qualities are reached (~95%) and the gas becomes the external phase, referred to as a mist. At low qualities (less than 52%), the interactions are minimal so the fluid viscosity more resembles one of the base fluids.

The limit at which the increase in viscosity can be seen is not 52% for all cases[5]. Thicker aqueous phase properties and beneficial surfactant conditions reduce the 52% limit by stabilizing foams at a lower gas fraction; this includes cross-linking the fluid[6]. Other parameters such as temperature, pH, crosslink delay, salt concentration in water, interaction with hydrocarbons, and shear history can cause foam to become unstable[7].

The rheology of foam (52 – 95% quality) has been characterized two ways. The first assumes that the foam is a single-phase fluid and then corrects the value of the power law parameters n and K for different qualities. The second way, normalizes all qualities into one parameter called the "volume expansion ratio," and utilizes one set of n and K values. This process is called the "Volume Equalized Principle."

An example of characterizing foams by the first method is done by Reidenbach et al, 1986[8]. In the study, correlations for both carbon dioxide and nitrogen foam are determined for both laminar and turbulent flow regimes. The experiments were done in a flow-loop using different HPG (hydroxypropyl guar) loadings. The laminar correlation takes the form of Equation 4.3. The empirical correlation value, C_1, for each HPG loading is shown in Table 4.1.

$$\frac{K}{K_o} = e^{C_1\Gamma + 0.75\Gamma^2} \tag{4.3}$$

Valko and Economides[9] came up with the "Volume Equivalence Principle" or VEP. The VEP introduces a new variable called the specific volume expansion ratio. It is defined as the ratio of specific volumes of foam to the base liquid:

$$\varepsilon_{VEP} = \frac{\rho_l}{\rho} \tag{4.4}$$

ε_{VEP} is used to normalize all foam qualities. The study also concludes that the Reynolds number and friction factor with the volume expansion ratio are:

$$\mathrm{Re} = \frac{D^n v^{2-n} \rho \varepsilon_{VEP}^{\ n-1}}{K} \tag{4.5}$$

$$f = \frac{2}{\mathrm{Re}}\left(\frac{2+6n}{n}\right)^{n} \tag{4.6}$$

The concentration of proppant is included in the internal phase quality because it has similar interactions with the base fluid[10]. This is why we use the term internal phase quality, and not gas fraction. It may be necessary to decrease the gas fraction with increasing the proppant concentration so that a constant internal phase quality is achieved.

Both the Reidenbach and Valko studies raise the effective viscosities of the fluid with increasing quality. However, it has been shown that the increase is only realized for qualities from 52 – 95%. Figure 4.4 shows a diagram of the effective viscosity (μ) changes with internal phase quality (Γ) varying from 0 to 100%. Before the 52% limit, the ratio of viscosity to the base viscosity is near 1 and drops slightly with increasing internal phase quality. The base viscosity of the gas is lower than that of the liquid, causing the overall viscosity to drop when more gas is added. Above 52%, the viscosity increases. The exact values are determined from Equation 4.3 with $C_1 = 1.0$, the value for CO_2 foams with 40 lb/Mgal HPG loading. Above 95%, the viscosity quickly drops down to near zero because the foam breaks down and almost all viscosity is lost. Please take note that multiplying the K value for a power law fluid by a certain value also increases the effective viscosity (μ) by the same factor.

In addition to the effect of internal phase quality, temperature also plays an important role on the fluid rheology. The effect of temperature on fracturing foams was studied by Khade and Shah[11]. The study includes a correlation that calculates the change in base rheology at 100 F:

$$\frac{K}{K_o} = 1 - C_2 (T - 100)^{C_3} \tag{4.7}$$

Where C_2 are C_3 are correlation values. All fluid viscosities, not just CO_2-H_2O foams, are modeled with the same functional form as Equation 4.7.

4.2 Mixture Properties of N_2-H_2O

After carbon dioxide, nitrogen is the most common gas energizer. N_2 is more easily available and more inert than CO_2. Like CO_2, N_2 is miscible with methane so its leak-off won't damage the formation (like water does). However, N_2 is less soluble in water than CO_2. The specific gravity of the N_2 rich phase is more like a pressurized gas with a maximum at about 0.4. The full details of the phase behavior of this fluid system are described in Section 4.2.1. The rheology of nitrogen and water-based fracturing fluids is similar to carbon dioxide and water systems, discussed in Section 4.2.2.

4.2.1 PHASE BEHAVIOR OF N_2-H_2O MIXTURES

The solubility of N_2 in water is much less than CO_2 in water, as seen in Figure 4.5. Its solubility is less than 0.5 mol % whereas CO_2 solubility can reach 3.5 mol %. The data shows that the solubility of N_2 in water is less sensitive to temperature than the solubility of CO_2. The question of whether the solubility of N_2 or CO_2 in water is enough to increase productivity from a fracture cannot be answered by looking at solubility data alone. This question is answered by Chapter 9 where we show results for CO_2 and N_2 energized fractures. However, solubility does play an important role.

The solubility shown in Figure 4.5 is confirmed with experimental data also shown in the figure[12]. This is accomplished with the following binary interaction parameter:

$$BIP_{H_2O-N_2} = -0.554 + 0.00194(T[^oF] - 113) \tag{4.8}$$

The density of the vapor phase was measured experimentally[13] and compared to PREOS calculated data in Figure 4.6. It is confirmed that the PREOS can predict correct gas phase densities. The volume shift parameters used to create Figure 4.6 are shown in Equation 4.9.

$$\begin{aligned} \bar{c}_{vs,H_2O}[\text{ft}^3/\text{lb-mol}] &= 0.0303 + .000184T[^oF] \\ \bar{c}_{vs,N_2}[\text{ft}^3/\text{lb-mol}] &= 0 \end{aligned} \tag{4.9}$$

The density of the gas phase is much less with N_2 compared to CO_2. The lighter phase density has two important consequences: 1) it increases the surface pressure requirements because of a lack of fluid weight at the bottom of the well and, 2) it will also allow more proppant settling.

4.2.2 RHEOLOGY OF N_2-H_2O MIXTURES

The rheology of N_2-H_2O mixtures is similar to CO_2-H_2O mixtures. As discussed earlier, the gas forms bubbles that interact with each other to increase fluid viscosity in high quality foams. The rheology is identical at low quality because both CO_2 and N_2 gas phases have lower phase viscosity as compared to the liquid phase. Figure 4.4 shows the effective viscosity divided by a base viscosity for all qualities. The only difference between CO_2 and N_2 viscosity is seen at qualities ranging from 52 -95% where the bubble interactions differ slightly depending on the gas. The empirical constant, C_1, used for the N_2 curve in Figure 4.4, is 1.2 (see Table 4.1) as compared to 1.0 for CO_2 at the same polymer loading; this results in slightly higher viscosity for a given base viscosity.

4.3 Mixture Properties of CO_2-H_2O-MeOH

Methanol treatments have been successfully applied in water sensitive formations. In 2001, Malone[14] reported results when cross-linked methanol is pumped to reduce the amount of water. Methanol, unlike water, will stop clay swelling problems thus eliminating water sensitivity. Gupta[15] reported use of methanol and water with CO_2 as a second phase.

The biggest logistical difference between methanol and other treatments is that additional safety measures need to be taken. Methanol's flash point at atmospheric pressure is 53 ^oF, making it a very volatile, flammable vapor. "CO_2 blankets" were used over all methanol areas creating a layer between any possible leaks and the oxygen fuel. Firefighting teams were on location at all times during a methanol treatment[14].

The phase behavior of fluid systems involving the CO_2, H_2O, and MeOH ternary system is discussed in Section 4.3.1. The rheology is in Section 4.3.2.

4.3.1 PHASE BEHAVIOR OF CO_2-H_2O-MEOH MIXTURES

Methanol is more volatile than H_2O but is still miscible with aqueous solutions. Systems of CO_2, H_2O and MeOH form two phases for most compositions, temperatures, and pressures during fracturing, just like the previously discussed systems. Properties of methanol promote miscibility so that a larger fraction of the gas can go into the liquid phase and more of the methanol partitions into the gas phase.

The Peng-Robinson EOS correctly predicts the phase behavior of ternary systems of CO_2, H_2O and MeOH. The solubility of CO_2 in the liquid phase is shown in Figures 4.7 and 4.8. Figure 4.7 is for 105 F and Figure 4.8 is for 250 F. Each of the lines and data sets in Figures 4.7 and 4.8 represent the solubility of CO_2 in the liquid phase for different compositions of methanol. The figures show good agreement between experimental[16] and predicted values with the binary interaction parameters in Table 4.2. The compositions reported in the figure are in mole fractions of methanol not including CO_2; this represents the methanol-to-water ratio in the system. The values range from 0.05 mol % to 0.95 mol % to show that near pure compositions of water and methanol can be predicted.

Both Figures 4.7 and 4.8 show that the solubility of CO_2 is increased when methanol is added to the water. This means that fluid systems that require stimulation of the invaded zone by solubility mechanisms will be more effective when methanol is added. Figure 4.9 shows the comparison between the solubility of all the fluid systems that we have discussed so far. As a result, methanol systems will be more effective as energized fluids.

The Peng-Robinson EOS also correctly predicts the phase density for this fluid system. The predicted liquid phase density is shown in Figure 4.10. The predictions correlate well with experimental values[17]. For simplicity, only two separate conditions of temperature and methanol composition are shown. The methanol composition is in mole fraction without CO_2, the same as the solubility figures. Increasing temperature and

methanol composition decreases the density by roughly 20% but does not change much with pressure. The liquid phase is near incompressible, even when methanol is added. The gas phase density is also compared to experimental values[17], shown in Figure 4.11. The gas phase density is dependent on temperature and pressure, much like the gas phases that are mentioned in previous sections. Methanol does not change the behavior of the gas-rich phase properties to a large degree. The volume shift parameters used for this fluid system is shown in Equation 4.10.

$$\begin{aligned} \bar{c}_{vs,H_2O}[\text{ft}^3/\text{lb-mol}] &= -0.0488 \\ \bar{c}_{vs,CO_2}[\text{ft}^3/\text{lb-mol}] &= -0.0300 \\ \bar{c}_{vs,MeOH}[\text{ft}^3/\text{lb-mol}] &= 0.06 \end{aligned} \tag{4.10}$$

4.3.2 RHEOLOGY OF CO_2-H_2O-MEOH MIXTURES

Foam fracturing fluids with methanol have not been studied as much as water-based CO_2 or N_2 foam because they have not been around as long. The only rheology tests on these fluid systems come from service companies or fracturing fluid providers. Even then, most of that information in not made public and is very limited. However, it is necessary to know the rheological behavior of this fluid system in order to model it. BJ Service Company has provided some test data for this research. The results are summarized below.

The data from BJ Services reported viscosities of the foam and base gels at 100 1/sec shear rate. Most of the tests were for fluid systems with 20 or 40% by volume methanol with the remainder of the base liquid consisting of water and other additives. 80% by volume of CO_2 was usually added to 20% of the base liquid. More than 90% of tests included the same composition of H_2O, CO_2, and MeOH because they used the common ratios mentioned above. Most tests were done to optimize specific additives. It is important that all fluids additives be compatible with the foam. We would like to model the rheology of the fluid with changing gas composition (quality) in a fluid system where the additives have already been optimized. Luckily, the data set provides one set

of tests that varied the CO_2 quality from 60, 70 and 80% and for two different polymer loadings.

Figure 4.12 shows the foam viscosity dependence on quality at two different loadings. The data is represented by points on the figure. The reported viscosities were once again divided by a base viscosity of the liquid. This makes the plot dimensionless and allows the effects of the base viscosity to be normalized out. This is similar to Figure 4.4 for non-methanol foams. We observed that the trend is linear and not exponential (as in Figure 4.4). Ideally we would need more than three points to confirm the linear trend but this data is the best estimation we have. We are assuming that the behavior of methanol foams, like regular foams, have a minimum and maximum quality where the increase in viscosity is observed. We can also assume that the mechanism of bubble-bubble interaction is the same for all foams so the minimum quality at which bubble-bubble interaction becomes significant will be around 52%. No increase in viscosity is seen under a quality of 52%. The upper limit is also assumed to be the same when mist is formed above 95% quality.

Two trend lines are drawn in Figure 4.12 to represent the rheological behavior of methanol foams at all qualities. Notice that the two trends lines are identical except from qualities ranging from 52 to 95%. Inside this range, the foam has increased viscosity. The level of increase is different for each polymer loading, shown by the slope of the line plotted on the figure. The two slopes are 17 and 23 for 41 lb/Mgal and 22 lb/Mgal loading, respectively. Because the viscosity ratio can be determined from only one factor, the slope of the line, a general the trend is established (Equation 4.11).

$$\frac{K}{K_o} = 0.52 + C_1(\Gamma - 0.52) \qquad (4.11)$$

Where the quality lies between 0.52 and 0.95. Equation 4.11 is equivalent to Equation 4.3 but for methanol foams. Notice that the exponential form of Equation 4.3 is replaced by a linear form of Equation 4.11. Also notice that each is a function of foam quality, Γ, with only one parameter to specify, C_1. Even though the functional behavior of methanol

and non-methanol foam is different, the increase in viscosity is still approximately the same (comparing Figure 4.4 with Figure 4.12).

4.4 Leak-off Behavior of Energized Fluids

Leak-off coefficients constitute another set of empirical parameters that need to be specified. Harris studied leak-off behavior for CO_2 and N_2 foam[18,19]. It was concluded that the wall-building leak-off coefficient is a function of core permeability, gelling agent concentration, and temperature. It was also concluded that the effluent collected was enriched in the aqueous phase. The leak-off coefficient for the aqueous phase is larger than the gas phase. There has been little done to verify whether these conclusions are correct. There is a lack of experiments and no way to measure phase dependant leak-off in the field. Currently, there is no public data or studies on the leak-off of methanol foam fluids.

Harris'[18,19] conclusions and data represent the best experimental evidence we have for multi-phase leak-off. More data is needed since the various mechanisms that control the leak-off of these fluids are not well understood. Chapter 8 includes a discussion of these mechanisms.

Nomenclature

BIP	Binary interaction parameter
$c_{vs,i}$	Volume shift parameter
C_1	Rheology correlation parameter, Quality
C_2	Rheology correlation parameter, Temperature
C_3	Rheology correlation parameter, Temperature
D	Diameter
f	Friction factor
K	Fluid consistency index
n	Power law index
Re	Reynolds number
T	Temperature
v	Velocity of fluid
Greek Symbols	
ε_{VEP}	Specific volume of expansion ratio
Γ	Foam quality
ρ	Density, overall
ρ_l	Density, liquid
ρ_g	Density, gas
μ	Fluid viscosity

References

1. Rumpf, B, Nicolaisen, H, and Maurer, G. 1994. Solubility of Carbon Dioxide in Aqueous Solutions of Sodium Chloride: Experimental Results and Correlation. *Journal of Solution Chemistry*, Vol. 23: No.3: 431-448.
2. Hnedkovshy, L, Wood, R.H, and Majer, V. 1996. Volumes of aqueous solutions of CH4, CO2, H2S, and NH3 at Temperatures from 298 K to 705 K and pressure to 35 MPa. *J. Chem. Thermodynamics*, 28: 125-142.
3. Spycher, N, Pruess, K. and Ennis-King, J. 2003. CO2-H2O mixtures in the geological sequestration of CO2. I. Assessment and calculation of mutual solubilities from 12 to 100 C and up to 600 bar. *Geochemica et Cosmochemica Acta*, Vol. 67: No. 16: 3015-3031.
4. Economides, M.J, Nolte, K.G. 2000. *Reservoir Stimulation*. John Wiley & Sons, LTD.
5. Watkins, E.K., and Wendorff, C.L. 1983. A New Crosslinked Foamed Fracturing Fluid. Paper SPE 12027 presented at the 58th Annual Technical Conference and Exhibition, San Francisco, California, 5-8 October.
6. Harris, P.C., and Heath, S.J. 1996. Rheology of Crosslinked Foams. *SPE Production & Facilities*, May: 113-116. SPE 28512.
7. Fredd, C.N, Miller, M.J, Quintero, B.W. 2004. Impact of Water-Based Polymer Fluid Characteristics on CO2 Foam Rheology. Paper SPE 86493 presented at the SPE

International Symposium and Exhibition on Formation Damage Control, Lafayette, Louisiana, 18-20 February.

8. Reidenbach, V.G., Harris, P.C., Lee, Y.N., and Lord, D.L. 1986. Rheological Study of Foam Fracturing Fluids Using Nitrogen and Carbon Dioxide. *SPE Production Engineering*, January: 31-41. SPE 12026.
9. Valko, P. and Economides, M.J. 1992. Volume Equalized Constitutive Equations for Foamed Polymer Solutions. *Journal of Rheology*, August 36(6): 1033-1055.
10. Harris, P.C., Klebenow, D.E., and Kundert, D.P. 1991. Constant-Internal-Phase Design Improves Stimulation Results. *SPE Production Engineering*, February: 15-19. SPE 17532.
11. Khade, S.D., and Shah, S.N. 2004. New Rheological Correlations for Guar Foam Fluids. *SPE Production and Facilities*, May: 77-85. SPE 88032.
12. Goodman, J.B, and Krase, N.W. 1931. Solubility of Nitrogen in Water at High Pressures and Temperatures. *Industrial and Engineering Chemistry*, April: 401-404.
13. Saddington, A.W, Krase, N.W. 1934. Vapor-Liquid Equilibria in the System Nitrogen-Water. *Journal of the American Chemical Society*, February(56): 353-361.
14. Malone, M.R. 2001. Fracturing with Crosslinked Methanol in Water-Sensitive Formations. Paper SPE 70009 presented at the SPE Permian Basin Oil and Gas Recovery Conference, Midland, Texas, 15-16 May.
15. Gupta, D.V.S. 2003. Field Application of Unconventional Foam Technology: Extension of Liquid CO2 Technology. Paper SPE 84119, presented at SPE Annual Technical Conference and Exhibition, Denver, Colorado 5-8 October.
16. Xia, J, Jdecke, M, Prez-Salado Kamps, I, and Maurer, G. 2004. Solubility of CO2 in (CH3OH + H2O). *Journal of Chemical Engineering Data*, 49(6): 1756-1759.
17. Urokova, I, Vorholz, J, and Maurer, G. 2006. Solubility of Carbon Dioxide in Aqueous Solutions of Methanol. Predictions by Molecular Simulation and Comparison with Experimental Data. *Journal of Physical Chemistry*, 110(30):14943-14949.
18. Harris, P.C. 1985. Dynamic Fluid-Loss Characteristics of Nitrogen Foam Fracturing Fluids. *Journal of Petroleum Technology*, October: 1847-1852.
19. Harris, P.C. 1987. Dynamic Fluid-Loss Characteristics of CO2-Foam Fracturing Fluids. *SPE Production Engineering*, May: 89-94.

Table 4.1. Rheology correlation values for CO_2 and N_2 foams[8]. See Equation 4.3.

HPG Load (lb/Mgal)	n (-)	K (lbf-sec^n/ft^2)	$C_1(CO_2)$ (-)	$C_1(N_2)$ (-)
0	1	0.00002	4.0	3.6
10	0.75	0.0053	2.6	2.1
20	0.607	0.00256	2.2	1.7
40	0.45	0.0152	1.0	1.2

Table 4.2. Binary interaction parameters for CO_2-H_2O-MeOH ternary system.

$BIP_{ij} = A_{ij} + B_{ij}(T[^oF]-113)$	A_{ij}	$B_{ij}[1/F]$
H_2O-CO_2	-0.094	0.000486
H_2O-MeOH	-0.1	0
MeOH-CO_2	0.116	0.000207

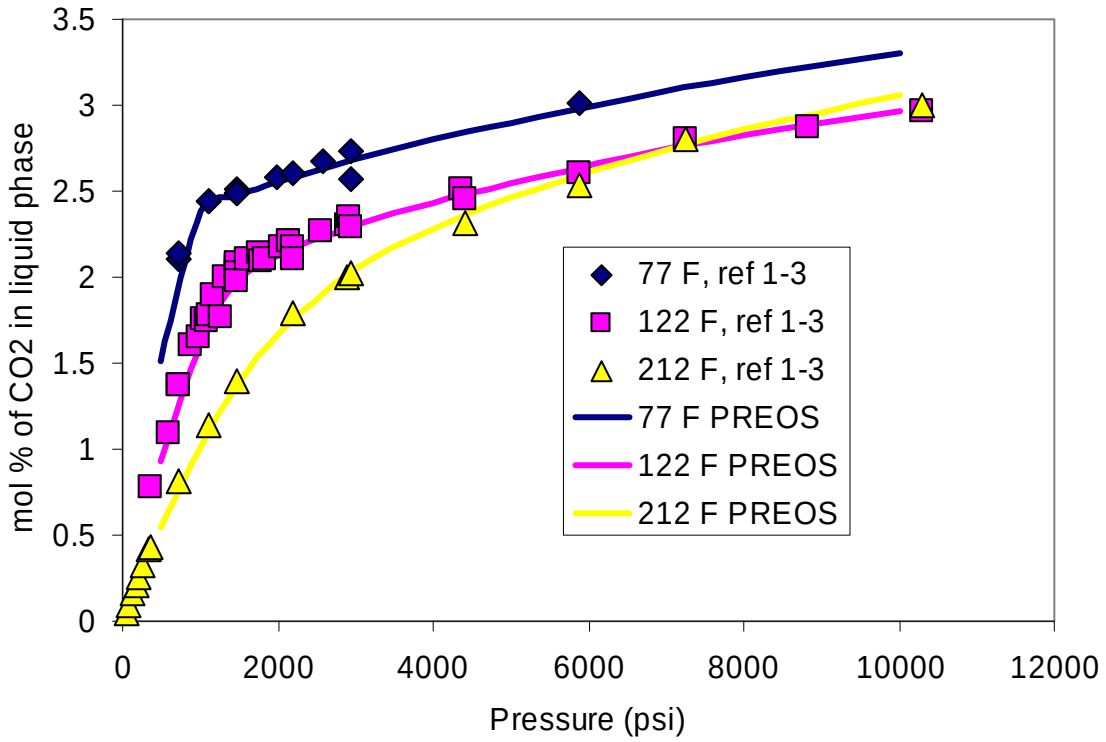

Figure 4.1. Solubility of CO_2 in H_2O. Compares experimental[1-3] values versus solubility predicated by the tuned Peng-Robinson EOS.

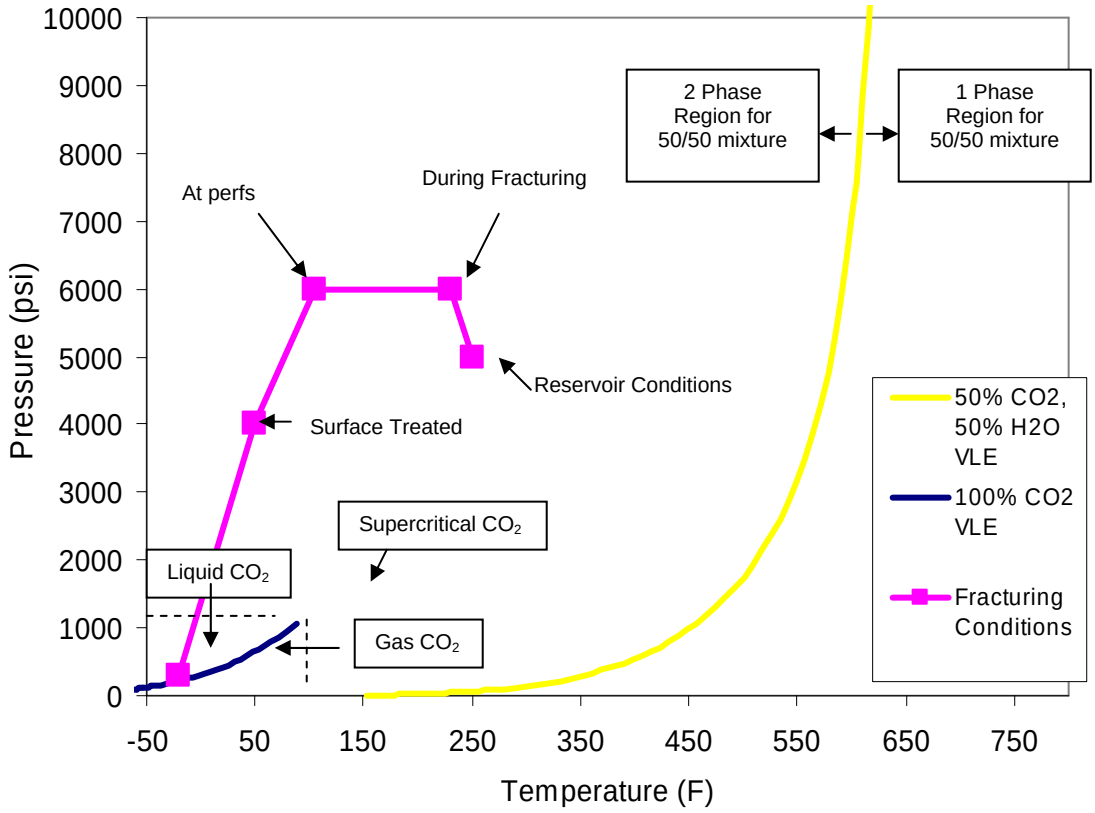

Figure 4.2. Phase diagram for CO_2-H_2O system predicted by PREOS.

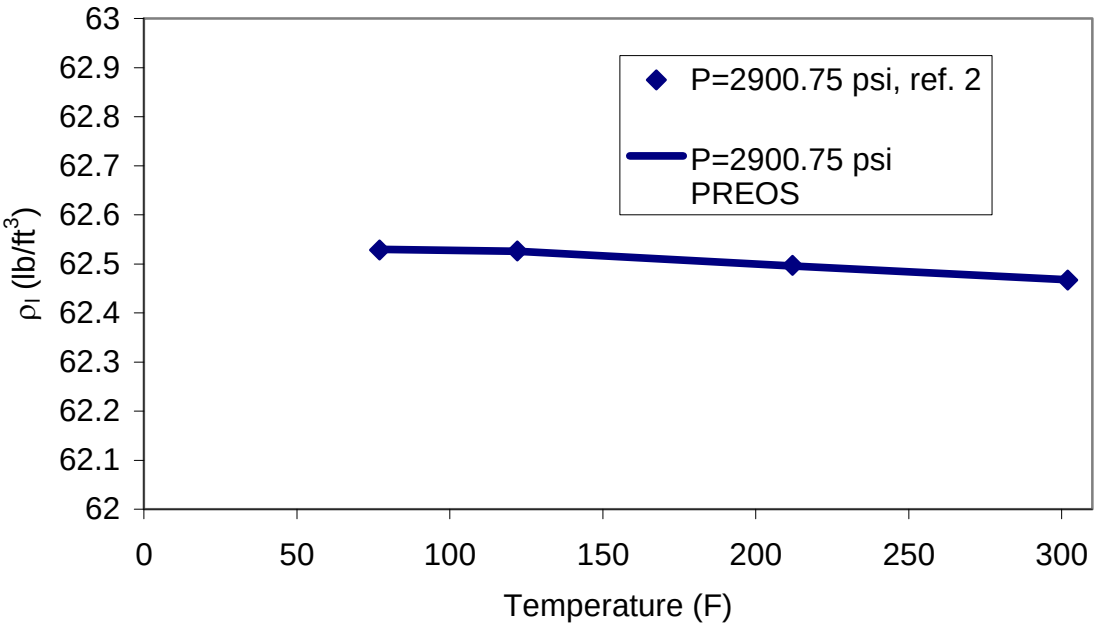

Figure 4.3. Density of liquid phase for CO_2-H_2O binary system. Compares experimental[2] values versus density predicated by the Peng-Robinson EOS.

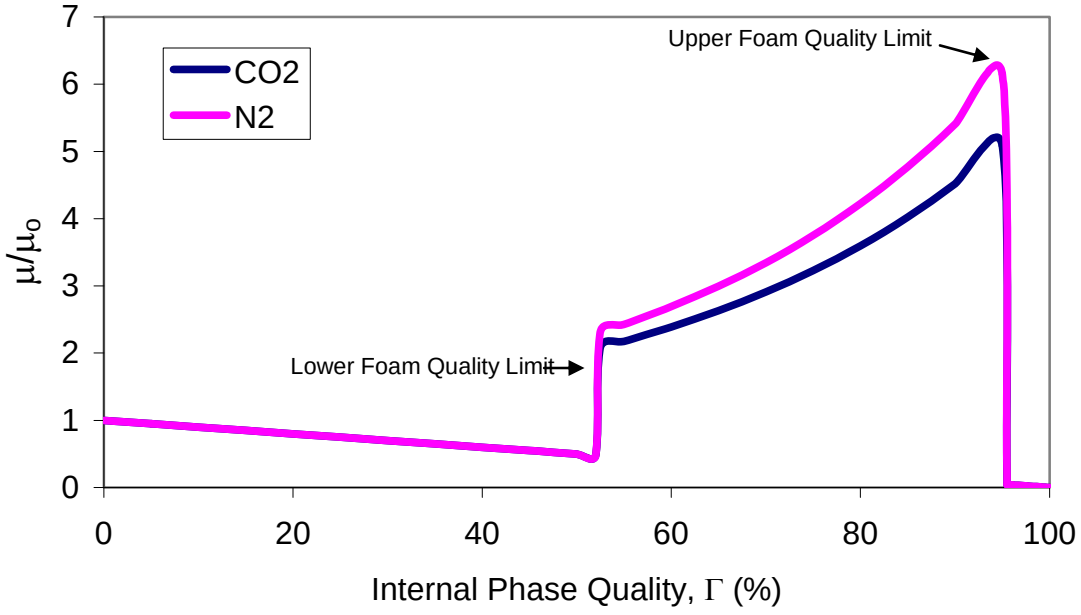

Figure 4.4. Viscosity as a function of internal phase quality for carbon dioxide and nitrogen foam with 40 lb/Mgal loading[8].

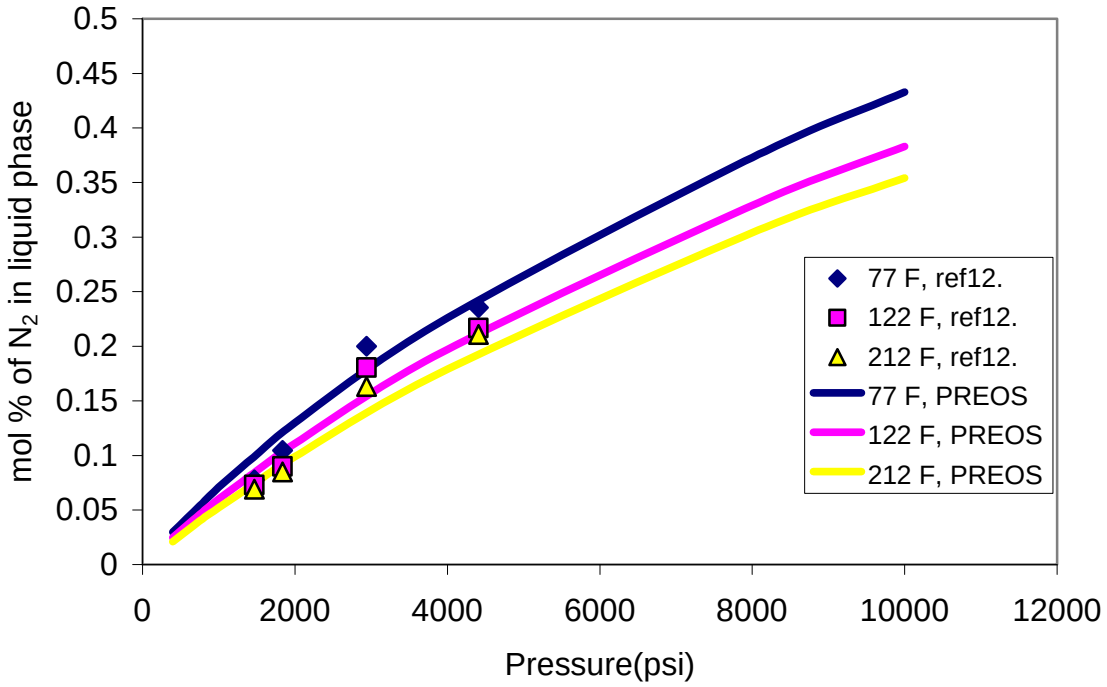

Figure 4.5. Solubility of N_2 in H_2O. Compares experimental[12] values versus solubility predicated by the Peng-Robinson EOS.

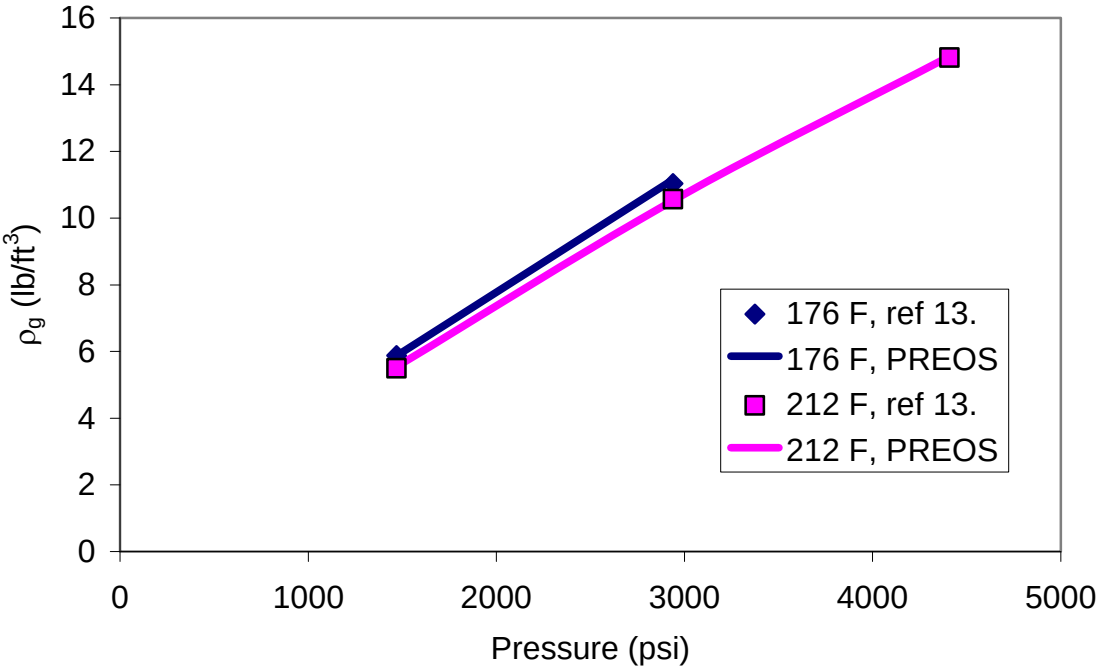

Figure 4.6. Density of gas (N_2 rich) phase for N_2-H_2O binary system. Compares experimental[13] values versus density predicated by the Peng-Robinson EOS.

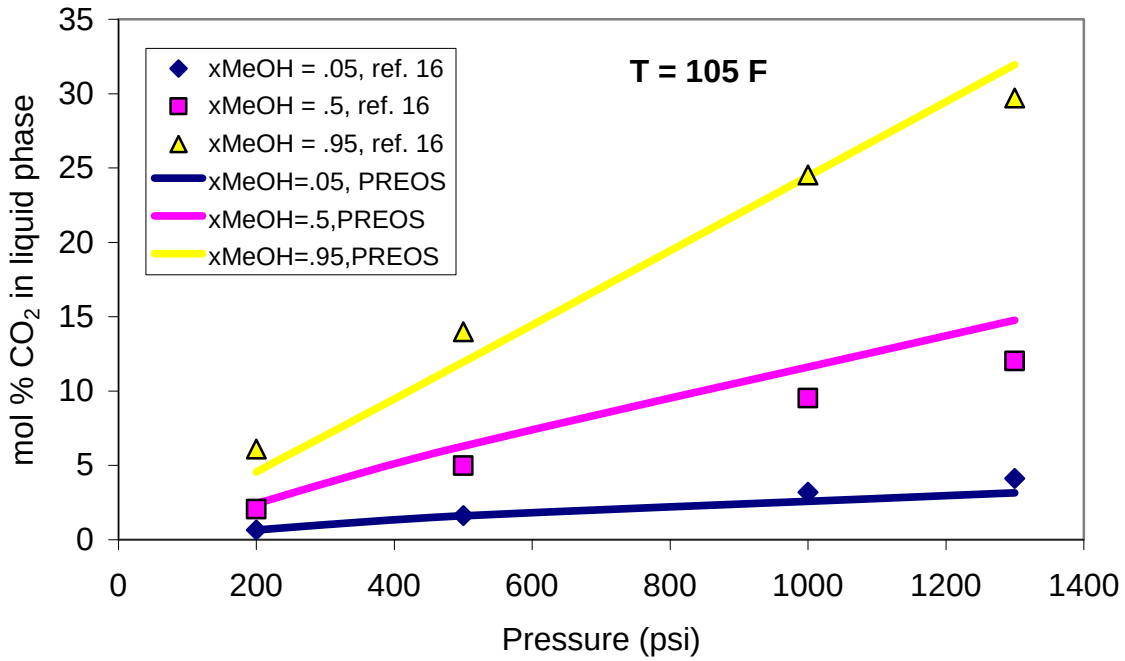

Figure 4.7. Solubility of CO_2 in liquid phase of H_2O-MeOH at 105 F. Methanol compositions are reported as CO_2 free mol fractions. Compares experimental16 values versus solubility predicated by the Peng-Robinson EOS.

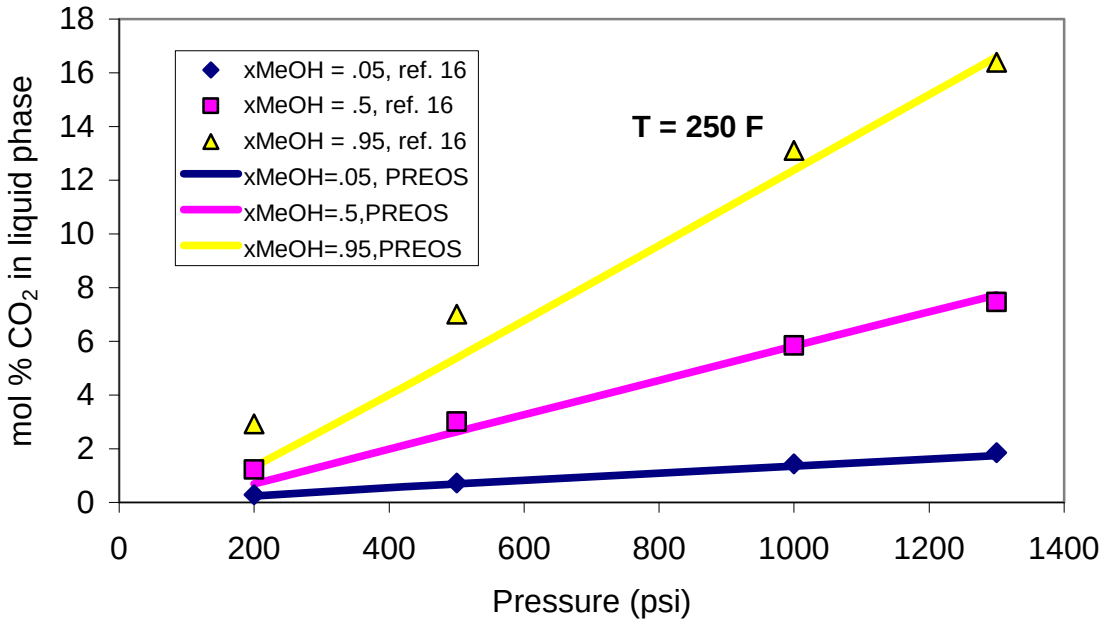

Figure 4.8. Solubility of CO_2 in liquid phase of H_2O-MeOH at 250 F. Methanol compositions are reported as CO_2 free mol fractions. Compares experimental[16] values versus solubility predicated by the Peng-Robinson EOS.

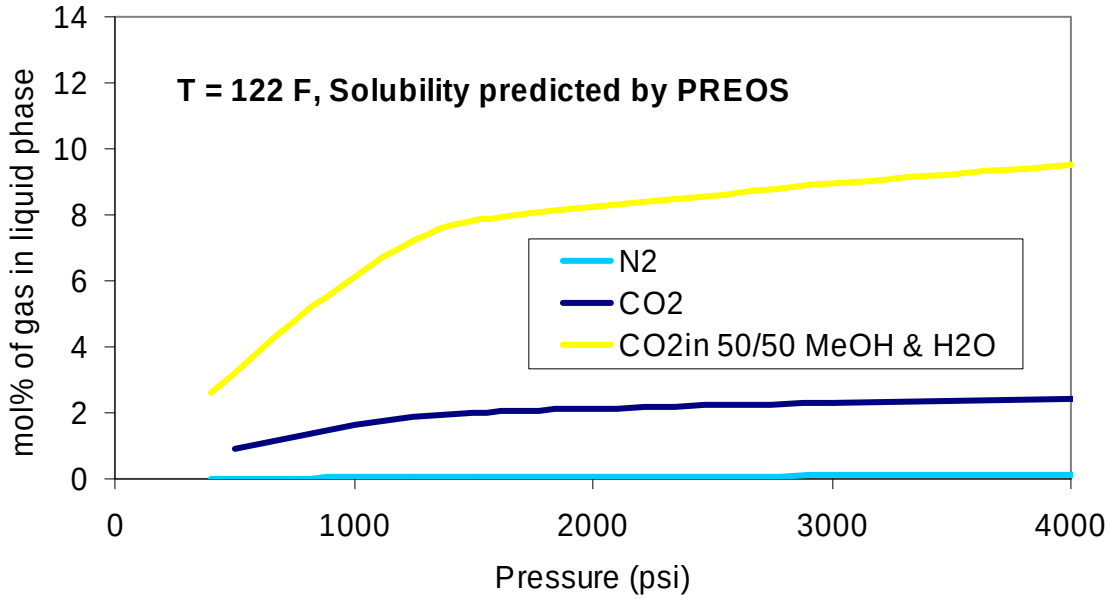

Figure 4.9. Solubility of gas components in liquid phase at 122 F.

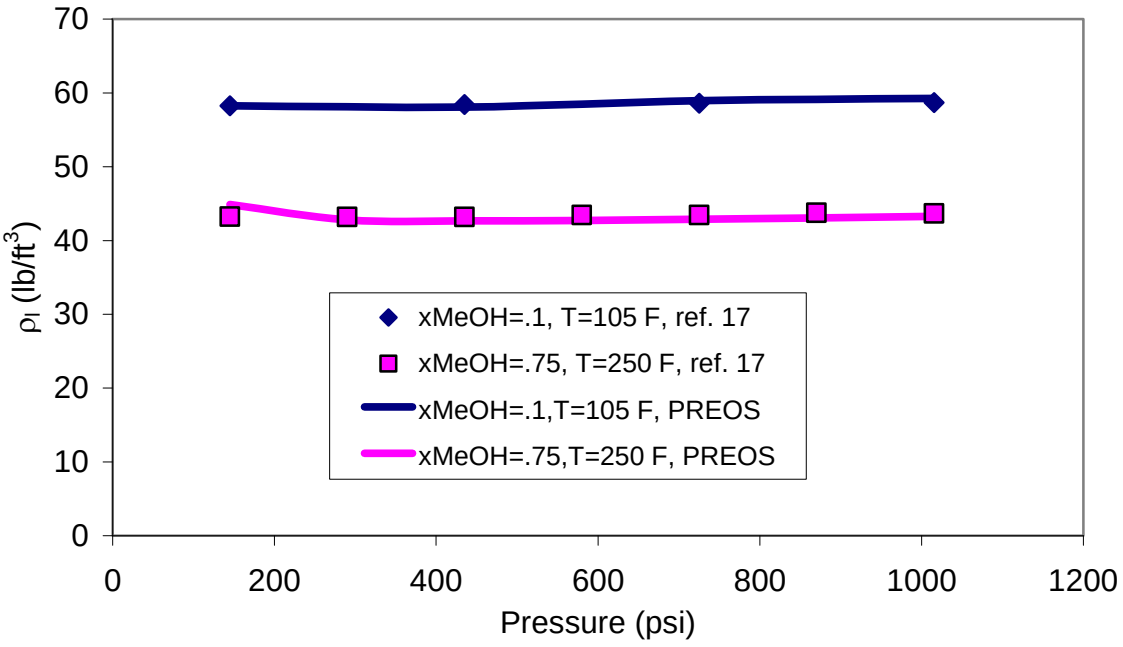

Figure 4.10. Density of liquid phase. CO_2-H_2O-MeOH ternary system. Compares experimental[17] values versus density predicated by the Peng-Robinson EOS.

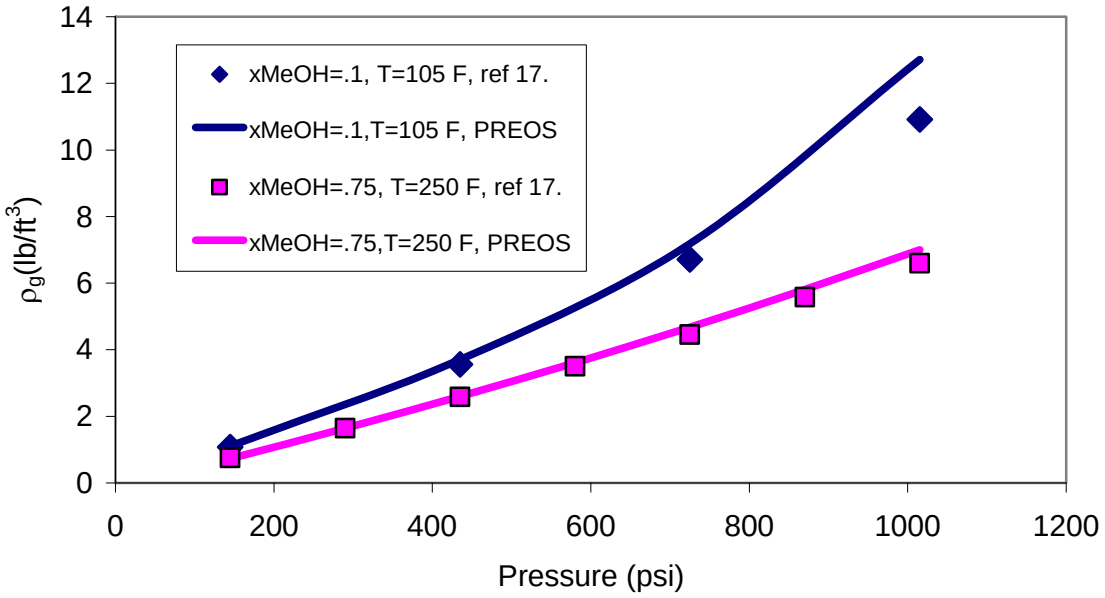

Figure 4.11. Density of gas (CO_2 rich) phase. CO_2-H_2O-MeOH ternary system. Compares experimental[17] values versus density predicated by the Peng-Robinson EOS.

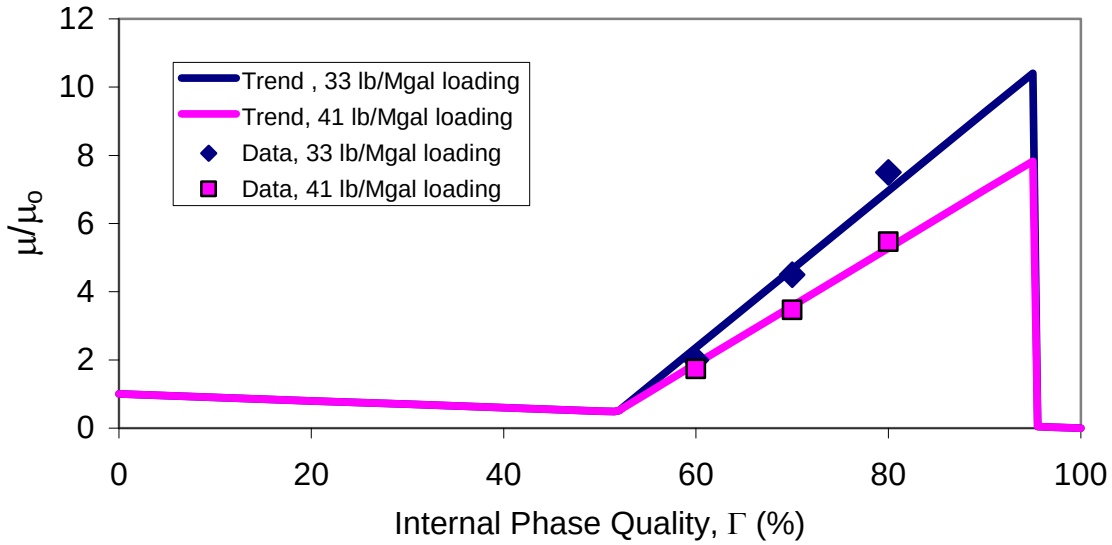

Figure 4.12. Viscosity as a function of internal phase quality for carbon dioxide foam with 40% methanol with water and additives. Data given by BJ Services.

CHAPTER 5: VERIFICATION OF MODEL AND PRELIMINARY RESULTS*

Chapter 3 described the formulation of the first model developed for energized fluid fracturing (EFRAC). Chapter 4 discussed the behavior of energized fluids and verified that the behavior of the fluid agrees with experimental data. This chapter illustrates the first attempts to model a complete energized fracturing scenario. The chapter is split into two sections. In the first section, a non-energized fluid case is run in the model so that it can be compared to the results of Nordgren[2]. In the second section, a base set of values are chosen and the model is set up for an energized fluid fracture. The output from the model represents the first energized fluid cases that are evaluated.

5.1 Model Verification Using Non-Energized Fluids

Every numerical model should be compared to analytical solutions or previous numerical results so that the model can be verified. In this case, we compared our numerical model with Nordgren's analytical and numerical results for fracture length and width. To make the comparison applicable, the assumptions made by Nordgren were applied to the new model. Nordgren assumed the fluid flow in the fracture is one-dimensional, isothermal, single-phase, Newtonian, and incompressible. A simple case was run in the new model with the assumptions: $T_{inj} = T_R$, number of phases = 1, number of components = 1, the fluid is Newtonian (n = 1), and the Peng-Robinson equation of state was turned off so the fluid remained incompressible. The other input values were specified but are not discussed here because the results are expressed in terms of the dimensionless variables[2]:

* Many of the ideas expressed in this chapter were first written for SPE 115750 by Friehauf and Sharma[1].

$$t_D = \frac{1}{\pi^2}\left[\frac{(1-\nu)\mu h q_{inj}^{\ 2}}{32C^5 G}\right]^{-2/3} t \tag{5.1}$$

$$L_D = \frac{1}{\pi}\left[\frac{(1-\nu)\mu h q_{inj}^{\ 5}}{256C^8 G}\right]^{-1/3} L \tag{5.2}$$

$$w_D = \left[\frac{16(1-\nu)\mu h q_{inj}^{\ 2}}{C^2 G}\right]^{-1/3} w \tag{5.3}$$

Where t_D, L_D, and w_D are dimensionless time, length, and width, respectively.

Figures 5.1 and 5.2 compare the results from the new model with the results of Nordgren[2]. The new model matches Nordgren's results for both dimensionless length and width. We concluded that the models are essentially identical when the previously mentioned assumptions are made. The only assumption that could not be applied is the one-dimensional flow assumption. The difference between one-dimensional and two-dimensional flow is negligible because the pressure gradients in the vertical direction are very small. This finding validates the methodology of averaging pressures at any fracture cross-section to simplify the fracture width calculation.

In cases where the leak-off of the fluid is either zero or is much greater than the convective transport, analytical solutions can be found for the 1D problem. These analytical solutions are also shown in Figure 5.1 and 5.2. The same comparison can be made between the difference in Nordgren's analytical and numerical solutions and the new numerical model and analytical solutions. The analytical and numerical results are significantly different because of the assumptions about leak-off, but the numerical results from each model match up well.

5.2 Preliminary Results Using Energized Fluids

This section shows results of fracture propagation for energized fluids (EFRAC). We chose several situations that display common issues that arise in energized fluid fracturing. For example, we show the expansion of the fracturing fluid by a temperature increase. We also show the effect of changing the phase leak-off and explain why

incorporating phase behavior might be important. In subsequent chapters, a more detailed study is done that predicts fracturing performance.

Four example cases, noted as a)-d), were run with the new model for energized fluids. The inputs common to all cases are shown in Table 5.1. Table 5.2 shows the inputs that vary from case to case. Notice that all four cases use 70 quality CO_2 foam and a 20 lb_m / Mgal HPG fluid in the aqueous phase. Case a) is isothermal at 75 F and has equal leak-off coefficients for both the aqueous and gas phases. This case represents a situation where the fluid remains at a cool temperature. Case b) is isothermal at 200 F with the same leak-off. This case represents a case in which the fluid is always at the reservoir temperature, an assumption that most models make. Case c) has an injection temperature of 75 F but the reservoir temperature is 200 F. Case d) has the same temperature effects as case c) but now has wall-building coefficients inferred from the work of Harris[3,4]. The non-wall-building coefficients were calculated and combined in the same way as described in Schechter[5] and in the section on modeling traditional leak-off in Chapter 2. The average leak-off coefficients for each phase are C_l = 0.00127 ft/min$^{1/2}$ and C_g = 0.0005 ft/min$^{1/2}$. The value is an average because of changes in temperature, as discussed by Harris.

Figure 5.3 shows the final fracture dimensions for all four cases. The difference in cases a) and b) can be explained by changes in fluid rheology with temperature. The 200 F case (b) has a higher temperature and, therefore, lower effective viscosity, resulting in thinner and longer fractures. Case a) is not realistic because reservoirs are much warmer than 75 F. Previous fracture models might give similar results to case b) because it is isothermal at reservoir temperature. In case c), the fracture is longer and wider than case b). The discrepancy in fracture volume happens because the fluid in case c) is injected at a lower temperature and then heated. Heating up the fluid allows it to expand as it travels down the length of the fracture. The expansion increases the overall volume of fluid that is pumped, creating a bigger fracture. Differences in cases c) and d) are due to leak-off. Lower leak-off of the gas phase in case d) creates an even longer and wider fracture, and is, therefore, better for proppant placement. Case d) is the most realistic case because it includes effects of temperature and multi-phase leak-off.

Figures 5.4 to 5.6 show more comparisons between cases c) and d). Figure 5.4 shows temperature contours for each case. Notice that temperature is high near all the fracture boundaries except the entrance. The temperature increases the most where the fluid is stagnant and the heat of conduction from the reservoir is greater than the convective transport. The opposite is true in the center regions, where more fluid travels, resulting in lower temperature to penetrate into the fracture. The lower leak-off in case d) allows the length of temperature penetration to be longer.

Figure 5.5 shows foam quality varying in each fracture. In case c), the leak-off for each phase is constant. Changes in quality can only occur due to changes in pressure and temperature, while the overall composition remains constant. Quality only changes by a few percent in case c). Case d) has much greater foam quality increase down the length of the fracture because of leak-off of each phase. Figure 5.5 shows a good example of how composition changes in different fracturing scenarios.

Figure 5.6 shows effective viscosity changes. In case c) two effects are evident: 1) the temperature decreases the effective viscosity down the length of the fracture, and 2) the lower shear rate at the top and bottom edges causes an increase in effective viscosity. Case d) shows the same effects but now includes the effect of foam quality on viscosity. Figure 5.6 shows all the effects that significantly change the rheology of foam (temperature, quality, shear rate). All these effects cannot be ignored when modeling foamed fluids.

In general, case d) shows how previous fracture mechanics can be combined with both the composition and thermal balances to predict changes in fracture dimensions, an effect seen for the first time. Case d) also shows the ability of CO_2 foams to create wider fractures, because of high effective viscosities and superior leak-off.

Nomenclature

C	Overall leak-off coefficient
C_l	Leak-off coefficient of aqueous phase
C_g	Leak-off Coefficient of gas phase
E	Young's modulus
G	Shear modulus
h	Fracture height
K_o	Base fluid consistency index
L	Fracture half length
L_D	Dimensionless length
n	Power law index
q_{inj}	Injection flowrate per unit height
Q_{inj}	Injection flowrate
t	Time
t_p	Total pumping time
T_{inj}	Injection temperature
T_R	Reservoir temperature
w	Fracture width
w_D	Dimensionless width

Greek Symbols

ν	Poisson's ratio
μ	Newtonian viscosity
Γ_{inj}	Injection quality
σ	Stress

References

1. Friehauf, K.E. and Sharma, M.M. 2008. A New Compositional Model for Hydraulic Fracturing With Energized Fluids. Paper SPE 115750 presented at the 2008 SPE Annual Technical Conference and Exhibition held in Denver, CO, 21-24 September.

2. Nordgren, R.P. 1972. Propagation of a Vertical Hydraulic Fracture. *Society of Petroleum Engineers Journal*, August: 306-314.

3. Harris, P.C. 1987. Dynamic Fluid-Loss Characteristics of CO2-Foam Fracturing Fluids. *SPE Production Engineering*, May: 89-94.

4. Harris, P.C. 1985. Dynamic Fluid-Loss Characteristics of Nitrogen Foam Fracturing Fluids. *Journal of Petroleum Technology*, October: 1847-1852.

5. Schechter, R.S. 1992. *Oil Well Stimulation*. Englewood Cliffs, New Jersey: Prentice Hall.

Table 5.1. Common inputs for all preliminary (Chapter 5) example cases.

Inputs
h = 100 ft
E = 5E6 psi
ν = 0.2
σ = 5000 psi
Q_{inj} = 30 BPM
Γ_{inj} = 70% CO_2
HPG loading = 20 lb_m/Mgal
n = 0.607
K_o = .00256 $lb_f s^n/ft^2$
t_p = 30 min

Table 5.2. Specific inputs for each preliminary (Chapter 5) example cases.

Case:	a)	b)	c)	d)
T_{inj} (F)	75	200	75	75
T_R (F)	75	200	200	200
C_l ($ft/min^{1/2}$)	0.00127	0.00127	0.00127	0.00127*
C_g ($ft/min^{1/2}$)	0.00127	0.00127	0.00127	0.0005*

*Average Value

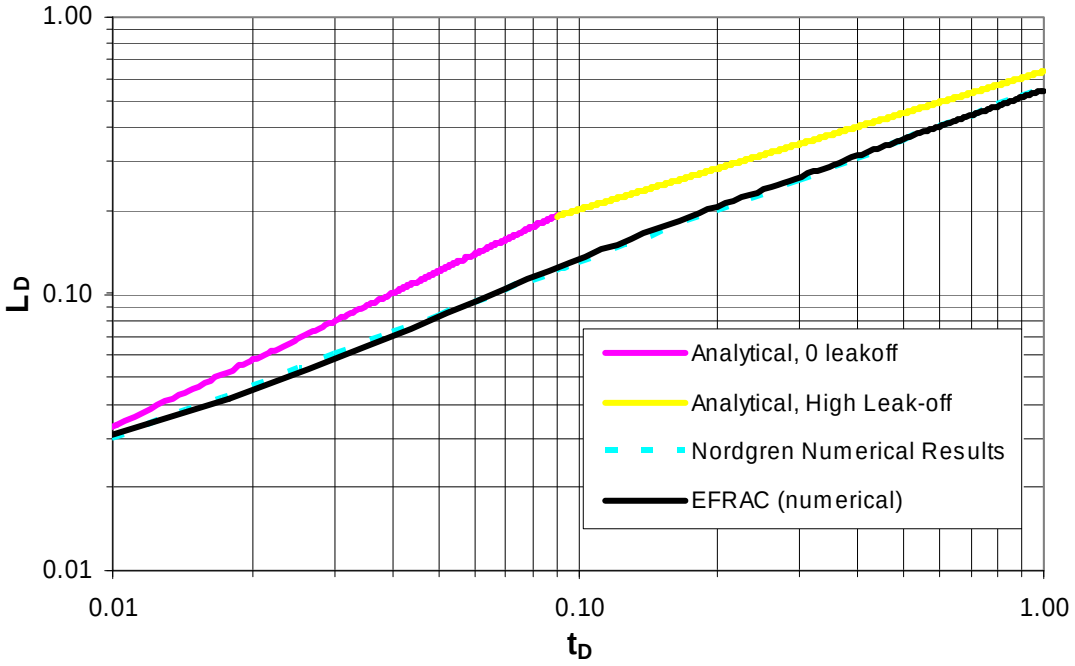

Figure 5.1. Comparison of Nordgren[1] to EFRAC, Dimensionless length.

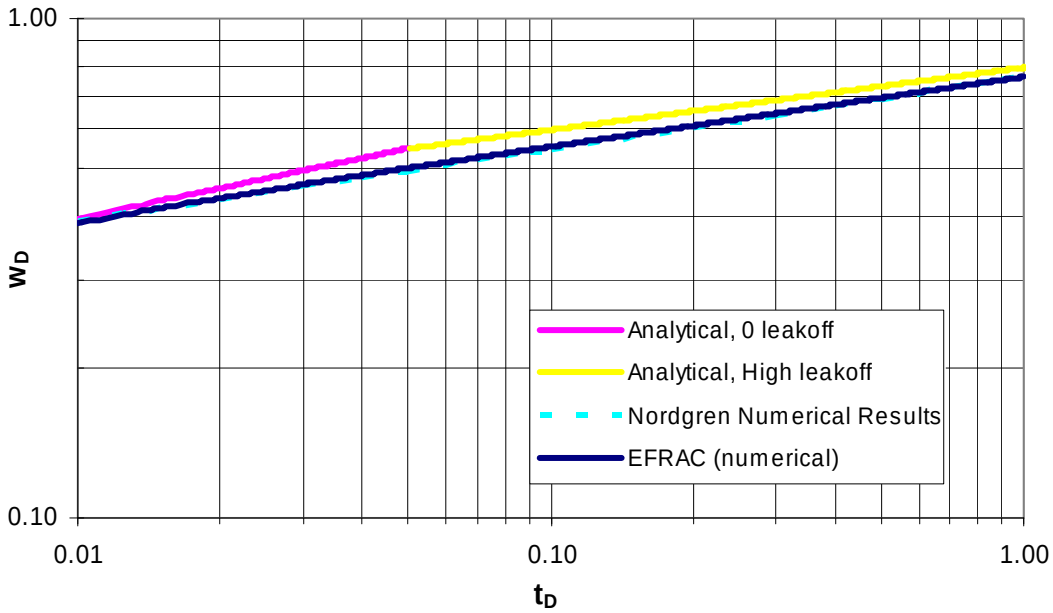

Figure 5.2. Comparison of Nordgren[1] to EFRAC, Dimensionless width.

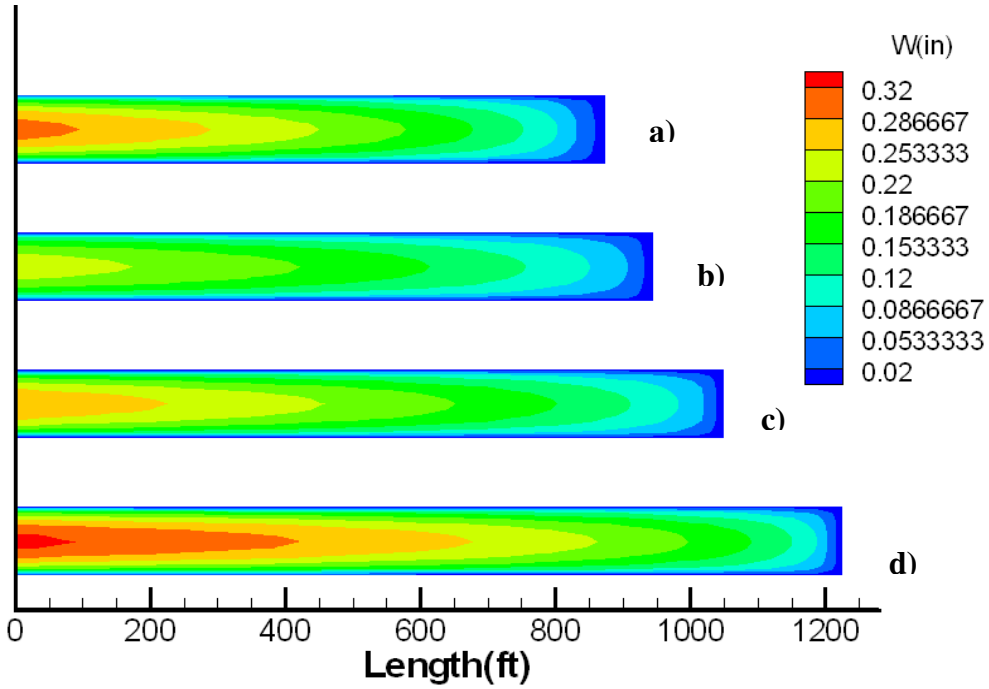

Figure 5.3. Final fracture widths and length for example cases: a) Isothermal, 75 F, equal phase leak-off; b) Isothermal, 200 F, equal phase leak-off; c) 75 F injection temperature, 200 F reservoir, equal phase leak-off; and d) 75 F injection temperature, 200 F reservoir, lower gas phase leak-off.

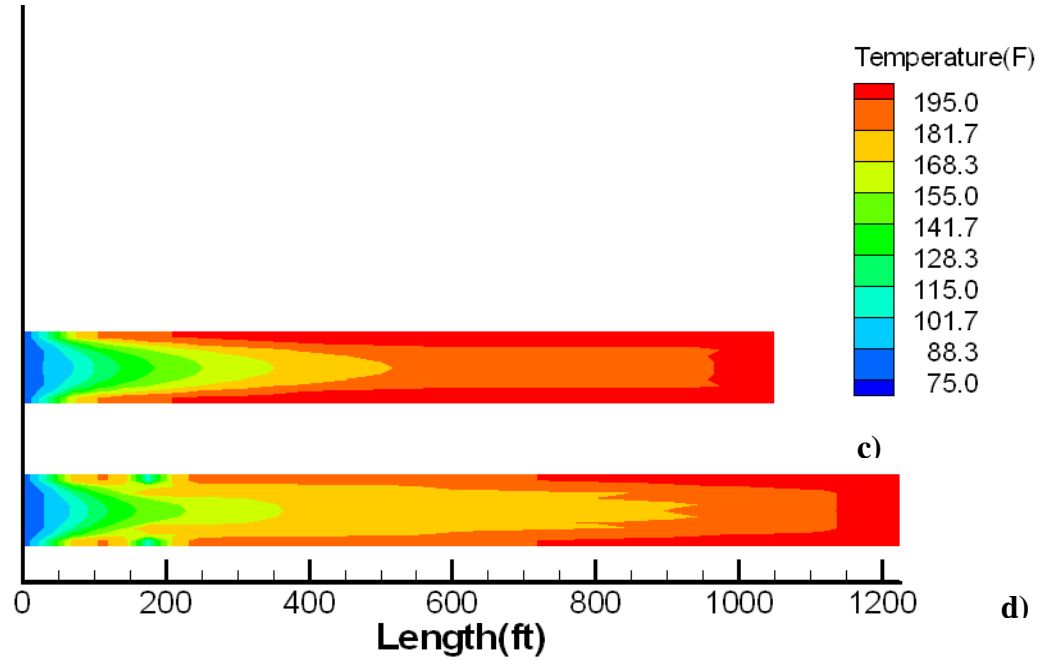

Figure 5.4. Final fracture temperature for example cases c) and d).

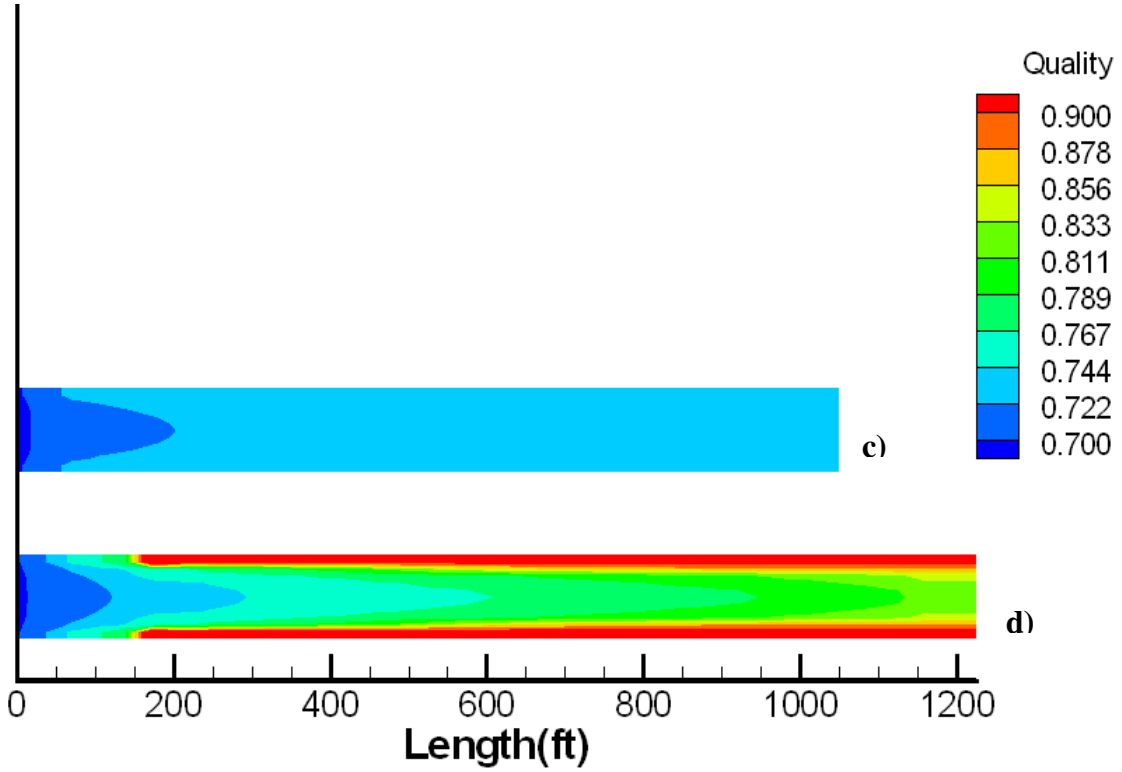

Figure 5.5. Final foam quality for example cases c) and d).

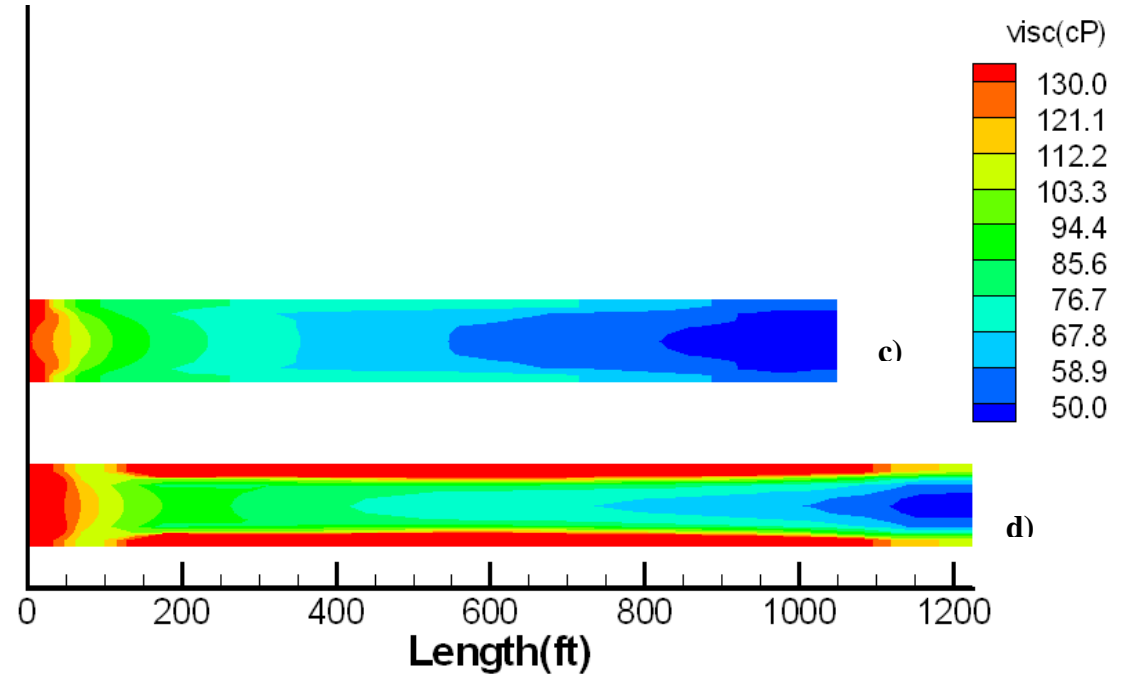

Figure 5.6. Final effective viscosities for example cases c) and d).

CHAPTER 6: A SIMPLE AND ACCURATE PRODUCTIVITY MODEL FOR HYDRAULICALLY FRACTURED WELLS*

Hydraulic fractures increase production of oil and gas wells by creating a highly conductive connection between the wellbore and the reservoir. Productivity of a fractured well is a function of the reservoir drainage area, fracture dimensions, fracture conductivity, formation conductivity, and the characteristics of any damage created during the process. There will always be some polymer gel and water that leaks-off into the formation. This area is called the invaded zone. In the invaded zone, high water saturation reduces the relative permeability of gas/oil.

There currently exist several models that calculate the productivity of fractured wells producing under steady-state or pseudo-steady-state conditions. However, none of these models can compute the productivity of a fractured well with a finite conductivity fracture and with damage in the invaded zone around and around the wellbore. Some models assume that the fluid enters the wellbore radially (Raymond[2]) while others assume an elliptical flow field (Prats[3]). An accurate productivity model for fractured wells is needed in conjunction with current fracture propagation models to better engineer the fracturing process.

Energized fractures reduce or eliminate damage in the invaded zone. This is why it is important to understand the level of damage that the invaded zone can incur. In situations where the damage due to leak-off of traditional fluids does not affect productivity, energizing the fracturing fluid may be unnecessary.

The model presented here is a useful tool because it takes the entire fracturing process down to one number, the productivity index. This allows direct comparison between different scenarios that are considered. The recommendations in upcoming chapters are based on differences in productivity indices calculated from this model.

* Many of the ideas expressed in this chapter were first written for SPE 119264 by Friehauf, Suri, and Sharma[1].

6.1 Background

Several authors have studied the effect of vertical fractures on hydrocarbon production[2-4]. Most present their results by plotting the productivity index, J ($q/\Delta P$), normalized by a base productivity index, J_o. J_o is defined as the productivity index of an unfractured, undamaged well in a circular drainage area. With some assumptions (see model formulation section), J_o for steady-state and pseudo-steady-state flow can be written as:

$$J_o = \frac{2\pi kh}{\mu \ln(r_e / r_w)} \quad ; \quad J_o = \frac{2\pi kh}{\mu \ln(r_e / r_w) + 0.5} \tag{6.1}$$

J/J_o is a dimensionless measure of the expected increase in productivity compared to an unfractured, undamaged well.

McGuire and Sikora[4] were the first authors to present systematic results for fractured well productivity. They developed a graphical method to estimate the productivity index of a well with a constant width fracture in a square drainage area. Their results are displayed as graphs of productivity index versus relative fracture conductivity.

Raymond and Binder[2] included the effect of variable fracture conductivity (non-constant fracture width) in their model. They also included the effect of a damaged zone around the wellbore. Their model assumes radial flow with an average radial permeability (averaged azimuthally). The radial permeability is a function of the fracture permeability, fracture width, and the reservoir permeability. This assumption is valid for short fractures where the flow is near radial around the wellbore. It is shown in this chapter that Raymond and Binder's model provides an overestimation of productivity for a fractured well.

Prats'[3] model assumes elliptical flow around the fractured well in an elliptical drainage area. The dimensions of the equi-pressure ellipses around the fractured well depend on a function of a dimensionless parameter "a_{prats}".

$$a_{\mathrm{Pr}ats} = \frac{\pi kL}{2k_f w_{ave}} \tag{6.2}$$

The model presented in this chapter also assumes a similar constant pressure ellipse around the fractured well. Prats introduced the effect of damage in the invaded zone for infinitely conductive fractures (but not for finitely conductive fractures), as shown below:

$$\frac{J}{J_o} = \frac{q_f}{q_o}\frac{q}{q_f} = \frac{\ln(\frac{r_e}{r_w})}{\ln(\frac{2r_e}{L}) + \frac{4h_{leak}}{\pi L}(\frac{k}{k_d} - 1)} \tag{6.3}$$

Cinco-Ley[5] included damage in the invaded zone in addition to finite fracture conductivity. Cinco-Ley did not assume steady-state but instead solved for the transient response of fractured wells. The goal of the Cinco-Ley model was to understand transient effects on rate and pressure so that well testing methods could be applied. The theory and application of their model to calculate the fractured well productivity is challenging to implement because of the mathematical effort needed to solve for rate and pressure as function of both time and position.

Suri and Sharma[6] used the Prats model as a starting point for their model for water injection in frac-packed wells. A resistor model was created to represent variable fracture conductivity and variable fracture face damage as a function of distance from the wellbore. The model assumed linear flow down the length of the fracture and perpendicular to the fracture face.

6.2 Model Formulation and Definitions

The following assumptions were made in developing the new model:

1. The reservoir is a single layer, homogeneous, and isotropic.
2. The fracture is vertical and spans the entire height of the reservoir.
3. Darcy's law is assumed in the reservoir, fracture, and damaged zone.

4. The production is bilinear inside the equi-pressure boundary around the fracture. A larger confocal equi-pressure ellipse, with area equal to the drainage area, surrounds the inner equi-pressure boundary around the fracture. In this outer area, the flow is assumed to be elliptical.
5. The pressure at the outer boundary is held constant at P_e.
6. The wellbore pressure is held constant at P_{wf}.
7. Propped fracture width, fracture half length, and damaged zone heights are functions of the reservoir petrophysical properties, fracturing fluid choice, and pumping schedule. These values can be estimated using a fracture growth model.
8. The production is single-phase, incompressible, and isothermal (at reservoir temperature).
9. There exists a damaged zone surrounding the fracture face caused by the leak-off of water or other fluids into the formation. The damage zone has a permeability of k_d and extends to a distance h_{leak} from the fracture face. This damaged zone should not be confused with damage that may occur directly around the wellbore from the filtration of fluids during drilling, completion, or any work-over operation.

For modeling purposes, the reservoir is split into 4 quarters of symmetry, shown in Figure 6.1. A single quarter is characterized by distances also shown in Figure 6.1. Notice that height of the inner ellipse (b_1), the fracture width (w), and the height of the invaded zone (h_{leak}) can be divided into constant value segments. The length of each segment is ΔX creating $L/\Delta X$ segments of the fracture.

The distances $b_{1,0}$ and a_1 in Figure 6.1 are calculated in a similar fashion as Suri[6] and Prats[3]. The distance a_1 is assumed to be slightly longer than the fracture length. The distance $b_{1,0}$ is a function of the dimensionless quantity a_{Prats} (Equation 6.2). A graphical representation of the inner equi-pressure boundary around the fractured well (with $b_{1,0}$ value), for different values of a_{Prats} is shown in Figure 6.2. Figure 6.2 was created from the results of Prats[3] for L/r_e of 0.4166. This model assumes that a_{prats} is the dominating

factor in controlling the inner ellipse size, $b_{1,0}$. This assumption of independent $b_{1,0}$ to L/r_e is later confirmed in this study and is presented in the results section.

The dimensions of the outer drainage ellipse are calculated by assuming a confocal ellipse around points x = -L and x = L, with an area equal to the drainage area (A) of the reservoir. The axes of the outer confocal ellipse (a_2, b_2) are calculated as:

$$b_2 = \frac{\sqrt{2(\sqrt{\pi^2 L^4 + 4A^2} - \pi L^2)}}{2\sqrt{\pi}} \tag{6.4}$$

$$a_2 = \frac{A}{\pi(b_2)} \tag{6.5}$$

J is calculated as the reciprocal of the total resistance.

$$J = \frac{q}{\Delta P} = \frac{1}{R_{tot}} \tag{6.6}$$

R_{tot} is calculated by the combination of the circuit given in Figure 6.3. The definition of each resistance and the algorithm combining the resistances are shown below.

We assume Darcy's law in all locations in the reservoir and the fracture. Depending on the flow geometry, the flow is modeled as elliptical, radial, or linear, and a flow resistance is appropriately defined. The elliptical flow resistance is specified from the constant pressure ellipse at the drainage boundary to the inner ellipse that encloses the fracture:

$$R_{out} = \frac{2\mu}{\pi hk} \ln\left(\frac{a_2 + b_2}{a_1 + b_{1,0}}\right) \tag{6.7}$$

The factor in Equation 6.7 is $2/\pi$ and not $1/2\pi$ because the model is only for a quarter of the drainage area. A radial flow resistor connects the wellbore to the inner ellipse. This resistor is the only path for the fluid to get to the wellbore without going through the fracture:

$$R_{el,0} = \frac{2\mu}{\pi hk} \ln(b_{1,0} / r_w) \tag{6.8}$$

If damage around the wellbore is present, the wellbore resistor has two parts, 1) the resistance from the wellbore through the damage, and 2) the resistance from the damage to the inner ellipse:

$$R_{el,0} = \frac{2\mu}{\pi h k_s} \ln(r_s / r_w) + \frac{2\mu}{\pi h k} \ln(b_{1,0} / r_s) \tag{6.9}$$

In Equation 6.9, r_s and k_s are the distance and permeability of the damaged zone around the wellbore, respectively.

For the flow to go through the fracture, the fluid must go through three sections of linear flow resistances. The first connects the inner ellipse to the damaged zone of the fracture face with the reservoir permeability:

$$R_{el,i} = \frac{(b_{1,i} - h_{leak,i})\mu}{kh\Delta X} \tag{6.10}$$

The second is the damaged zone perpendicular to the fracture:

$$R_{d,i} = \frac{h_{leak,i}\mu}{k_d h\Delta X} \tag{6.11}$$

The third is flow inside the fracture:

$$R_{f,i} = \frac{2\Delta X\,\mu}{k_f h w_i} \tag{6.12}$$

The last resistor, $R_{el,t}$, simply connects the inner ellipse to the fracture tip:

$$R_{el,t} = \frac{b_{1,t}\mu}{kh(a_1 - L)} \tag{6.13}$$

The following algorithm combines the individual resistances of the circuit into one total resistance. R_p and R_s are combined resistances of circuits in parallel and series at different locations in the fracture, i.

For i = L/ΔX to 0
  if (i = L/ΔX) then
    $1/R_{p,i} = 1/R_{el,t} + 1/(R_{d,i} + R_{el,i})$
    $R_{s,i} = R_{p,i} + R_{f,i}$

else
$1/R_{p,i} = 1/R_{s,i+1} + 1/(R_{d,i} + R_{el,i})$
if (i <> 0) then
$R_{s,i} = R_{p,i} + R_{f,i}$
end if
end if
Loop i
$R_{tot} = R_{p,0} + R_{out}$

J/J_o is calculated by dividing Equation 6.6 by Equation 6.1 and correcting for only one quarter of the area.

$$\frac{J}{J_o} = \frac{2\mu \ln(r_e / r_w)}{\pi k h R_{tot}} \tag{6.14}$$

6.3 Damage in the Invaded Zone During Production

A damaged zone is formed when leak-off of water occurs during creation of the fracture. The zone may or may not cause significant damage to the fracture productivity based on the extent of the leak-off. Figure 6.4 shows a schematic of damage in the invaded zone after hydraulic fracturing and during production. For cases where the permeability and drawdown pressures are high, the water is removed efficiently. In cases with low permeability and low drawdown pressure, the damage remains significant because the viscous flowing forces are not sufficient to overcome the capillary forces. We assume that the capillary force is the main force trapping the water, and that the relative permeability to gas/oil is a function of the capillary properties of the rock and the drawdown pressure only. The following simple model shows how relative permeability to gas/oil is estimated in the invaded zone.

For illustration purposes, the Brooks[7] and Corey[8] models were used for calculating the capillary pressure and relative permeability of gas/oil as a function of phase saturations.

$$P_c = P_c^o (S_w^*)^{-1/b} \tag{6.15}$$

$$\text{Where, } S_w^* = \frac{S_w - S_{wr}}{1 - S_{wr}} \tag{6.16}$$

$$\frac{k_d}{k} = k_{rnw} = k_{rnwo}(1 - S)^n \tag{6.17}$$

$$\text{Where, } S = \frac{S_w - S_{wr}}{1 - S_{wr} - S_{nwr}} \tag{6.18}$$

Note that b is the Brooks-Corey exponent that depends on the pore throat distribution of the rock. S_{wr} and S_{nwr} refer to the residual saturation of the wetting and non-wetting phases, respectively. Water is assumed to be the wetting phase, making the recovery of water by gas/oil a drainage process.

If the capillary pressure is much higher in the damaged zone than in the fracture (likely to be the case), the capillary pressure in the invaded zone is equal to the drawdown pressure across the invaded zone. Equations 6.15 and 6.17 are solved for an explicit expression that relates the damaged zone effective permeability, k_d, to the drawdown pressure, ΔP:

$$\frac{k_d}{k} = k_{rnwo}\left[1 - \frac{(1 - S_{wr})(\frac{\Delta P}{P_c^o})^{-b}}{1 - S_{nwr} - S_{wr}}\right]^n \tag{6.19}$$

The dependence on P_c^o can be taken out by defining a dimensionless drawdown pressure:

$$\Delta P^* = \frac{\Delta P}{P_c^o} \tag{6.20}$$

The parameter P_c^o, defined in Equation 6.15, is a measure of the capillary pressure at high water or wetting saturation. If the region around the fracture is fully saturated with the wetting phase, P_c^o represents the minimum drawdown that any wetting phase could be recovered from that region. If the drawdown is less than P_c^o, the water saturation will remain high, causing relative permeability damage that may permanently inhibit gas from flowing into the fracture.

Leverett[9] discusses capillary pressure in porous solids. The study concludes that the capillary pressure is a function of the absolute permeability, porosity, and surface forces. The results collapse onto one dimensionless plot of capillary pressure versus the saturation of the wetting phase. The capillary pressure approaches the value P_c^o at high wetting phase saturation. Equation 6.21 shows how the calculation is accomplished. The 0.42 in Equation 6.21 is the dimensionless capillary pressure at high wetting phase saturation. The other terms re-dimensionalize 0.42 into units of pressure. As an example, if the permeability is 0.1 md, porosity is 20%, and $\sigma\cos\theta$ = 50 dynes/cm, the value of P_c^o is 133.8 psi (beware of the units, 1 dyne/cm/md$^{1/2}$ = 4.617 psi).

$$P_c^o = 0.42\sigma\cos\theta\sqrt{\frac{\phi}{k}} \tag{6.21}$$

6.4 Results

The results in this section were obtained by using the model presented with fracture and reservoir properties shown in Table 6.1. The fracture dimensions are set by the ratio L/r_e and w_{max}. The fracture width starts at the maximum, w_{max}, at the wellbore and reduces elliptically to zero at L. The ratio h_{leak}/w, a constant, simulates the invaded zone distances being proportional to the fracture width at any location. This simulates a hypothetical fractured case that is meant to represent a typical system. Situations that differ from the base scenario are evaluated by changing one variable at a time and discussed with subsequent figures.

6.4.1 NON-DAMAGED FRACTURED WELL PRODUCTIVITY

Figure 6.5 shows a comparison of the productivity indices obtained from the different models as a function of dimensionless fracture conductivity, F_{cd}.

$$F_{CD} = \frac{k_f w_{ave}}{kL} \tag{6.22}$$

The value of F_{CD} was varied by changing k_f/k. It is clearly seen that the productivity increase predicted by our model is consistent with Prats' model. Both these models compute a productivity enhancement that is significantly lower than that predicted by the Raymond[2] and McGuire[4] models. Thus, results from Raymond's and McGuire's model should be considered overly optimistic (except for F_{CD} values less than 1) in terms of the expected performance of hydraulically fractured wells.

The differences between the models arise because of unreasonable assumptions in the earlier models. The Raymond[2] model assumes radial flow in the reservoir. The permeability is calculated by averaging the reservoir and fracture permeability at each radial location around the wellbore. Assuming radial iso-potential lines, results in an unrealistic increase in calculated productivity. This is not the case in bi-linear flow models where the fracture only helps stimulate the part of the region that is fractured, rather than the entire circular area. The differences between the McGuire[4] model and our model are harder to quantify since insufficient details of the model are provided in the original paper. Differences could be a result of the assumptions of a square drainage area and constant width fracture, which are different from the assumptions in the Prats[3] and this model. The primary reason for the discrepancy might be that McGuire's[4] model is based on physical experiments that do not represent the fractured well system accurately. Both the McGuire[4] and Raymond[2] models have been extensively quoted in the literature. Field observations for the productivity of fractured wells almost invariably significantly under-perform predictions made on the basis of these models. The results show that at least a part of the explanation lies in the fact that the models over-predict the productivity enhancement due to the creation of the hydraulic fracture.

The agreement between Prats'[3] model and the model presented here is to be expected since the isopotential ellipses are calculated in the same way. The model presented here, however, allows us to specify any distribution of damage around the fracture (this is not possible in Prats' model). For $L/r_e = 0.5$ the results from the two models are shown to match. Results for extreme values of L/r_e (0.1 and 0.99) are also shown in Figure 6.6. Both models give similar results for all values of L/r_e even though $b_{1,0}$ is estimated for an L/r_e value of 0.4166 in the new model. This confirms that $b_{1,0}$ is

dependent on the fracture conductivity, but is not dependant on L/r_e. The value $b_{1,0}$ is calculated using Figure 6.2, no matter what the L/r_e value is.

Figure 6.5 also shows the new model giving more reasonable results than Prats[2] at low conductivity because J/J_o approaches one for $F_{CD} \sim 0$. This is because radial flow would persist if the fracture had no conductivity. When fracture conductivity is low, the radial resistor is the smallest and, therefore, the dominant resistor in the model circuit. This results in a J value equal to J_o, giving us a value of near 1. This is not the case in Prats'[2] solution where J/J_o is closer to 2 for very small F_{cd}.

Figure 6.7 shows a complete set of results of the new model without damage around the fracture. This figure can be used as a master plot to calculate J/J_o for finite conductivity fractures with no matrix damage around the fracture face. Any gel-induced damage in the fracture can be accounted for by varying the fracture conductivity.

6.4.2 DAMAGED FRACTURED WELL PRODUCTIVITY

This section discusses what happens when a damaged invaded zone around the fracture is added. Figure 6.8 shows results for two cases of damage, k_d/k of 0.01 and k_d/k of 0.001. The results can only be compared to the Prats[3] model for infinite conductivity fractures. The value of J/J_o is close to Prats'[3] solution at high conductivity for k_d/k of 0.01 but not 0.001. In the case of large damage, the new model redirects the flow from the damaged fracture into the radial wellbore flow resistor, giving the fluid a low resistance pathway. Prats'[3] model assumes that flow must go though the fracture in order to get to the wellbore, therefore, the higher the damage, the more Prats'[3] and the new model will disagree. The new model yields a more accurate prediction of J/J_o because it will redirect the fluid into the non-damaged wellbore instead of forcing it through a highly damaged fracture.

Figure 6.9 shows both the size and permeability of the invaded zone contributing to the reduction of productivity in fractured systems. The reduction can be of paramount importance if either property reaches an extreme value, shown by the productivity index ratio dropping to near 1 in some cases. For most cases, the reduction is negligible if the ratio $k_d/k > 0.1$. In other words, the invaded zone has to reduce in permeability by over

90% in order to cause any significant impact on well PI. This means that some water leak-off is acceptable, as long as it does not reduce the hydrocarbon relative permeability by more than an order of magnitude. In low permeability sands and sandstones (tight gas sands and shales), the gas relative permeability has been shown to decrease by up to 3 or 4 orders of magnitude as the water saturation is increased. In addition, the trapped water is difficult to remove since the capillary pressure is high.

Figure 6.10 shows the same data as Figure 6.9 for h_{leak}/w =100 with the x-axis converted to the dimensionless drawdown, ΔP^* (Equations 6.19 and 6.20). Figure 6.10 shows the results for three different values of b, the Brooks-Corey exponent for capillary pressure. The effect of P_c^o is taken out by reporting the drawdown pressure in dimensionless terms. The results confirm that the higher drawdown pressures will effectively recover all the water and cause no damage. The opposite will be true for low drawdown pressures. If the drawdown pressure is less than P_c^o then the water will remain trapped and it may be necessary to energize the fracturing fluid by adding a gas component. The gas component will keep the saturation of water low in the invaded zone and, therefore, keep the gas relative permeability high.

6.4.3 FRACTURED WELL PRODUCTIVITY WITH AN INITIAL DAMAGED WELL

The previous section discussed damage around the fracture that occurred because of leak-off during the creation of the fracture. This section discusses the effect of damage around the wellbore that may exist before a fracture is created. This is the type of damage that is present from drilling and well completion fluids around the wellbore. Figure 6.11 is another figure that shows the productivity index ratio versus fracture conductivity using the parameters in Table 6.1.

There are six different scenarios shown in Figure 6.11. Three levels of damage around the wellbore (skin = 0, 10, 100) are shown, and each is shown with a damaged and undamaged fracture. The skin, which is a dimensionless measure of pressure drop around the wellbore, is commonly calculated by combining the permeability and depth of the damage:

$$s = \left(\frac{k}{k_s} - 1\right) \ln(r_s / r_w) \tag{6.23}$$

where r_s and k_s are the radius and permeability of the damaged zone around the wellbore, respectively. At low fracture conductivity, the productivity index ratio is below one for wells with skin. Remember that J_o is defined as a productivity index for an unfractured, undamaged well in a circular drainage area. Wells with damage around the wellbore and low fracture conductivity will produce less than that amount, resulting in J/J_o less than one. At high conductivity, we see that the curves for all cases with no damage around the fracture face converge to a single point. With high fracture conductivity, the extent of the damage around the wellbore does not matter because all the flow occurs through the fracture. If damage is present in the invaded zone, this is no longer the case. No matter how conductive the fracture is, the damage around it will impede the flow into the fracture. Figure 6.11 shows how the well productivity can decrease because of both damage around the wellbore and damage in the invaded zone.

6.5 Conclusions

1. Productivity indices for hydraulically fractured wells predicted by earlier models by McGuire[4] and Raymond[2] significantly over-estimate the impact of the fracture on well productivity.
2. A flow resistor model presented in this chapter can be used to predict productivity enhancement for fractured wells with damage in the invaded zone and for variable fracture conductivities.
3. The model is shown to be consistent with the Prats[3] model for finite conductivity fractures with no damage.
4. The model is shown to provide a more accurate estimate of the productivity (compared to Prats' model) for low conductivity fractures and fractures with significant damage in the invaded zone.

5. The model also allows any permeability damage to be specified around a finite conductivity fracture (not possible in other models).
6. Damage around the fracture face is significant only when the damaged zone is very impermeable, $k_d/k < 0.1$.
7. The amount of permeability damage is dependant on the capillary properties of the formation and the drawdown pressure across the invaded zone. If capillary forces are low, and drawdown pressure is high, enough water will be recovered resulting in a negligible damage.
8. For situations where the drawdown cannot be raised, fracturing fluids should be energized with a gas component so that the permeability of the damaged zone can be increased.

Nomenclature

a_1	Inner ellipse dimension in direction of fracture
a_2	Outer ellipse dimension in direction of fracture
a_{prats}	Fracture conductivity defined by Prats
A	Drainage area
b	Brooks-Corey model for capillary pressure exponent
b_1	Inner ellipse dimension in direction perpendicular to fracture
$b_{1,i}$	Distance from fracture to inner ellipse boundary for fracture segment i
b_2	Outer ellipse dimension in direction perpendicular to fracture
ϕ	Porosity
F_{cd}	Dimensionless fracture conductivity
h	Height of fracture
h_{leak}	Height of damaged zone around fracture face
J	Productivity Index
J_o	Productivity Index of a unfractured, undamaged reservoir in a circular drainage area
k	Reservoir permeability
k_d	Damaged zone permeability (effective permeability of the producing phase i.e. oil/gas)
k_f	Fracture permeability
k_{rnw}	Relative permeability of non-wetting phase
k_{rnwo}	Endpoint relative permeability of non-wetting phase
k_s	Permeability of damage around the wellbore
L	Fracture half length
μ	Reservoir viscosity
n	Gas relative permeability exponent
P_c	Capillary pressure
P_c^o	Endpoint capillary pressure, Brook-Corey
P_e	Outer boundary pressure
P_{wf}	Production wellbore pressure
ΔP	Drawdown pressure
ΔP^*	Dimensionless drawdown pressure
q	Production flowrate
q_o	Production flowrate from unfractured, undamaged reservoir in a circular drainage area
q_f	Production flowrate from and undamaged fracture
r_e	Drainage radius
r_s	Radius of damage around the wellbore
r_w	Wellbore radius
R	Fluid resistance [$q = \Delta P/R$]
R_p	Fluid resistance, a combination of resistances in parallel
R_s	Fluid resistance, a combination of resistances in series
R_{tot}	Total fluid resistance for the fracture system
s	Skin, damage around the wellbore
$\sigma\cos\theta$	Interfacial tension
S_w	Wetting phase saturation
S_{wr}	Residual wetting phase saturation
S_{nwr}	Residual non-wetting phase saturation
w_{ave}	Average width of fracture
w_i	Width of fracture at fracture segment i
ΔX	Length of fracture segment

References

1. Friehauf, K.E., Suri, A., and Sharma, M.M. 2009. A Simple and Accurate Model for Well Productivity for Hydraulically Fractured Wells. Paper SPE 119264 presented at the SPE Hydraulic Fracturing Technology Conference, The Woodlands, Texas, 19-21 January.
2. Binder, I.R., and Raymond, G.G. 1967. Productivity of Wells in Fractured, Damaged Formations. *JPT* January: 12-130. SPE 1454.
3. Prats, M. 1961. Effect of Vertical Fractures on Reservoir Behavior – Incompressible Fluid Case. *SPEJ* June 1961:105-117. SPE 1575-G.
4. McGuire W.J., and Sikora, V.J. 1960. The Effect of Vertical Fractures on Well Productivity. *JPT* October: 72-75. SPE 1618.
5. Cinco-Ley, H., and Samaniego, F. 1978. Effect of Wellbore Storage and Damage on the Transient Pressure Behavior of Vertically Fractured Wells. Paper SPE 6752 presented at the 52nd Annual Fall Technical Conference and Exhibition of the Society of Petroleum Engineers of AIME, Denver, Colorado, 9-12 October.
6. Suri, A., and Sharma M.M. 2007. A Model for Water Injection in Frac-Packed Wells. Paper SPE 110084 presented at the 2007 SPE Annual Technical Conference and Exhibition held in Anaheim, California. 11–14 November.
7. Brooks, R.H., and Corey, A.T. 1966. Properties of Porous Media Affecting Fluid Flow. *Jour. Irrigation and Drainage Div., Proc. Amer. Soc. Of Civil Engr.* June: 61-88.
8. Corey, A.T. 1977. *Mechanics of Immiscible Fluids in Porous Media.* Fort Collins, Colorado: Water Resources Publications.
9. Leverett, M.C. 1940. Capillary Behavior in Porous Solids. *Petroleum Technology*. August: 152-169.

Table 6.1. Base case inputs for productivity model

Constant Values				
k	0.01	md		
w_{max}	0.10	Inches		
A	40	Acre		
r_w	3	Inches		
Ratios				
L/r_e	0.5			
k_d/k	0.001			
h_{leak}/w	100			
k_f/k	1000000			
Necessary for Drawdown Pressure Calculation				
S_{wr}	0.2			
S_{nwr}	0.2			
k_{rnwo}	0.9			
n	3			

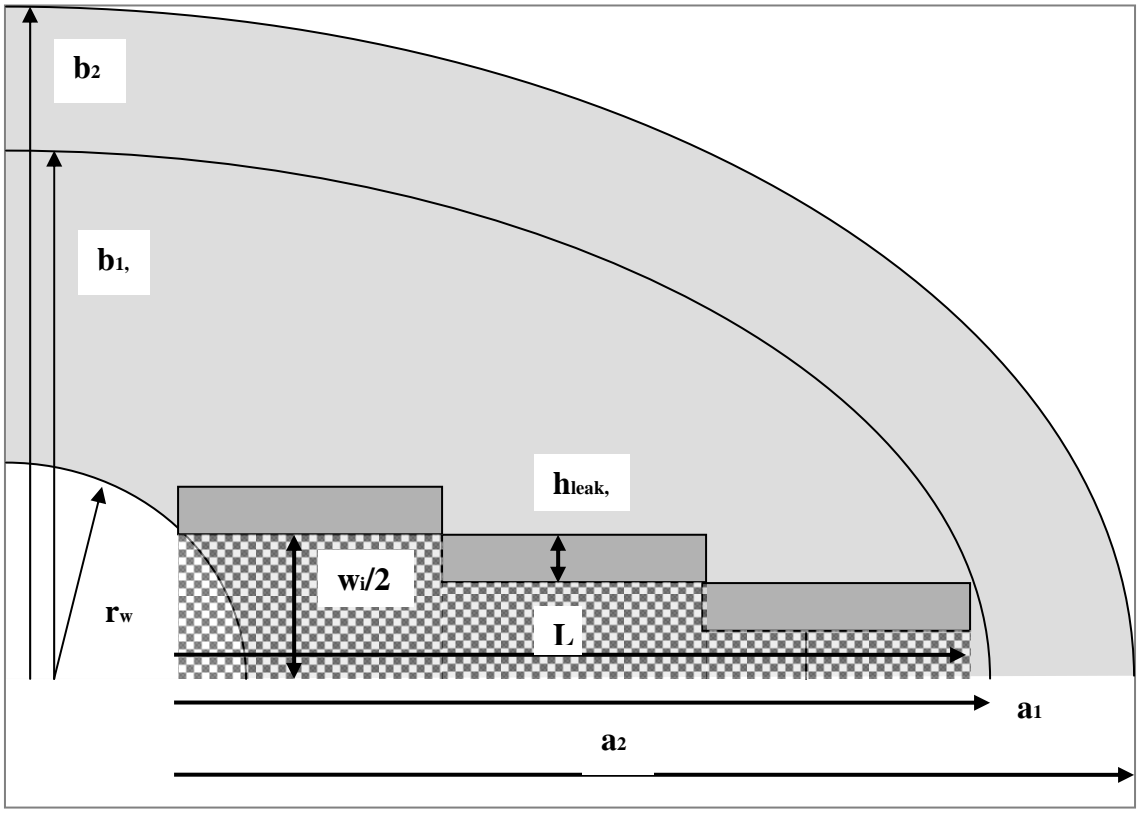

Figure 6.1. Definition of distances in a quarter of the fractured well system.

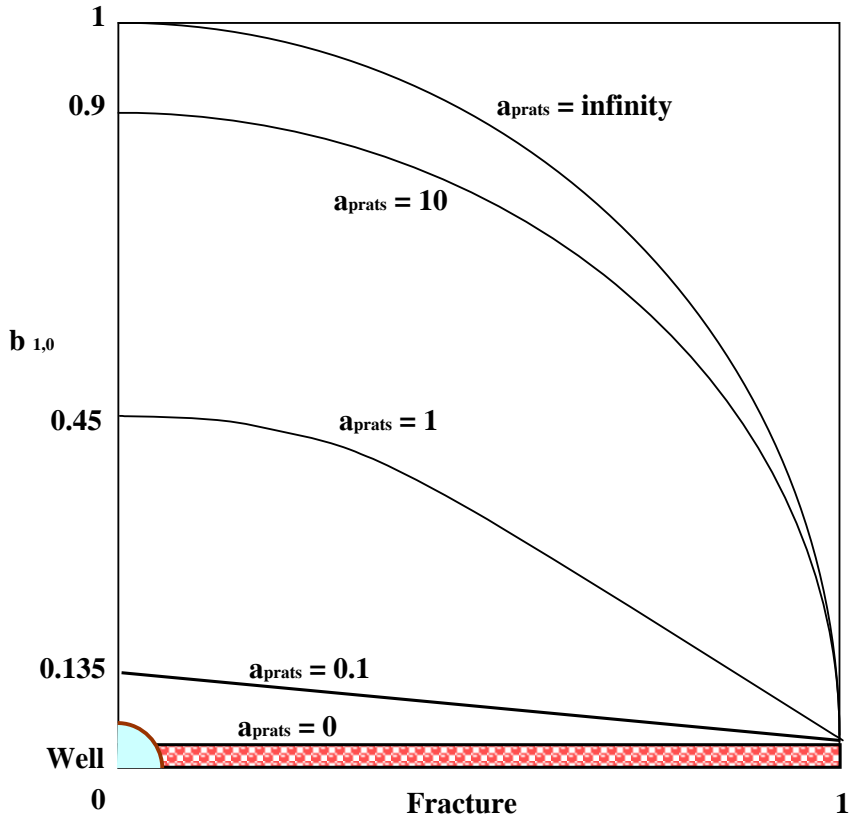

Figure 6.2. Inner ellipse minor axis vs "a_{prats}" conductivity. Figure taken from Suri and Sharma[6].

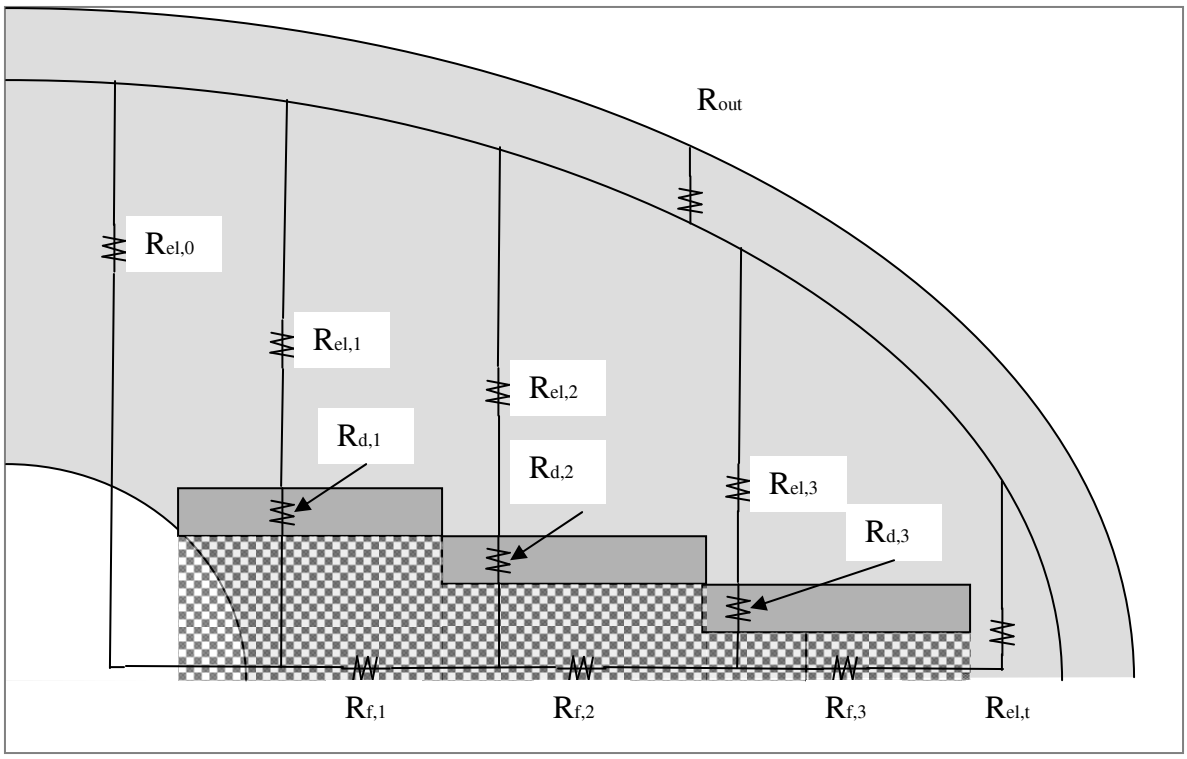

Figure 6.3. Resistors in current productivity model.

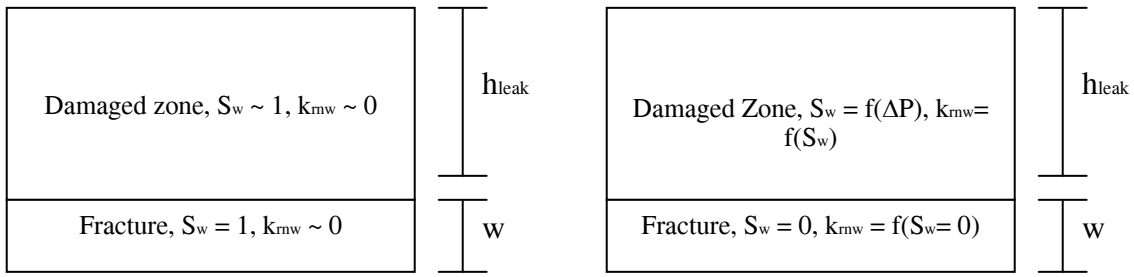

Figure 6.4. (a): Saturation of water in and around the fracture after hydraulic fracturing. (b): Steady saturation of water in and around the fracture during production.

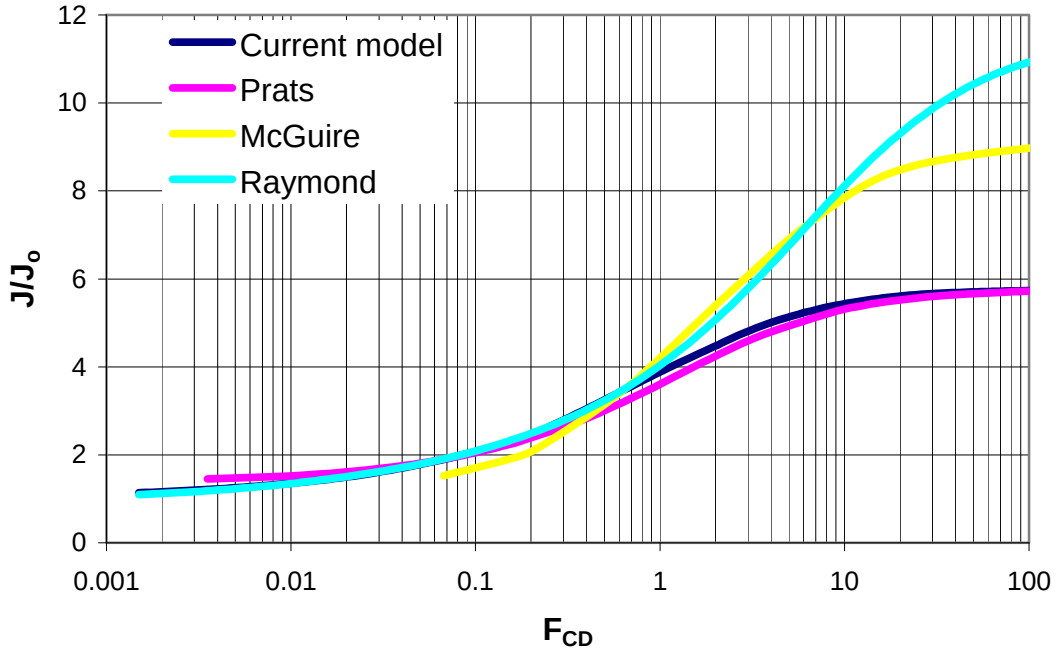

Figure 6.5. Comparison of production models for fractured wells with no damage.

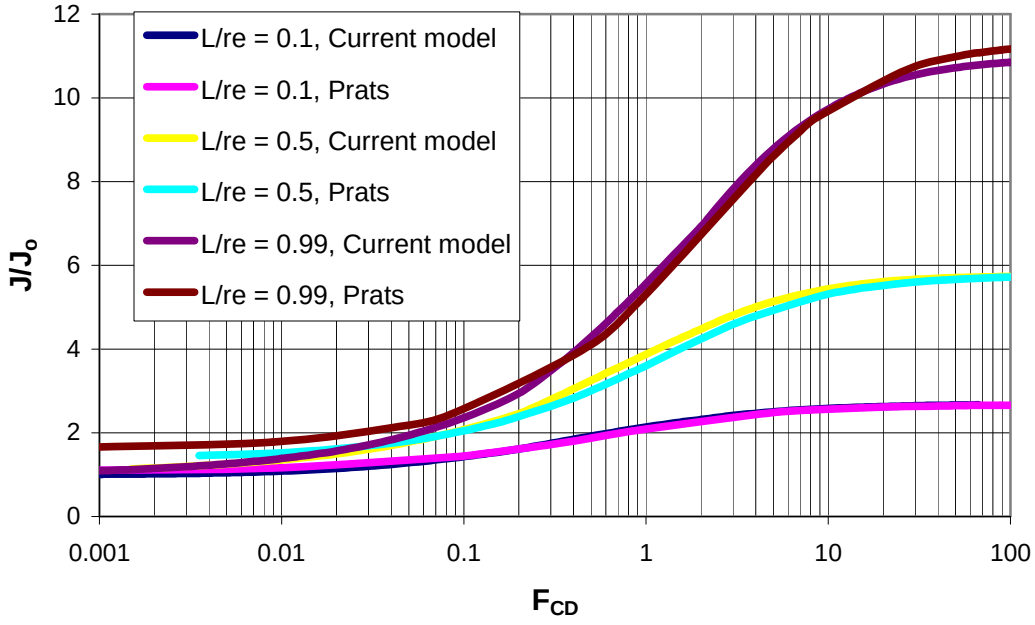

Figure 6.6. Comparison of current model to Prats'[3] model (finite conductivity fractures with no damage).

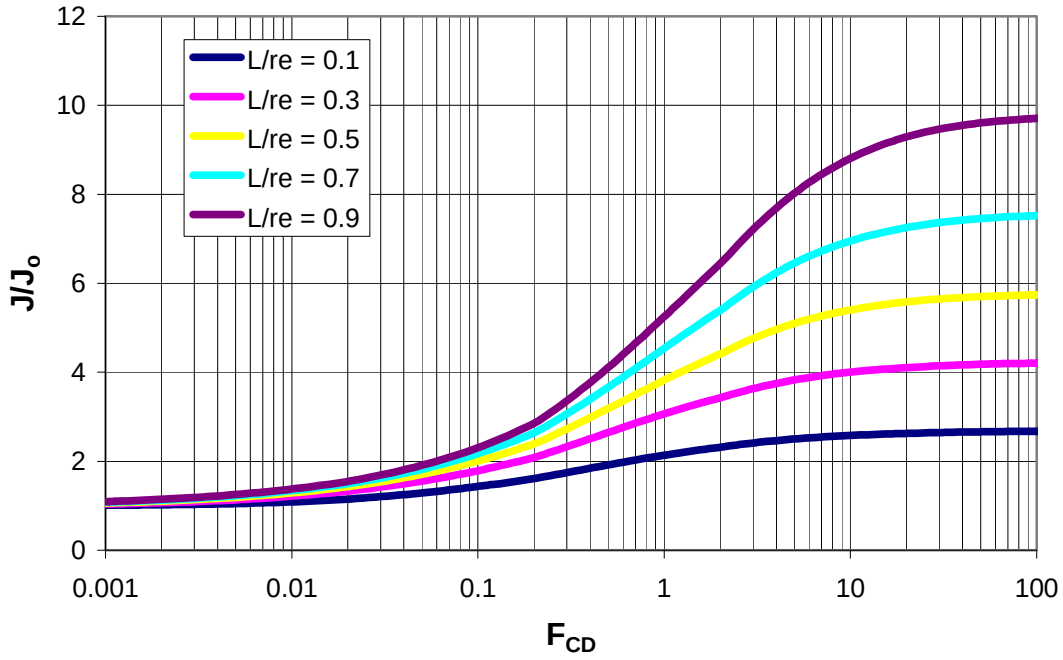

Figure 6.7. Current productivity model master plot for undamaged fractures with finite conductivity.

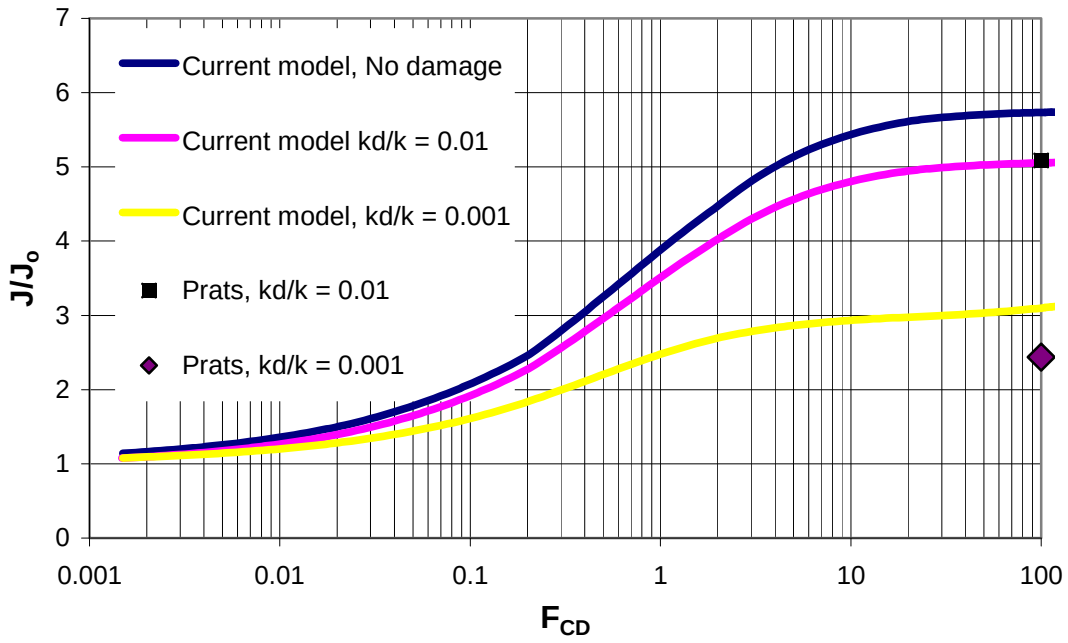

Figure 6.8. Effect of damage in the invaded zone predicted by the productivity model.

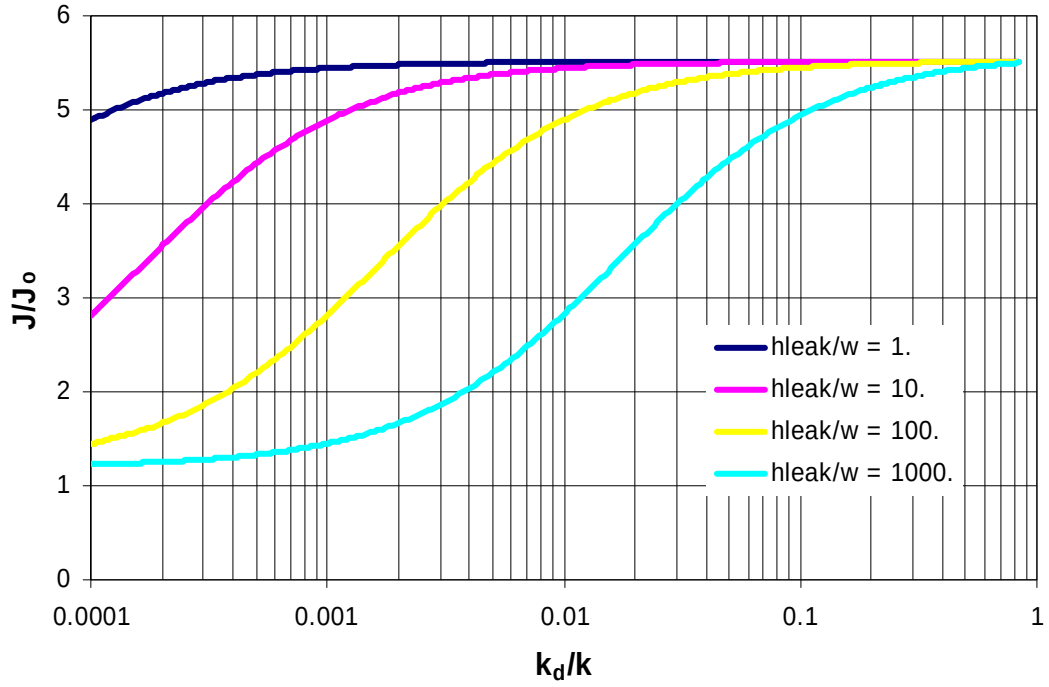

Figure 6.9. Effect of depth and permeability of the invaded zone on fractured well productivity as predicted by the current model.

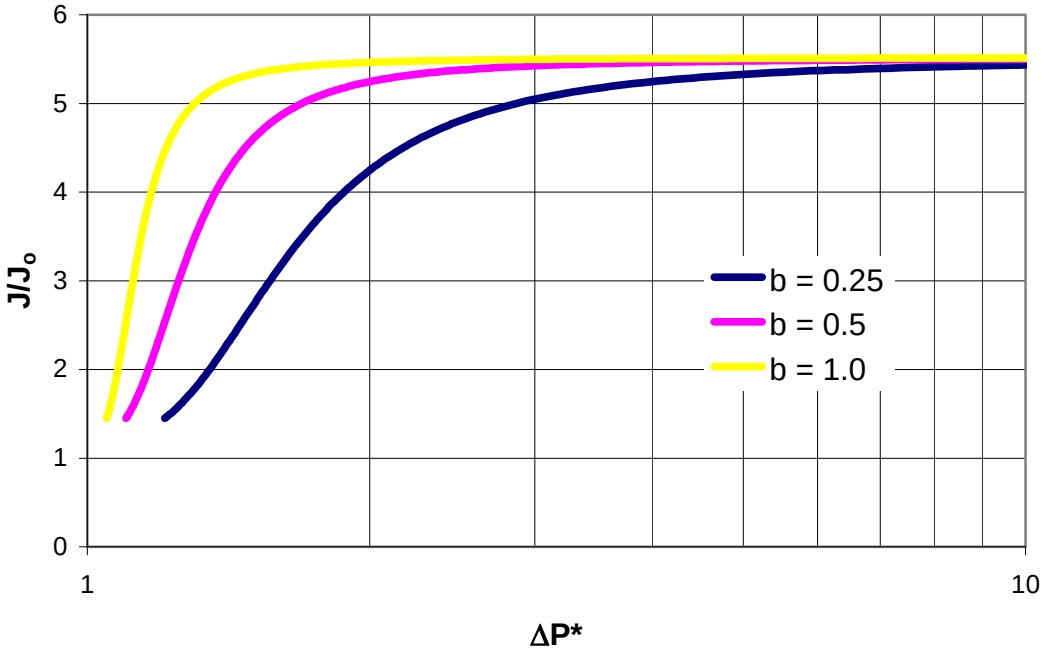

Figure 6.10. Effect of drawdown pressure predicted by the current model. $h_{leak}/w = 100$.

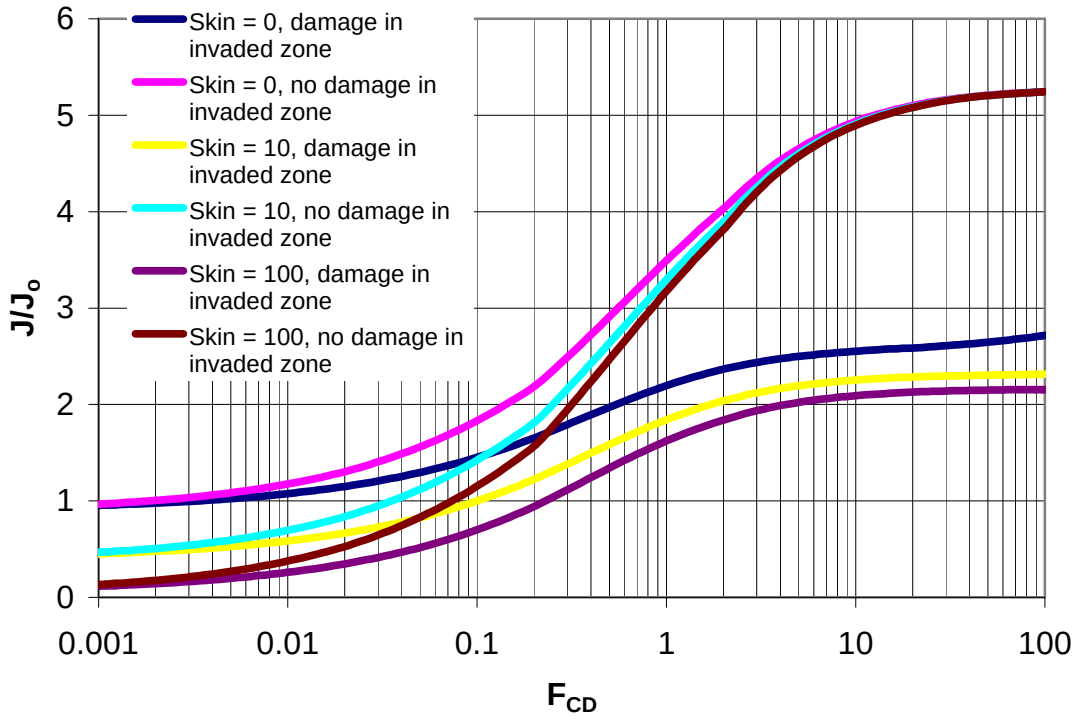

Figure 6.11. Effect of damage around wellbore predicted by the current model.

CHAPTER 7: APPLICATION OF THE FRACTURE PROPAGATION MODEL - A SOUTH TEXAS CASE STUDY*

This chapter discusses the first application of the fracture model (EFRAC) on actual fracture designs. Modeling and evaluation of previous fractures is shown on tight gas wells in South Texas. The operator expects to perform similar fracturing treatments in the future; therefore it is necessary to evaluate the design before more treatments are pumped. It is shown that this model can be used instead of costly trial-and-error methods in the field to help improve upon the design of the treatments.

This chapter involves the fracture propagation model disused in Chapter 3, the phase behavior and rheology of the CO_2-H_2O system discussed in Chapter 4, and the productivity index calculation in Chapter 6. All of these topics come together so that predicted fracture performance is evaluated. This chapter serves as an example of how my research aids actual operators and engineers.

This study has two primary goals. The first goal is to achieve an accurate model for energized fracture jobs that have been previously pumped with very few adjustable parameters. Several typical fracturing jobs were chosen in a South Texas gas field operated by Anadarko. The model is used to history match the net pressure and rate data from the field treatments. The second goal is to study variations in the energized fracture design using the model. Results of the model can be used to improve fracture design in the field. The findings are discussed in the Results and Conclusion sections.

7.1 History of Fracture Treatments in South Texas Field

Recently, energized fluids have been used to fracture tight gas wells in South Texas. It became necessary to energize the fracturing fluid because depletion had caused low well productivities when traditional fluids (slick-water or cross-linked gels) were used. In many of the original treatments, many dollars and man hours were being spent

* Many of the ideas expressed in this chapter were first written for SPE 119265 by Friehauf., Sharma, and Sullivan[1].

on swabbing the wells before they could be put into production. CO_2 was chosen as the energizing fluid. Low volume fraction, or quality, of gas was pumped during the treatment. To limit costs, an effort was made to minimize the amount of gas needed while still creating adequate recovery of fluid. The base fluid was a 40 lbm/Mgal zirconium crosslinked polymer gel.

The following is a description of the South Texas area. It was originally written for SPE 119265 by Friehauf , Sharma, and Sullivan[1] and was contributed primarily by Richard Sullivan of Anadarko Petroleum Corp.

> *The Lower Vicksburg in the study area is Oligocene in age and occurs as an expanded section downthrown to the main Vicksburg fault zone. The reservoirs in the study area were deposited as a series of shelf margin deltas. There are four basic sand packages, the S, T, U, & V which each represent an entire delta complex. Faulting is extremely common within each delta complex.*
>
> *The Lower Vicksburg is encountered at depths ranging from 8,000 – 12,500 ft. The initial pressure gradients range from 0.7 psi/ft at 8,000 ft to 0.85 psi/ft at 12,500 ft. Botttom hole temperatures can be up to 320 deg F. The sand packages have varying net pay thicknesses, with most in the range of 20-150 ft. Average porosities are 16-18% with average permeabilities ranging from 0.01 – 0.2 md.*
>
> *Development of the Frio & Vicksburg began in the early 1940's and was primarily driven by a market for the gas condensate. The low GOR (20,000 – 30,000 scf/STB) associated with these gas reservoirs allowed an adequate volume of liquids to be recovered to justify the expenditures. A strengthening gas market in the 1960's was the primary driver for continual development. Advances in hydraulic fracturing technology has been paramount to the continual development of these tight gas sands.*
>
> *During the initial development of this field, pressure depletion was not an issue. However, in later development stages of these complex faulted reservoirs, these sand packages differentially depleted sections of the field. Consequently, it is not uncommon to find reservoirs that are at initial in-situ reservoir pressure in the same*

wellbore with reservoirs that have varying amounts of pressure depletion.

Cross-linked aqueous-based fracturing fluids have been the predominant fluid of choice in South Texas for the last 20-30 years. However, we are finding that gas assisted treatments are becoming increasingly necessary as some reservoirs encounter further pressure depletion. The decision of whether to use a gas assisted fracturing fluid is based on the amount of depletion observed from repeat formation testing and/or breakdown pressures after perforating. Our field experience in this area has shown that depletion must be below a normal water gradient before a gas assisted fluid will be advantageous compared to a normal cross-linked fluid.

Wells that have pressure gradients that are slightly below 0.44 psi/ft are treated using an energized frac fluid that has a 30-35% gas fraction. Wells that are significantly below 0.44 psi/ft are treated using a 70-75% gas fraction. Carbon dioxide has become the preferred gaseous phase over nitrogen in the past few years due to its higher density and water solubility. The fracture treatments presented in [this chapter] are treatments that have significantly improved well productivity in reservoirs that are depleted below a normal water gradient.

7.2 Description of Energized Fluid Used in South Texas

This section discusses the properties of the energized fluid used in fracturing treatments in South Texas. The properties of the fluid need to be specified so that the fracture model can correctly predict the behavior of the fluid. Three fluid properties need to be understood: First, the phase behavior of the fluid; second, the rheological properties; and third, the leak-off.

7.2.1 PHASE BEHAVIOR

The fracture model is designed to include any number of components and fluid phases. The flash calculation is limited to two fluid phases. In these treatments in South Texas, CO_2 is added to a zirconium cross-linked guar-based aqueous fluid. We consider

all additives completely soluble in the aqueous phase, and therefore, we will not need to include any of them as a fluid component. Proppant is also not considered a component or phase. The transport of proppant is calculated separately from the other component balances. Therefore, there are only two fluid phases, aqueous and gas, and two components, water and carbon dioxide.

Compressibility and solubility are also tracked in the model. Both are determined by the equation of state. The Peng-Robinson equation of state (PREOS) was chosen. With proper interaction coefficients, the PREOS had already been verified to match measured data for the CO_2-H_2O system (Section 4.1.1 of Chapter 4).

7.2.2 RHEOLOGY

Rheology of energized fluids has been discussed in a general sense in Chapter 4, specifically Section 4.1.2. This section covers the same ideas but covers only the narrow range of fluid types that were used on the South Texas well in question.

The rheology of the fluid is a function of the base fluid, internal phase quality, and temperature. The base viscosity is 450 and 350 centipoise for the pad and proppant stages respectively. This was determined by fluid tests before fracturing at a shear rate of 100 1/sec. The differences in the two viscosities are due to the different additives put into each stage. The base values of viscosity already include the effect of the crosslinker.

Figure 7.1 shows a diagram of how the effective viscosity (μ) changes with internal phase quality (Γ) compared to the base value (μ_o). Before the 52% limit, the value is near 1 and drops slightly with increasing internal phase quality. The base viscosity of the gas is lower than that of the liquid, causing the overall viscosity to drop when more gas is added. Above 52%, the viscosity increases. The exact values are determined from a correlation from Reidenbach et al.[2], shown in Equation 7.1.

$$\frac{\mu}{\mu_o} = e^{1.0\Gamma+0.75\Gamma^2} \tag{7.1}$$

The correlation value of 1.0 is chosen for the correct polymer loading that was used, 40 lbm/Mgal. Above 95%, the viscosity quickly drops down to near zero because the foam breaks down and almost all viscosity is lost.

In addition to the effect of internal phase quality, temperature also plays an important role on the fluid rheology. The effect of temperature on fracturing foams was studied by Khade and Shah[3]. The study includes a correlation that calculates the change in base rheology at 100 F:

$$\frac{\mu}{\mu_o} = 1 - C_2(T - 100)^{C_3} \tag{7.2}$$

Where C_2 are C_3 are correlation values. For this case, values of 0.0193 and 0.7 are chosen for C_2 and C_3 respectively.

7.2.3 LEAK-OFF

Leak-off coefficients that are used in this study are calculated from the conclusions presented by Harris[4]. It would be beneficial if more concrete correlations or trends could be established that verified the leak-off of this fluid system. This should be the focus of future research. For the purposes of this study, Harris' work gives the best approximation for leak-off for both fluid phases.

7.3 Results and Discussion

The theory and assumptions involved in the fracture model are discussed in Chapter 3. The model is used to evaluate the impact of different fracture design parameters when energized fluids are used. Before this can be done, it is important to history match the rate and net-pressure response of several treatments so that we are reasonably confident that the essential physics of the problem is being captured by the model. This is done in Section 7.3.1. Sections 7.3.2-4 focus on recommended improvements of the fracture design to be implemented in future treatments.

Productivity indexes are calculated from the model in Chapter 6. Final fracture dimensions are calculated by the fracture model and given as an input to the productivity

model. The productivity model also has the ability to calculate the damage in the invaded zone. With non-energized fluids, the only way to remove the damage from the invaded zone is to apply large drawdowns that recover the water and cause no relative permeability damage. For energized fluids, damage can be removed by an increase in gas saturation in the invaded zone due to the presence of a gas component in the fracturing fluid. The in-situ gas saturation is calculated by flashing the components that have leaked off into the invaded zone with an equation of state. The flash is done at reservoir temperature and pressure. It is important to note that the gas saturation at reservoir conditions is significantly higher than the gas saturation that is leaked during fracturing because more gas comes out of solution at lower reservoir pressure.

We quantify the ability for the fracture to produce by comparing the productivity index at a given set of conditions; this allows us to directly justify fracturing decisions made in the field without costly trial-and-error methods from well to well.

7.3.1 VERIFYING THE MODEL BY COMPARISON TO FIELD DATA (WELL A)

The properties of Well A are shown in Tables 7.1 and 7.2. Table 7.1 shows the properties that are needed as input to the fracture model. Table 7.2 shows properties that are needed to calculate the production from the well. In addition to these values, heat capacities are needed so that temperature in the fracture can be calculated. Heat capacities of all phases in this example are assumed to be 1 BTU/lb_mF, roughly the heat capacity of water. The injection (wellhead) temperature is 50 F; this is an estimation based on the temperature of the fluids that are stored, inlet composition, and temperature increase through the pumps.

The pumping schedule for this treatment is shown in Figure 7.2. For modeling purposes, the treatment was split into 10 different stages. A new stage was created whenever rate, fluid composition, or proppant concentration changed. The rates were very erratic in the first five minutes of pumping; we did not attempt to model this behavior. The first 5 minutes are modeled at a constant rate of 35 BPM.

Figure 7.3 shows a comparison between measured and calculated surface pressures. As can be seen in Figure 7.3, the calculated and measured pressures match up fairly well. Figure 7.4 shows the final calculated fracture geometry and proppant concentration for the base design. The propped fracture half length is about 200-250 feet but the fracture itself is opened to around 600 feet. The figure shows very little proppant setting and no place where the proppant could be trapped to cause a screen-out.

The gas rate from the well after fracturing was recorded in the field. The average production from this well was 2000 Mscfd over a two month span after fracturing. The predicted rate calculated by the production model using the data in Table 7.2 is 1400 Mscfd. The actual gas rate was higher than the predicted rate. The difference is a result of the different assumptions involved in the production model. The production model makes simplifying assumptions about the compressibility of the fluids, homogeneity of the reservoir, and geometry of the flow that can result in differences between calculated and measured rates. Given these simplifying assumptions, it is gratifying to see that the predicted and observed rates are comparable and adequately predict the productivity of the well.

Additional comparisons with other wells were made and some of these comparisons are presented in the following sections.

7.3.2 VARIATION ON THE BASE DESIGN, IMPROVING DESIGN IN THE FIELD (WELL A)

In the last section, we showed how the new fracture model for energized fluids successfully estimated the fracture growth for field treatments in South Texas. In this section, we will evaluate the specific designs used, starting with Well A as a base case. By looking at one variable at a time, we can establish trends to see if the design can be improved. In this way, future fracture treatments can be made more effective. In this section, we will look at the effect of drawdown pressure, inlet quality, inlet temperature, flowrate, and base viscosity. Suggested improvements in the design are based on improvements in the calculated well productivity index.

7.3.2.1 Drawdown Pressure

Drawdown pressure may be the most important parameter to establish when deciding whether to use energized fluids. If the drawdown pressure is high enough to recover the water used during fracturing, energizing the fluid is not necessary. As reservoirs deplete, the capillary forces in the formation keep the water trapped for extended periods of time and this causes a severe reduction in gas relative permeability and well productivity.

For the base design, a dimensionless drawdown pressure ($\Delta P/P_c^o$) of 1.11 is used. This means the drawdown pressure is about 10% higher than the capillary forces. With these conditions, a productivity index ratio of 4.3 is calculated for the actual fracture treatment. With the same drawdown pressure, a simulation was run that included the same volume of fluid and proppant but with no CO_2. When we eliminated the CO_2, the fracture dimensions changed slightly because of the property differences between CO_2 and H_2O. The biggest difference is that the leak-off contains no gas (free or in solution). In the non-energized case, we calculated a productivity index of 1.6, about three times lower than the energized case. This difference comes from damage that the non-energized fluid creates in the invaded zone.

Figure 7.5 shows the dependence of productivity on drawdown pressure for both energized and non-energized cases. When energized designs are used, there is no real dependence on drawdown because there is always gas present to remove the damage. With non-energized cases, the production is lowest when $\Delta P/P_c^o$ is less than 1; very little of the leak-off water is recovered and the invaded zone is fully damaged and will not allow gas to travel into the fracture. The productivity approaches the energized fracture limit when drawdown pressures are large ($\Delta P/P_c^o >> 1$). In such cases, it may not be worth the logistics and complication of energizing the fluid for such a marginal benefit.

7.3.2.2 Inlet Internal Phase Quality

Changing the inlet internal phase quality has two consequences. First, it changes the rheology of the fluid, especially if the quality is high enough for bubble-bubble interactions; this is described in the rheology section in Chapter 4. The second

consequence occurs because the more gas that is added to the inlet, the higher the ratio of gas to water in the leak-off zone, causing a smaller volume of water to leak-off and allowing a higher gas saturation around the fracture.

The base design's inlet quality varies from stage to stage. The starting value is around 36% and then drops as time passes. This is offset by the addition of proppant in later stages. Internal phase quality is kept constant by reducing the gas fraction while simultaneously increasing the proppant concentration, diminishing the amount of gas for stimulation. As a result of the gas content not being constant, inlet quality was varied in each case by adding or subtracting a set fraction to all stages in units of 10%.

Figure 7.6 shows the bottom-hole pressures during fracturing for all cases. There are two distinct groupings in the figure. The foamed cases (high quality) result in higher bottom-hole pressures, which lead to shorter and wider fractures. Figure 7.7 shows the proppant placement for each case. Once again, there are two different groupings; foamed and un-foamed. Only very slight differences are seen within each group, and none of the differences seem to affect the near wellbore region. The dimensionless fracture conductivity is shown in Figure 7.7 as well. Dimensionless fracture conductivity is defined as:

$$F_{CD} = \frac{k_f w_{ave}}{kL} \tag{7.3}$$

where k_f is the fracture permeability, k is the formation permeability, w_{ave} is the average propped fracture width, and L is the propped length. Figure 7.7 shows that the high quality cases have higher fracture conductivity because there is more proppant in the near wellbore region (higher w_{ave}/L).

Figure 7.8 shows the calculated productivity for each case as the inlet internal phase quality changes. The figure shows an optimum internal phase quality of around 30% for this specific set of conditions. An internal phase quality lower than 30% results in water damage because not enough gas has been used to stimulate the damaged zone. For high qualities, the propped fracture length is not optimum because it creates shorter and wider fractures compared to lower quality fluids. It is recommended that in this field

30% quality be used in future fracturing treatments. This number may increase for cases where fracture conductivity near the wellbore can be justified over fracture length. It is not recommended to drop the quality below 30% because an energized effect might not be observed. If a quality less than 30% is being considered, it might be more practical to use a non-energized fluid.

7.3.2.3 Inlet Temperature

Inlet temperature has a larger effect on energized fluids than non-energized fluids. Water is less sensitive to differences in temperature and pressure. In addition, the water is usually stored at ambient temperature. The temperature increases through the pump and down the wellbore, making the temperature difference between the fluid entering the fracture and reservoir small (a few degrees). The same assumption is not true for CO_2 because it is stored as a cold liquid. This brings up the question: does it matter what temperature the fluid is at when it enters the fracture? If so, would it be worth the effort to change the fluid inlet temperature?

Figure 7.9 shows the propped dimensions for several different inlet temperatures. As a reminder, lets remember that all of these cases are of the base design; the only parameter changing is the inlet temperature. Each scenario has the same volumetric flowrates, and because the phase density changes, the mass in each case is not constant. Fracture length grows with decreasing inlet temperature, a trend that is seen in Figure 7.9. This is explained by the expansion of the gas phase. If the fluid enters the fracture at a low temperature i.e. a dense state, it will eventually expand to conditions associated with the warm reservoir temperature. The cooler the fluid that enters, the more the expansion that occurs, and the bigger the fracture volume expected. The effects of fracture expansion are not seen until the furthest end of the fracture, where the fluid is fully expanded. Very little proppant gets to the end of the fracture and, therefore, it has very little effect on the overall proppant placement.

Figure 7.10 shows the calculated productivity indexes for each inlet temperature case. The values do not vary significantly in this temperature range. The lack of variation is because proppant placement near the wellbore (Figure 7.9) and the properties

of the invaded zone are almost unchanged from case to case. Because the expected change in production is insignificant, it is recommended that no steps be taken to change the inlet temperature of these fluids. However, the fluid / fracture volumes need to be corrected for fluid expansion.

7.3.2.4 Flowrate

The flowrate of the fluid changes the surface pressure during the treatment and, therefore, the horsepower required. The flowrate might be lowered so that less horsepower can be used, but also might be raised to get optimum bottom-hole pressure for fracture width and proppant carrying velocity. The base design starts at 35 BPM (Figure 7.2). Several different starting flowrates were modeled from 15 to 55 BPM. For each starting flowrate, all pumping stages were kept at constant volume. The large flowrate caused larger bottom-hole pressure, causing larger widths, leading to shorter fractures for a constant volume. Figure 7.11 shows the calculated productivity index calculated by varying flowrates. There is only a slight dependence of productivity on flowrate, favoring some of the lower flowrates. Lower flowrates increase fracture length, which has a greater benefit in tight formations. The flow rate should be chosen on the basis of the expected fracture length and the ability of the fluids to place the proppant. This is true whether the fluids are energized or not.

7.3.2.5 Base Viscosity

The viscosity of the fluid is usually chosen by the engineer to achieve optimum properties of fracture width, height growth, and proppant settling. Energized fluids bring an extra complication to this issue because of the compositional effects associated with them. In this study, we look at this issue in a simple way; we varied the base viscosity by a certain factor and observed the response. Figure 7.12 shows the calculated productivity index for each base viscosity chosen. The figure shows that the original viscosity of fluid is optimum. Much like the reasons explained in the flowrate section, the base viscosity will affect the fracture length. The viscosity is not lowered enough in any case to significantly increase the proppant settling. However, cases were not run in the model

below one-half the base viscosity because of proppant transport issues. Lowering the viscosity is not recommended because of the increased risk of screen out.

7.3.3 IMPROVING FRACTURE DESIGN IN THE FIELD (WELL B), THE EFFECT OF RESERVOIR PRESSURE

This section covers another fracture treatment, referred to as Well B, which was previously done in South Texas. The properties of Well B are shown in Table 7.1. We will discuss additional issues that arise from Well B's treatment that were not covered in our discussion of Well A's treatment. The flowrates and proppant pumped for Well B's treatment are shown in Figure 7.13. Both Well A's and Well B's treatments are comparable in overall volume, and in the amount of CO_2 pumped. Well B has a lower flowrate (25 BPM) and larger fracture height (200 ft). The biggest difference between the two cases is the reservoir pressure. Well A's reservoir pressure is 2900 psi while well B's is 800 psi.

The calculated final proppant concentration for Well B's treatment is shown in Figure 7.14. The final length is smaller than Well A's final length because Well B has a larger height and it has larger leak-off due to low reservoir pressure. The calculated J/J_o is 4.5. As was the case with Well A, the productivity index showed no dependence on drawdown pressure, revealing that enough gas was used to stimulate the invaded zone effectively. In the next step, we decreased the inlet composition of CO_2 to find an optimum inlet quality. The productivity indexes calculated for each quality are shown in Figure 7.15. The figure shows that the productivity should reach a plateau with an inlet quality as low as 10-15%. This is lower than the optimum inlet quality for Well A's treatment of 30%. The difference between the optimum qualities calculated for these two wells occurs because the gas phase is allowed to expand more when the reservoir pressure is lower. To illustrate this point, all we have to do is look at the phase density of the CO_2-rich phase at each reservoir condition. The density is about 31 lb_m/ft^3 at 2900 psi and reservoir temperature, roughly half the density of water. At 800 psi it is only 5

lb_m/ft^3, roughly 12 times lower than water. This means that less gas is needed to get the same gas saturation in the invaded zone.

It is recommended that future treatments that are similar to Well B be stimulated with less CO_2. The actual treatment that was pumped with an inlet quality of 40% should be lowered to around 20%. This reduces the cost by lowering the amount of CO_2 while still maintaining proper stimulation of the invade zone. Once again, it should be pointed out that the results shown in Figure 7.15 are for low drawdown pressures. The drawdown pressure is ~10% higher than the capillary pressure, the same ratio used in comparing cases for Well A. In this case, drawdown pressures are limited to begin with because the reservoir pressure is low, so energizing the fluid might be the only option.

7.3.4 IMPROVING FRACTURE DESIGN IN THE FIELD (WELL C), ENERGIZING SPECIFIC PUMPING STAGES

As a third example, we modeled another treatment that was done in South Texas (Well C). The treatment applied to Well C is very similar to the treatments in Wells A and B. Properties of Well C are shown in Table 7.1. The reservoir pressure is closer to Well A than Well B at 2400 psi. The full pumping schedule is shown in Figure 7.16. The biggest difference is that Well C's treatment only included CO_2 in the proppant stages. Thus, the overall amount of CO_2 is reduced. In this section, we will review whether putting the gas in specific stages during pumping could be an effective practice.

The calculated final proppant concentration for Well C's treatment is shown in Figure 7.17. The calculated J/J_o is 3.5. When drawdown pressure was varied, productivity only had a slight dependence. This means that the invaded zone had a high enough gas saturation so that damage is reduced but not eliminated. We then tested what would happen if the gas was pumped at different times during fracturing. To test this idea we ran three additional cases; the results are shown in Figure 7.18. The first case included gas in all stages. The J/J_o calculated was 4.2. Adding gas increased production by fully stimulating the invaded zone. The obvious drawback to this is that it used about

twice as much CO_2, which would increase the cost of the treatment. The difference in production might not be worth that increased cost. As a second test, we ran the model with gas during the pad stages, but not the proppant stages. This keeps the total amount of CO_2 pumped almost the same as the original case. The calculated J/J_o for this case is 3.2. This value is lower than the previous two cases, but still does not reduce the production by a significant amount. We postulate that in cases where the gas is added to the pad, the gas leak-off will be uniform down the length of the fracture, but may result in zones that do not have enough gas for stimulation. In contrast, adding the gas to the proppant stages will ensure more gas leak-off where the proppant is placed and enough gas will leak-off for effective stimulation. As a final test, a non-energized case was looked at. The calculated J/J_o was 1.4 under the same drawdown conditions as Well A and B. This clearly shows that adding the gas to any stage may be better than not energizing the fluids at all.

7.4 Conclusions

1. A new model for energized fracturing was successfully used to simulate several fracture treatments in a gas field in South Texas.
2. Based on production estimates, energized fluids may be required when drawdown pressures are smaller than the capillary forces in the formation. If drawdown pressures are high, the added benefit of energizing the fracturing fluid is minimal.
3. It is shown that there is an optimum quality that should be used in the treatment. Too high a quality results in more viscous foams. The increased viscosity causes wider, shorter fractures. Such fractures are not beneficial in tight formations where creating fracture length is essential. Using too low a quality results in insufficient gas saturation in the invaded zone and inadequate cleanup.
4. The optimum quality depends on the specific conditions of the reservoir i.e. the reservoir pressure, temperature, permeability, and the conditions of flowback. For example, for the field cases studied, the minimum quality recommended is 30% for moderate differences between fracture and reservoir pressures (2900 psi reservoir,

5300 psi fracture). The minimum quality is reduced to 20% when the difference between pressures is large, resulting in additional gas expansion in the invaded zone.

5. The larger the difference between inlet and formation temperature, the larger the expansion of the gas phase during fracturing. The expansion has a significant effect on fracture dimensions. However, simulations show that the expansion takes place gradually down the length of the fracture and may not affect the placement of proppant, and therefore, has a small effect on the overall production from the fracture. It is recommended to not use any resources to change the inlet temperature of the fluid, but it may be necessary to make fluid volume corrections based on the expansion of the gas phase.
6. For the field cases studied, varying the flowrate and base viscosity did not have a significant effect on fracture production because proppant was successfully placed in all cases.
7. If energizing the fluid is necessary, every stage of the fracturing treatment should be energized with a gas component to ensure high gas saturation in the invaded zone. If this is not possible, effective stimulation may be achieved in some cases by energizing only the pad or proppant stages without a major loss of production.

Nomenclature

b_{cap} Brooks-Corey model for capillary pressure exponent
C_2 Rheology correlation parameter, Temperature
C_3 Rheology correlation parameter, Temperature
E Young's modulus
F_{cd} Dimensionless fracture conductivity
h Height of fracture
J Productivity index
J_o Productivity index of a un-fractured, undamaged reservoir in a circular drainage area
k Reservoir permeability
k_f Fracture permeability
k_{rgo} Endpoint relative permeability of gas
L Fracture propped length
$n_{rel.perm}$ Gas relative permeability exponent
P_c^o Endpoint capillary pressure, Brook-Corey
P_R Reservoir pressure
r_e Drainage radius
r_w Wellbore radius
S_{wr} Residual liquid phase saturation
S_{gr} Residual gas phase saturation
T Temperature
T_R Reservoir temperature
w_{ave} Average fracture width
z Depth
Greek Symbols
ΔP Drawdown pressure
ϕ Porosity
Γ Quality
μ Viscosity
μ_o Base viscosity
ν Poisson Ratio
ρ_R reservoir density
σ minimum horizontal stress

References

1. Friehauf, K.E., Sharma, M.M, and Sullivan, R. 2009. Application of a New Compositional Model for Hydraulic Fracturing With Energized Fluids: A South Texas Case Study. Paper SPE 119265 presented at the SPE Hydraulic Fracturing Technology Conference, The Woodlands, Texas, 19-21 January.
2. Reidenbach, V.G., Harris, P.C., Lee, Y.N., and Lord, D.L. 1986. Rheological Study of Foam Fracturing Fluids Using Nitrogen and Carbon Dioxide. *SPE Production Engineering*, January: 31-41. SPE 12026.
3. Khade, S.D., and Shah, S.N. 2004. New Rheological Correlations for Guar Foam Fluids. *SPE Production and Facilities*, May: 77-85. SPE 88032.
4. Harris, P.C. 1987. Dynamic Fluid-Loss Characteristics of CO2-Foam Fracturing Fluids. *SPE Production Engineering*, May: 89-94. SPE 13180.

Table 7.1. Fracturing properties, used as input to fracture model for South Texas field study.

Well A	Well B	Well C
h = 145 ft	h = 200 ft	h = 230 ft
E = 2.62E6 psi	E = 2.62E6 psi	E = 2.62E6 psi
$\nu = 0.25$	$\nu = 0.25$	$\nu = 0.25$
σ = 5300 psi	σ = 4967 psi	σ = 5172 psi
z = 7554 ft	z = 8564 ft	z = 7388 ft
k = 0.09 md	k = 0.09 md	k = 0.09 md
$\phi = 0.15$	$\phi = 0.15$	$\phi = 0.10$
ρ_R = 161.2 lb_m/ft^3	ρ_R = 161.2 lb_m/ft^3	ρ_R = 161.2 lb_m/ft^3
T_R = 220 F	T_R = 230 F	T_R = 219 F
P_R = 2900 psi	P_R = 800 psi	P_R = 2400 psi

Table 7.2. Properties to calculate production for South Texas field study.

Inputs
k_f = 10 Darcy
$\Delta P/P_c^o$ = 1.11
r_e = 1000 ft
S_{wr} = 0.2
S_{gr} = 0.2
$n_{rel.perm}$ = 3
k_{rgo} = 0.9
b_{cap} = 0.5

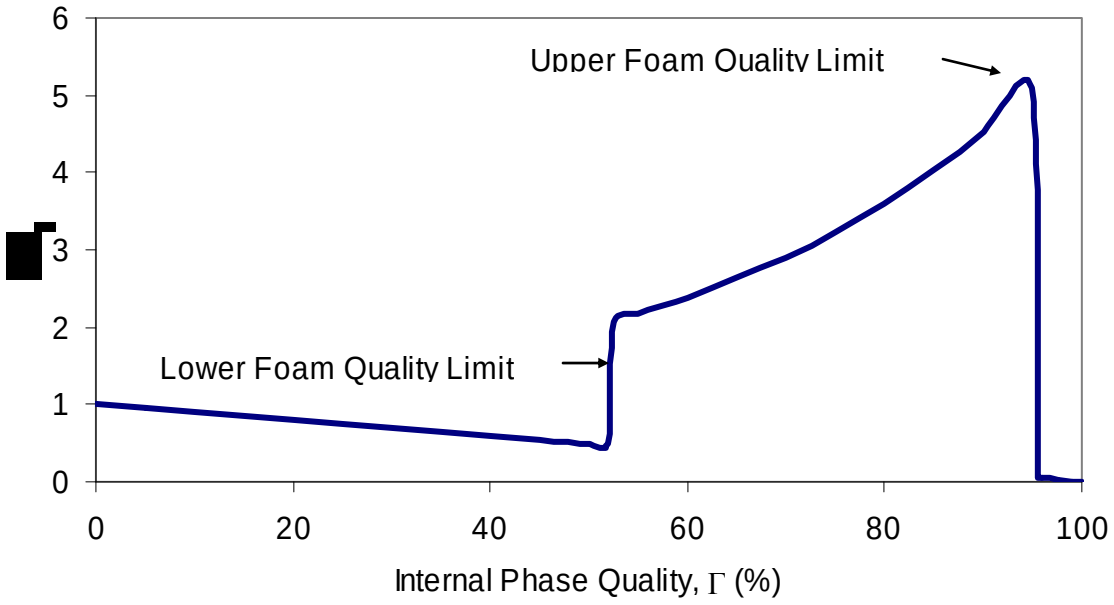

Figure 7.1. Viscosity as a function of internal phase quality for the fluid system used in South Texas fracture treatments.

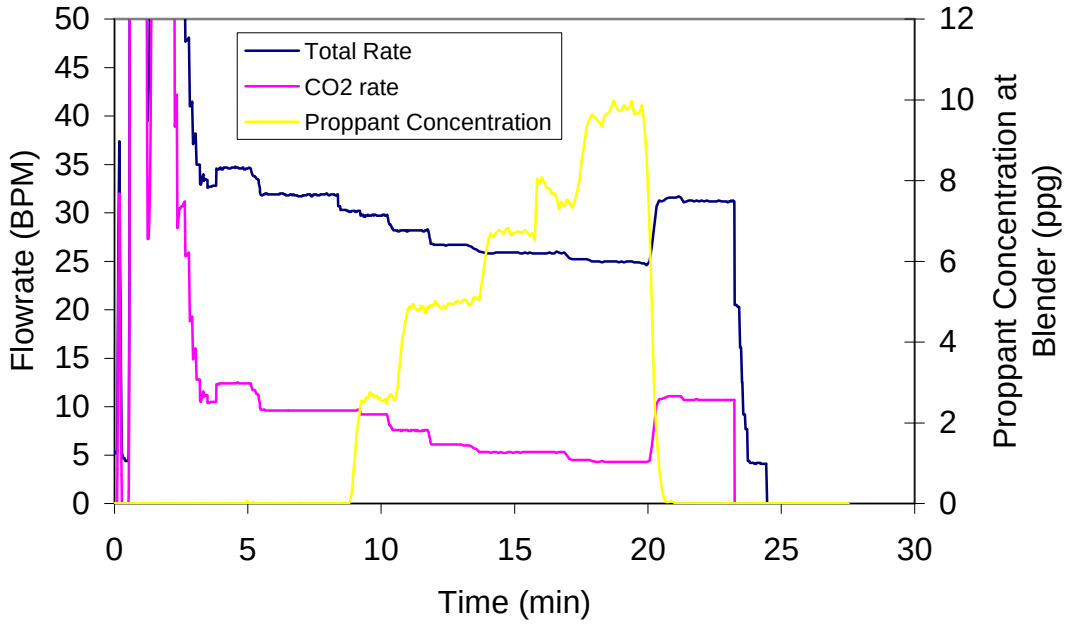

Figure 7.2. Pumping schedule of real fracturing treatment for the base design of Well A using energized fluids fracturing in South Texas.

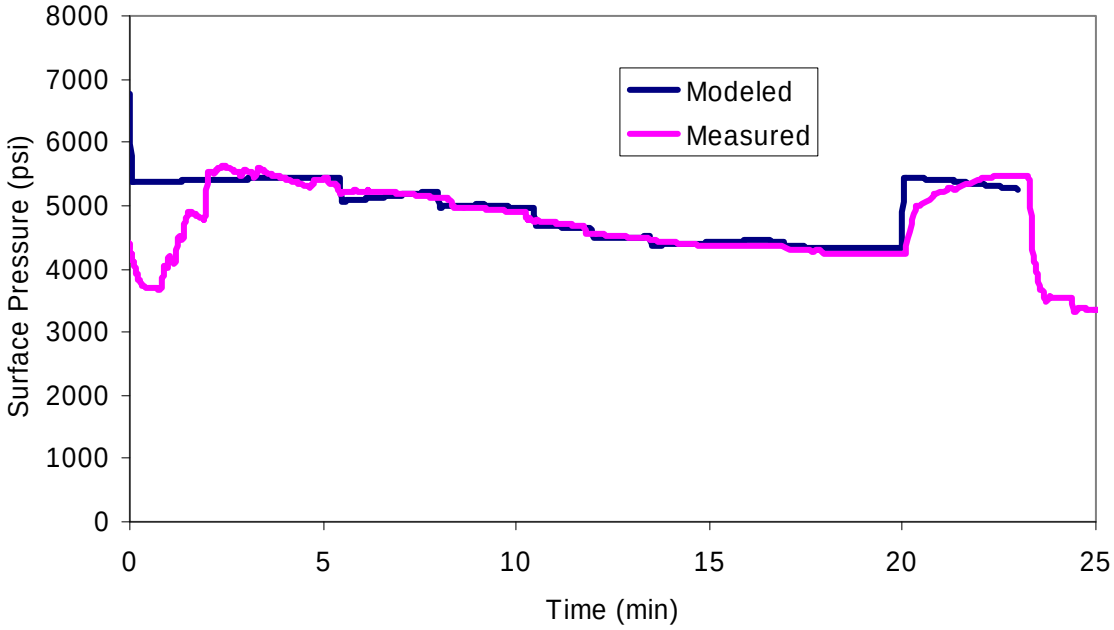

Figure 7.3. Comparison between measured and modeled surface pressure for the base design of Well A using energized fluids fracturing in South Texas.

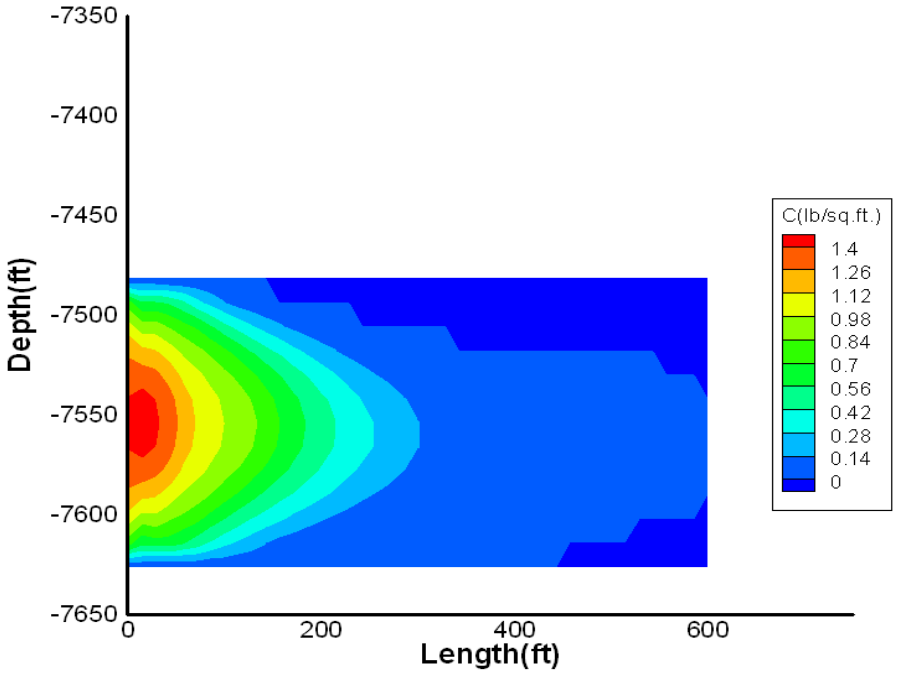

Figure 7.4. Modeled final proppant concentration for the base design of Well A using energized fluids fracturing in South Texas.

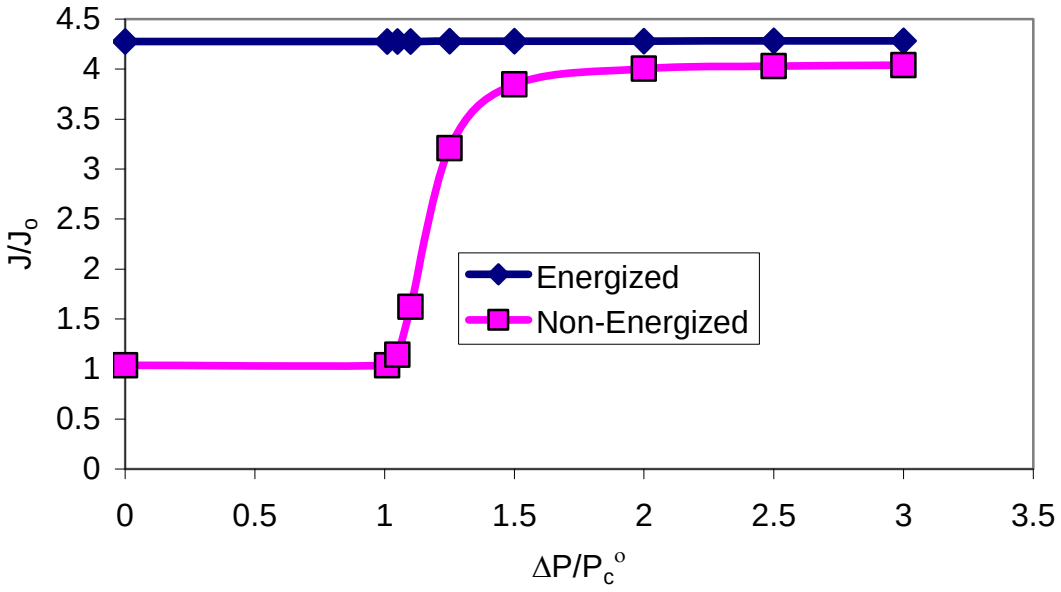

Figure 7.5. Calculated production when drawdown pressure is varied from the base design of Well A. Comparison of energized and non-energized treatments also shown.

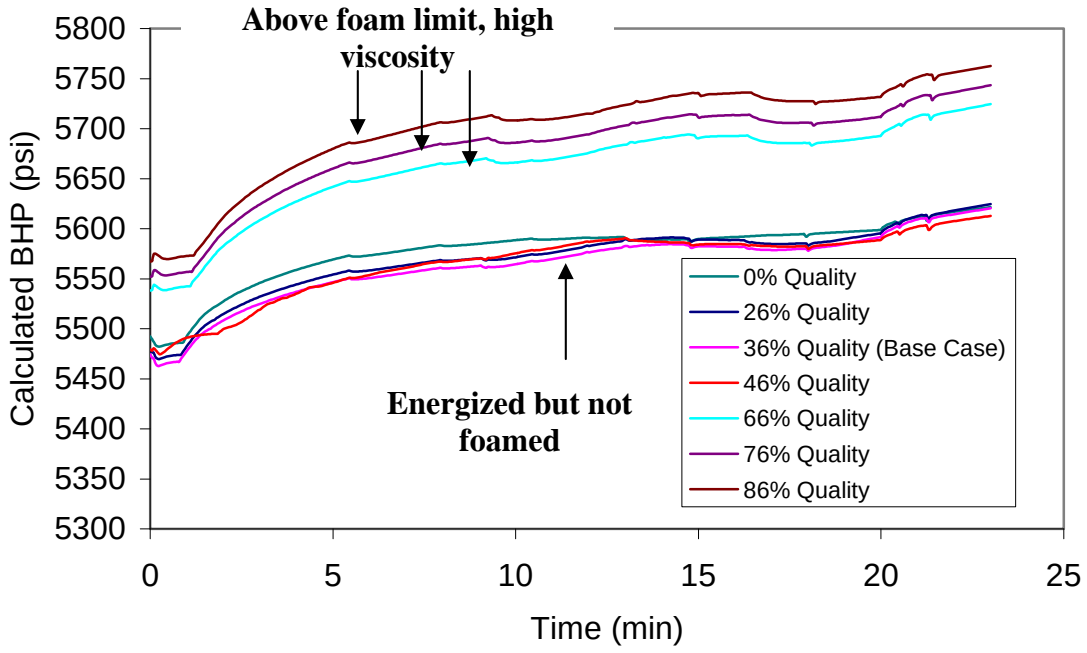

Figure 7.6. Comparison between predicted bottom-hole pressures when inlet gas quality is varied from base design of Well A.

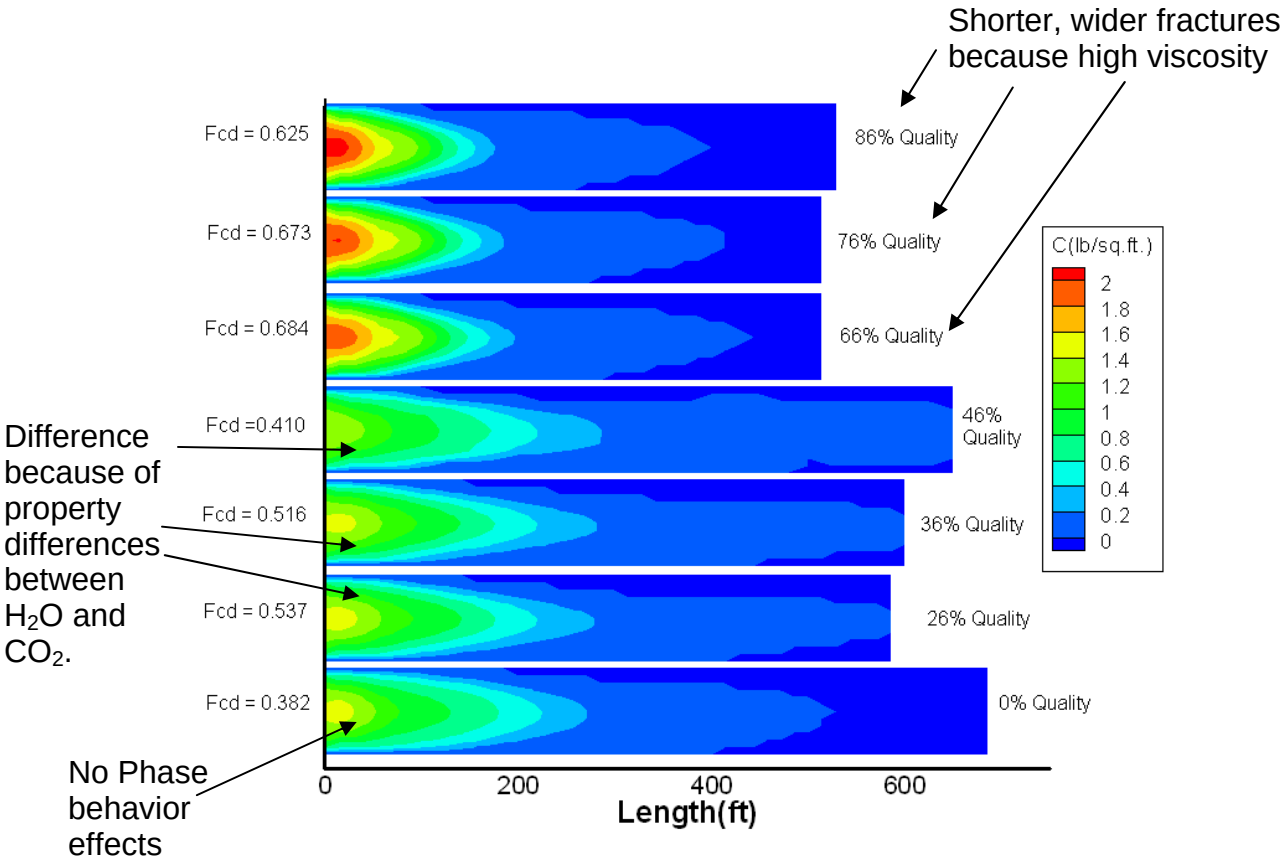

Figure 7.7. Comparison between predicted final proppant concentrations when inlet gas quality is varied from base design of Well A.

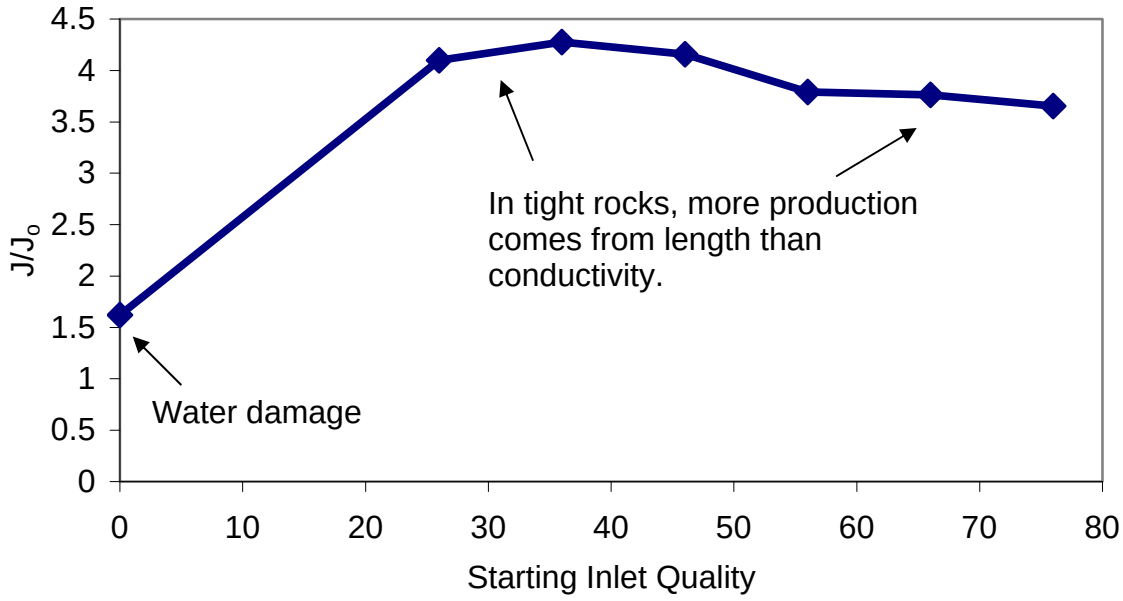

Figure 7.8. Comparison between predicted gas production when inlet gas quality is varied from base design of Well A.

Normally when non-energized fluid are used:
Higher temperature → lower viscosity → longer, thinner fractures.

When energized fluid are used:
Higher Temperature → Fluid is already at warm temperature → Fluid does not expand → smaller fractures.

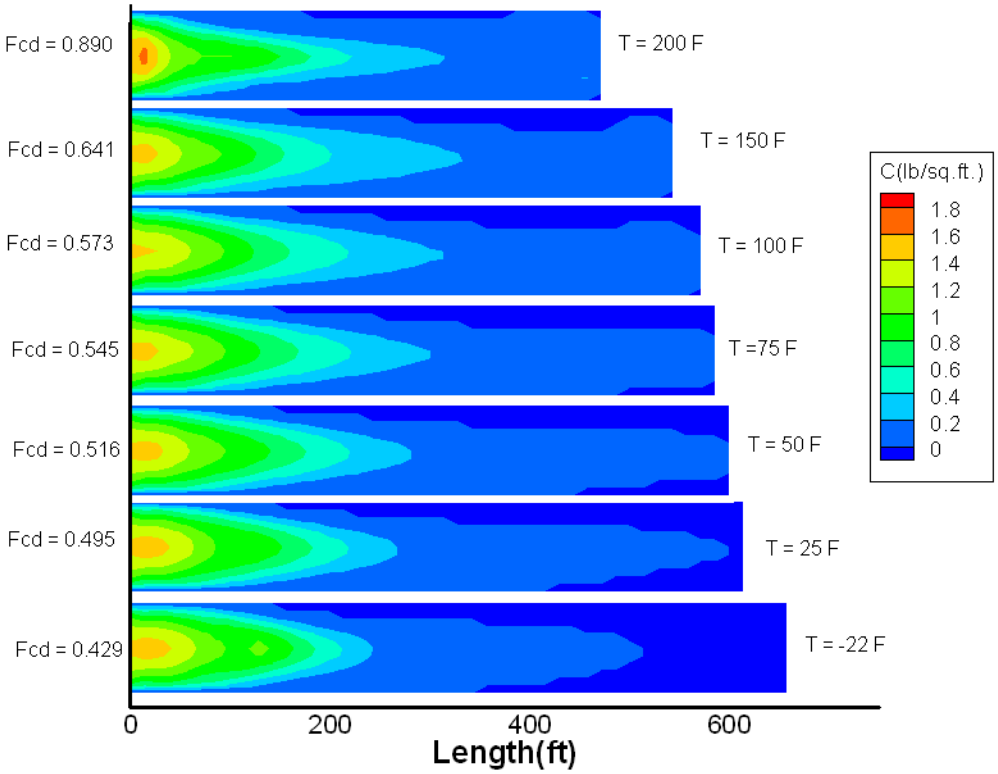

Figure 7.9. Comparison between predicted final proppant concentrations when inlet temperature is varied from base design of Well A.

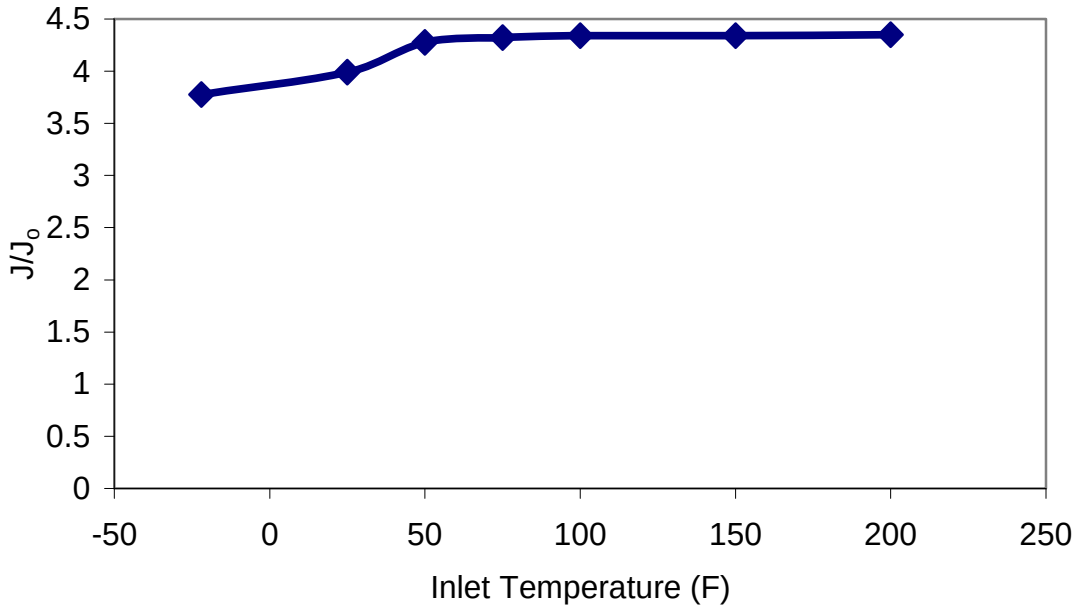

Figure 7.10. Comparison between predicted production when inlet temperature is varied from base design of Well A.

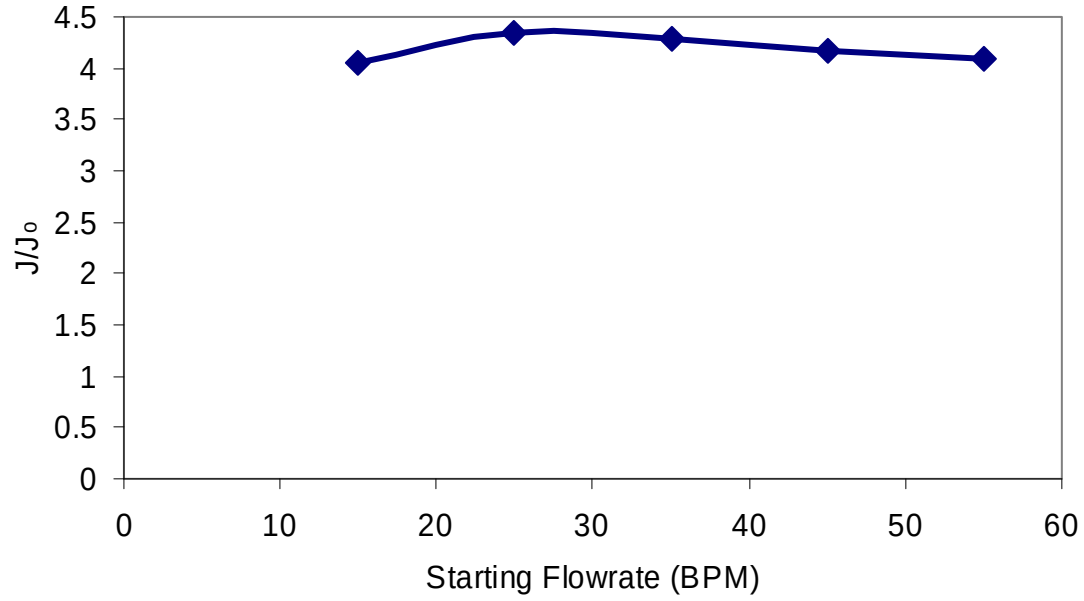

Figure 7.11. Comparison between predicted production when the starting flowrate is varied from base design of Well A.

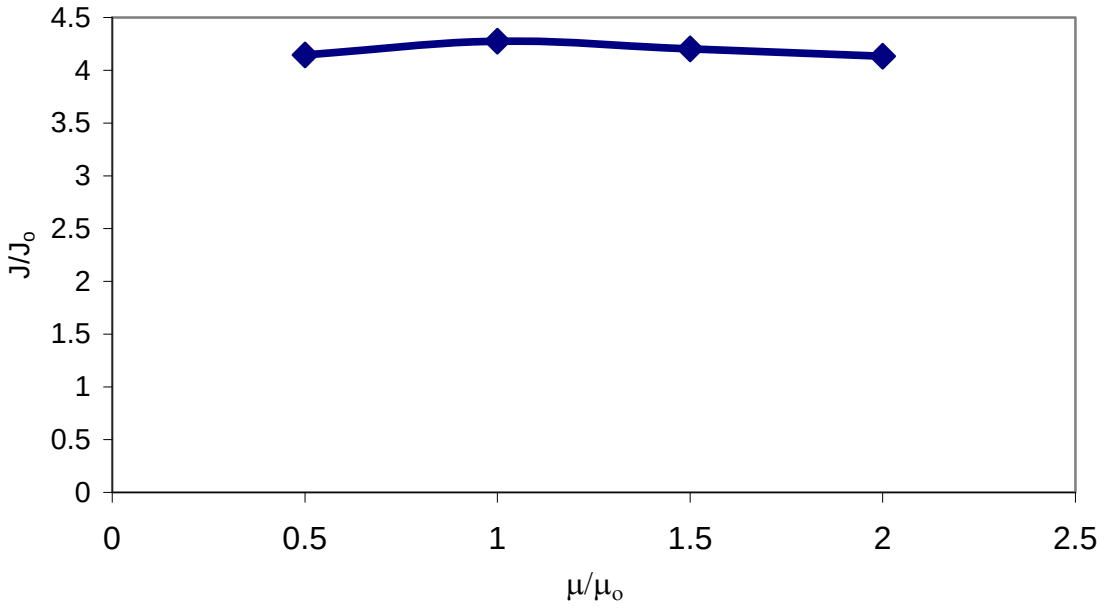

Figure 7.12. Comparison between predicted production when base viscosity is varied from base design of Well A.

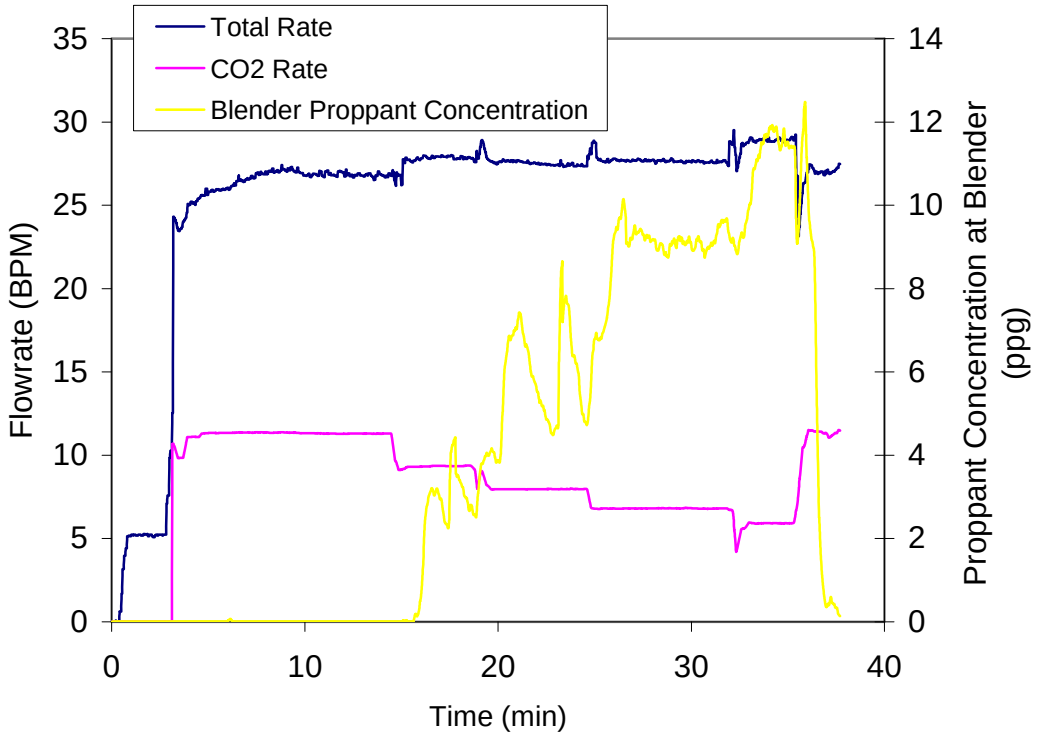

Figure 7.13. Pumping schedule of real fracturing treatment for the base design of Well B using energized fluids fracturing in South Texas.

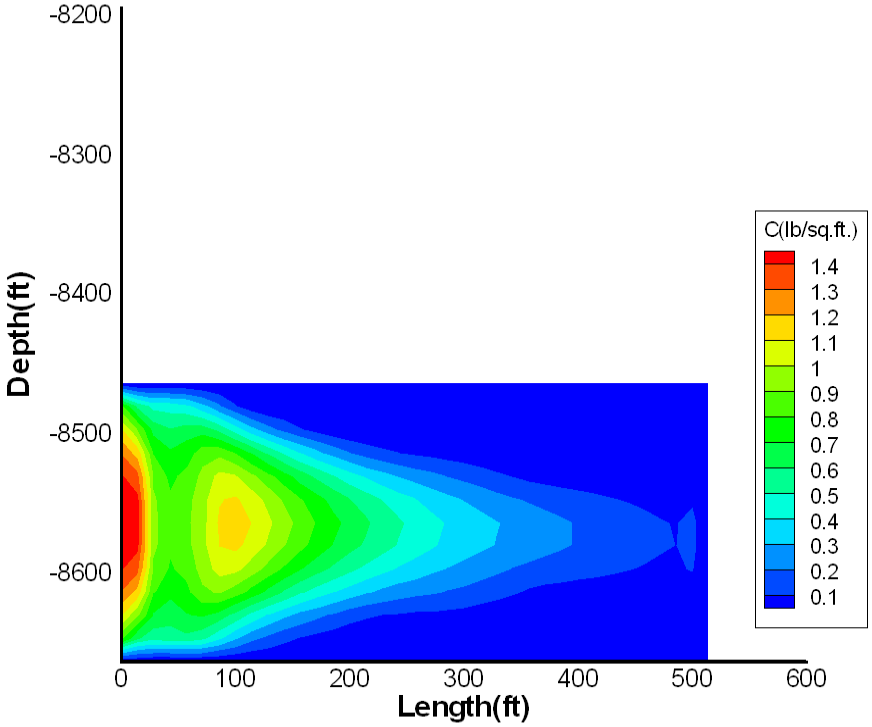

Figure 7.14. Modeled final proppant concentration for the base design of Well B using energized fluids fracturing in South Texas.

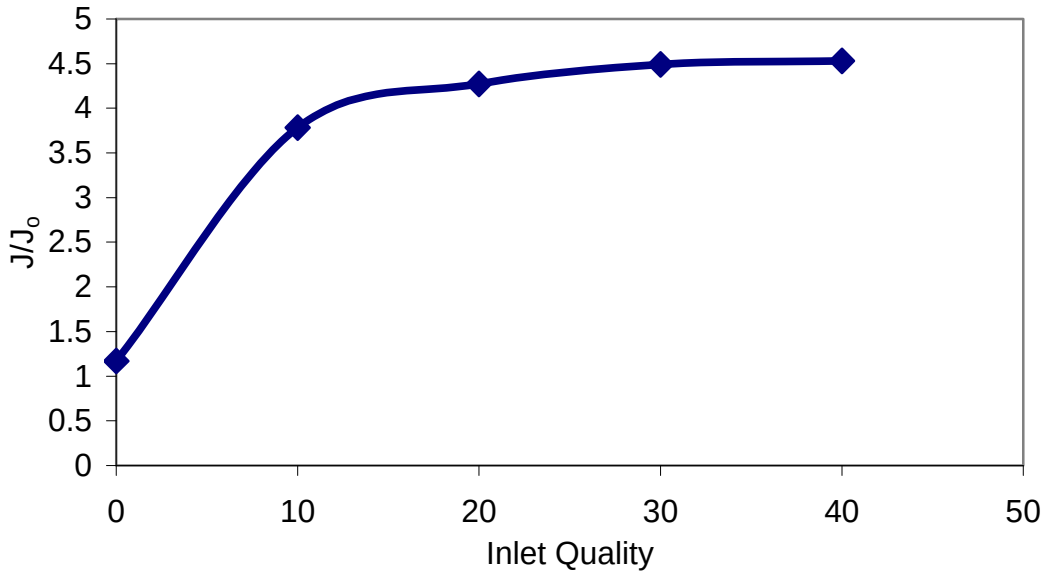

Figure 7.15. Comparison between predicted gas production when inlet gas quality is varied from base design of Well B.

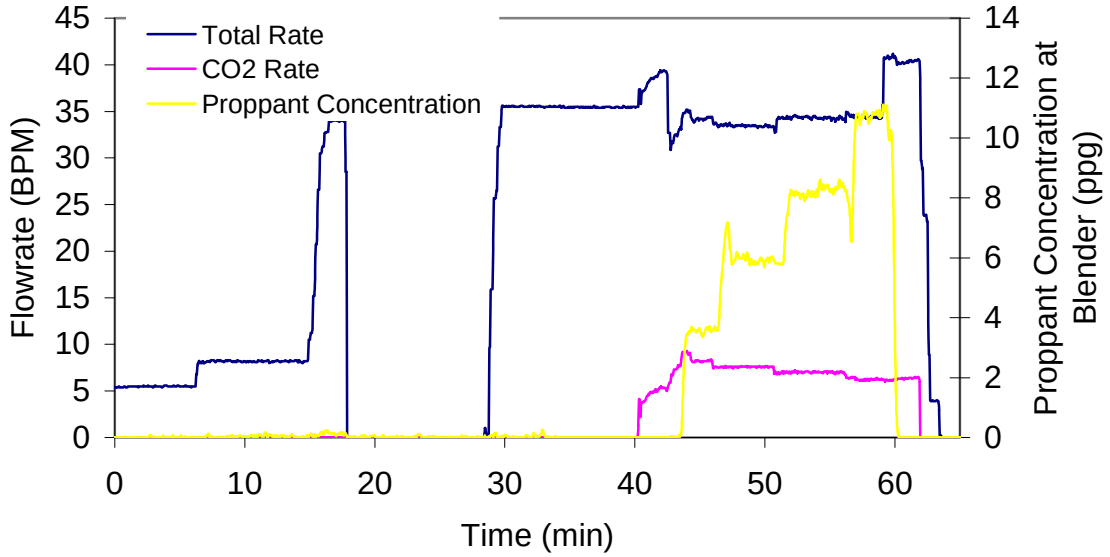

Figure 7.16. Pumping schedule of real fracturing treatment for the base design of Well C using energized fluids fracturing in South Texas.

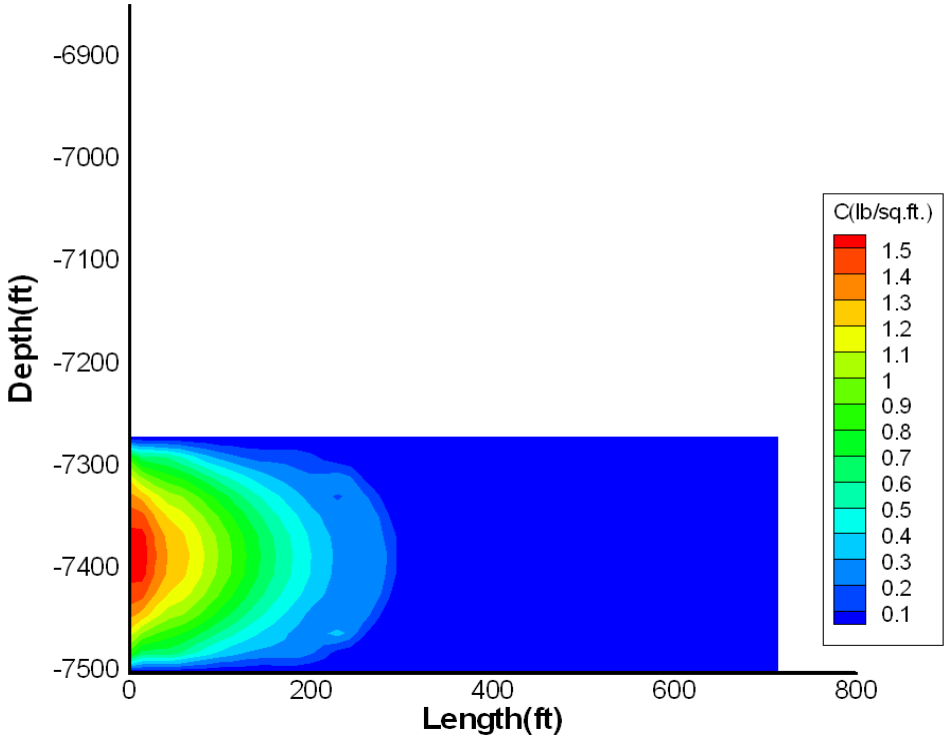

Figure 7.17. Modeled final proppant concentration for the base design of Well C using energized fluids fracturing in South Texas.

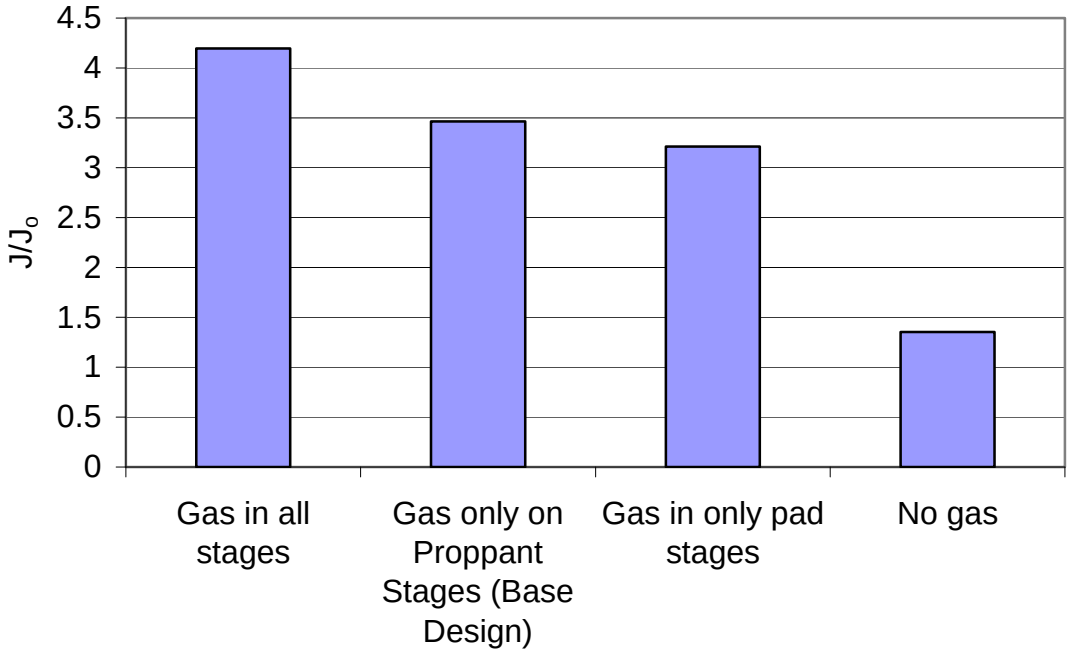

Figure 7.18. Comparison between predicted gas production when gas is added to different stages, Well C.

CHAPTER 8: MECHANISMS FOR THE DYNAMIC LEAK-OFF OF MULTI -PHASE FRACTURING FLUIDS

Leak-off is one of the most important parameters controlling fracture geometry and performance. When multi-phase fluids are used, the leak-off not only determines the ratio of fracture volume to the fluid pumped, but is also the main reason why fluid compositional changes occur in the fracture. The leak-off behavior tells us what components are lost to the formation. If water is lost, the well productivity can be severely impaired due to liquid trapped in the rock. If leak-off of a gas component is optimized, the gas relative permeability remains high, resulting in high well productivities. Too much gas leak-off can lead to tip screenouts and additional expense incurred on the gas used.

The importance of leak-off is obvious, but our clear understanding of what occurs during multi-phase leak-off is incomplete. There have been many models and laboratory experiments performed (Outmans[1], Gulbis[2], Roodhart [3], Mayerhofer et al.[4], just to name a few) for traditional single-phase fluids, but work on foam, multi-phase, or energized fracturing fluid leak-off is limited to only a few sources (King[5], Harris[6,7]).

In this chapter, we discuss possible mechanisms of multi-phase leak-off and compare models we have developed for these mechanisms with experimental data collected to date. The theory and assumptions for each mechanism are discussed. Calculations for each mechanism show the probability of each mechanism occurring during dynamic leak-off experiments and field treatments when using multi-phase fluids.

We postulate four possible mechanisms that can explain multi-phase leak-off behavior in the presence of a discontinuous phase.

1. Bubbles can be held on the surface of the porous media, plugging pore entrances.
2. Bubbles can be held both in and on the filter cake and impede the flow of the continuous phase.

3. Bubbles can penetrate into the porous medium from the bulk foam.
4. Soluble gas at high pressure can be released as pressure drops and the free gas can impede the flow of the continuous phase.

Before the details of each mechanism are presented, a review of leak-off models used in the past is provided.

8.1 Background

8.1.1 REVIEW OF FILTRATION MODELS

All fracture propagation models require estimation of the leak-off coefficient, C. In the field, leak-off is estimated by doing a mini-frac test where a small volume of fluid is injected and the pressure response gives an estimation of the leak-off[8]. In the absence of such data, reservoir properties are used to provide an estimation of the leak-off. Section 2.3 of Chapter 2 has already covered the definition, estimation, and combination of the three different types of leak-off coefficients. It is suggested that the reader review Section 2.3 of Chapter 2 before proceeding to read this chapter. This section discusses additional topics that move beyond the material presented in Section 2.3.

Outmans[1] modeled static filtration by solving the diffusion equation (for pressure). The study assumes static filtration, Darcy's law through an incompressible filter cake, and no particle invasion. The resulting cumulative filtrate volume per unit area is:

$$Q^* = \sqrt{\frac{2\Delta P k_{cake}(1-c_o-\phi_{cake})t}{\mu c_o}} \tag{8.1}$$

where k_{cake} is the permeability of the filter cake, c_o is the concentration (vol/vol) of solids in the suspension, and ϕ_{cake} is the porosity of the filter cake. Equation 8.1 is used as an explicit expression for the wall-building coefficient, C_w, but is usually not used because most of the assumptions are invalid.

Outmans recognized that filter cake compressibility was the most questionable assumption. He presented a second solution where the compressibility (a) of the filter cake is expressed as

$$a = a_1 \Delta P^{-\nu} . \tag{8.2}$$

In order to make analytical solutions possible, additional assumptions were made to linearize the diffusion equation. The solution for this linearized equation is:

$$Q^* = \sqrt{\frac{2\Delta P^{-\nu+1} k_1 (1 - c_o - \phi_{cake1}) t}{\mu(-\nu+1)c_o}} \tag{8.3}$$

Where, the subscript 1 refers to the value at 1 psi filtration pressure. A log-log plot of cumulative filtrate versus filtration pressure calculates ν, the compressibility exponent in Equation 8.2.

Zydney[9] did filtration experiments through a packed bed of red blood cells. The experiments were done under static conditions. The focus of the study was to determine the effect of applied pressure on filter cake properties, i.e. permeability and porosity. Equation 8.4 shows the correlation for permeability of the packed bed. The terms n and b are correlation factors determined to be 0.49 +/- 0.02 and 1.1 +/- 0.5E-16 kg*m/s^2 respectively. The terms k_o and ϕ_o refer to values at zero filtration pressure.

$$k_{cake} = k_o \frac{1 - \phi_{cake,o}}{1 - \phi_{cake}} [1 + \frac{k_o (1 - \phi_{cake,o})}{bn} \Delta P]^{(n-1)} \tag{8.4}$$

The porosity is related to the compressibility (a) of the packed bed, shown in Equation 8.5.

$$a\Delta P = \frac{\phi_{cake,o}}{\phi_{cake}} + \frac{\phi_{cake}}{\phi_{cake,o}} - 2 \tag{8.5}$$

The original reference by Zydney uses the term ε as porosity and uses ϕ as the fraction of pores that are plugged by the red blood cells. The symbol for porosity in Equations 8.4 and 8.5 is consistent with the rest of this document.

Sherwood[10] modeled the filtration behavior of emulsions as droplets that form a filter-cake. The continuous fluid and the emulsion droplets are incompressible but the theory should also apply to compressible fluids. Sherwood states that the emulsion droplets will form a cubic array, shown in Figure 8.1. The stress acting on the droplets will cause deformations that will close pore space and increase hydraulic resistance. This model predicts that filtration pressure has little effect on the rate of filtration. Sherwood and others have shown that the increased driving force is balanced out by the decrease in permeability of the filter-cake. This property makes emulsions and foams excellent choices for completion and drilling fluids.

Both Sherwood and Zydney postulated compressible filter-cakes but neither study examined the ability of the particles to travel through the rock. With energized fluids, it is possible that both the continuous liquid phase and the discontinuous gas phase will leak-off. The liquid phase may contain solid particles or polymer that can create filter-cakes. Also, the gas phase can remain trapped causing further resistance as the filter-cake gets thicker and the continuous fluid has to move around it.

Sherwood's and Zydney's studies assume static filtration. Under dynamic conditions, the shear stress caused by the moving fluid impedes the growth of filter-cakes. Jiao and Sharma[11] studied the mechanisms that occur during dynamic filtration when the cake is continuously eroded away by the flowing fluid.

Jiao and Sharma show that a particle is held to the filter-cake by the filtration pressure or leak-off flux, and is eroded away by the shear stress acting on the cake wall. Particle sliding can occur when the shear force is greater than the frictional forces. Rolling can occur due to the torque of the passing fluid. The authors show that smaller and smaller particles are deposited in the filter-cake during dynamic filtration. Eventually the filter-cake reaches an equilibrium thickness. These effects are not taken into account by static filtration models or experiments. Leak-off during fracturing is a dynamic filtration process.

8.1.2 LEAK-OFF OF FOAM FRACTURING FLUIDS: EXPERIMENTAL RESULTS AND CONCLUSIONS

The studies discussed in the previous section can be applied to any filtration conditions for single-phase fluids, foams, and emulsions. Experiments on actual energized fracturing fluids are limited at best. Tests are not routinely done because of cost. As mentioned previously, mini-frac or other field tests are commonly used to analyze leak-off. However, mini-frac tests lack the ability to consider any multi-phase or multi-component effects. Field tests can tell how much fluid is being lost but do not measure what component in the fluid is being lost.

Forshee and Hurst[12] were the first to report the decrease in dynamic leak-off by the addition of a gas phase. They did experiments with 10 -20% quality, or volume fraction, nitrogen. A decrease in leak-off was observed due to a gas block forming in the pore channels. Only liquid effluent volume was measured.

King[5] did dynamic leak-off tests on higher quality (up to 90%) nitrogen foams. He concluded that foam was not a wall-building material without additives. The gas effluent was measured using a wet-test meter, but only for a limited number of experiments. The effluent gas-to-liquid ratio remained almost constant for an experiment with 0.5 md permeability, 80 quality foam, and no additives.

Harris[6,7] conducted two sets of dynamic leak-off studies with foam (one for nitrogen and one for carbon dioxide). Unlike King, Harris used a linear gel as the base fluid so that wall-building conditions were established. Harris concludes that similar leak-off behavior is observed for both N_2 and CO_2 foams. Harris concluded that the overall leak-off coefficient is a function of core permeability, gelling-agent concentration, and temperature. All of these parameters also affect single-phase leak-off. Inlet quality did not have an effect on the nitrogen foam experiments and only had an effect on carbon dioxide experiments when the core permeability was above 5 md. Five md is the limit of permeability where foam passed through the core intact. The effluent quality was enriched in the liquid phase in all cases but no conditions were reported where zero gas leak-off occurred.

8.2 Possible Leak-off Mechanisms

This section details four different mechanisms we have postulated to reduce leak-off rates due to the presence of a gas phase. Referenced in the introduction to this chapter, these mechanisms are again listed below:

1. Bubbles can be held on the surface of the porous media, plugging pore entrances.
2. Bubbles can be held both in and on the filter cake and impede the flow of the continuous phase.
3. Bubbles can penetrate into the porous medium from the bulk foam.
4. Soluble gas at high pressure can be released as pressure drops and the free gas can impede the flow of the continuous phase.

8.2.1 MECHANISM 1: BUBBLES HELD ON THE SURFACE OF THE POROUS MEDIA

In this mechanism, we consider whether a gas bubble traveling in an open fracture can be held onto the surface of the fracture as leak-off occurs. If allowed to do so, the bubbles collecting on the face impede the flow of liquid into the rock by blocking pore entrances and forcing the fluid around the bubble. This will decrease the leak-off.

Consider the drawing in Figure 8.2 picturing a bubble in a continuous liquid phase. The bulk fluid containing the bubble and liquid is flowing through a narrow slot of width, W, and at a rate Q. The fluid in the slot exhibits power law behavior. The walls of the slot are porous with permeability, k, and area, A_c. A constant pressure drop is applied across the porous medium. Leak-off occurs perpendicular to the bulk flow through the fracture (slot flow). The slot represents the fracture and the porous medium represents the fracture face exposed to leak-off.

In this mechanism, we analyze the forces applied to a single bubble. The presence of other bubbles is ignored. This is representative of low quality foam where the bubbles are not concentrated enough to interfere with the streamlines around a single bubble. Gravity is ignored because leak-off occurs horizontally in a vertical fracture.

If the forces keeping the bubble attached to the surface (F_y in Figure 8.2) are larger than the shear forces that will keep the bubble moving in the direction of bulk flow (F_x in Figure 8.2), the bubble is held in place on the surface of the porous media. F_y is estimated by calculating the drag force on the bubble in a velocity field of V_y. If inertial effects are small (Reynolds number less than 0.01) then the drag force is[13]

$$F_y = 12\pi R^{2-n} \frac{1}{2^n} K V_y{}^n f_n[n] f_\mu[\mu_{bubble} / \mu_l] \quad (8.6)$$

Where

$$f_n[n] = 3^{(3n-3)/2}\left(\frac{33n^5 - 63n^4 - 11n^3 + 97n^2 + 16n}{4n^2(n+1)(n+2)(2n+1)}\right) \quad (8.7)$$

f_μ corrects the drag force for a viscous particle[14].

$$f_\mu\left[\frac{\mu_{bubble}}{\mu_l}\right] = \left(\frac{2 + 3\frac{\mu_{bubble}}{\mu_l}}{3 + 3\frac{\mu_{bubble}}{\mu_l}}\right) \approx 2/3 \quad (8.8)$$

The viscosity of bubbles is much less than the viscosity of the surrounding fluid therefore; f_μ is roughly 2/3.

F_x is the shear stress of the bulk fluid at the wall integrated over the area of the bubble. The shear stress of a power law fluid in a slot is a function of the shear rate at the wall. Equation 8.9 shows this expression[11]:

$$F_x = 4\pi R^2 \tau_w = 4\pi R^2 K\left(\frac{(4 + 2/n)Q}{A_c W}\right)^n \quad (8.9)$$

For a bubble to remain trapped on the surface:

$$F_y > F_x \quad (8.10)$$

Equations 8.6-8.10 are combined to obtain the inequality:

$$R < \frac{A_c W 2^{1/n-1}}{Q(4 + 2/n) f_n{}^n} V_y \quad (8.11)$$

The filtration velocity, V_y, can be substituted in Darcy's law through the porous media.

$$R < \frac{A_c W 2^{1/n-1}}{Q(4+2/n) f_n^{\ n}} \frac{k\Delta P}{\mu_l L_{core}} \tag{8.12}$$

Bubbles that are smaller than R from Equation 8.12 are held to the surface of the core. If the radius calculated in Equation 8.12 is larger than any bubble in the slot, no bubbles should attach to the surface. Notice that all the parameters in Equation 8.12 are specified in a lab experiment or are known in the field.

8.2.2 MECHANISM 2: BUBBLES HELD ON THE SURFACE OF THE FILTER CAKE

In Mechanism 1, bubbles are on the edge of the porous media but not within it. Mechanism 2 evaluates whether the bubble can remain on the surface after or during the creation of an external filter cake.

In our analysis, we assume that filter cakes grow as polymer or other suspended solids get trapped on the surface of the porous media as the liquid passes through. If the initial filtration rate (without filter cake) is high enough, the bubbles attach to the surface by the first mechanism. However, the filtration rate will slow down with time because the filter cake growth causes increased hydraulic resistance and lower leak-off velocities. This will result in: 1) The filtration rate decreasing to a point where the filtration force acting on the bubble is no longer enough to hold the bubble on the surface, or 2) the filter cake reaching an equilibrium thickness with bubbles still able to attach to the surface.

Figure 8.3 is similar to Figure 8.2 but shows the addition of the filter cake. This represents a snapshot in time where the filter cake is either growing or is at an equilibrium thickness.

The analysis of this mechanism is the same as Mechanism 1 up to Equation 8.11. Now, the filtrate velocity includes an additional pressure drop due to the filter cake.

$$R < \frac{A_c W 2^{1/n-1}}{Q(4+2/n) f_n^{\ n}} \left(\frac{\Delta P}{\frac{L_{core}}{\left(\frac{k}{\mu_l}\right)} + \frac{h_{cake}}{\lambda_{cake}}} \right) \tag{8.13}$$

Where h_{cake} is the thickness of the filter cake and λ_{cake} is the mobility (k/μ) of the liquid in the filter cake.

Equation 8.13 will always yield a smaller radius than Equation 8.12 because of the increased resistance of the filter cake. Bubbles are held to the filter cake if they are smaller than the radius calculated in Equation 8.13. If bubble sizes are smaller than the radius calculated by Equation 8.12, but are larger than the radius calculated by Equation 8.13, only Mechanism 1 will be plausible. If bubbles are able to collect on the surface of the core (Mechanism 1) and on the surface of the filter cake (Mechanism 2) then it is possible that the bubbles can collect inside the filter cake, shown in Figure 8.4. This assumes that the bubbles are approximately the size of the filter cake. An extreme case of Figure 8.4 results in bubbles interacting with each other inside the filter cake. This is similar to Figure 8.1[10], where the stress (pressure) applied to the filter cake will change the properties of the filter cake.

The likelihood of this and other phenomena is discussed in Section 8.3, after all mechanisms are explained.

8.2.3 MECHANISM 3: BUBBLES PENETRATING INTO POROUS MEDIA

The mechanism in this section explores conditions where gas bubbles move into the porous medium. Once in the porous medium, gas bubbles occupy pore space that would normally allow the filtration of the continuous liquid, thus reducing leak-off. This mechanism accounts for gas flowing into the core in a leak-off experiment, something that Mechanisms 1 and 2 do not consider.

In order for a bubble to penetrate into the porous medium, the pressure gradient across a pore has to be larger than the capillary forces it takes to push the bubble into and through the pore neck. Oh and Slattery[15] reported the pressure drop required to push an oil droplet (non-wetting phase) through an idealized pore, shown in Figure 8.5.

Figure 8.6 shows the dimensionless pressure drop it takes to displace a given bubble size through an ideal pore under water-wet conditions[15]. Notice the values of the angles and pore dimensions given in the table in Figure 8.6. The trend shown in the

figure is periodic. This means the trend will repeat as bubble volume increases. The dimensionless pressure drop never reaches a value of one. The authors report that below $V_{bub}/r_n^3 = 46$ the bubble is not displaced through the pore because capillary effects will force it back to the original position. We can assume that this effect goes away when the volume of the bubble is near the volume of the pore neck ($V_{bub}/r_n^3 = 1$).

The ratio between the total pressure drop and the pressure drop required to displace a bubble will determine if and how far a bubble will be able to travel into the porous medium. Equation 8.14 shows how to calculate the radius of a bubble that will be able to travel into the porous medium at least one bubble diameter.

$$R = \frac{\Delta P_{total}}{2(\frac{\Delta P r_n}{2\sigma})_{crit}\frac{2\sigma}{r_n}} L_p \tag{8.14}$$

In Equation 8.14, σ is the interfacial tension between the phases, r_n is the pore neck radius, and L_p is the pore length. $(\Delta P r_n/2\sigma)_{crit}$ is the dimensionless pressure drop. Figure 8.6 shows the value for $(\Delta P r_n/2\sigma)_{crit}$ under water-wet conditions.

In our analysis, $(\Delta P r_n/2\sigma)_{crit}$ will remain an adjustable variable. This is not only to take into account the bubble volume and wettability, but also to take into account the ability of the liquid film to break instead of being pushed through by the bubble. If this happens, $(\Delta P r_n/2\sigma)_{crit}$ will be lower than calculated by Oh and Slattery. This mechanism is described by Holm[16]. Holm's study was referenced by Harris[6,7] to explain why the effluent had a significant quantity of gas.

8.2.4 MECHANISM 4: SOLUBLE GAS RELEASED AS PRESSURE DROPS

It is possible that a gas phase forms inside the porous medium because of gas solubility in the liquid filtrate. A pressure decrease causes gas release when the liquid travels into the porous medium.

The explanation of this mechanism is discussed in two sections. The first section shows how solubility is accounted for in a leak-off experiment. The second section

covers the behavior of leak-off if only the liquid phase leaks-off and free gas is released in the porous medium.

8.2.4.1 Correcting for solubility during a leak-off experiment

In multi-phase leak-off experiments, the fraction of each phase that leaks-off is measured. Unfortunately, it is very hard to measure the volume of each phase under high pressure. It is more convenient to measure the gas at atmospheric conditions and compute the phase volumes at high pressure.

In experiments by Harris, the fluid expansion was accounted for but gas solubility was not. The purpose of this section is to discuss when solubility is a factor and show whether Harris' conclusions change after the corrections are made.

Recordable data from Harris' experiments include volume of gas and liquid that has passed through the core (effluent). The measurements are usually at atmospheric pressure so that no pressurized mass flow meters are needed. The goal is to calculate the volume fraction of gas at inlet conditions. For this example, the temperature is 75^{o} F and the inlet pressure is 1200 psi. The inlet is a mixture of CO_2 and H_2O. Table 8.1 shows properties of both the liquid and gaseous phases under several conditions. These properties were predicted by the Peng-Robinson equation of state.

For this example calculation, Rows 1 and 3 of Table 8.1 are important. Row 1 shows the atmospheric (14.7 psi) properties and Row 3 shows them at 1200 psi. ρ_l and ρ_g are the phase density of the liquid and gaseous phases, respectively, and X_{gl} represents the mass fraction of the gas component in the liquid phase, a measure of gas solubility at these conditions.

To make the calculation general, let's refer to the outlet (atmospheric) condition as "1" and the inlet (high pressure) condition as "2". The term V refers to a volume of either liquid or gaseous phases. The known volumes are V_{g1} and V_{l1}. The unknown volumes are V_{g2} and V_{l2}.

If there is no change in solubility between conditions 1 and 2, then the volumes can be correct using conservation of mass:

$$\rho_1 V_1 = \rho_2 V_2 \tag{8.15}$$

However, in this example we have $X_{gl,1} = 0.0011$ and $X_{gl,2} = 0.0522$ (Table 8.1). The difference is roughly 5% by mass. 5% of the mass of the gas component is unaccounted for if we assume no effect of solubility. Equation 8.16 is the same as Equation 8.15, but is corrected for solubility.

$$\begin{aligned} \rho_{g1}(V_{g1} - V_g^{sol}) &= \rho_{g2} V_{g2} \\ \rho_{l1}(V_{l1} + V_l^{sol}) &= \rho_{l2} V_{l2} \end{aligned} \tag{8.16}$$

The equation shows a subtraction from the measured gas volume (V_{g1}-V_g^{sol}) and an addition to the measured liquid volume (V_{l1}+V_l^{sol}). The effect of the presence of H_2O in the gaseous phase is not taken into account.

The volume of the gas and liquid that come out of solution at condition 1 is

$$\begin{aligned} V_g^{sol} &= V_{l2} \frac{\rho_{l2}}{\rho_{g1}} (X_{gl,2} - X_{gl,1}) \\ V_l^{sol} &= V_{l2} \frac{\rho_{l2}}{\rho_{l1}} (X_{gl,2} - X_{gl,1}) \end{aligned} \tag{8.17}$$

.

Notice that each is proportional to the difference in solubility at each condition. Equations 8.16 and 8.17 are combined to obtain:

$$\begin{aligned} V_{l2} &= V_{l1} \frac{\rho_{l1}}{\rho_{l2}} \frac{1}{1-(X_{gl,2} - X_{gl,1})} \\ V_{g2} &= \frac{\rho_{g1}}{\rho_{g2}} (V_{g1} - V_{l1} \frac{\rho_{l1}}{\rho_{g1}} \frac{X_{gl,2} - X_{gl,1}}{1-(X_{gl,2} - X_{gl,1})}) \end{aligned} \tag{8.18}$$

Equation 8.18 shows the liquid and gas volumes at inlet conditions in terms of all known quantities. If the measured data is V_{l1} = 1 ml, V_{g1} = 207 ml, and the data from Rows 1 and 3 of Table 8.1 are used, then V_{l2} = 1.04 ml and V_{g2} = 0.372 ml. This gives an effluent quality of $V_{g2}/(V_{g2}+V_{l2})$ = 0.263 or 26%. Notice that $V_{l2} \sim V_{l1}$ because water is incompressible, but $V_{g2} << V_{g1}$ because of gas expansion. If solubility was ignored ($X_{gl,2}$-$X_{gl,1}$ = 0) but expansion was not, an effluent quality of 30% is reported. The 4%

difference in calculated values represents the error that is introduced by ignoring solubility.

There is no need to correct for solubility for experiments using N_2 as the gas component because the solubility of N_2 in liquid is so low under most experimental conditions. See Table 8.1 for a measure of the N_2 solubility.

Harris reports effluent qualities for experiments on CO_2 foams, 1200 psi inlet pressure, and 75° F (Figure 7 in reference 7). Unfortunately, this is the only set of conditions where effluent qualities are reported. In the report, Harris makes note of the fact that he corrects for expansion of the gas phase with the equation[7]:

$$V_{g2} = 0.00207 V_{g1} \tag{8.19}$$

Equation 8.19 is used to recalculate the volume of gas at atmospheric conditions with the reported qualities.

$$V_{g1,Harris} = \frac{\Gamma_{Harris}}{0.00207(1-\Gamma_{Harris})} [\text{ml gas}]/[1 \text{ ml liquid}] \tag{8.20}$$

Corrected volumes (V_{g2} and V_{l2}) are calculated with V_{l1} = 1 ml, V_{g1} calculated from Equation 8.20, Equation 8.18, and the properties in Table 8.1. Figure 8.7 shows the results from that calculation. The first line in Figure 8.7 shows the corrected effluent quality based on the original measured quality. The second is a 45° line used as a reference point. If there were no change in corrected versus measured quantities, then the two lines would match up. Figure 8.7 shows a small discrepancy at large measured qualities and a large discrepancy at low quality. This is because the effective volume of gas that can be accounted for with solubility is constant under this set of experimental conditions. The volume that corrects for solubility is a large fraction of the collected gas if the effluent quality is low. That is why there is a larger percent change at low effluent qualities. When effluent quality is large, the solubility volume is small compared to the total volume collected, and a small discrepancy is seen.

Figure 8.8 shows a corrected version of Figure 7 (in Reference 7 by Harris) and includes Harris' originally reported data. The figure shows corrected values lower in

effluent quality under all conditions but it does not change the trends of the figure. The conclusions made by Harris remain unchanged. Harris' data suggest that there is another mechanism (besides gas solubility) that is responsible for gas flowing through the core.

8.2.4.2 Behavior of leak-off with solubility

As described above, two things need to happen in order for this mechanism to work. First, gas molecules have to get into the porous media in some manner. For this analysis, we can assume that gas enters the porous medium because the liquid that invades the porous medium is saturated with the gas component. Second, the pressure drop has to be large enough so that the gas molecules are released from the liquid phase and expand to create a large gas saturation. This section describes the equations that can be used to quantify this behavior.

The overall mass fraction of gas inside the porous medium, z_{gas}, is given by Equation 8.21.

$$z_{gas} = \frac{(1-S_{gr})\rho_l[P_{in}]X_{gl}[P_{in}] + S_{gr}\rho_g[P_{out}]X_{gg}[P_{out}]}{(1-S_{gr})\rho_l[P_{out}] + S_{gr}\rho_g[P_{out}]} \tag{8.21}$$

Notice that Equation 8.21 shows two sources adding to the composition of gas. The term $(1\text{-}S_{gr})\rho_l X_{gl}$ represents the mass of gas added to the pores by invasion of saturated liquid. The other term $S_{gr}\rho_g X_{gg}$ represents the gas that was originally in place due to residual gas saturation. For simplicity, the original gas in place is assumed to be the same component as the gas invading the pores. The pressure that each parameter is evaluated at is shown in brackets in Equation 8.21. Notice that all parameters are evaluated at outlet conditions except for the term $\rho_l X_{gl}$.

The gas composition, temperature, and pressure are related to the gas and liquid saturation through an equation of state. This is shown symbolically in Equation 8.22. Equation 8.23 shows a Corey type relationship between the relative permeability of liquid and the liquid saturation.

$$S_w = 1 - S_g = EOS[T, P, z_i] \tag{8.22}$$

$$k_{rl} = k_{rl}^{\,o}\left(\frac{S_w - S_{wr}}{1 - S_{wr} - S_{gr}}\right)^{n_{relperm}} \tag{8.23}$$

At any given time, the flowrate can be calculated using Darcy's law and three flow resistances: 1) the invaded zone of the porous media that includes a relative permeability to liquid; 2) the un-invaded porous media, and; 3) the filter cake. This is shown in Equation 8.24.

$$q_l = \frac{A_c \Delta P}{\frac{L_{front}}{\frac{k k_{rl}}{\mu_l}} + \frac{(L_{core} - L_{front})}{\frac{k}{\mu_l}} + \frac{h_{cake}}{\lambda_{cake}}} \tag{8.24}$$

where q_l is the flowrate (volume/time), A_c is the cross-sectional area, ΔP is the total pressure drop, L_{front} is the location of the injected fluid front, L_{core} is the length of the core, k is the permeability of the core, k_{rl} is the liquid relative permeability, μ_l is the liquid viscosity, h_{cake} is the thickness of the filter cake, and λ_{cake} is the mobility (k/μ) of the filter cake.

Filter cake growth is calculated assuming that the bulk fluid contains wall-building material. The filter cake will start at zero thickness and grow in proportion to the leak-off rate (Equation 8.25).

$$h_{cake}[t + \Delta t] = h_{cake}[t] + \beta \frac{q_l}{A_c} \Delta t \tag{8.25}$$

Where $h_{cake}[0] = 0$. The proportionality constant, β, in Equation 8.25, represents the ability of the fluid to form a filter cake. β is a function of the concentration of polymer in the bulk fluid as well as the ability of the pores to trap the polymer. Δt is the size of the time steps. A maximum cake height, $h_{cake,max}$, can occur because of shear forces on the cake (similar to the forces described above).

The gas saturated front is tracked through time with Equation 8.26.

$$L_{front}[t + \Delta t] = L_{front}[t] + \frac{q_l}{A_c} \Delta t \tag{8.26}$$

Where $L_{front}[0] = 0$.

The front is divided into segments of length ΔX. A new ΔX is created at each time step. The size of ΔX is equal to $q_l/A_c\Delta t$ (see Equation 8.27), the same distance the front moves in a given time step. This makes the number of time steps equal to the number of segments.

$$\Delta X_i = \frac{q_{l,i}}{A_c}\Delta t \tag{8.27}$$

Each segment has a saturation based on the pressure at that location, making the relative permeability different for each segment. Equation 8.28 shows a corrected version of Equation 8.24. The invaded zone resistance is represented by a sum over all segments.

$$q_l = \frac{A_c \Delta P}{\sum_i^N \frac{\Delta X_i}{\frac{k k_{rl,i}}{\mu_l}} + \frac{(L_{core} - L_{front})}{\frac{k}{\mu_l}} + \frac{h_{cake}}{\lambda_{cake}}} \tag{8.28}$$

The equations above show that leak-off is reduced through time because of an increase in filter cake growth as well as a decrease in liquid relative permeability due to the presence of a gas phase. The next section discusses where this mechanism fits into the leak-off involving all of the proposed mechanisms.

8.3 Investigating the Possibility of Each Mechanism

The previous sections show the characteristics of each of the four proposed mechanisms. This section compares the likelihood of each mechanism occurring during a leak-off experiment. The conclusions can be applied directly to field applications.

Equations 8.12, 8.13, and 8.14 are the equations that can be used to calculate the bubble radius that would be needed for Mechanisms 1, 2 and 3 to be important. Table 8.2 shows the parameters of a possible leak-off experiment. Most of the parameters in Table 8.2 are taken from experiments conducted by Harris[7]. Other properties are estimated

with reasonable approximations. For example, the pore radius, r_p, is dependent on the permeability, k, by assuming a 100 md rock has a pore radius of 10 μm and further assuming that k is proportional to r_p^2.

Figure 8.9 was created using the data in Table 8.2 and Equations 8.12, 8.13, and 8.14. Increasing the rock permeability increases the filtration rate and the drag force keeping larger bubbles on the surface of the core (Mechanism 1). The same can be said for Mechanism 2, where larger bubbles can be held on the surface of the filter cake. The filter cake has such a large flow resistance that it will limit the filtrate, even when high permeability cores are used. This is why the bubble radius levels out for Mechanism 2 in Figure 8.9. Bubbles will enter the rock when the pressure drop exceeds the capillary forces. The figure also shows the pore neck radii for each permeability as a reference point relative to the size of the pores.

Figure 8.10 shows bubble diameters measured by Harris for his foamed fluids. The lowest radius shown is roughly 100 μm. Note that, in the figure, the data is reported as a volume frequency. If the figure was redone as the number frequency of bubbles, and not by volume, it would look highly skewed to the smaller bubble sizes because a bubble's volume is proportional to D^3. It is hard to determine the smallest bubble size possible from Figure 8.10. Figure 8.11 shows a different distribution of bubbles in foam[17]. This figure shows that average bubble diameters of 0.002 inches (roughly 50 μm) are common for all foam qualities. If 25 μm radius bubbles can exist in foam, it is reasonable to assume that some bubbles less than 10 μm in radius can exist too.

Figure 8.9 shows that when filtrate flow is very high (k_{core} > 10 md), bubbles greater than 100 μm will participate in Mechanisms 1 and 3. Bubbles greater than 100 μm will never participate in Mechanism 2. This means that it is very unlikely that any of the first three mechanisms will occur unless the filtration rate is very high. However, it is possible that Mechanisms 1 and 3 will occur in low permeability rocks if bubble sizes of 1 to 10 μm exist (even in small proportions). Determining the smallest possible bubble size is the most important parameter that determines if leak-off is reduced due to

Mechanisms 1, 2, or 3. Without the existence of small bubbles, it is unlikely that the bubbles in foam will reduce the leak-off.

The possibility of Mechanism 4 occurring is demonstrated by PVT calculations. For this example, the high pressure is 1200 psi and the low pressure is 200 psi, giving a total ΔP of 1000 psi. Mechanism 4 is the only mechanism where absolute pressure is important. Figure 8.12 shows the calculated gas saturation due to solubility for the experimental conditions given in Table 8.2. CO_2 has the highest solubility, therefore, it will have a much larger saturation than N_2. It is important to point out the liquid relative permeability calculated by Equation 8.23 is 0.01 for CO_2 and 0.82 for N_2. This means that the leak-off rate is more affected when CO_2 is used. This calculation also shows that solubility can be a major factor contributing to the reduction of leak-off rates because liquid relative permeability can be reduced by up to a factor of 100.

Figure 8.13 shows the leak-off rate calculated using Equation 8.28 and parameters in Table 8.2. With low filter cake fluid mobility (λ_{cake} = 3.3E-6 md/cp) the leak-off rate is reduced quickly at early time because the filter cake is being formed. This is also true for λ_{cake} = 4E-5 md/cp. The "no cake" line in Figure 8.13 shows a scenario where no cake is formed and, therefore, shows only the effects of solubility. In this case, the rate is constant until about 20 minutes, at which point it starts to decline. The constant rate occurs because the invaded fluid has yet to penetrate far enough in the core to reach a gas saturation that is above the residual gas saturation, making k_{rl} = 1.0.

Figure 8.14 includes the same scenarios as Figure 8.13 but shows the calculated pressure down the length of the core after 30 minutes of filtration. The filter cake fluid mobility controls the pressure drop into the entrance of the core. The figure shows that the filter cake drops the pressure to about half the overall pressure for the moderate cake mobility. Figure 8.14 shows the variety of penetration depths that can occur under each scenario. The front travels very small distances when the filter cake reduces the flowrate quickly.

Figures 8.13 and 8.14 also show two cases with a cake mobility of 4E-5 md/cp, one where solubility is included and one where it is not. The leak-off rate does not

change much for the two different cases. This is because the resistance of the porous media is negligible compared to the filter cake, even when gas release occurs. This is important to point out because it shows that the gas released due to solubility will only reduce the leak-off rate if the wall-building or filter cake material does not create a large flow resistance to leak-off. In cases where this is true, the pressure is still too high in the invaded zone to release gas above a saturation of S_{gr}. This shows that mechanism 4 is very likely to occur with CO_2 fluids, but it will only be a factor when filter cakes are not formed.

The results shown in Figure 8.13 are dependant on the inlet and outlet absolute pressures (not just the pressure difference). Figure 8.15 shows the leak-off rate with no filter cake at different absolute pressures. The figure shows that the leak-off rate will decline at a slower rate if pressures are high. At a pressure of 1700 psi inlet and 700 psi outlet, essentially no reduction is seen. Pressures lower than 200 psi are not shown in the figure because the gas saturation could reach above $1-S_{wr}$. In this case, a gas block would occur.

We conclude that CO_2 experiments should be run with no less than 200 psi back-pressure so that a gas block does not occur. In contrast, experiments should be run with backpressure above 700 psi to eliminate the solubility effects altogether.

In contrast to experiments, field cases can differ in several ways. In the experiments, the core is initially saturated with liquid with a residual saturation of gas. In the field, the pores are saturated with methane gas with a residual saturation of liquid. The methane is miscible with CO_2 and N_2 but will alter phase behavior in a way that is not discussed here. Also, fracturing pressures are usually thousands of psi. The reservoir pressure can also be thousands of psi but can reach lower levels with depletion. The absolute pressures involved in this process are usually high enough that CO_2 solubility differences during leak-off are negligible. A larger gas release occurs after fracturing and during flowback. The gas-saturated liquid that has leaked-off during fracturing is then subjected to a low bottom-hole pressure and can release a large volume of soluble gas.

8.4 Conclusions and Recommendations for Future Work

This chapter discusses four mechanisms that we have postulated to describe how a gas component in a fracturing fluid impacts fluid leak-off. Based on the equations derived in this chapter, we can reach the following conclusions:

1. For fluid properties and rates that are typical in fracturing conditions, the bubbles in a fluid traveling across the face of a porous medium are not likely to attach to the surface of the rock, the filter cake, or penetrate far into the porous medium.
2. At very high filtration rates (k_{core} >10 md) or if small (R < 10 μm) bubbles exist, the presence of gas bubbles in an external filter cake can play a role in reducing fluid leak-off.
3. The release of a free gas phase can reduce leak-off if CO_2 or another soluble component is used as the gas component. The gas phase does not play an important role if N_2 is used because it is relatively insoluble in water.
4. Even when CO_2 is used, a thick and low permeability filter cake can dominate leak-off control.

Unfortunately, experimental data is limited. Harris's experiments show that the effluent collected is enriched in the liquid phase but does not eliminate the leak-off of the gas phase. This is still true when Harris' data is corrected for solubility. Based on the calculations made in this study, leak-off of the gas phase into the core is unlikely under dynamic leak-off conditions. More systematic experiments need to be conducted to prove whether a free gas phase does indeed leak-off under typical fracturing conditions.

Future experiments should be designed with the following in mind:

1. The size of the smallest bubble needs to be measured (not just the bubble size distribution). This will determine which of Mechanisms 1, 2, or 3 are likely.
2. With no wall-building material in the bulk fluid, the leak-off rate should decrease with time if CO_2 is used and should remain constant if N_2 is used. A backpressure of 200 psi should be enough to eliminate the possibility of a gas block in the porous

medium. A backpressure of 700 psi or greater should be used to minimize the soluble gas release mechanism.

3. N_2 versus CO_2 results can be used to determine the importance of solubility effects in the experiment because it can be assumed that the solubility of N_2 in water is negligible.

4. Pressure taps across the length of the core should be used to determine wether a high resistance occurs in the filter cake or down the length of the core. This can provide evidence of the specific leak-off mechanisms that occur.

Nomenclature

a	Compressibility of filter cake (1/pressure)
A_c	Cross-section area of core in experiment
b	Correlation factor in Zydney[9]
c_o	Concentration of solids in bulk suspension (vol/vol)
f_μ	Drag force correction factor for bubble viscosity
f_n	Drag force correction factor for power law exponent
F_x	Force applied to bubble due to shearing of bulk flow
F_y	Force applied to bubble due to filtration
h_{cake}	Thickness of filter cake
k or k_{core}	Permeability of core
k_{cake}	Permeability of filter cake
k_{rl}	Relative permeability to liquid
k_{rl}^o	Endpoint relative permeability to liquid
K	Power law index
L_{core}	Length of core
L_{front}	Distance that invaded fluid has traveled into core
L_p	Length of a single pore
n	Power law exponent / correlation factor in Zydney[9]
$n_{relperm}$	Relative permeability exponent
P	Pressure
P_{in}	Inlet pressure
P_{out}	Outlet pressure
q_l	Filtration flowrate (vol/time) of liquid phase
Q	Bulk flowrate in slow representing fracture (vol/time)
Q^*	Cumulative flow per unit area (vol/area) from Outmans[1]
r_n	Pore neck radius
r_p	Pore radius
R	Bubble radius
S_g	Saturation of gas
S_{gr}	Residual saturation of gas
S_w	Saturation of liquid
S_{wr}	Residual saturation of liquid
t	Time
T	Temperature
V	Volume

V_{bub}	Volume of bubble
V_y	Filtration velocity
W	Width of slot representing fracture
X_{gl}	Mass fraction of gas component in liquid phase
z_i	Overall mass fraction of component i
z_{gas}	Overall mass fraction of gas component

Greek Symbols

β	Proportionality constant between filtration rate and cake growth
ΔP	Pressure difference
Δt	Time step
ΔX	Segment size
ϕ_{cake}	Porosity of filter cake
Γ	Foam quality
Γ_{Harris}	Effluent quality calculated by Harris [6,7]
λcake	Mobility (permeability/viscosity) of filter cake
μ or μl	Viscosity of liquid
μ_{bubble}	Viscosity of bubble
ν	Compressibility exponent by Outmans[1]
ρ	Density
σ	Interfacial tension
τ_w	Wall shear stress

References

1. Outmans, H.D. 1963. Mechanics of Static and Dynamic Filtration in the Borehole. *Society of Petroleum Engineers Journal*, September: 236-244.
2. Gulbis, J. 1983. Dynamic Fluid Loss of Fracturing Fluids. Paper SPE 12154 presented at the SPE 58th Annual Technical Conference and Exhibition held in San Francisco, California, 5-8 October.
3. Roodhart, L.P. 1985. Fracturing Fluids: Fluid-Loss Measurements Under Dynamic Conditions. *Society of Petroleum Engineers Journal*, October: 629-636. SPE 11900.
4. Mayerhofer, M.J, Economides, M.J. and Nolte, K.G. 1991. An Experimental and Fundamental Interpretation of Fracturing Filter-Cake Fluid Loss. Paper SPE 22873 presented at the SPE 68th Annual Technical Conference and Exhibition held in Dallas, Texas, 6-9 October.
5. King, G.E. 1977. Factors Affecting Dynamic Fluid Leakoff With Foam Fracturing Fluids. Paper SPE 6817 presented at the 52nd Annual SPE Fall Technical Conference and Exhibition held in Denver, Colorado, 9-12 October.
6. Harris, P.C. 1985. Dynamic Fluid-Loss Characteristics of Nitrogen Foam Fracturing Fluids. *Journal of Petroleum Technology*, October: 1847-1852.

7. Harris, P.C. 1987. Dynamic Fluid-Loss Characteristics of CO2-Foam Fracturing Fluids. *SPE Production Engineering*, May: 89-94.

8. Nolte, K.G, Mack, M.G. and Lie, W.L. 1993. A Systematic Method for Applying Fracturing Pressure Decline. Paper SPE 25845 presented at the SPE Rocky Mountain Regional Low Permeability Symposium, Denver, Colorado, 12-14 April.

9. Zydney, A.L. 1989. Hydraulic Resistance of Red Cell Beds in an Unstirred Filtration Cell. *Journal of Engineering Science*, Vol. 44: No. 1: 147-159.

10. Sherwood, J.D. 1993. A Model for Static Filtration of Emulsions and Foams. *Chemical Engineering Science*, Vol. 48: No. 19: 3355-3361.

11. Jiao, D. and Sharma, M.M. 1994. Mechanism of Cake Buildup in Crossflow Filtration of Colloidal Suspensions. *Journal of Colloid and Interface Science*, 162: 454-462.

12. Forshee, W.C. and Hurst, R.E. 1965. Improvement of Well Stimulation Fluids by Including a Gas Phase. *Journal of Petroleum Technology*, July: 768-772.

13. Acharya, A.R. 1986. Particle Transport in Viscous and Viscoelastic Fracturing Fluids. *SPE Production Engineering*, March: 104-110.

14. Chhabra, R.P. 2007. *Bubble, Drops, and Particles in Non-Newtonian Fluids*. Taylor and Francis.

15. Oh, S.G. and Slattery, J.C. 1979. Interfacial Tension Required for Significant Displacement of Residual Oil. *Society of Petroleum Engineers Journal*. April: 83-96.

16. Holm, L.W. 1968. The Mechanism of Gas and Liquid Flow Through Porous Media in the Presence of Foam. *Society of Petroleum Engineers Journal*, December: 359-369. SPE 1848.

17. Ozbayoglu, E.M, and Akin, S. 2005. Foam Characterization Using Image Processing Techniques. Paper SPE 93860 presented at the SPE Western Regional Meeting, Irvine, California, 30 March – 1 April.

Table 8.1. Phase properties of binary gas and aqueous systems.

Gas	P	T	ρ_l	ρ_g	X_{gl}
(-)	(psi)	(F)	(lb/ft^3)	(lb/ft^3)	(lb/lb)
CO_2	14.7	75	63.87	0.11	0.0011
CO_2	200	75	64.07	1.66	0.0146
CO_2	1200	75	64.7	52	0.0522
CO_2	2500	75	64.92	60.67	0.0562
CO_2	14.7	200	59.19	0.0536	0
CO_2	200	200	60	1.25	0.0062
CO_2	1200	200	60.45	9.83	0.0321
CO_2	2500	200	60.84	28.1	0.05
N_2	14.7	75	60.98	0.0711	0
N_2	200	75	60.98	0.981	3.11E-04
N_2	1200	75	61.04	5.95	7.78E-04
N_2	2500	75	61.11	12.07	1.56E-03

Table 8.2. Input parameters for leak-off model example calculations.

Property		Units
k_{core}	0.7	md
ΔP	1000	psi
L_{core}	0.59	in
Q	0.25	L/min
W	0.25	in
n	0.7	
h_{cake}	50	μm
λ_{cake}	3.30E-06	md/cP
μ_l	40	cP
A_c	2.64	in^2
σ	30	dynes/cm
r_p/r_n	2.5	
L_p/r_n	6	
T	75	F
S_{wr}	0.2	
S_{gr}	0.2	
$n_{relperm}$	3	

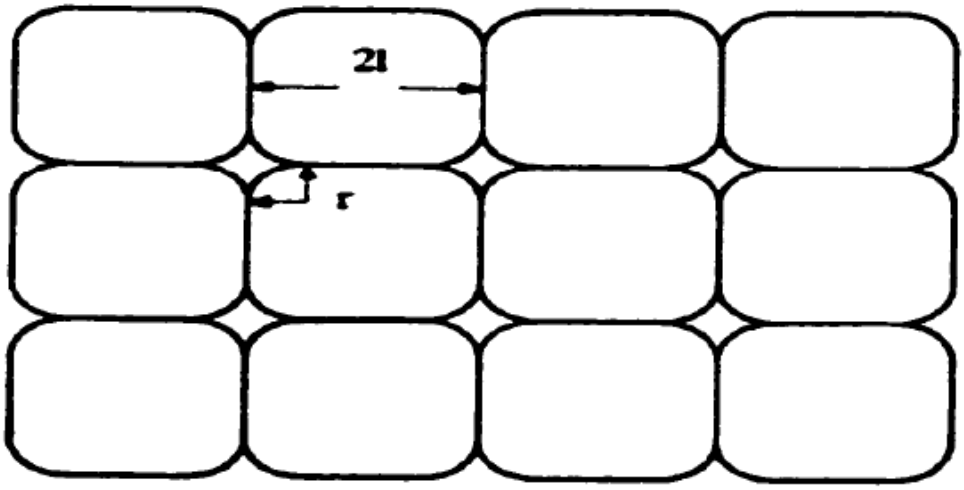

Figure 8.1. Cubic arrangement of emulsion droplets modeled by Sherwood[10].

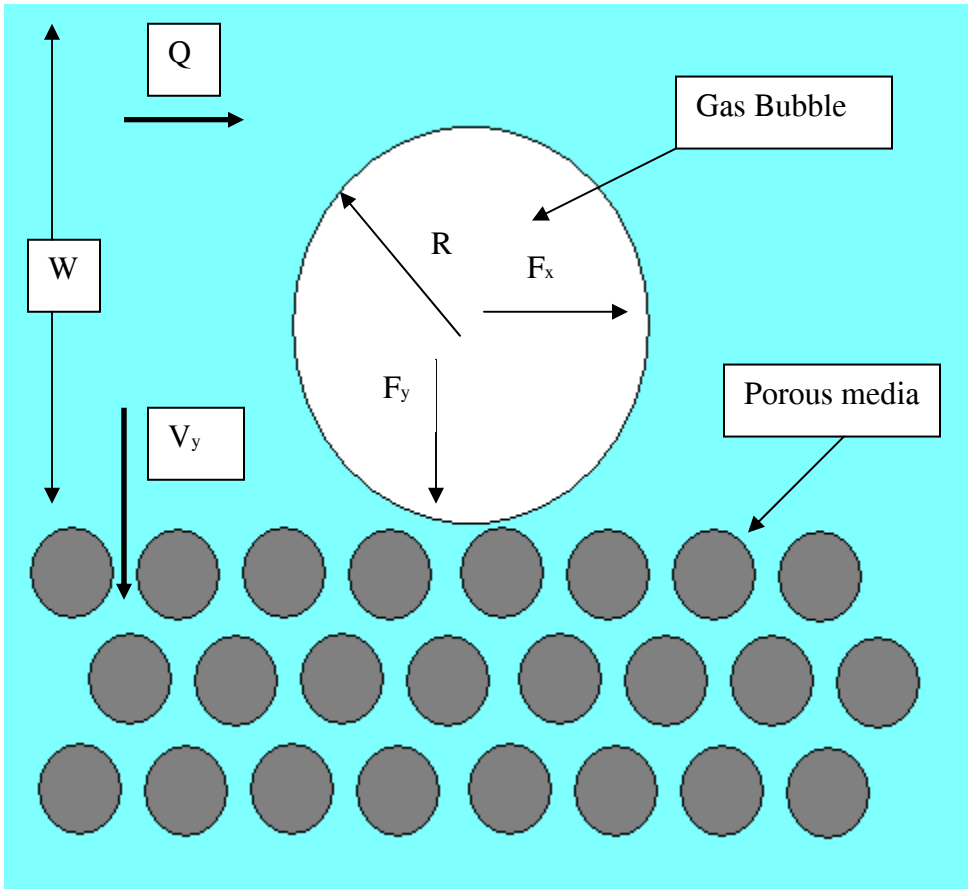

Figure 8.2. Drawing of a bubble of gas that is held onto the surface of porous media during leak-off.

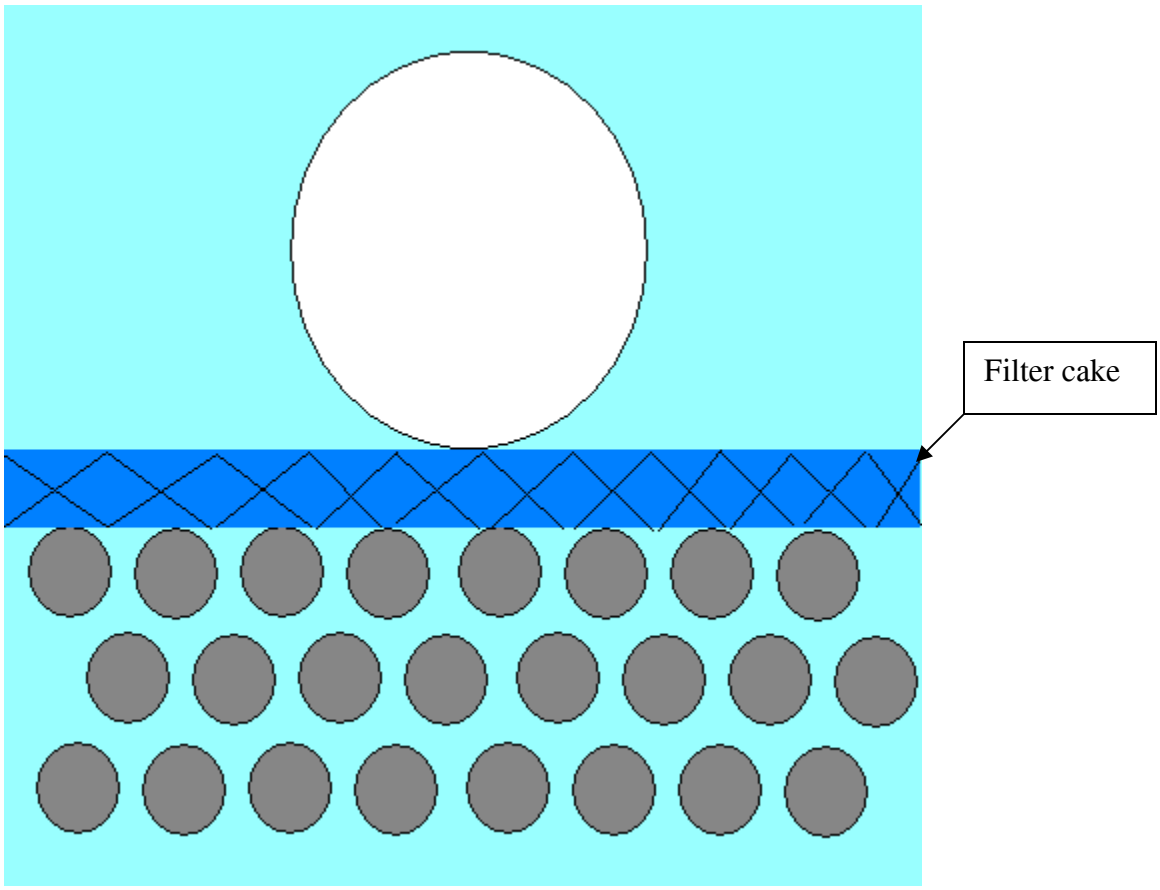

Figure 8.3. Drawing of a bubble of gas that is held onto the surface of filter cake during leak-off

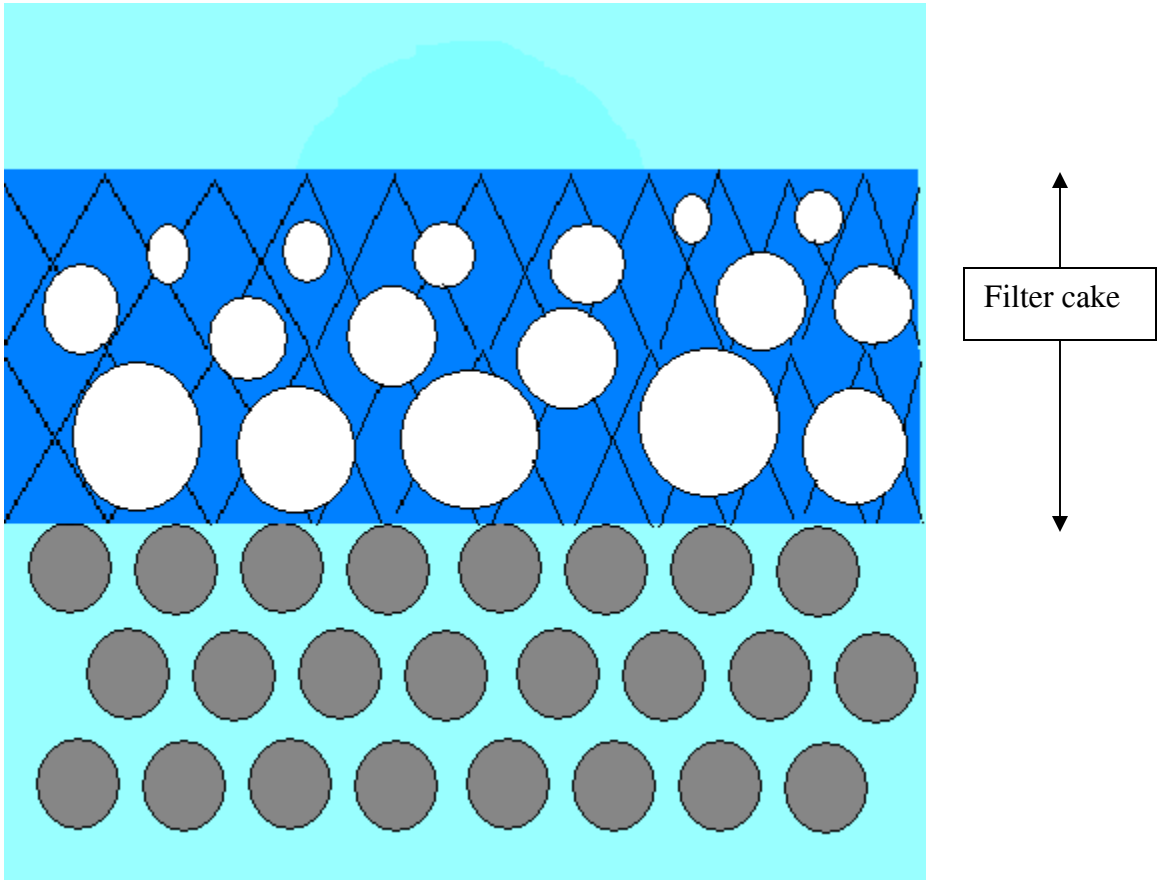

Figure 8.4. Drawing of bubbles of gas inside filter cake.

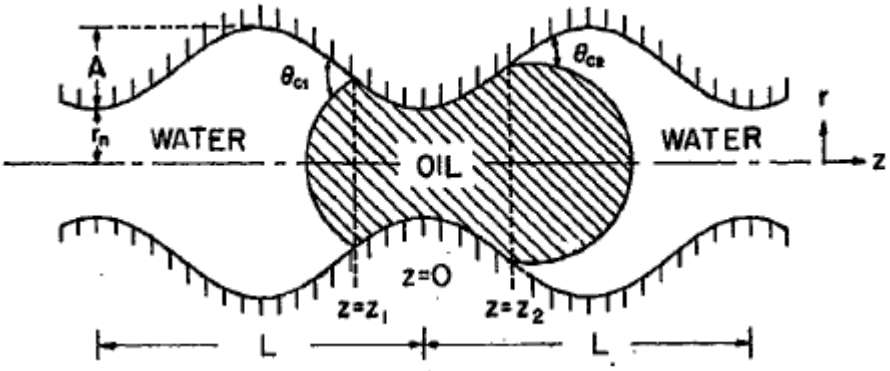

Figure 8.5. Pore geometry from Oh and Slattery[15].

TABLE 1 — TYPICAL WATER-WET CASE

V_o/r_n^3	$\left(\frac{\Delta p r_n}{2\sigma}\right)_{max}$
46.00*	0.323
50	0.676
56.48	0.884**
60	0.755
70	0.523
80	0.431
90	0.376
100	0.339
105.42†	0.323

Maximum value of $\frac{\Delta p r_n}{2\sigma}$ as a function of z_1/L for several values of V_o/r_n^3, assuming a typical water-wet behavior and Morrow's Class III contact angle hysteresis.[30] (In particular, $\theta_{cint} = \theta_{c1} = 40°$, $\theta_{c2} = 4°$, $A/r_n = 1.5$, and $L/r_n = 6$.)

* $(1/r_n^3)\, V_d$.

**Maximum value of $\left(\frac{\Delta p r_n}{2\sigma}\right)_{max}$.

† $(1/r_n^3)\,(V_d + V_p - V_{wi})$.

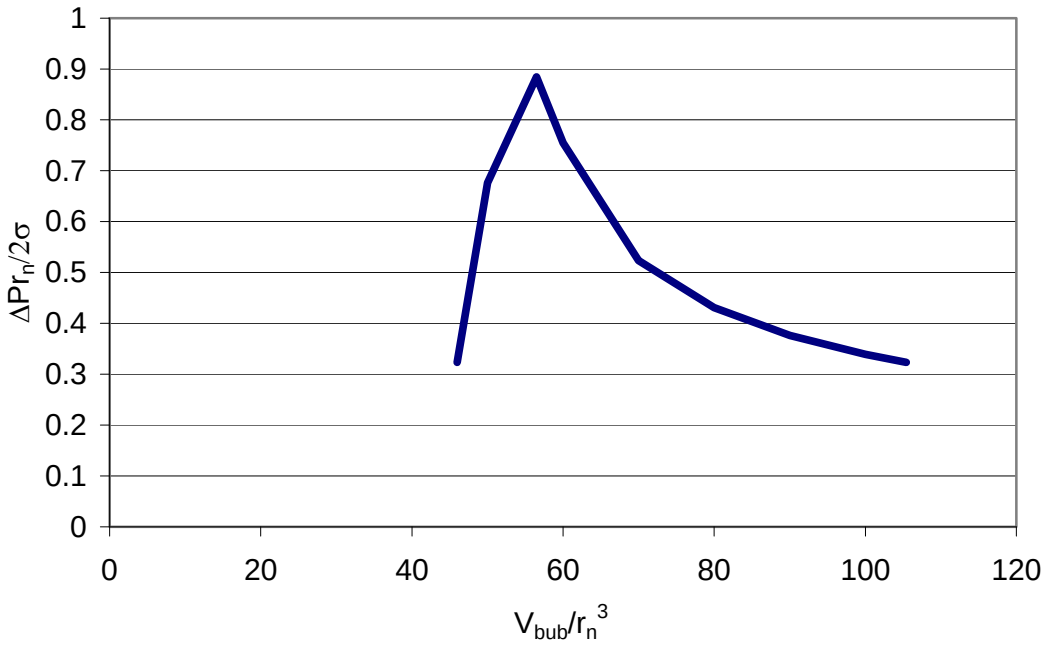

Figure 8.6. Dimensionless pressure drop required to displace a given bubble size under water wet conditions[15].

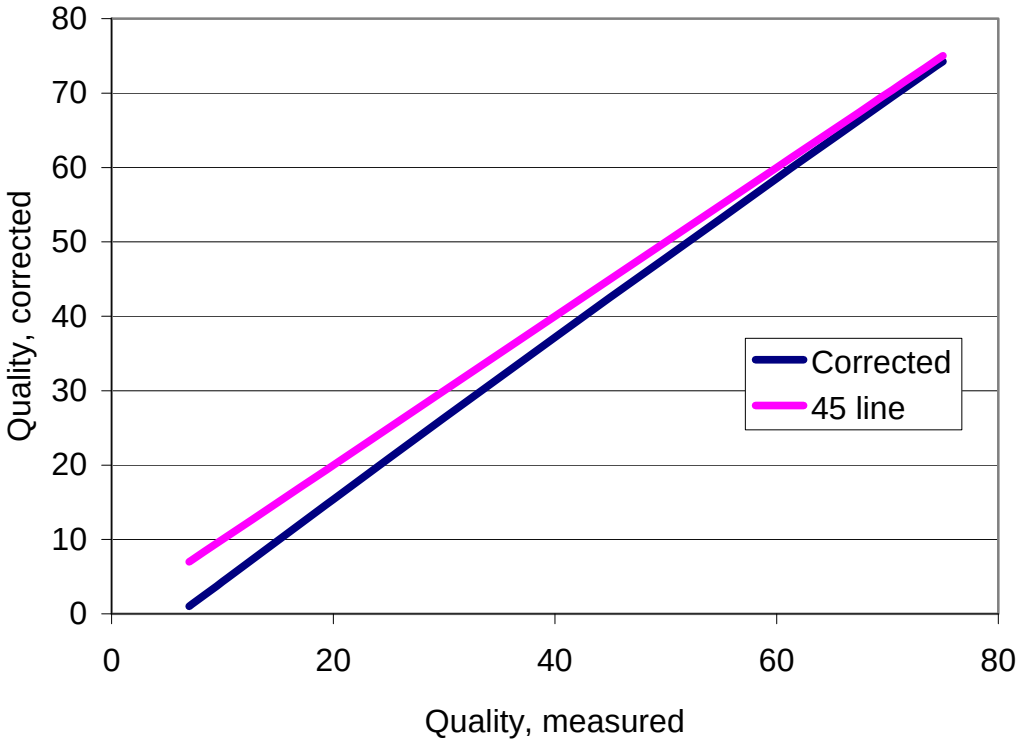

Figure 8.7. Effluent quality measured by Harris[7] vs the solubility corrected value.

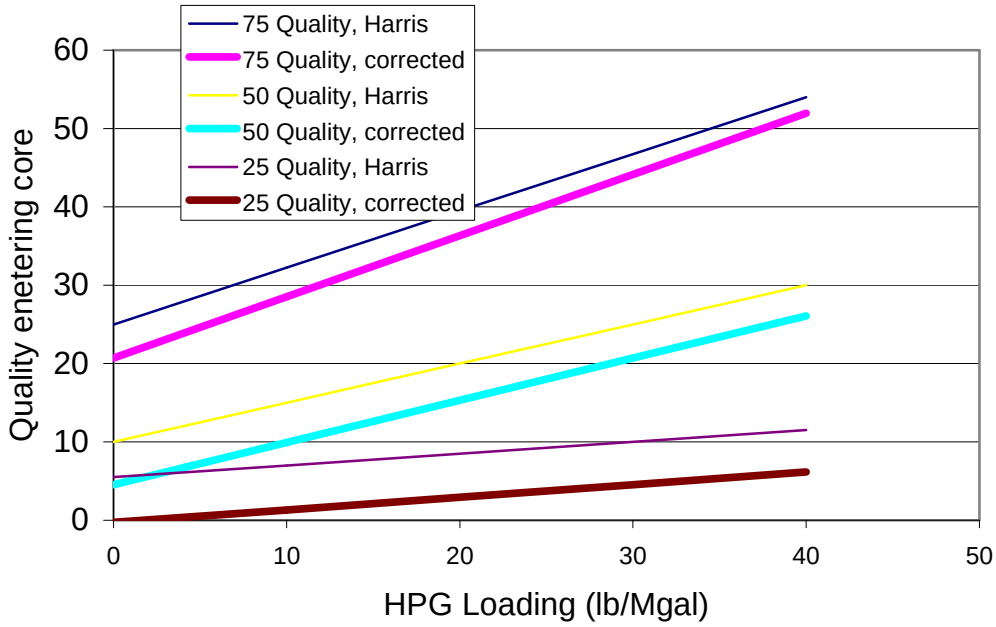

Figure 8.8. Comparison of Figure 7 in reference 7 by Harris to the corrected values.

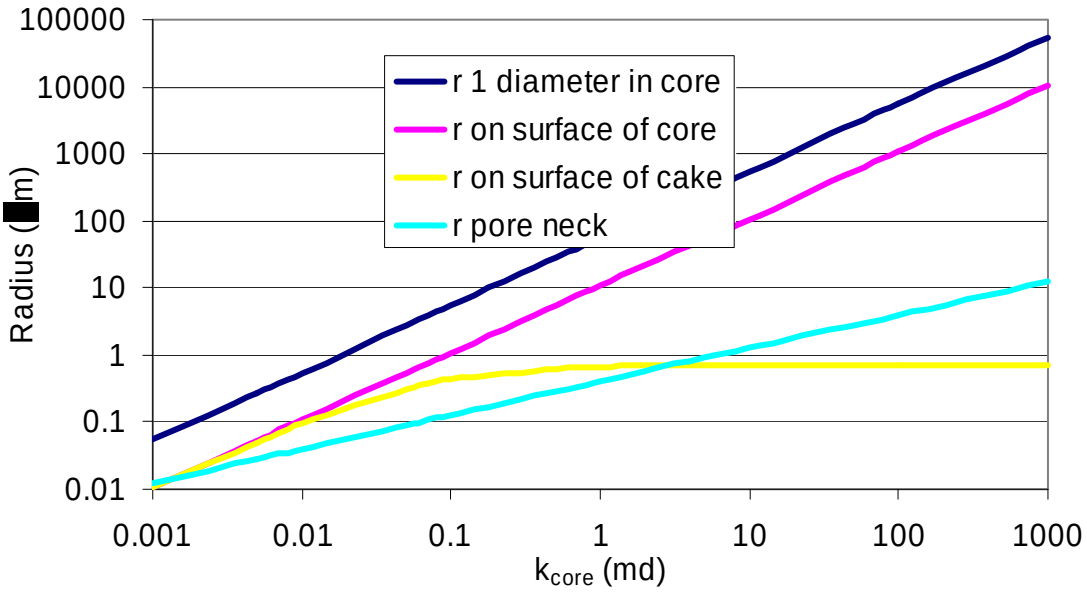

Figure 8.9. Characteristic radii vs permeability of the core given the data in Table 8.2.

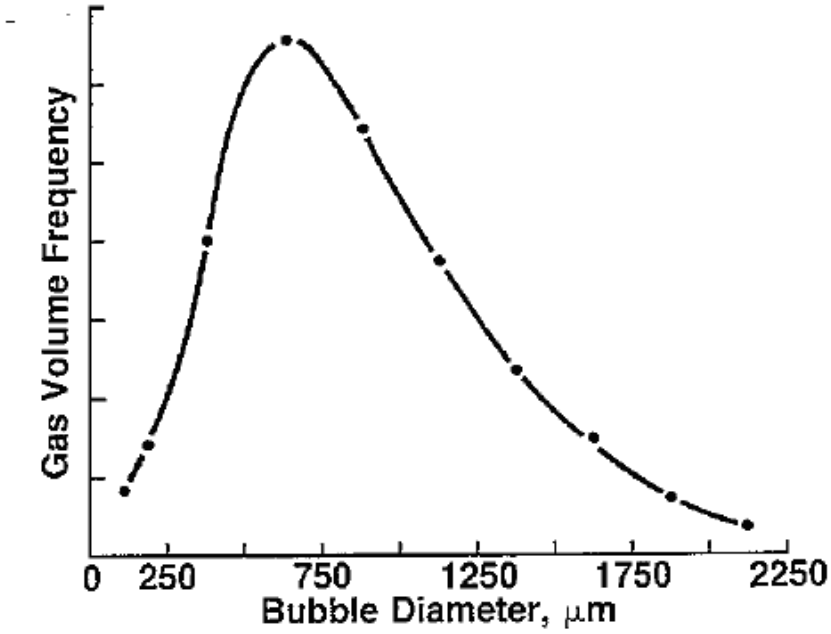

Figure 8.10. Bubble size distribution in bulk foam[6].

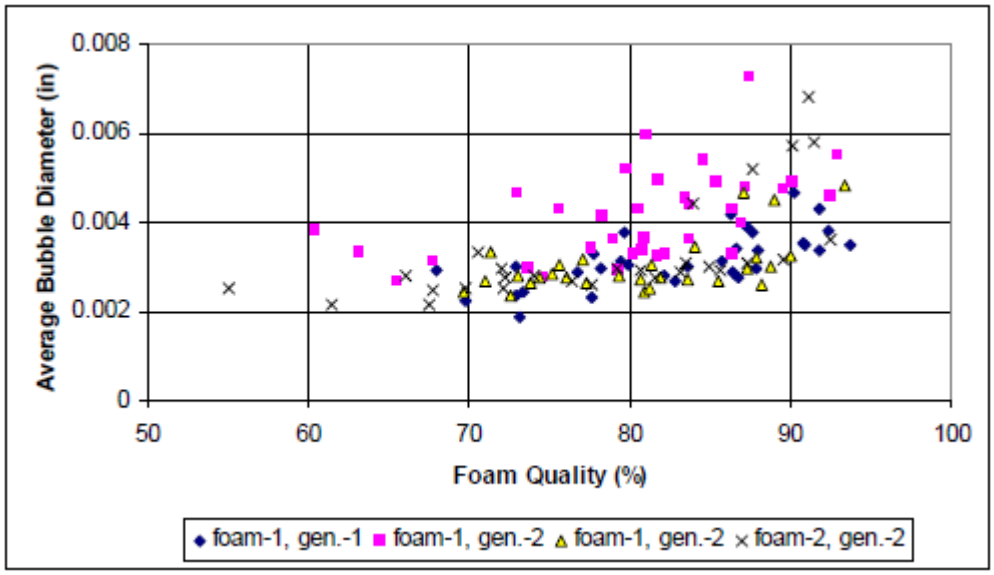

Figure 8.11. Average bubble size for all foam samples in reference 17 by Ozbayoglu. Note: 0.002 inches is roughly 50 μm.

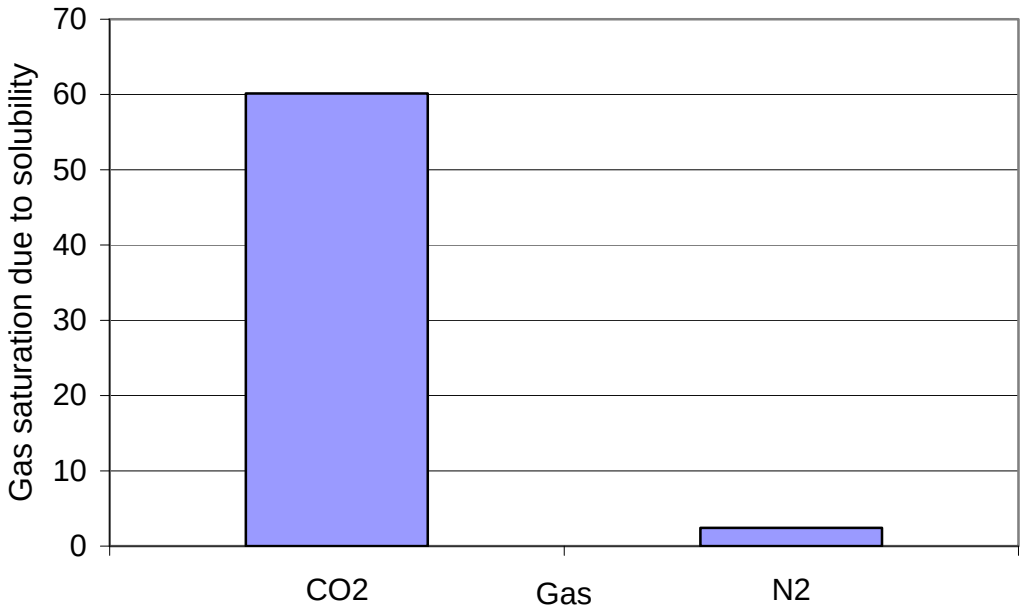

Figure 8.12. Gas saturation due to solubility differences in saturated liquid at 1200 psi to 200 psi, 75°F.

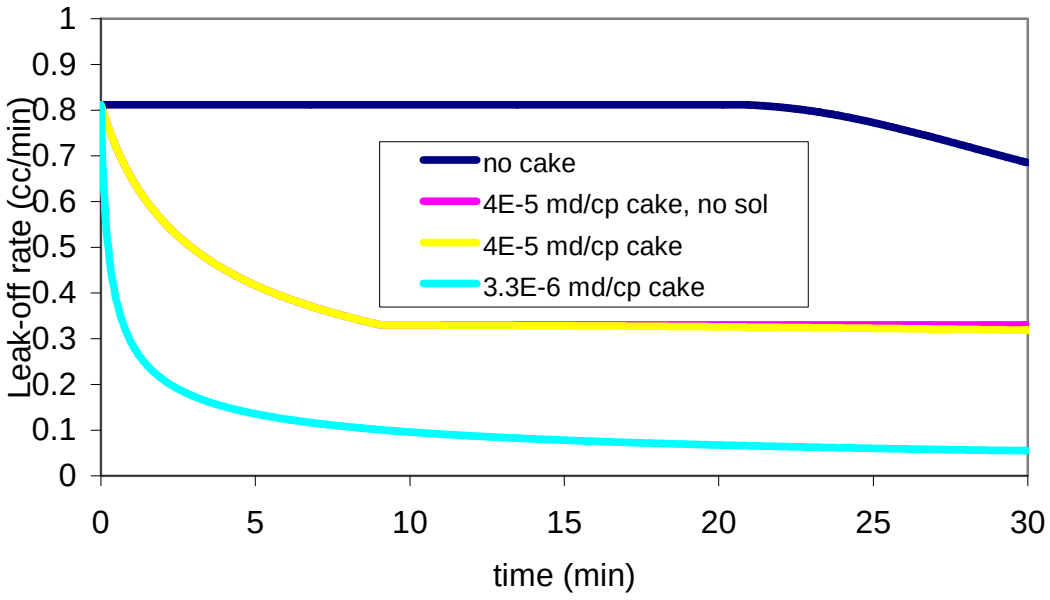

Figure 8.13. Leak-off rate versus time and filter cake mobility.

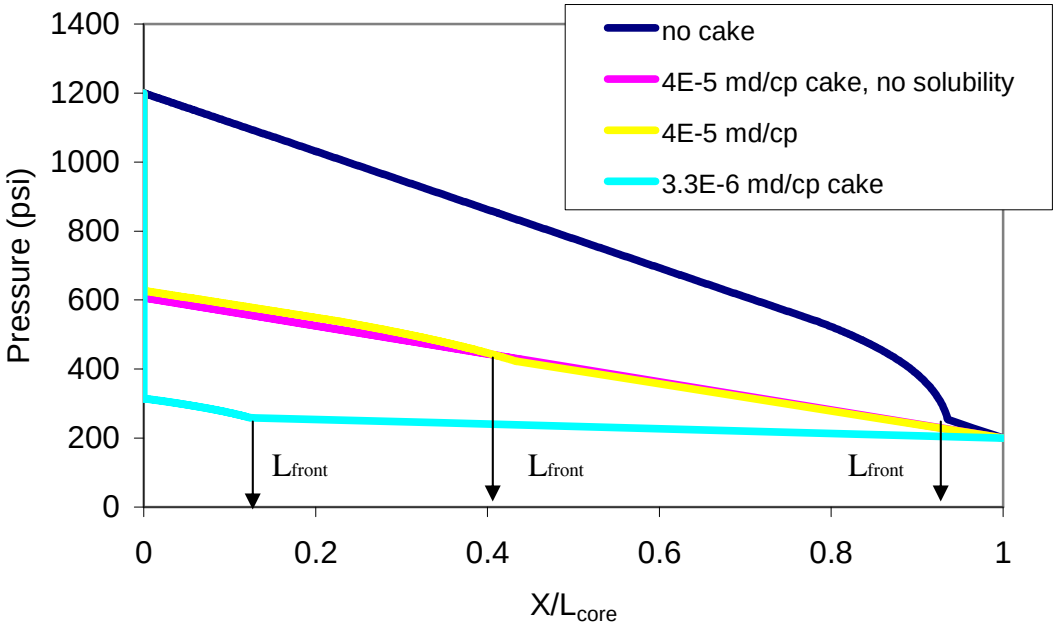

Figure 8.14. Pressures drop as a function of core distance at 30 minutes.

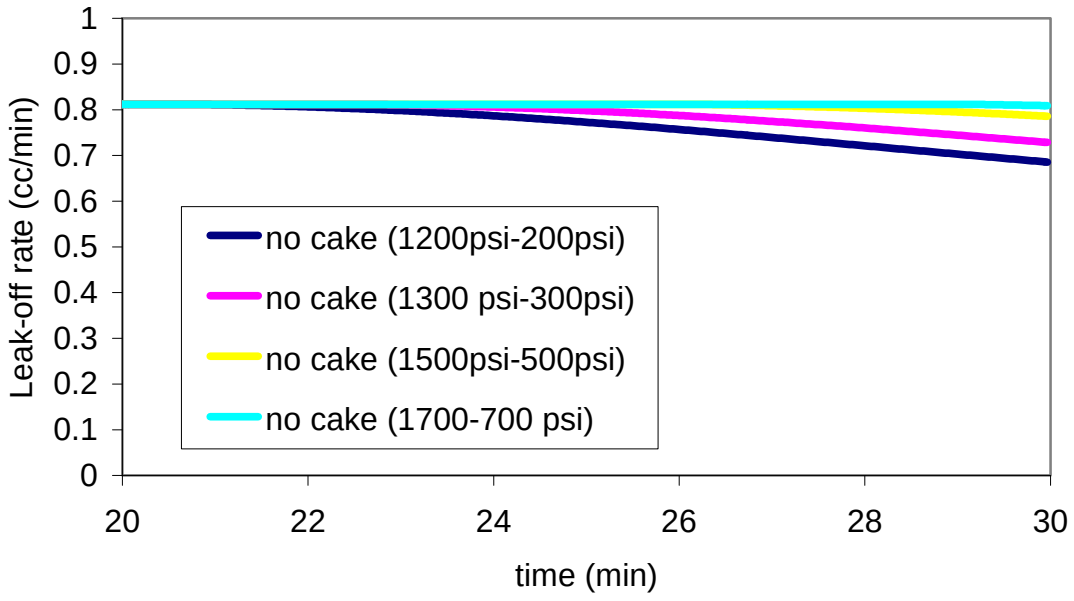

Figure 8.15. Filtration rate versus time and absolute pressure.

CHAPTER 9: IMPORTANT FACTORS IN ENERGIZED FRACTURE DESIGN - A SENSITIVITY STUDY

In this chapter, we will discuss the factors that are important in energized fracture design. We present a sensitivity study to identify important parameters so that optimally designed fractures may be pumped without field trails, saving time and money. In conducting this study we have used the model in Chapter 3, the fluid behavior in Chapter 4, and the productivity index model in Chapter 6. Since our discussion is based on these earlier chapters, it would be useful to review those chapters before reading on, especially Chapter 4 because it discusses fundamental differences between the phase behavior and rheology of the different types of energizing components.

Chapter 7 focused on modeling actual field data to optimize the design for a single field in South Texas. Chapter 7 was limited to the reservoir parameters that were already being used in the field and only one energizing component, CO_2. This chapter shows the sensitivity to a wider range of reservoir parameters and components, such as N_2 and methanol. The ideas presented in this chapter are applied to more general tight gas situations, compared to the one specific field and fluid type discussed in Chapter 7.

This chapter will answer the following questions: When should we use energized instead of traditional fluids (Section 9.2)? Which gas component works best, and when (Section 9.3)? How does leak-off and closure affect energized fracture performance (Section 9.4)? What quality (volume fraction of gas) works best (Section 9.5)? What permeability rocks are more suitable for energized fractures (Section 9.6)? What other factors are important (Section 9.7)? As each question is answered, we will give an explanation of how important each factor is to fracture performance.

9.1 Base Case Design

Table 9.1 shows the input values used for the base case simulation. Please notice that the table is split into two categories, pumping schedule inputs and reservoir inputs. Pumping schedule inputs include the parameters that are under the control of the fracturing engineer. The flowrate is 40 BPM for 19 total minutes of pumping. The proppant is added after 9.9 minutes of pad. The proppant concentration is ramped from 1 to 8 lb/gal. The first proppant stage (1 lb/gal) equals 4,000 lbs of total proppant. Stages with 2, 4, 6, and 8 lb/gal proppant each have an equal mass of proppant of 9,000 lbs each. This gives a total of 40,000 lb proppant. The inlet quality of the base design is held at a constant value of 70%. Both pad and proppant stages include the same inlet composition of gas. The viscosity of the base fluid (μ_o) is 150 cp. The base fluid refers to the liquid phase only. The overall viscosity is a function of the base viscosity, local gas quality, and temperature. Chapter 4's sections on rheology show how each fluid system is modeled. The wall-building leak-off coefficient is 0.0005 ft/min$^{1/2}$. This coefficient is only for the liquid phase and represents only the wall-building portion of the coefficient. Review Section 2.3 for definitions of the three types of leak-off coefficients. The gas leak-off is zero for the base design. The sensitivity to gas leak-off is discussed in Section 9.4.

The second section in Table 9.1 shows the reservoir inputs. We chose parameters representative of a tight gas reservoir. Most of the values in Table 9.1 are typical values required for all fracturing models. The exception is the petrophysical inputs, S_{wr} to P_c^o in Table 9.1. These inputs are needed to calculate the damage in the invaded zone, a feature that previous productivity index models do not include. Please review Section 6.3 for details.

The following sections represent the simulation results based on this design.

9.2 When To Use Energized Fluids Over Traditional Fluids? The Effect of Drawdown Pressure

The first question that arises with energized fluids is when to use them. As it turns out, the answer to this question always involves formation damage and fluid recovery. If only water-based fluids are used, the leak-off of the fracturing fluid will displace the gas in the invaded zone, leaving only a residual gas saturation. The water that invades the rock may cause clay swelling as well as gel damage that inhibits the flow of gas into the fracture. Under ideal circumstances, the damage is removed because the drawdown across the invaded zone recovers most of the liquid. Unfortunately, this is not always possible, especially in tight formations where a very high drawdown is needed to recover the liquid.

Figure 9.1 shows the base design's productivity index dependence on drawdown pressure. The figure shows the response for three different energized components and one non-energized scenario. The reason why the three energizing components give different answers is discussed in Section 9.3. Here let's focus our discussion on two of the curves in Figure 9.1, the non-energized curve and the CO_2 curve. In the non-energized case, the calculated J/J_o is near 1 for all drawdown pressures below 316 psi, which is P_c^o, a representative capillary pressure for the gas/liquid system at 0.01 md permeability. The values are near one in this range because no fluid is being recovered from the invaded zone, causing a zero relative permeability to gas. The infinite resistance around the fracture makes the fracture ineffective. In comparison, the CO_2 curve in Figure 9.1 shows that J/J_o is 4.79 at low drawdown pressure. The better performance is due to the ability of the CO_2 present in the invaded zone to create a higher than residual gas phase saturation. The damage around the invaded zone is minimal.

When the drawdown is larger than 316 psi the recovery of the fluid is increased and both the CO_2 and non-energized cases perform better. In the non-energized case, the J/J_o increases very rapidly and then plateaus at a value of 6.2. The CO_2 case also has increased performance but with a smaller percentage, also reaching a plateau at 6.2. The invaded zone is not fully stimulated by gas in the energized case because additional fluid is recovered when the drawdown is increased.

Figure 9.2 shows the same data as Figure 9.1 but for 0.1 md permeability. The exact same trends are observed for 0.1 md as 0.01 md but the absolute values are different. The J/J_o values are lower for the higher permeability. The same fracture will be less effective in a higher permeability formation because the flow resistance between the formation and the fracture is not as high. Also, the level of drawdown needed with 0.1 md is less because the capillary forces are lower in a high permeability rock. The P_c^o at 0.1 md is 100 psi. This is consistent with the idea that the capillary pressure is inversely proportional to the square root of permeability in sandstones[1] (see Equation 6.21).

Figures 9.1 and 9.2 show that energized fluids outperform non-energized fluids at low drawdown because they stimulate the formation by means other than fluid recovery. At high drawdown pressure, the differences are negligible because all damage is removed regardless of the composition in the invaded zone. The use of energized fluids is not justified in this case. The level where drawdown pressures are considered "low" or "high" is a function of the capillary pressure which is in turn a function of the permeability. Figure 9.3 shows the minimum drawdown (P_c^o) needed versus permeability. Figures 9.1 and 9.2 show that J/J_o reaches a plateau at roughly 1.5 times the minimum drawdown. We recommend that drawdown pressures exceed this limit to make sure that recovery of traditional fluids is possible. If drawdown pressure cannot exceed this limit, energized fracturing is recommended.

9.3 Choosing the Best Energizing Fluid

Once it is determined that energizing the fluid is the way to go, it is necessary to evaluate which energizing component works best. In this section, we evaluate three different systems used in energized fluids: CO_2, N_2, and CO_2 with 20% methanol in the liquid phase. Please note that the 20% methanol is by mass on a CO_2 free basis, meaning the inlet liquid phase is 80% H_2O and 20% MeOH and then CO_2 is added on top of that.

It is not a coincidence that Chapter 4 discusses systems of CO_2/H_2O, N_2/H_2O, and CO_2/H_2O/MeOH so that the behavior can be incorporated into the fracturing model and the results are shown in this chapter. We realize that other components are possible but they cannot all be evaluated in this study. The EFRAC model is deigned to evaluate other components in the future.

We have already determined that the energized fluids should be used in low permeability rocks when drawdown pressures are low. Therefore, we focus our analyses on these cases. Figure 9.1 shows that for CO_2 $J/J_o = 4.79$, for N_2 $J/J_o = 1.0$ and CO_2 with 20% methanol in the liquid phase J/Jo = 5.08 at low drawdown. This means that CO_2 and CO_2 with methanol perform adequately but N_2 does not. This is because the solubility of CO_2 in H_2O is larger than N_2. With zero gas phase leak-off, the only way for the gas component to go into the invaded zone is by solubility in the liquid phase. The solubility of N_2 in H_2O is nearly zero; therefore no gas comes out of solution when the pressure drops. The invaded zone has only residual gas saturation and, therefore, remains fully damaged. CO_2 with methanol outperforms plain CO_2 because the methanol increases the solubility of CO_2. However, the incremental benefit of adding methanol is marginal because CO_2 alone helps stimulate the invaded zone to a large degree.

At high drawdown, notice that the three different energizing components give different productivity index results. This is because each component has different rheological properties that change the fracture dimensions slightly. Figure 9.4 shows the final proppant concentrations for each of the three energizing components and the non-energized case. It appears that the CO_2 and non-energized cases have the right combination of conductivity and length to have the highest J/J_o, N_2 is too short and does not have enough length, and CO_2 with methanol does not have the optimum conductivity (lowest F_{cd}). However, at high drawdown, non-energized fluids are recommended because of experience with them and the higher cost of energizing the fluid.

From the above observations, we can conclude that CO_2 outperforms N_2 in all cases, or in general, a soluble gaseous component is better than an insoluble component. There are exceptions that may make N_2 comparable to CO_2 involving leak-off and closure issues. This is discussed in the next section.

9.4 Importance of Leak-off and Closure

The last two sections assume that the leak-off of the gas phase is zero. It also assumes that the fracture is forced closed by flowing back the fluid immediately after pumping the fracture. In other words, the gas phase does not reach the invaded zone during the propagation of the fracture, nor does it during closure of the fracture. The latter is because the fluids present in the fracture are recovered during the forced closure of the fracture. This is a conservative view of the situation because it means that the gas component can only reach the invaded zone by being soluble in the liquid phase. We discuss the effectives of gas components when these assumptions are changed in this section.

Figure 9.5 shows the dependence of J/J_o on the base design using CO_2 for three different leak-off and closure options. Notice that the "Forced Closure" curve in the figure is the same as the "CO_2" curve in Figure 9.1. The results are plotted with drawdown pressure on the x-axis to show whether the scenario predicts a fully stimulated invaded zone or if more recovery is possible. The "Un-Forced Closure" line in Figure 9.5 was calculated assuming that the fluid present at the end of pumping is eventually leaked-off into the formation during a long shut-in period. As the fracture closes on the proppant, the gas phase will have to leak into the formation because it will have nowhere else to go. If this occurs, the model predicts that there will be enough gas component to stimulate the invaded zone; shown by the "Un-Forced Closure" having no dependence on drawdown pressure.

The "Non Zero Gas Phase Leak-off" curve in Figure 9.5 assumes that the leak-off coefficient of the gas phase is not zero. The overall coefficients are 0.00027 $ft/min^{1/2}$ for the liquid phase and 0.00025 $ft/min^{1/2}$ for the gas phase. The coefficients are inferred from the work of Harris[2,3]. This allows the gas phase, which is rich in the gas component, to leak-off into the formation during propagation of the fracture. Again, this permits enough gas component to fully stimulate the invaded zone. Figure 9.6 shows the quality

of gas in the fracture at the final pumping time when zero and non-zero gas leak-off coefficients are used. The gas fraction goes up dramatically down the length of the fracture with zero gas phase leak-off because the composition changes. The composition does not change as much with non-zero leak-off of gas. The change in quality changes the rheology of the fluid and therefore the fracture dimensions. However, the effect on J/J_o is mainly due to the increased stimulation in the invaded zone.

Figure 9.5 doesn't show a significant decrease in productivity when CO_2 is used with any of the leak-off and closure assumptions. This is not true with N_2. Figure 9.7 shows the same scenario as Figure 9.5 but now with N_2 as the gas energizer. The "Forced Closure" curve in Figure 9.7 is equivalent to the "N_2" curve in Figure 9.1. The figure shows that nitrogen is ineffective with this set of leak-off and closure assumptions. However, if the gas leaks-off either during the creation of the fracture or during closure, nitrogen can be used as an effective energized fluid.

The key to energizing the fluid is to make sure that the gas component is present in the invaded zone. We have shown three different mechanisms in which this can happen. They are: 1) the liquid phase that invades the formation is saturated with a significant percentage of the gas component. When pressure is reduced for flowback, the gas component will come out of solution. 2) The fracture is allowed to close naturally during shut-in. This process forces the gas phase to bleed into the formation as the fracture closes. The gas component will be present in the invaded zone. 3) The gas phase leaks into the invaded zone during fracture creation. If any of these mechanisms occur, there will almost certainly be enough gas in the invaded zone to reduce all significant damage. There is evidence that CO_2 can leak-off by all three mechanisms, making it the ideal choice for energized systems. An insoluble gas such as nitrogen needs to have mechanism 2 or 3 to occur to be effective.

There needs to be more research done on multi-phase fluid leak-off to determine whether the gas phase leaks-off during fracturing. Harris[2,3] concludes that there is significant leak-off of the gas phase. Chapter 8 concludes that it is unlikely that the gas

phase leaks into the formation in tight rocks. Until this question can be resolved, questions about how to most effectively use energized fluids will remain open.

9.5 What is the Effect of Gas Quality?

In Sections 9.2 and 9.3 we answered the important questions:

(a) When should we use energized fluids?

(b) What gas should be used to energize fluids?

This section will answer the question: (c) How much gas should we use?

Figure 9.8 shows the productivity index ratio dependence on CO_2 quality. The three different leak-off and closure options are also shown. The productivity index ratio is nearly constant for quality ranging from 10 to 70%. Under 10% it drops to 1.0 because the non-energized case will create a fully damaged zone around the fracture. As long as the fluid is above the solubility limit at fracturing temperature and pressure, the liquid that leaks-off should be saturated with CO_2 and minimal damage will occur. The difference in J/J_o values between quality ranging from 10 to 70% is due to the levels of damage around the fracture face. The J/J_o "Forced Closure" curve in Figure 9.8 steadily increases with quality because less damage is calculated, because less water is pumped. Each quality results in different fracture dimensions but the effect that the fracture dimensions has on productivity is negligible compared to the effect of damage.

Figure 9.9 shows the effect of quality for the three different energized systems. Figures 9.10 - 9.12 show the proppant concentration at the end of pumping for all three systems and for five different qualities. The "CO_2" curve in Figure 9.9 shows the same data as Figure 9.8. The "N_2" curve in Figure 9.9 shows that all N_2 simulations provided a J/J_o of 1. This is because of the same reasoning as in the previous sections; N_2 is not soluble enough to energize the invaded zone. The fracture dimensions do not matter if the fracture is surrounded by a fully damaged (liquid-saturated) zone. The "CO_2 with 20% methanol in the liquid" curve shows some interesting results with 10% quality. The

quality is defined by the volume of CO_2 and liquid phase pumped at the surface. The quality is expected to change as fluids travel down the wellbore into the reservoir. The more soluble the gas is in the liquid, the more it will change. In this case, 10% gas is not enough gas to fully saturate the liquid with CO_2. When the pressure is dropped, it does not necessarily means that a release of gas will occur. That is why the 10% value is still at $J/J_o = 1.0$. This problem does not occur with the 20% simulation because there is enough gas.

Figure 9.9 shows an opposite trend in quality for CO_2 and CO_2 with methanol. The productivity index increases for CO_2 and decreases for CO_2 with methanol as quality increases. This is an example of how damage around the fracture face, fracture length, and fracture conductivity all play an important role in fracture performance. Some damage is present in the invaded zone of the CO_2 case, but not the CO_2 with methanol case. When quality is increased in the CO_2 case, less water is used, and therefore, there is less water leak-off. The smaller amount of water reduces the damage and J/J_o is increased. On the other hand, the damaged zone is fully stimulated for all qualities for CO_2 with methanol. In this case, the fracture performance is not based on damage but on the optimum fracture dimensions. Figure 9.12 shows the proppant concentration at the end of pumping for CO_2 with methanol. The figure shows that longer but thinner fractures result from lower quality (20 and 30%) and shorter but more conductive fractures result from high quality (60 and 70%) foam. For most tight gas sands, including this case, longer fractures are favored because they create more contact area with the reservoir. This is why the lower quality fluids are preferred.

To conclude, 30 to 50% quality energized fluids are optimum because they allow enough gas to saturate the liquid while giving the best fracture dimensions for tight gas sands. The higher the solubility of the gas, the higher the quality needed to make sure the liquid is fully saturated. Higher quality (up to 70%) may be necessary if shorter and wider fractures are preferred.

9.6 What Permeability Should Energized Fluids Be Applied?

Until now our analysis was limited to 0.01 md permeability reservoirs. This section discusses changes to the base design when the permeability is changed. Figure 9.3 shows the minimum and recommended drawdown pressure needed for any permeability. Only small drawdown pressures are needed to recover the fluids at high permeability. Damage is not an issue in these cases. It is important to use energized fluids when high drawdowns are needed to recover the fluid. The following simulated results demonstrate this idea.

Figure 9.13 shows the calculated J/J_o values for four permeabilities: 1.0, 0.1, 0.01, and 0.001 md. The same trend occurs at all permeabilities. CO_2 with methanol outperforms CO_2 which outperforms N_2. This is for the same solubility reasons discussed in Section 9.3. The figure shows that the lower permeabilities give the highest J/J_o. However, we must point out that J_o is proportional to the permeability, see Equation 9.1.

$$J_o = \frac{2\pi kh}{\mu \ln(r_e / r_w)} \tag{9.1}$$

Figure 9.14 shows a corrected version of Figure 9.13 but now J is made dimensional by multiplying it by J_o. Figure 9.14 shows that the higher permeability formations give higher flowrates, even after fracturing. This shows that since the highest permeability layers have the highest flowrates, they are more important to stimulate. It can be concluded that energized fluids should be applied to high permeability formations only when traditional fluids cannot be recovered by flowback. For example, if depletion has limited the drawdown to 500 psi or less. Figure 9.3 shows that 500 psi is enough for 0.01 md or more. Traditional fluids are recommended in formations with permeability greater than 0.01 md but energized fluids will have the highest value when they are applied to formations that are under 0.01 md.

Figure 9.15 shows the J/J_o dependence on permeability with un-forced closure. This is included in our discussion to show that nitrogen can be almost as effective as CO_2. Also, Figure 9.15 shows how much productivity index can change with the different components. At 0.001 md, the figure shows a large difference in productivity for each

component. The differences seen at 0.001 md is because the propped fracture length is highest with CO_2 with methanol and lowest with N_2. Figures 9.16-9.18 show the proppant concentration at the end of pumping for every situation shown in Figure 9.15. The figures show how far the proppant is placed into the fracture. More contact area is always beneficial at such low permeability so the longest fracture is optimum.

9.7 Other Factors Controlling Energized Fracture Performance

9.7.1 WATER SENSITIVITY

In the previous sections, the formation is assumed to not have any water sensitivity. The petrophysics of the formation is modeled by simple relative permeability and capillary pressure models. The damage is created by a presence of high water saturation. Some rocks that contain clays and other fines can show sensitivity to water. Interactions of swelling or migrating clays with water will result in large reductions in permeability when water is introduced into the formation[4]. An example of a water sensitive formation is the Muddy formation in Wyoming.

A modeling parameter that can simulate water sensitivity is the effective permeability in the invaded zone; the lower the effective permeability, the higher the water sensitivity. Figure 9.19 shows the dependence of productivity index on the effective permeability in the invaded zone, k_d/k. This figure shows that effective permeabilities have to be orders of magnitude lower than the formation permeability to cause damage just by being exposed to water. As result, low and moderate water sensitive formations should be able to either recover water or be stimulated by a gas component. Only highly water sensitive formations should be affected.

9.7.2 INLET TEMPERATURE, BASE VISCOSITY, FLOWRATE

The effect of inlet temperature, base viscosity, and flowrate is shown in Section 7.3.2.3-7.3.2.5 of Chapter 7. The findings were not repeated for this chapter's base case but the conclusions are the same. The base viscosity and flowrate were found to have the same effect on energized fractures as traditional fractures. The base viscosity and flowrate should be high enough to open the fracture and limit proppant settling, but not too high, otherwise vertical height growth and fracture widening will limit fracture length. Inlet temperature has an effect on fracture growth because low temperature decreases the viscosity and impacts expansion of the gas phase. Pumping volumes of energized fluids should be corrected for gas expansion.

Figure 9.20 shows temperature profiles at the end of pumping for the base design and the three different energizing components. The figure shows where the temperature reaches the reservoir temperature in each case. Figure 9.20 proves that the isothermal assumption used in all current fracture models is invalid because each case gives very different profiles. The temperature profile is very much a function of the width of the fracture. High width fractures protect the fluid from the hot reservoir. Cool fluid is transported far into the fracture (N_2 case in Figure 9.20). Thin fractures with a lot of contact area expose the fluid to the heat more and the fluid heats up very quickly. The temperature in the fracture should be viewed on a case-by-case method.

Injection of a cold fluid can lower the minimum horizontal stress by causing the rock to contract[5]. This issue is important in fractured injection wells[5]. It has yet to be determined whether thermal stresses have an effect on hydraulic fracturing performance. In preceding discussions on hydraulic fracturing, the issue of thermoelastic stresses has been ignored because the time scale is so short. The time scale for fractured injectors is months and years, compared to minutes for a hydraulic fracture. With energized fluids, the cooler fluid injection temperatures could cause a thermoelastic effect that cannot be ignored. More study is needed to determine the effect of injection temperature during hydraulic fracturing.

9.7.3 STRESS AND RESERVOIR PRESSURE

The phase behavior of energized fluids is dependant on the absolute pressure that the components are exposed to. Therefore, stress and reservoir pressure can be important parameters affecting performance. Tight gas formations can range from 3000 to 8000 psi in minimum horizontal stress and can range from 5000 to a couple hundred psi in reservoir pressure, depending on the level of depletion. The example cases shown in this chapter have a minimum horizontal stress of 5000 psi and a reservoir pressure of 3000 psi. The absolute values of the two parameters determine how much the gas will expand after fracturing. Two thousand psi difference will cause gas phase expansion so that only a small amount of CO_2 is needed to cause high gas saturation. When the reservoir pressure is decreased, more CO_2 comes out of solution and the gas expands to a lower density. This phenomenon explains why less CO_2 is needed to stimulate the invaded zone when the reservoir is highly depleted. Section 7.3.3 covers this in detail.

The in-situ stress has little effect on the productivity of energized fractures. From 3000 to 8000 psi the CO_2 phase is very liquid like in density and, therefore, does not have a large effect on fracture performance. Changes in physical properties are more dramatic with pressure when they are below 2000 psi.

When designing energized fractures, it is recommended that the density and solubility at the flowing bottom-hole pressure and the minimum horizontal stress be calculated. The difference between the two provides an estimate of how much gas will be released in the damaged zone during flowback.

9.8 Conclusions

Based on the simulations conducted and presented in this chapter, the following conclusions can be made.

1. Damage around the fracture face induced by the loss of water-based fracturing fluids can be removed during flowback if the drawdown pressure exceeds the capillary forces holding the liquid in place.

2. Energized fluids are effective when the gas component leaks-off into the invaded zone. This results in a high gas saturation in the invaded zone that will not restrain the flowback of gas into the fracture.
3. Common energizing components are CO_2 and N_2. Both have different phase density and solubility in water, therefore, should not be viewed as having the same benefit. Simulations show that CO_2 outperforms N_2 in most cases because it has higher solubility at fracturing temperatures and pressures.
4. Fluids with higher solubility in aqueous solutions will increase the fluid's ability to reduce damage in the invaded zone.
5. Adding a component such as methanol to an energized system increases the solubility of CO_2 in the liquid phase and alleviates clay swelling in some sandstones.
6. The gas component can leak into the invaded zone by three mechanisms, at least one of the mechanisms need to occur for the energized fracture to be effective. They are: 1) the liquid phase that invades the formation has a significant mole fraction of the gas dissolved in it. When pressure is reduced for flowback, the gas component comes out of solution. 2) The fracture is allowed to close naturally during shut-in. This process forces the gas phase to bleed into the formation as the fracture closes. The gas component will be present in the invaded zone. 3) The gas phase leaks into the invaded zone during fracture creation. If this happens, there will almost certainly be enough gas in the invaded zone to reduce damage. More leak-off data is needed to determine which mechanism is dominant.
7. 30 to 50% quality energized fluids are optimum because they allow enough gas to saturate the liquid to maximize gas flowback and they yield long fractures. The higher the solubility of the gas, the higher the foam quality needed to make sure the liquid is fully saturated.
8. Higher quality (up to 70%) may be necessary if shorter and wider fractures are preferred.

9. Energized fluids should be applied to rocks when the drawdown pressure is insufficient to remove the liquid. This corresponds to a drawdown pressure of ~200 psi for 0.1 md formations, ~500 psi for 0.01 md, and ~1500 psi for 0.001 md.

Nomenclature

A	Drainage Area
b_{cap}	Brooks-Corey model for capillary pressure exponent
C_w	Wall-building leak-off coefficient
D_{prop}	Proppant diameter
E	Young's modulus
F_{cd}	Dimensionless fracture conductivity
h	Height of fracture
J	Productivity index
J_o	Productivity index of a un-fractured, undamaged reservoir in a circular drainage area
k	Reservoir permeability
k_d	Invaded zone permeability
k_f	Fracture permeability
k_{rgo}	Endpoint relative permeability of gas
$n_{rel.perm}$	Gas relative permeability exponent
P_c^o	Endpoint capillary pressure, Brook-Corey
P_R	Reservoir pressure
Q_{inj}	Injection flowrate
r_e	Outer boundary radius
r_w	Wellbore radius
S_{wr}	Residual liquid phase saturation
S_{gr}	Residual gas phase saturation
t_p	Pumping time
T	Temperature
T_{inj}	Injected temperature
T_R	Reservoir temperature
Greek Symbols	
ΔP	Drawdown pressure
ϕ	Porosity
Γ	Quality
Γ_{inj}	Injected quality
μ	Viscosity
μ_o	Base viscosity
ν	Poisson Ratio
σ	Minimum horizontal stress

References

1. Leverett, M.C. 1940. Capillary Behavior in Porous Solids. *Petroleum Technology*. August: 152-169.
2. Harris, P.C. 1985. Dynamic Fluid-Loss Characteristics of Nitrogen Foam Fracturing Fluids. *Journal of Petroleum Technology*, October: 1847-1852.
3. Harris, P.C. 1987. Dynamic Fluid-Loss Characteristics of CO2-Foam Fracturing Fluids. *SPE Production Engineering*, May: 89-94.
4. Malone, M.R. 2001. Fracturing with Crosslinked Methanol in Water-Sensitive Formations. Paper SPE 70009 presented at the SPE Permian Basin Oil and Gas Recovery Conference, Midland, Texas, 15-16 May.

5. Perkins, T.K, and Gonzalez, J.A. 1985. The Effect of Thermoelastic Stresses on Injection Well Fracturing. *SPE Journal*, February: 78-88. SPE 11332.

Table 9.1. Input parameters for sensitivity study base case (Chapter 9).

Pumping Schedule Information		
Q_{inj}	40	BPM
t_p	19	min
Γ_{inj}	0.7	
μ_o	150	cp
T_{inj}	75	F
D_{prop}	0.027	in
C_w*	0.0005	$ft/min^{1/2}$
Reservoir Inputs		
A	40	Acre
r_w	3	in
E	3.E+06	psi
ν	0.25	
T_R	250	F
h	200	ft
k	0.01	md
ϕ	0.15	
σ	5000	psi
P_R	3000	psi
S_{wr}	0.2	
S_{gr}	0.2	
k_{rgo}	0.5	
$n_{rel.perm}$	3	
b_{cap}	0.5	
P_c^o**	316.23	psi
k_f	10	Darcy

*Coefficient is only for liquid phase.
**P_c^o changes with permeability proportional to $k^{-1/2}$

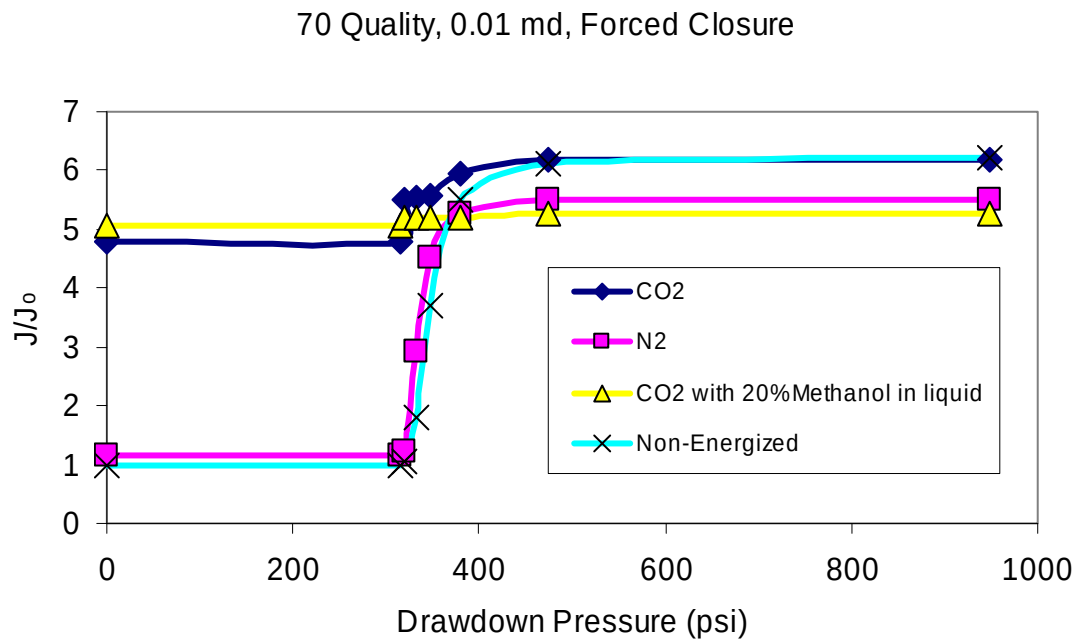

Figure 9.1. Productivity index dependence on drawdown pressure and energizing component. 70 Quality, k = 0.01 md, and Forced closure.

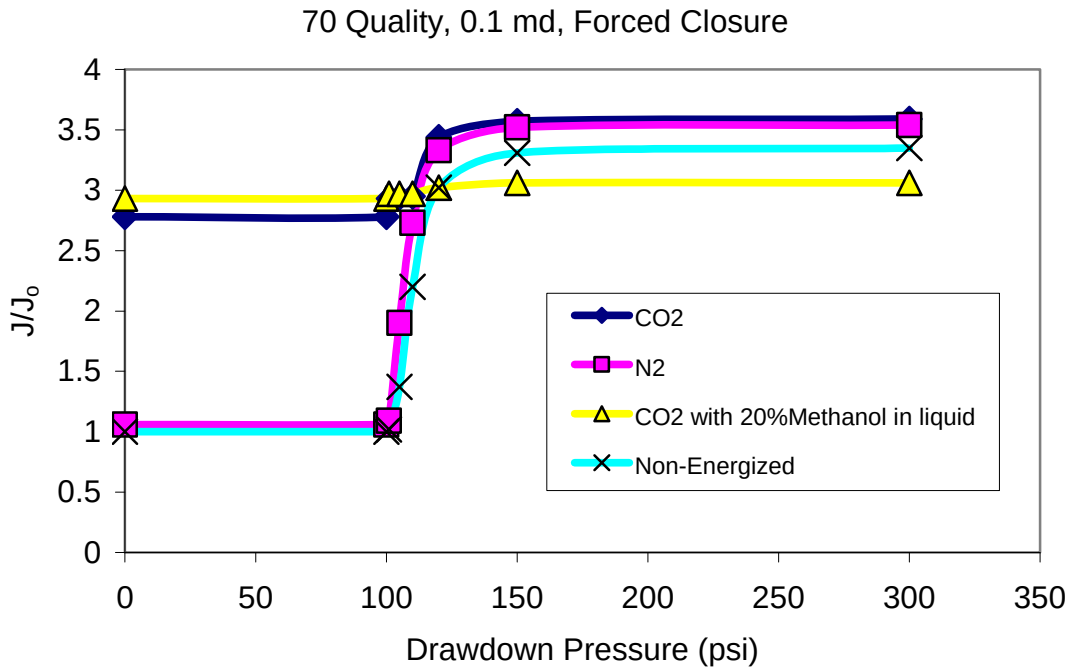

Figure 9.2. Productivity index dependence on drawdown pressure and energizing component. 70 Quality, k = 0.1 md, and Forced closure.

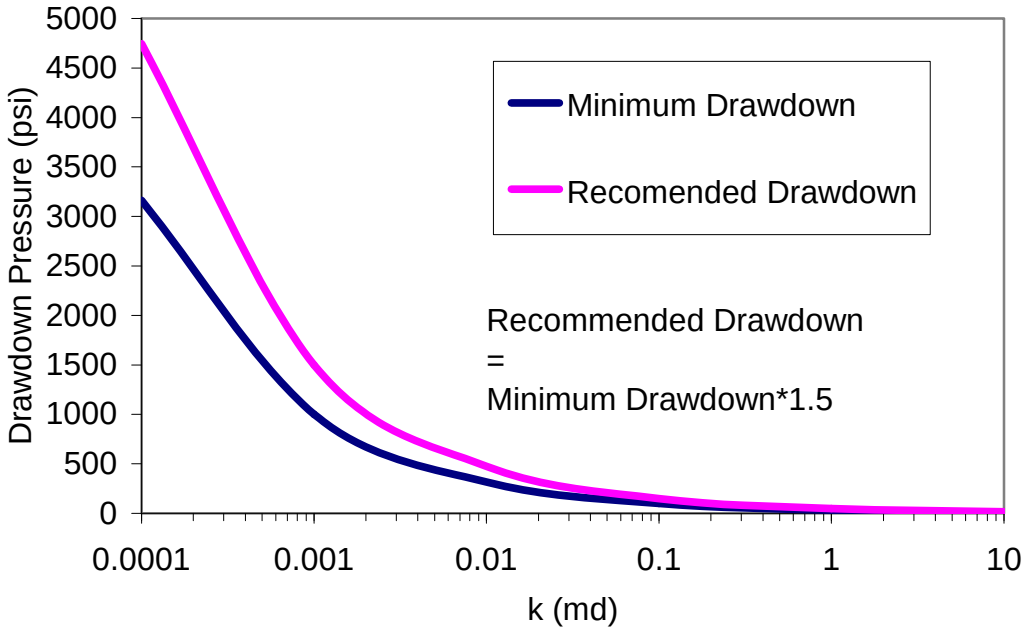

Figure 9.3. Drawdown necessary to remove damage in invaded zone. If recommended drawdown cannot be achieved, then energizing the fluid may be nessesary.

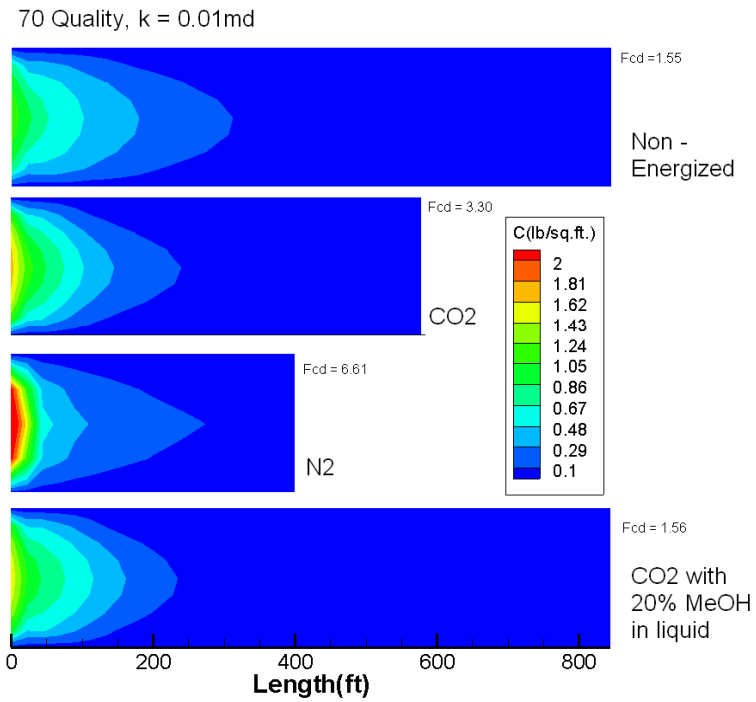

Figure 9.4. Proppant concentration at end of pumping for each energizing component. 70 Quality, k = 0.01 md.

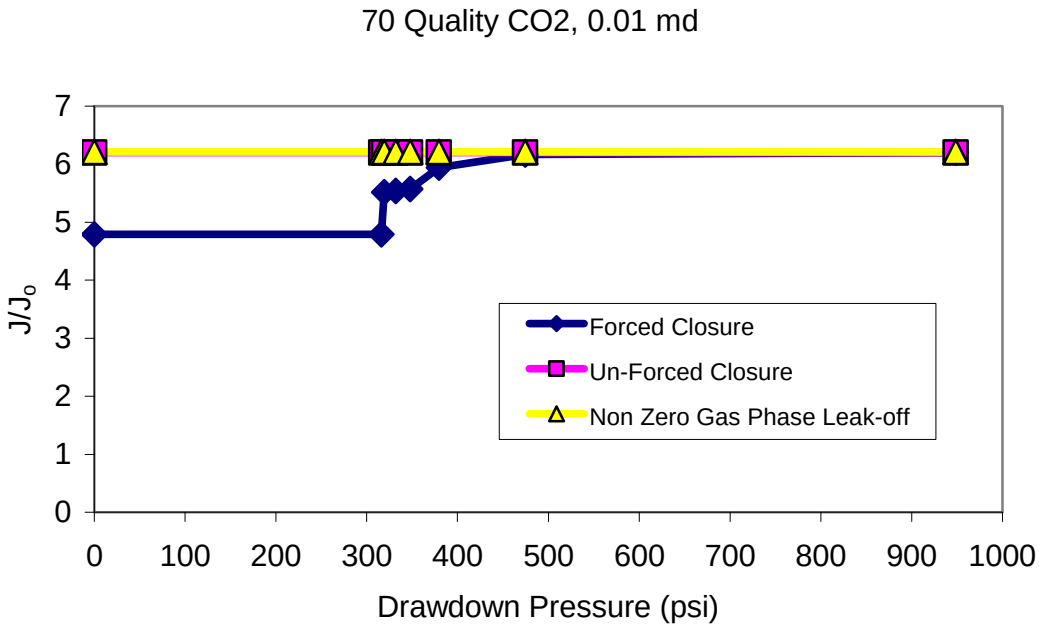

Figure 9.5. Productivity index dependence on drawdown pressure and leak-off assumption. 70 Quality, CO_2, k = 0.01 md.

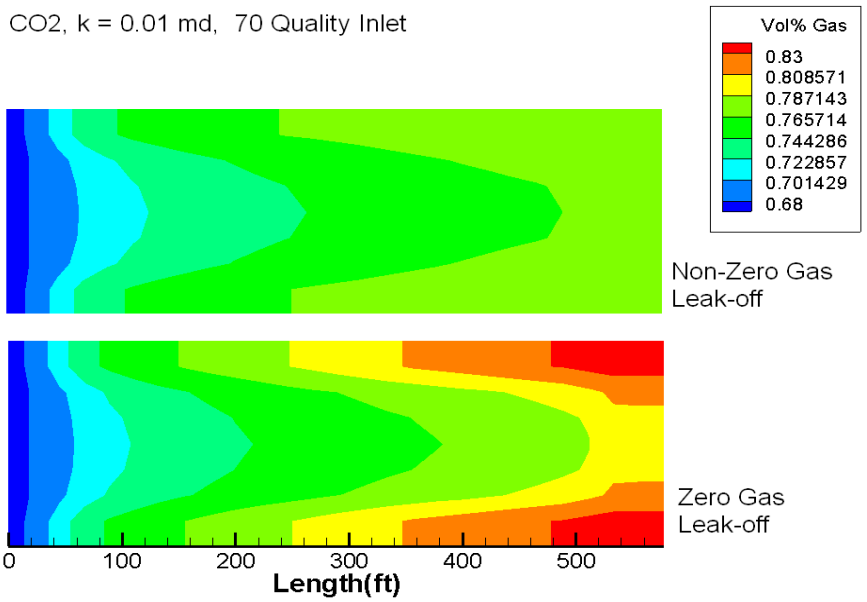

Figure 9.6. Quality of fluid at end of pumping for zero gas leak-off and non-zero gas leak-off. 70 Quality, CO_2, k = 0.01 md.

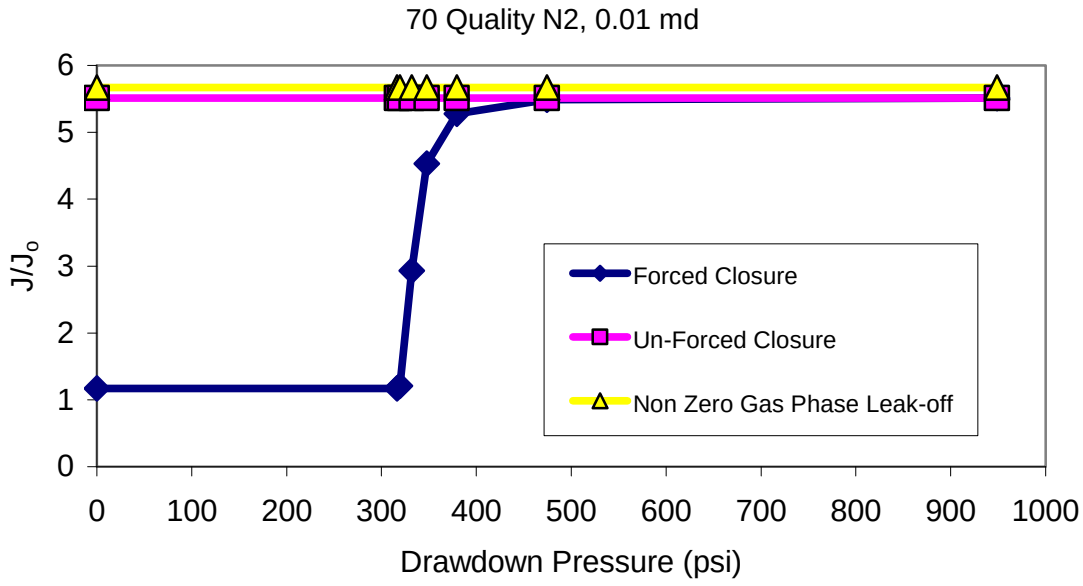

Figure 9.7. Productivity index dependence on drawdown pressure and leak-off assumption. 70 Quality, N_2, k = 0.01 md.

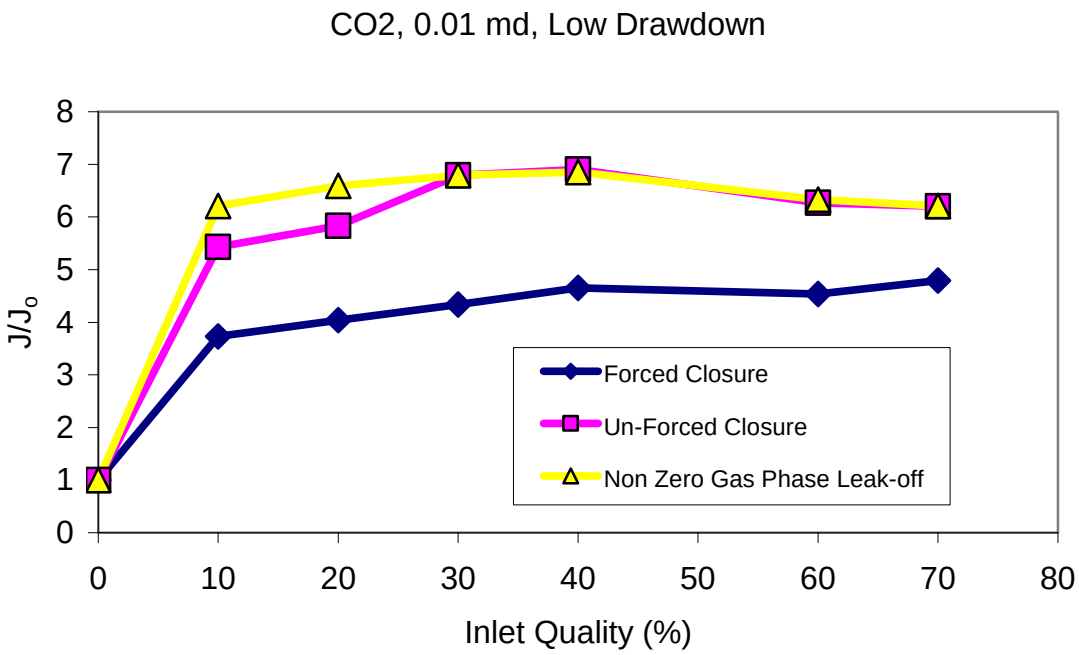

Figure 9.8. Productivity index dependence on inlet quality and leak-off assumption. CO_2, k = 0.01 md, Low Drawdown.

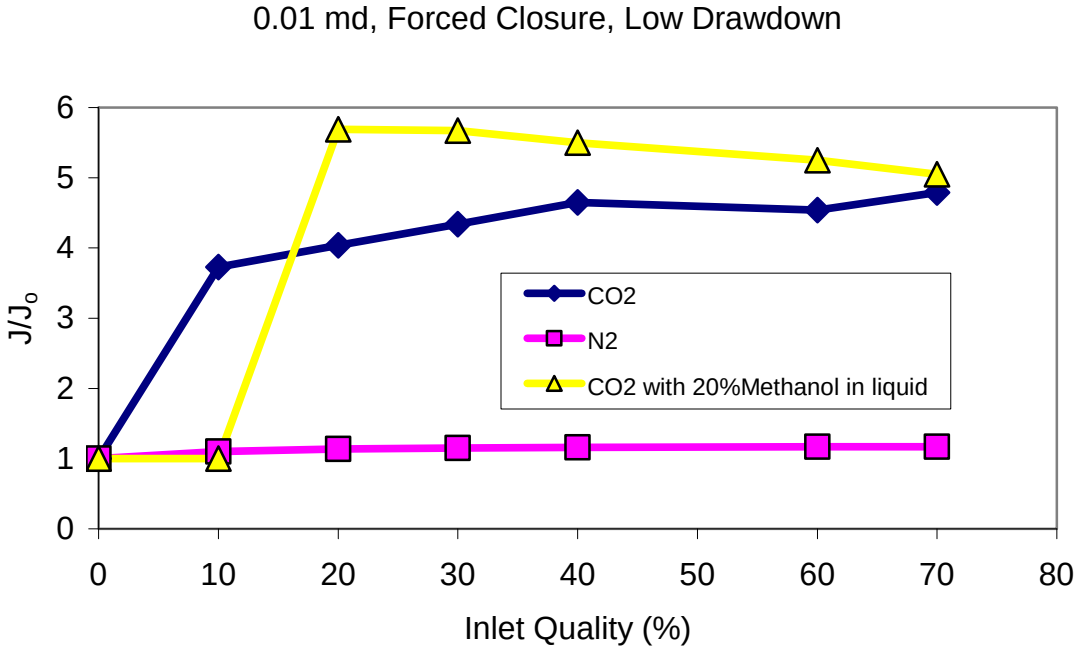

Figure 9.9. Productivity index dependence on inlet quality and energizing component. Forced Closure, k = 0.01 md, Low Drawdown.

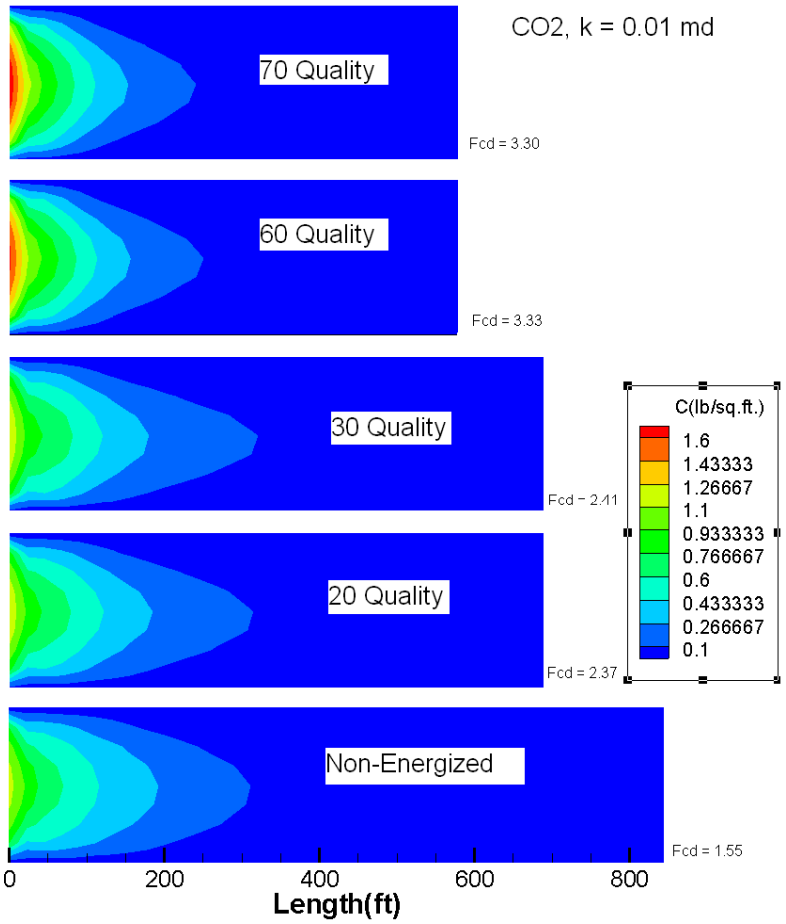

Figure 9.10. Proppant concentration at end of pumping for range of inlet quality. CO_2, k = 0.01 md.

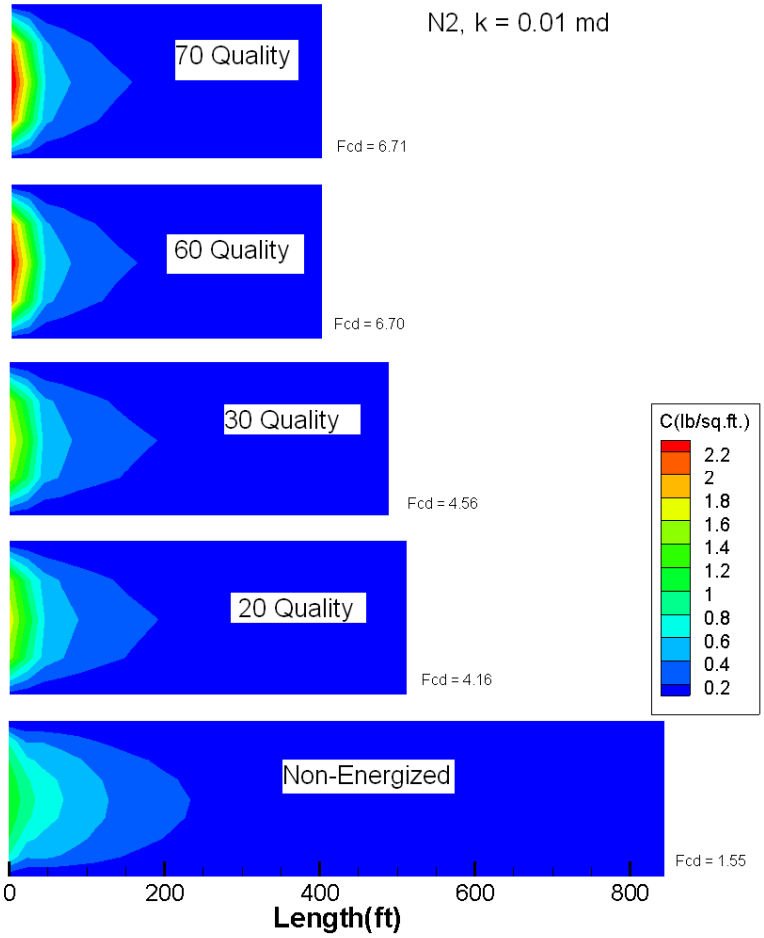

Figure 9.11. Proppant concentration at end of pumping for range of inlet quality. N_2, k = 0.01 md.

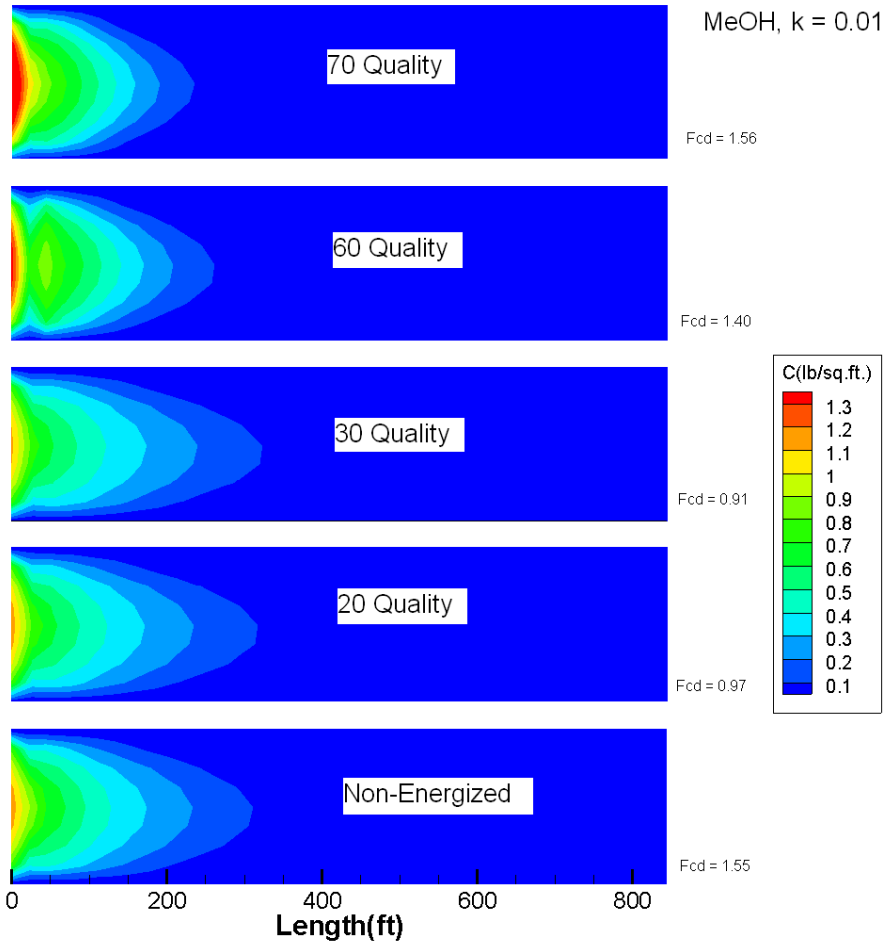

Figure 9.12. Proppant concentration at end of pumping for range of inlet quality. CO_2 with 20% methanol in liquid phase, k = 0.01 md.

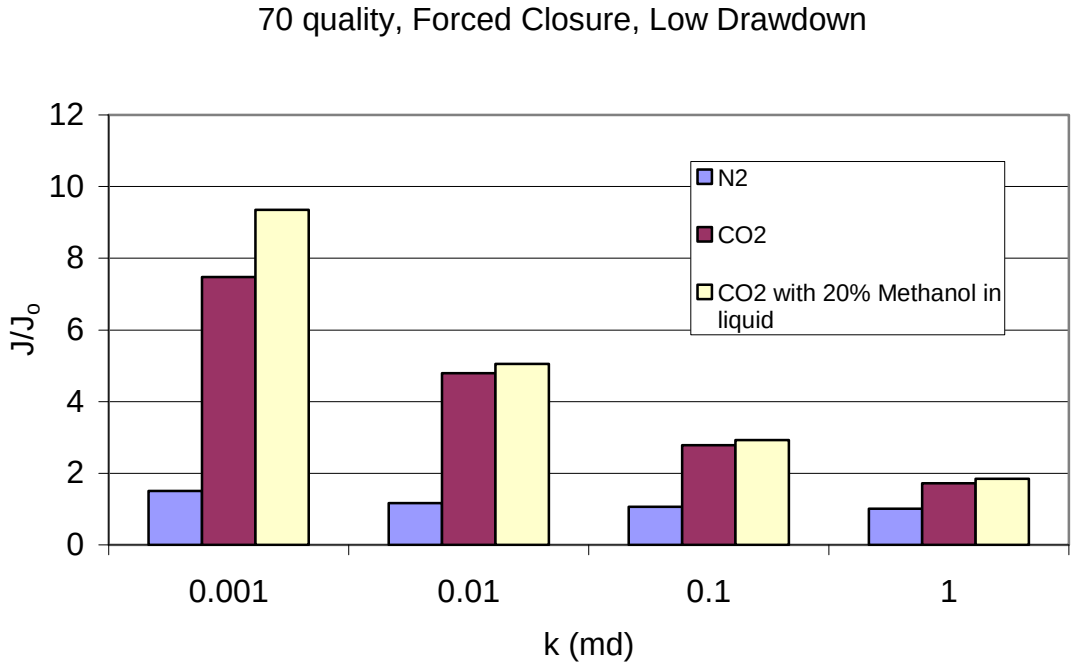

Figure 9.13. Productivity index dependence on permeability and energizing component. Forced closure, 70 quality, low drawdown.

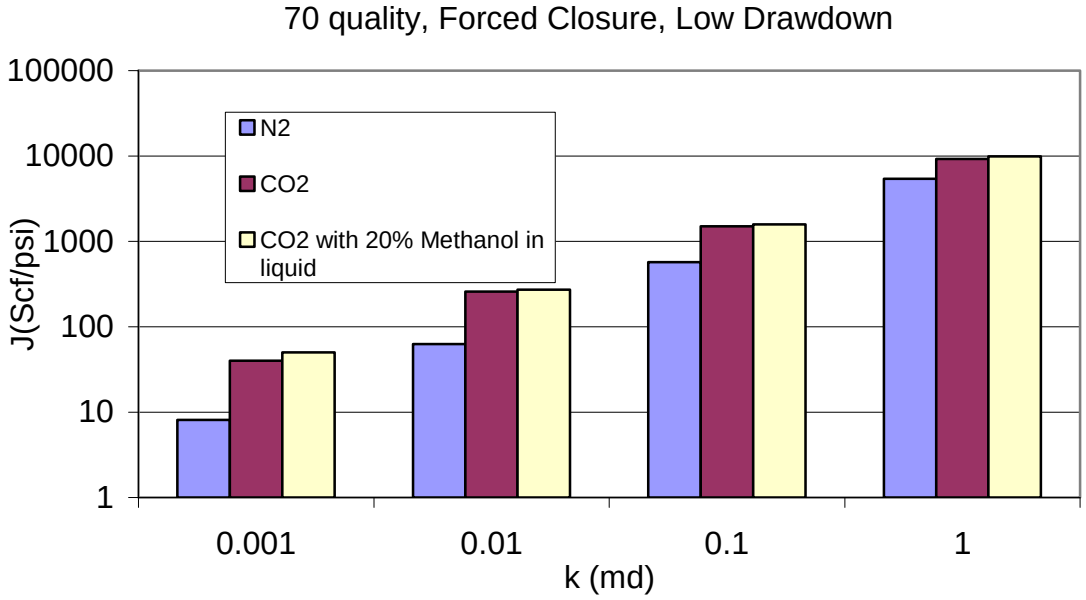

Figure 9.14. Dimensional productivity index dependence on permeability and energizing component. Forced closure, 70 quality, low drawdown.

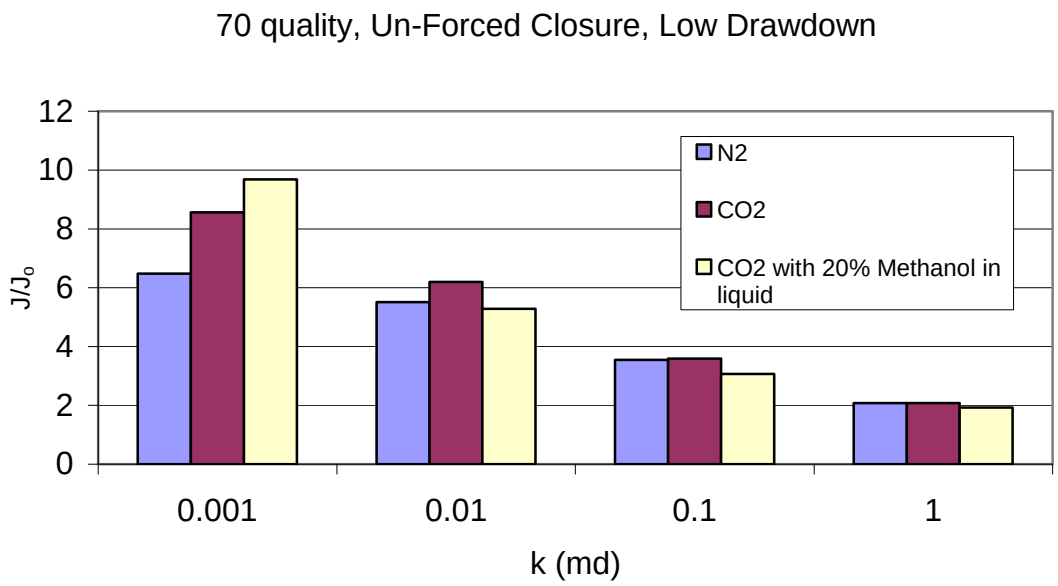

Figure 9.15. Productivity index dependence on permeability and energizing component. Un-forced closure, 70 quality, low drawdown.

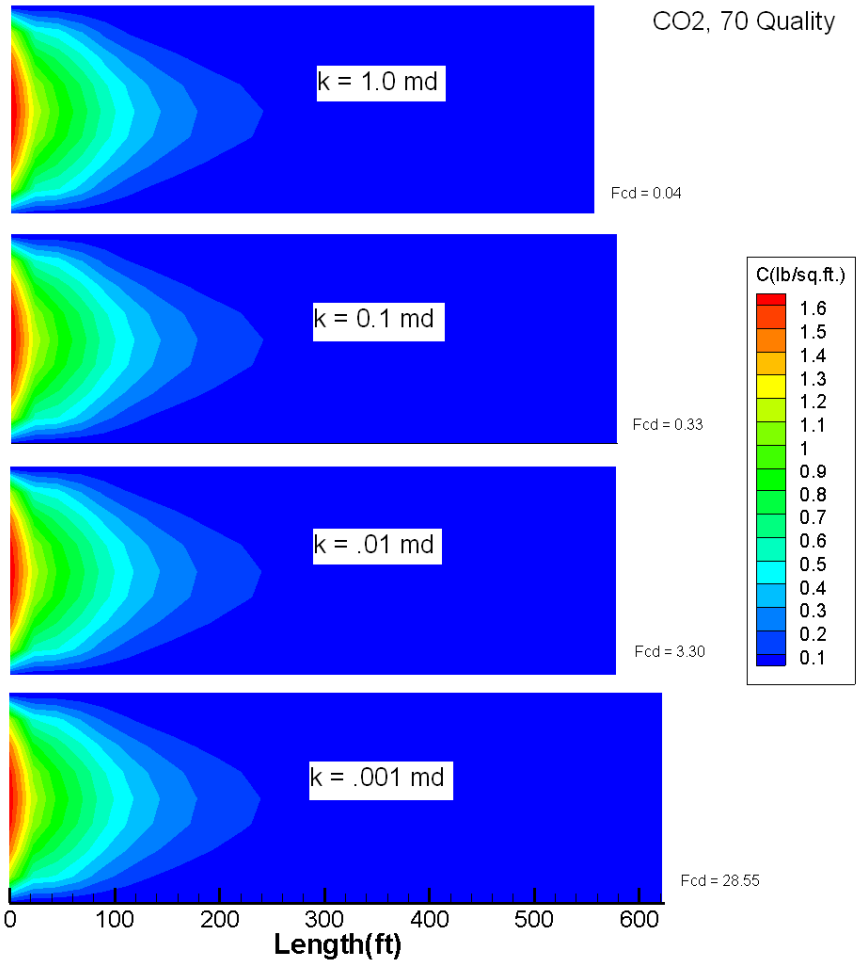

Figure 9.16. Proppant concentration at end of pumping for a range of permeability. CO_2, 70 quality.

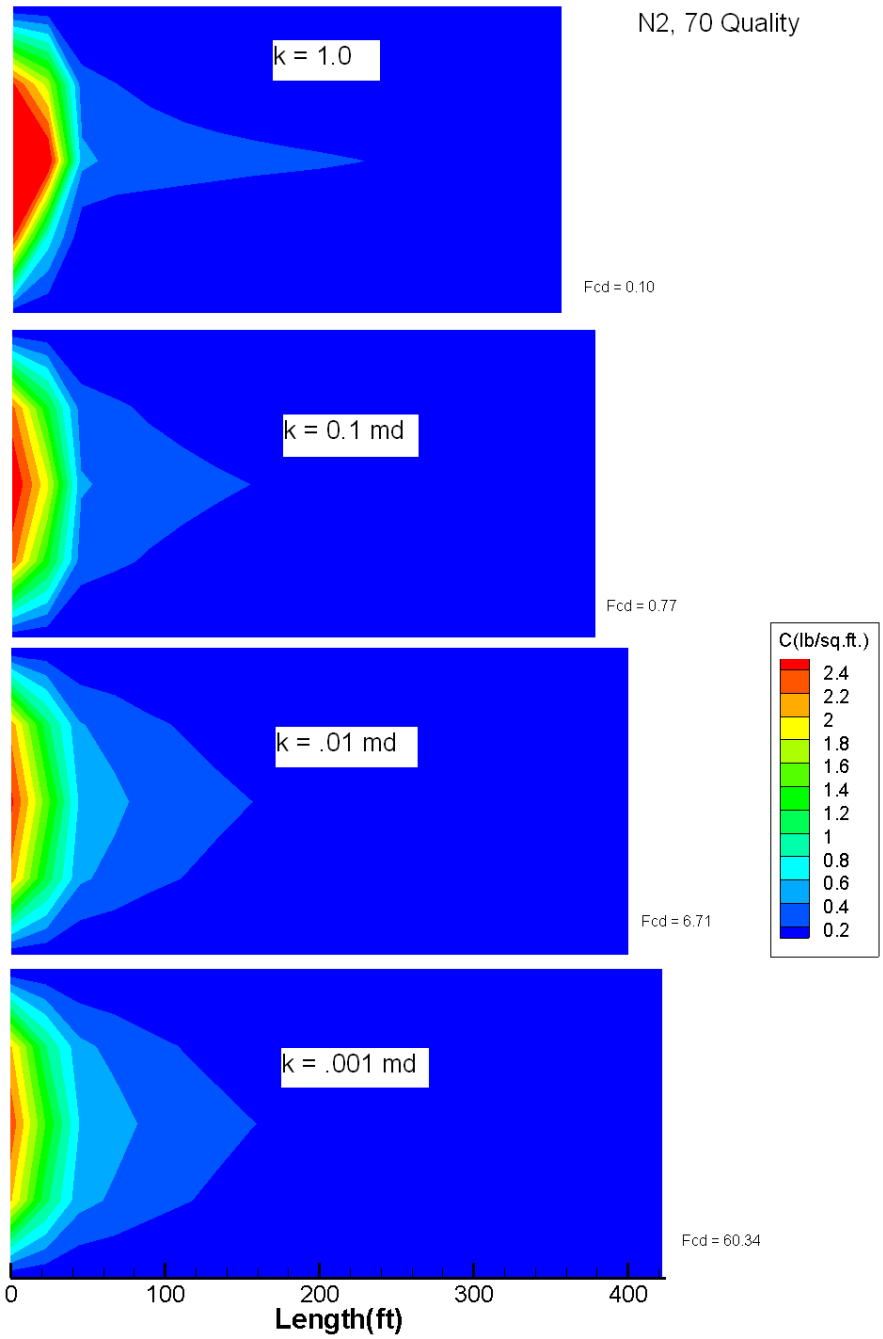

Figure 9.17. Proppant concentration at end of pumping for a range of permeability. N_2, 70 quality.

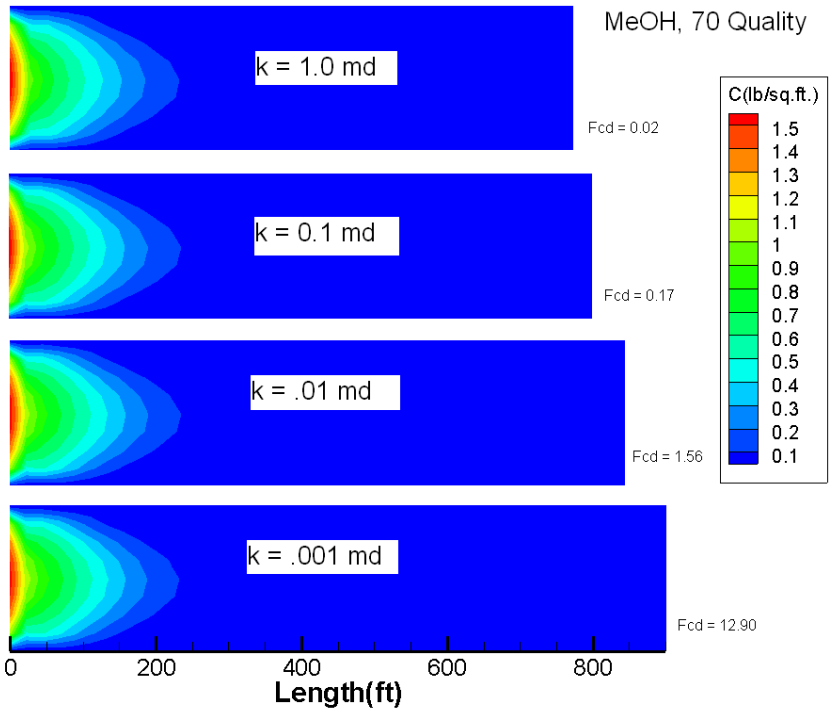

Figure 9.18. Proppant concentration at end of pumping for a range of permeability. CO_2 with 20% methanol in the liquid phase, 70 quality.

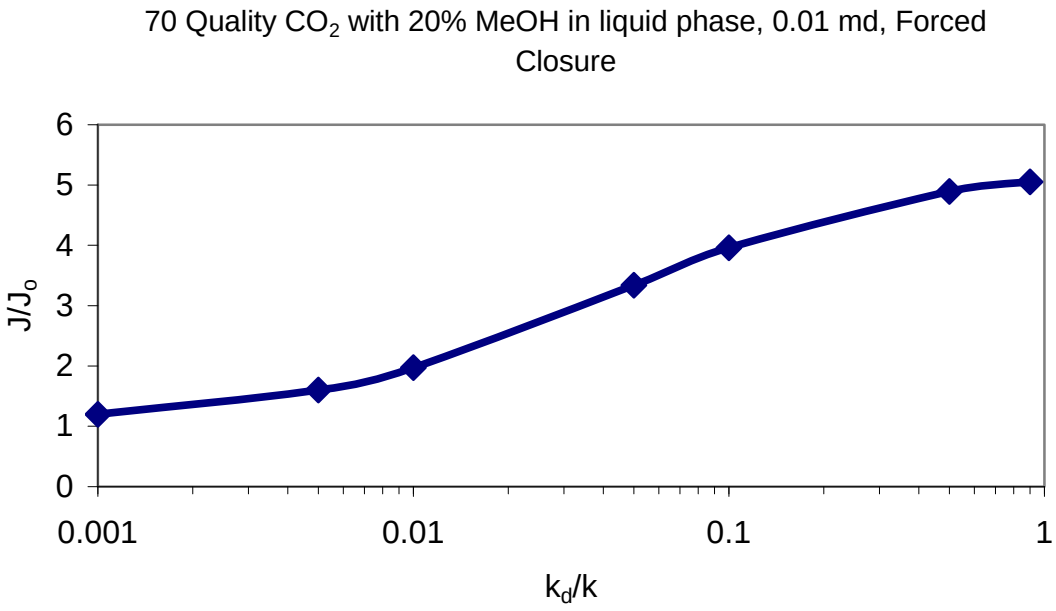

Figure 9.19. Productivity index dependence on effective permeability in the invaded zone. 70 quality CO_2 with 20% methanol in liquid phase, 0.01 md, Forced closure.

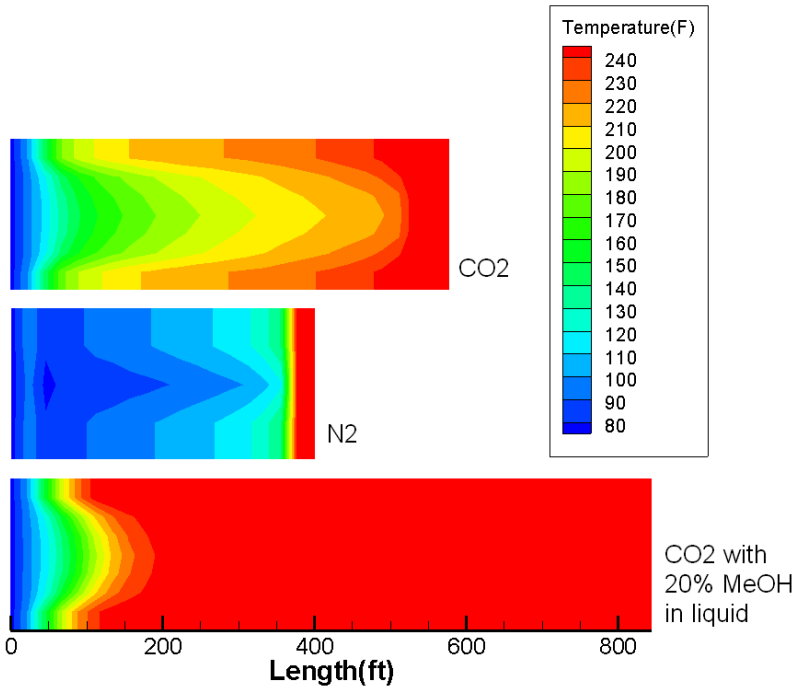

Figure 9.20. Temperature profile at end of pumping for 3 energizing components. 70 quality.

CONCLUSION

10.1 Summary

Hydraulic fracturing is a proven stimulation technique to increase productivity from oil and gas wells. Fracturing is done by injecting fluid into the petroleum containing rock at high pressure, cracking the rock. Solid particles, referred to as proppant, are added to the fluid and placed in the crack. When pumping is stopped, the fracture closes on the proppant and leaves a conductive channel for oil and gas to flow through into the wellbore. Most fracturing treatments use water and gelling agent as fracturing fluid. The water is not recovered when drawdown pressures are low. The un-recovered water leaves a water-saturated zone around the fracture face that stops the flow of gas into the fracture. Depletion (lower reservoir pressures) causes a limitation on the drawdown pressure that can be applied. Sometimes the water, which may be incompatible with the clays in the sandstone, causes irreversible damage to the formation around the fracture face.

A hydraulic fracturing process can be energized by the addition of a compressible, sometimes soluble, gas phase into the treatment fluid. When the well is produced, the energized fluid expands and gas comes out of solution. This, coupled with the high mobility of the fluid in the fracture, results in a rapid cleanup of the fracturing fluid as it is blown out of the well by the liberated gas phase[4].

Unlike traditional fracturing fluids, energized fluid systems involve the injection of multiple components. Several mechanisms (phase behavior, leak-off, multi-phase flow) can cause compositional changes of the fluid during fracturing. In addition, phase changes can occur as a result of changes in temperature and pressure. Fracture dimensions, as well as proppant carrying ability, depend both on the overall composition and the phase properties of the fracturing fluid.

A new hydraulic fracturing model has been created (EFRAC). This is the first model to include:

- Changes in composition of the fracturing fluid in the fracture,
- Changes in temperature in the fracture,
- Use of an equation of state to evaluate the phase behavior of the fluid
- The coupling of all effects with mechanical fracture growth criterion.

In addition to the fracture propagation model, we have also introduced a new model for fractured well productivity. This is the first model that takes into account both finite fracture conductivity and damage in the invaded zone in a simple analytical way. New types curves for productivity index calculations are presented that should replace existing ones in Raymond and Binder[5] or McGuire and Sikora[6]. The productivity model is connected to the fracture propagation model to show the effect of pumping schedule choices on the productivity of the well. Predicting changes in productivity from fracturing decisions is a useful tool to justify changes in fracture design.

The effect of multiple phases on fracturing fluid leak-off is discussed mechanistically. Four mechanisms are postulated and their viability explored. The work done here will work in conjunction with future leak-off experiments.

The full model was tested in two different sensitivity studies. The first was on an actual tight gas field in South Texas. The discussion was limited to the properties of that specific field and the CO_2 with crosslinked gels that were pumped in the past. Issues with drawdown pressure, foam quality, temperature, reservoir pressure, and energizing only certain stages were investigated. The second sensitivity study involved energized fractures in a more general sense because it was not applied to only one field and fluid choice. The study investigated the effect of different energized components (CO_2, N_2, and MeOH), leak-off, fracture closure, and formation permeability. This includes a more general discussion on when to energize the fluid at all and what is the optimum quality.

10.2 Conclusions

The following conclusions have been made based on the results presented in this report.

1. A new model (EFRAC) has been developed and presented for energized fracture treatments. The model tracks the composition of multiple phases (and any number of fluid components) during fracturing. The new model also tracks temperature changes in the wellbore and in the fracture through an energy balance. The changes in fluid pressure, temperature, and composition are used together with an equation of state for updating phase volumes and properties. Combining this compositional model with models/data for fluid rheology and fracture mechanics allows us to model, for the first time, changes in bottom-hole pressure, fluid composition, and fracture dimensions for energized fracture treatments.

2. This new model reduces to a PKN fracture model when incompressible and Newtonian fluids are used, and the system is isothermal. Several examples are shown that illustrate the power and usefulness of the model. As an example, the total fracture volume varies significantly when the fluid is injected at a low temperature and exposed to a hot reservoir. This is due to expansion of fluids with increased temperature.

3. A new model is developed that calculates the productivity of a hydraulically fractured well, including the effect of damage of the fracture face from fluid leak-off. Results of the new model are compared with three previous models (Raymond[5], McGuire[6], and Prats[7]). The existing models assume either elliptical or radial flow around the well with permeability varying azimuthally. Significant differences in the calculated well productivity indicate that earlier assumptions made about the flow geometry can lead to significant overestimates of well productivity index (PI). Agreement with Prats'[6] analytical solution is achieved for finite conductivity fractures and no fracture damage. It is shown that the use of either Raymond's[5] or McGuire and Sikora's[6] model to estimate improvement in well PI in fractured wells can lead to a significant over-estimation of the well PI. The new model provides a useful tool to quickly calculate the productivity of wells that have both a finite-conductivity fracture and damage in the invaded zone.

4. Clean-up of the damage in the invaded zone depends on the capillary properties of the formation and the drawdown pressure applied across the damaged zone during

production. If capillary forces are small, and drawdown pressure is high, the water will be recovered, resulting in negligible damage. It is found that the invaded zone can cause significant damage when the permeability of the damaged zone is reduced by over 90%.

5. EFRAC was successfully used to simulate several fracture treatments in a gas field in South Texas. Sensitivities of several variables were investigated. The following conclusions were made from that study:

    a. Based on production estimates, energized fluids may be required when drawdown pressures are smaller than the capillary forces in the formation. If drawdown pressures are high, the added benefit of energizing the fracturing fluid is minimal.

    b. The optimum quality depends on the specific conditions of the reservoir i.e. the reservoir pressure, temperature, permeability and the conditions of flowback. For this field, the minimum quality recommended is 30% for moderate differences between fracture and reservoir pressures (2900 psi reservoir, 5300 psi fracture). The minimum quality is reduced to 20% when the difference between pressures is larger, resulting in additional gas expansion in the invaded zone.

    c. The larger the difference between inlet and formation temperature, the larger the expansion of the gas phase during fracturing. The expansion has a significant effect on fracture dimensions. However, simulations show that the expansion takes place gradually down the length of the fracture and may not affect the placement of proppant, and therefore, has a small effect on the overall production from the fracture. It is recommended to not use any resources to change the inlet temperature of the fluid, but it may be necessary to make fluid volume corrections based on the expansion of the gas phase.

    d. If energizing the fluid is necessary, every stage of the fracturing treatment should be energized with a gas component to ensure high gas saturation in the invaded zone. If this is not possible, effective stimulation may be achieved in

some cases by energizing only the pad or proppant stages without a major loss of production.

6. Four mechanisms were postulated to describe how a gas component in a fracturing fluid impacts fluid leak-off. We can reach the following conclusions from those mechanisms:
    a. For fluid properties and rates that are typical in fracturing conditions, the bubbles in a fluid traveling across the face of a porous medium are not likely to attach to the surface of the rock, the filter cake, or penetrate far into the porous medium.
    b. At very high filtration rates (k_{core} >10 md) or if small (R < 10 μm) bubbles exist, the presence of gas bubbles in an external filter cake can play a role in reducing fluid leak-off.
    c. The release of a free gas phase can reduce leak-off if CO_2 or another soluble component is used as the gas component. The gas phase does not play an important role if N_2 is used because it is relatively insoluble in water.
    d. Even when CO_2 is used, a thick and low permeability filter cake can dominate leak-off control.
7. The following conclusions were drawn based on sensitivity study:
    a. Damage around the fracture face induced by the loss of water-based fracturing fluids can be removed during flowback if the drawdown pressure exceeds the capillary forces holding the liquid in place.
    b. Energized fluids are effective when the gas component leaks-off into the invaded zone. This results in a high gas saturation in the invaded zone that will not restrain the flowback of gas into the fracture.
    c. Common energizing components are CO_2 and N_2. Both have different phase density and solubility in water, therefore, should not be viewed as having the same benefit. Simulations show that CO_2 outperforms N_2 in most cases because it has higher solubility at fracturing temperatures and pressures.

d. Fluids with higher solubility in aqueous solutions will increase the fluid's ability to reduce damage in the invaded zone.

e. Adding a component such as methanol to an energized system increases the solubility of CO_2 in the liquid phase and alleviates clay swelling in some sandstones.

f. The gas component can leak into the invaded zone by three mechanisms; at least one of the mechanisms need to occur for the energized fracture to be effective. They are: 1) the liquid phase that invades the formation has a significant mole fraction of the gas dissolved in it. When pressure is reduced for flowback, the gas component comes out of solution. 2) The fracture is allowed to close naturally during shut-in. This process forces the gas phase to bleed into the formation as the fracture closes. The gas component will be present in the invaded zone. 3) The gas phase leaks into the invaded zone during fracture creation. If this happens, there will almost certainly be enough gas in the invaded zone to reduce damage. More data is needed to determine which mechanism is dominant.

g. 30 to 50% quality energized fluids are optimum because they allow enough gas to saturate the liquid to maximize gas flowback and they yield long fractures. The higher the solubility of the gas, the higher the foam quality needed to make sure the liquid is fully saturated.

h. Higher quality (up to 70%) may be necessary if shorter and wider fractures are preferred.

i. Energized fluids should be applied to rocks when the drawdown pressure is insufficient to remove the liquid. This corresponds to a drawdown pressure of ~200 psi for 0.1 md formations, ~500 psi for 0.01 md, and ~1500 psi for 0.001 md.

10.3 Recommendations for Future Work

We recommend that the following research should be done in the future:

1. We have shown that the leak-off of gas into the invaded zone is the key to the effectiveness of energized fractures. Unfortunately, there are still questions remaining about how the gas phase changes leak-off behavior. The recommendations in Chapter 8 give an outline of how energized leak-off experiments should be designed. Once the leak-off behavior is understood by laboratory experiments, the behavior can be modeled using EFRAC. The model can then show the optimum use of energized fluids by optimizing leak-off.

2. We have used some simplifications in modeling the interaction between leak-off and flowback. We assume that the invaded zone has only one fluid composition, tracked by the composition of the fluid that leaks-off. In reality, leak-off is a complicated process where the fracturing fluid is displacing a methane-rich gas phase. It is not fully understood what the interactions between the fluids would be. The same is true for flowback when the flow is reversed. It would be possible to investigate this process by connecting the EFRAC model to a compositional reservoir simulator.

3. The EFRAC model uses the simplest fracture growth criteria for the given fracture geometry. A real fracture would require additional resistance to propagate the fracture at the tip. Future research should be aimed at adding this feature to the model. Other issues related to fracture mechanics can be added too. For example, fracture height growth, non-uniform stress fields, non-elliptical cross-sections, and thermal stresses can be added.

4. The model is set up with the Peng-Robinson equation of state. This means that any component that can be modeled by the PREOS can be used in the fracture model. This research focused on the components H_2O, CO_2, N_2, and MeOH. The effect of other components should be investigated in the future. For instance, hydrocarbons have been used as fracturing fluids and the phase behavior should have an important impact on fracture design. In addition, the oil and gas service industry is always

coming up with new and innovative fracturing fluids. This model can be used with any of those fluids as well.

5. To this point, this research has had limited field verification. Now that a simulator is available, more work is needed to make sure the conclusions that the model predicts can be seen in the field. Flowback, production, and fracture treatment data will be required to confirm results.

References

1. Friehauf, K.E. and Sharma, M.M. 2008. A New Compositional Model for Hydraulic Fracturing With Energized Fluids. Paper SPE 115750 presented at the 2008 SPE Annual Technical Conference and Exhibition held in Denver, CO, 21-24 September.
2. Friehauf, K.E., Suri, A., and Sharma, M.M. 2009. A Simple and Accurate Model for Well Productivity for Hydraulically Fractured Wells. Paper SPE 119264 presented at the SPE Hydraulic Fracturing Technology Conference, The Woodlands, Texas, 19-21 January.
3. Friehauf, K.E., Sharma, M.M, and Sullivan, R. 2009. Application of a New Compositional Model for Hydraulic Fracturing With Energized Fluids: A South Texas Case Study. Paper SPE 119265 presented at the SPE Hydraulic Fracturing Technology Conference, The Woodlands, Texas, 19-21 January.
4. Wendorff, C.L. and Ainley, B.R. 1981. Massive Hydraulic Fracturing of High-Temperature Wells with Stable Frac Foams. Paper SPE 10257 presented at the Fall Technical Conference and Exhibition, San Antonio, Texas, 5-7 October.
5. Binder, I.R., and Raymond, G.G. 1967. Productivity of Wells in Fractured, Damaged Formations. *JPT* January: 12-130. SPE 1454.
6. McGuire W.J., and Sikora, V.J. 1960. The Effect of Vertical Fractures on Well Productivity. *JPT* October: 72-75. SPE 1618.
7. Prats, M. 1961. Effect of Vertical Fractures on Reservoir Behavior – Incompressible Fluid Case. *SPEJ* June 1961:105-117. SPE 1575-G.

BIBLIOGRAPHY

Acharya, A.R. 1986. Particle Transport in Viscous and Viscoelastic Fracturing Fluids. *SPE Production Engineering*, March: 104-110.

Antoci, J.C, Briggiler, N.J. and Chadwick, J.A. 2001. Crosslinked Methanol: Analysis of a Successful Experience in Fracturing Gas Wells. Paper SPE 69585 presented at the SPE Latin America and Caribbean Petroleum Engineering Conference, Buenos Aires, Argentina, 25-28 March.

Binder, I.R., and Raymond, G.G. 1967. Productivity of Wells in Fractured, Damaged Formations. *JPT* January: 12-130. SPE 1454.

Blauer, R.E. and Kohlhaas, C.A. 1974. Formation Fracturing with Foam. Paper SPE 5003 presented at the 49th SPE-AIME Annual Fall Meeting, Houston, Texas, October.

Brooks, R.H., and Corey, A.T. 1966. Properties of Porous Media Affecting Fluid Flow. *Jour. Irrigation and Drainage Div., Proc. Amer. Soc. Of Civil Engr.* June: 61-88.

Cambell, S.M, Fairchild, N.R. Jr., and Arnold, D.L. 2000. Liquid CO2 and Sand Stimulations in the Lewis Shale, San Juan Basin, New Mexico: A Case Study. Paper SPE 60317 presented at the SPE Rocky Mountain Regional/Low-Permeability Reservoirs Symposium and Exhibition, Denver, Colorado, 12-15 March.

Chhabra, R.P. 2007. Bubble, Drops, and Particles in Non-Newtonian Fluids. Taylor and Francis.

Cinco-Ley, H., and Samaniego, F. 1978. Effect of Wellbore Storage and Damage on the Transient Pressure Behavior of Vertically Fractured Wells. Paper SPE 6752 presented at the 52nd Annual Fall Technical Conference and Exhibition of the Society of Petroleum Engineers of AIME, Denver, Colorado, 9-12 October.

Corey, A.T. 1977. *Mechanics of Immiscible Fluids in Porous Media*. Fort Collins, Colorado: Water Resources Publications.

Economides, M.J, Nolte, K.G. 2000. *Reservoir Stimulation*. John Wiley & Sons, LTD.

Forshee, W.C. and Hurst, R.E. 1965. Improvement of Well Stimulation Fluids by Including a Gas Phase. *Journal of Petroleum Technology*, July: 768-772.

Fredd, C.N, Miller, M.J. and Quintero, B.W. 2004. Impact of Water-Based Polymer Fluid Characteristics on CO2 Foam Rheology. Paper SPE 86493 presented at the SPE International Symposium and Exhibition on Formation Damage Control, Lafayette, Louisiana, 18-20 February.

Friehauf, K.E. and Sharma, M.M. 2008. A New Compositional Model for Hydraulic Fracturing With Energized Fluids. Paper SPE 115750 presented at the 2008 SPE

Annual Technical Conference and Exhibition held in Denver, CO, 21-24 September.

Friehauf, K.E., Sharma M.M, and Sullivan, R. 2009. Application of a New Compositional Model for Hydraulic Fracturing With Energized Fluids: A South Texas Case Study. Paper SPE 119265 presented at the 2009 SPE Hydraulic Fracturing Technology Conference, Woodlands, Texas, 19–21 January.

Friehauf, K.E., Suri, A., and Sharma, M.M. 2009. A Simple and Accurate Model for Well Productivity for Hydraulically Fractured Wells. Paper SPE 119264 presented at the SPE Hydraulic Fracturing Technology Conference, The Woodlands, Texas, 19-21 January.

Gabris S.J. and Taylor J.L. III. 1986. The Utility of CO2 as an Energizing Component for Fracturing Fluids. *SPE Production Engineering*. September: 351-358. SPE 13794.

Gadde, P.B, Liu, Y, Norman, J, Bonnecaze, R, and Sharma, M.M. 2004. Modeling Proppant Settling in Water Fracs. Paper SPE 89875 presented at the SPE Annual Technical Conference and Exhibition, Houston, Texas, 26-69 September.

Goodman, J.B, and Krase, N.W. 1931. Solubility of Nitrogen in Water at High Pressures and Temperatures. *Industrial and Engineering Chemistry*, April: 401-404.

Gulbis, J. 1983. Dynamic Fluid Loss of Fracturing Fluids. Paper SPE 12154 presented at the SPE 58th Annual Technical Conference and Exhibition held in San Francisco, California, 5-8 October.

Gupta, D.V.S. 2003. Field Application of Unconventional Foam Technology: Extension of Liquid CO2 Technology. Paper SPE 84119 presented at SPE Annual Technical Conference and Exhibition, Denver, Colorado, 5-8 October.

Harris, P.C. 1985. Dynamic Fluid-Loss Characteristics of Nitrogen Foam Fracturing Fluids. *Journal of Petroleum Technology*, October: 1847-1852.

Harris, P.C. 1987. Dynamic Fluid-Loss Characteristics of CO2-Foam Fracturing Fluids. *SPE Production Engineering*, May: 89-94.

Harris, P.C. 1995. A Comparison of Mixed-Gas Foams with N2 and CO2 Foamed Fracturing Fluids on a Flow-Loop Viscometer. *SPE Production and Facilities,* August: 197-202. SPE 20642.

Harris, P.C. and Heath, S.J. 1996. Rheology of Crosslinked Foams. *SPE Production and Facilities,* May: 113-116. SPE 28512.

Harris, P.C., Klebenow, D.E., and Kundert, D.P. 1991. Constant-Internal-Phase Design Improves Stimulation Results. *SPE Production Engineering*, February: 15-19. SPE 17532.

Harris, P.C. and Reidenbach, V.G. 1987. High Temperature Rheological Study of Foam Fracturing Fluids. *Journal of Petroleum Technology*, May: 613-619. SPE 13177.

Hasan, A.R. and Kabir, C.S. 2002. *Fluid Flow and Heat Transfer in Wellbores*. Society of Petroleum Engineers.

Hnedkovshy, L, Wood, R.H, and Majer, V. 1996. Volumes of aqueous solutions of CH4, CO2, H2S, and NH3 at Temperatures from 298 K to 705 K and pressure to 35 MPa. *J. Chem. Thermodynamics*, 28: 125-142.

Holditch, S.A. 2006. Tight Gas Sands. *Journal of Petroleum Technology*, June: 86-93. SPE 103356.

Holm, L.W. 1968. The Mechanism of Gas and Liquid Flow Through Porous Media in the Presence of Foam. *Society of Petroleum Engineers Journal*, December: 359-369. SPE 1848.

Jiao, D. and Sharma, M.M. 1994. Mechanism of Cake Buildup in Crossflow Filtration of Colloidal Suspensions. *Journal of Colloid and Interface Science*, 162: 454-462.

Kenyon, D.E. 1993. CO2 Foam Slurry Friction Correlations. Paper SPE 26152 presented at the SPE Gas Technology Symposium, Calgary, Alberta, Canada, 28-30 June.

Khade K.D. and Shah, S.N. 2004. New Rheological Correlations for Guar Foam Fluids. *SPE Production & Facilities*, May: 77-85.

King, G.E. 1977. Factors Affecting Dynamic Fluid Leakoff With Foam Fracturing Fluids. Paper SPE 6817 presented at the 52nd Annual SPE Fall Technical Conference and Exhibition held in Denver, Colorado, 9-12 October.

King, G.E. 1986. Foam and Nitrified Fluid Treatments-Stimulation Techniques and More. This paper is based on a speech presented as a Distinguished Lecture during the 1985-1986 season. SPE 14477.

Leverett, M.C. 1940. Capillary Behavior in Porous Solids. *Petroleum Technology*. August: 152-169.

Liu, Y, and Sharma, M.M. 2005. Effect of Fracture Width and Fluid Rheology on Proppant Settling and Retardation: An Experimental Study. Paper SPE 96208 presented at the SPE Annual Technical Conference and Exhibition, Dallas, Texas, 9-12 October.

Malone, M.R. 2001. Fracturing with Crosslinked Methanol in Water-Sensitive Formations. Paper SPE 70009 presented at the SPE Permian Basin Oil and Gas Recovery Conference, Midland, Texas, 15-16 May.

Mayerhofer, M.J, Economides, M.J. and Nolte, K.G. 1991. An Experimental and Fundamental Interpretation of Fracturing Filter-Cake Fluid Loss. Paper SPE

22873 presented at the SPE 68th Annual Technical Conference and Exhibition held in Dallas, Texas, 6-9 October.

Mazza, R.L. 2001. Liquid-Free CO2/Sand Stimulations: An Overlooked Technology – Production Update. Paper SPE 72383 presented at the SPE Eastern Regional Meeting held in Canton, Ohio, 17-19 October.

McGuire W.J., and Sikora, V.J. 1960. The Effect of Vertical Fractures on Well Productivity. *JPT* October: 72-75. SPE 1618.

Meyer, B.R. 1989. Heat Transfer in Hydraulic Fracturing. *SPE Production Engineering*, November: 423-429.

Nolte, K.G, Mack, M.G. and Lie, W.L. 1993. A Systematic Method for Applying Fracturing Pressure Decline. Paper SPE 25845 presented at the SPE Rocky Mountain Regional Low Permeability Symposium, Denver, Colorado, 12-14 April.

Nordgren, R.P. 1972. Propagation of a Vertical Hydraulic Fracture. *Society of Petroleum Engineers Journal*, August: 306-314.

Oh, S.G. and Slattery, J.C. 1979. Interfacial Tension Required for Significant Displacement of Residual Oil. *Society of Petroleum Engineers Journal*. April: 83-96.

Okuno, R and Johns, R.T. 2008. Application of a Reduced Method in Compositional Simulations. Paper SPE 119657 accepted for journal publication in SPE Journal.

Okuno, R, Johns, R.T, and Sepehrnoori, K. 2008. A New Algorithm for Rachford-Rice for Multiphase Compositional Simulation. Paper SPE 117752 presented at the SPE Eastern Regional / AAPG Eastern Section Joint Meeting, Pittsburgh, Pennsylvania, 11-15 October.

Okuno, R, Johns, R.T, and Sepehrnoori, K. 2009. Three-Phase Flash in Compositional Simulation Using a Reduced Method. Paper presented at the 15th European Symposium on Improved Oil Recovery, Paris, France, 27-29 April.

Outmans, H.D. 1963. Mechanics of Static and Dynamic Filtration in the Borehole. *Society of Petroleum Engineers Journal*, September: 236-244.

Ozbayoglu, E.M, Akin, S. and Eren, T. 2005. Foam Characterization using image Processing Techniques. Paper SPE 93860 presented at the SPE Western Regional meeting, Irvine, California, 30 March – 1 April.

Penny, G.S, Conway, M.S. and Lee, W. 1985. Control and Modeling of Fluid Leakoff During Hydraulic Fracturing. *Journal of Petroleum Technology*, June: 1071-1081.

Perkins, T.K, and Gonzalez, J.A. 1985. The Effect of Thermoelastic Stresses on Injection Well Fracturing. *SPE Journal*, February: 78-88. SPE 11332.

Prats, M. 1961. Effect of Vertical Fractures on Reservoir Behavior – Incompressible Fluid Case. *SPEJ* June 1961:105-117. SPE 1575-G.

Reidenbach, V.G, Harris, P.C, Lee, Y.N. and Lord, D.L. 1986. Rheological Study of Foam Fracturing Fluids using Nitrogen and Carbon Dioxide. *SPE Production Engineering*, January : 31-41.

Rodvelt, G, Dials, G.A. and Monte, H. 1999. Case History: Carbon Dioxide Foam Stimulates Rome in Eastern Kentucky. Paper SPE 57430 presented at the SPE Eastern Regional Conference and Exhibition, Charleston, West Virginia, 21-22 October.

Roodhart, L.P. 1985. Fracturing Fluids: Fluid-Loss Measurements Under Dynamic Conditions. *Society of Petroleum Engineers Journal*, October: 629-636. SPE 11900.

Rumpf, B, Nicolaisen, H, and Maurer, G. 1994. Solubility of Carbon Dioxide in Aqueous Solutions of Sodium Chloride: Experimental Results and Correlation. *Journal of Solution Chemistry*, Vol. 23: No.3: 431-448.

Saddington, A.W, Krase, N.W. 1934. Vapor-Liquid Equilibria in the System Nitrogen-Water. *Journal of the American Chemical Society*, February(56): 353-361.

Sandler, S.I. 1999. *Chemical and Engineering Thermodynamics*. John Wiley & Sons Inc.

Schechter, R.S. 1992. *Oil Well Stimulation*. Englewood Cliffs, New Jersey: Prentice Hall.

Sharma M.M. 2004. Advanced Fracturing Technology for Tight Gas: An East Texas Field Demonstration. DOE report, The University of Texas, Austin, Texas, September.

Sherwood, J.D. 1993. A Model for Static Filtration of Emulsions and Foams. *Chemical Engineering Science*, Vol. 48: No. 19: 3355-3361.

Spycher, N, Pruess, K. and Ennis-King, J. 2003. CO2-H2O mixtures in the geological sequestration of CO2. I. Assessment and calculation of mutual solubilities from 12 to 100 C and up to 600 bar. *Geochemica et Cosmochemica Acta*, Vol. 67: No. 16: 3015-3031.

Suri, A., and Sharma M.M. 2007. A Model for Water Injection in Frac-Packed Wells. Paper SPE 110084 presented at the 2007 SPE Annual Technical Conference and Exhibition held in Anaheim, California. 11–14 November.

Taylor, R, Khallad, A, Cheng, A, Barree, B, Byrnes, J, Kelly, K, Conway, M, Caufield, R, and Tourigny, S. 2002. Optimized Gas-Well Stimulating using CO2-Miscible, Viscosified Hydrocarbon Fracturing Fluids. Paper SPE 75666 presented at the SPE Gas Technology Symposium, Calgary, Alberta, Canada, 30 April – 2 May.

Urokova, I, Vorholz, J, and Maurer, G. 2006. Solubility of Carbon Dioxide in Aqueous Solutions of Methanol. Predictions by Molecular Simulation and Comparison with Experimental Data. *Journal of Physical Chemistry*, 110(30):14943-14949.

Valko, P. and Economides, M.J. 1992. Volume Equalized Constitutive Equations for Foamed Polymer Solutions. *Journal of Rheology*, August: 1033-1055.

Valko, P. and Economides, M.J. 1995. *Hydraulic Fracture Mechanics*. John Wiley & Sons Inc.

Watkins, E.K., and Wendorff, C.L. 1983. A New Crosslinked Foamed Fracturing Fluid. Paper SPE 12027 presented at the 58th Annual Technical Conference and Exhibition, San Francisco, California, 5-8 October.

Wendorff, C.L. and Ainley, B.R. 1981. Massive Hydraulic Fracturing of High-Temperature Wells with Stable Frac Foams. Paper SPE 10257 presented at the Fall Technical Conference and Exhibition, San Antonio, Texas, 5-7 October.

Xia, J, Jdecke, M, Prez-Salado Kamps, I, and Maurer, G. 2004. Solubility of CO2 in (CH3OH + H2O). *Journal of Chemical Engineering Data*, 49(6): 1756-1759.

Yew, C.H. 1997. *Mechanics of Hydraulic Fracturing.* Gulf Pub Co.

Zydney, A.L. 1989. Hydraulic Resistance of Red Cell Beds in an Unstirred Filtration Cell. *Journal of Engineering Science*, Vol. 44: No. 1: 147-159.

LIST OF ACRONYMS AND ABBREVIATIONS

A	Parameter relating flowrate per unit height to pressure gradient
B	Parameter relating net fluid pressure to fracture width
c	Proppant concentration (vol/vol)
c_{in}	Proppant concentration, inlet
C_k	Leak-off coefficient of j phase
C^*_k	Integral of $2*C_k/(t-\tau)^{1/2}$ from time t to t + Δt
C_p	Heat capacity
$C_{p,k}$	Phase heat capacity
$C^*_{p,k}$	Proppant corrected heat capacity
C_{pR}	Reservoir heat capacity (fluid and rock)
F_k	Fractional flowrate of each phase
h	Fracture height
K_R	Thermal conductivity, reservoir
k_{ret}	Proppant retardation factor
Numj	Number of vertical nodes
NC	Number of components
NP	Number of phases
P	Pressure
q_{inj}	Injection rate per unit height
q_x	Flowrate per unit height
q_z	Flowrate per unit length
S_k	Phase saturation
t	Time
T	Temperature
T_{inj}	Temperature, inlet
T_R	Reservoir temperature
V_{set}	Proppant settling velocity
w	Fracture width
x_{Ik}	Fraction of component i in phase j
z_i	Overall mass fraction of component i
$z_{I,inj}$	Overall mass fraction of component i, inlet

Greek Symbols

Δt	Time step
Δx	Distance between nodes in horizontal direction
Δz	Distance between nodes in vertical direction
ρ_R	Density, earth
ρ_k	Density, phase
ρ_k^*	Proppant corrected phase density
ρ_p	Density, proppant
σ	Stress
Φ	Heat blockage correction factor for thermal resistance of leaked-off fluid
Ψ	Heat blockage correction factor for cooling of reservoir by leak-off
τ	Fracture opening time

APPENDIX A: FINITE DIFFERENCE EQUATIONS

Note: i and j in Equations A.2-A.5 represent the nodal numbering in the horizontal and vertical direction respectively. Capital "I" refers to the component, k, the phase, and n, the time step.

Note: The flow terms in the finite difference equations are in terms of the fractional flow of each phase, F_k. From Equation 3.21-3.23, remember that:

$$q_{x,k} = A_k \frac{dP}{dx} = F_k A \frac{dP}{dx} = F_k q_x \tag{A.1}$$

The equations are listed in the order in the EFRAC model, not the order in Chapter 3.

Equation A.2 – Finite difference formula for pressure equation (Equation 3.24)

$$\frac{\Delta t}{\Delta x^2}[\sum_k^{NP} A^n(i,j)\rho^*{}_k{}^n(i,j)F_k{}^n(i,j) + A^n(i-1,j)\rho^*{}_k{}^n(i-1,j)F_k{}^n(i-1,j)]P^{n+1}(i,j)$$
$$+\frac{\Delta t}{2\Delta z^2}[\sum_k^{NP} A^n(i,j+1)\rho^*{}_k{}^n(i,j+1)F_k{}^n(i,j+1) + A^n(i,j-1)\rho^*{}_k{}^n(i,j-1)F_k{}^n(i,j-1)]P^{n+1}(i,j)$$
$$-\frac{\Delta t}{\Delta x^2}[\sum_k^{NP} A^n(i,j)\rho^*{}_k{}^n(i,j)F_k{}^n(i,j)]P^{n+1}(i+1,j)$$
$$-\frac{\Delta t}{\Delta x^2}[\sum_k^{NP} A^n(i-1,j)\rho^*{}_k{}^n(i-1,j)F_k{}^n(i-1,j)]P^{n+1}(i-1,j)$$
$$-\frac{\Delta t}{2\Delta z^2}[\sum_k^{NP} A^n(i,j+1)\rho^*{}_k{}^n(i,j+1)F_k{}^n(i,j+1)]P^{n+1}(i,j+1)$$
$$-\frac{\Delta t}{2\Delta z^2}[\sum_k^{NP} A^n(i,j-1)\rho^*{}_k{}^n(i,j-1)F_k{}^n(i,j-1)]P^{n+1}(i,j-1)$$
$$-\sum_{jj}^{Numj}\sum_k^{NP}[\rho^*{}_k{}^n(i,j)S_k{}^n(i,j)]B^n(j)P^{n+1}(i,jj)/Numj$$
$$=\sum_k^{NP}\rho_k{}^n(i,j)C^*{}_k{}^n(i,j)S_k{}^n(i,j) - w^n(i,j)\sum_k^{NP}\rho^*{}_k{}^{n-1}(i,j)S_k{}^{n-1}(i,j)$$

Where:

$$C^*_k(i,j) = \int_t^{t+\Delta t} \frac{2C_k(i,j)}{\sqrt{t-\tau}} = 4C_k(i,j)[\sqrt{t+\Delta t-\tau} - \sqrt{t-\tau}]$$

with boundary conditions:

$$\frac{\Delta t}{\Delta x^2}[\sum_k^{NP} A^n(1,j)\rho^{*}_k{}^n(1,j)F_k{}^n(1,j)]P^{n+1}(i,j)$$
$$+\frac{\Delta t}{2\Delta z^2}[\sum_k^{NP} A^n(1,j+1)\rho^{*}_k{}^n(1,j+1)F_k{}^n(1,j+1) + A^n(1,j-1)\rho^{*}_k{}^n(1,j-1)F_k{}^n(1,j-1)]P^{n+1}(1,j)$$
$$-\frac{\Delta t}{\Delta x^2}[\sum_k^{NP} A^n(1,j)\rho^{*}_k{}^n(1,j)F_k{}^n(1,j)]P^{n+1}(2,j)$$
$$-\frac{\Delta t}{2\Delta z^2}[\sum_k^{NP} A^n(1,j+1)\rho^{*}_k{}^n(1,j+1)F_k{}^n(1,j+1)]P^{n+1}(1,j+1)$$
$$-\frac{\Delta t}{2\Delta z^2}[\sum_k^{NP} A^n(1,j-1)\rho^{*}_k{}^n(1,j-1)F_k{}^n(1,j-1)]P^{n+1}(1,j-1)$$
$$-\sum_{jj}^{Numj}\sum_k^{NP}[\rho^{*}_k{}^n(1,j)S_k{}^n(1,j)]B^n(j)P^{n+1}(1,jj)/Numj$$
$$=$$
$$\sum_k^{NP}\rho_k{}^n(1,j)C^{*}_{Ik}{}^n(1,j)S_k{}^n(1,j)$$
$$-w^n(1,j)\sum_k^{NP}\rho^{*}_k{}^n(1,j)S_k{}^n(1,j)$$
$$-\frac{\Delta t}{\Delta x}[q_{inj}]\sum_k^{NP}\rho^{*}_k{}^n(1,j)F_k{}^n(1,j)$$

$$P^{n+1}(i,1) = \sigma$$
$$P^{n+1}(i,Numj) = \sigma$$
$$P^{n+1}(Numi,j) = \sigma$$

Equation A.3 – Finite Difference formula for Proppant Concentration (Equation 3.6)

$$
\begin{aligned}
&-\frac{q_x^{n+1}(i,j)k_{ret}(i,j)}{\Delta x}c^n(i,j) \\
&+\frac{q_x^{n+1}(i-1,j)k_{ret}(i-1,j)}{\Delta x}c^n(i-1,j) \\
&-\frac{q_z^{n+1}(i,j+1)-V_{set}(i,j+1)w^{n+1}(i,j)}{2\Delta z}c^n(i,j+1) \\
&+\frac{q_z^{n+1}(i,j-1)-V_{set}(i,j-1)w^{n+1}(i,j)}{2\Delta z}c^n(i,j-1) \\
&+\frac{w^n(i,j)}{\Delta t}c^n(i,j) \\
&= \\
&\frac{w^{n+1}(i,j)}{\Delta t}c^{n+1}(i,j)
\end{aligned}
$$

$$c^{n+1}(1,j) = c_{in}$$

Equation A.4 – Finite Difference formula for Energy Balance (Equation 3.25)

$$4\sqrt{\frac{\rho_R K_R Cp_R}{\pi}}[\sqrt{t+\Delta t}-\sqrt{t}](T_R - T^n(i,j))\Psi(i,j)\Phi(i,j)$$
$$+w^n(i,j)\sum_k^{NP} C^*{}_{p,k}{}^n(i,j)S_k{}^n(i,j)\rho_k{}^n(i,j)T^n(i,j)$$
$$-\sum_k^{NP} C_{p,k}{}^n(i,j)S_k{}^n(i,j)\rho_k{}^n(i,j)C_k{}^*(i,j)T^n(i,j)$$
$$-\frac{\Delta t}{\Delta x}q_x{}^{n+1}(i,j)\sum_k^{NP} C^*{}_{p,k}{}^n(i,j)\rho_k{}^n(i,j)F_k{}^n(i,j)T^n(i,j)$$
$$+\frac{\Delta t}{\Delta x}q_x{}^{n+1}(i-1,j)\sum_k^{NP} C^*{}_{p,k}{}^n(i-1,j)\rho_k{}^n(i-1,j)F_k{}^n(i-1,j)T^n(i-1,j)$$
$$-\frac{\Delta t}{2\Delta z}q_z{}^{n+1}(i,j+1)\sum_k^{NP} C^*{}_{p,k}{}^n(i,j+1)\rho_k{}^n(i,j+1)F_k{}^n(i,j+1)T^n(i,j+1)$$
$$+\frac{\Delta t}{2\Delta z}q_z{}^{n+1}(i,j-1)\sum_k^{NP} C^*{}_{p,k}{}^n(i,j-1)\rho_k{}^n(i,j-1)F_k{}^n(i,j-1)T^n(i,j-1)$$
$$=w^{n+1}(i,j)\sum_k^{NP} C^*{}_{p,k}{}^n(i,j)S_k{}^n(i,j)\rho_k{}^n(i,j)T^{n+1}(i,j)$$

$$T^{n+1}(1,j)=T_{in\,j}$$

Equation A.5 – Finite Difference formula for Component Balance (Equation 3.5)

$$w^n(i,j)[1-c^n(i,j)]\sum_k^{NP} S_k{}^{n-1}(i,j)\rho_k{}^{n-1}(i,j)z_I{}^n(i,j)$$
$$-\sum_k^{NP} S_k{}^n(i,j)\rho_k{}^n(i,j)C_k{}^*(i,j)x_{Ik}{}^n(i,j)$$
$$-\frac{\Delta t}{\Delta x}q_x{}^{n+1}(i,j)[1-c^n(i,j)]\sum_k^{NP}\rho_k{}^n(i,j)F_k{}^n(i,j)x_{Ik}{}^n(i,j)$$
$$+\frac{\Delta t}{\Delta x}q_x{}^{n+1}(i-1,j)[1-c^n(i-1,j)]\sum_k^{NP}\rho_k{}^n(i-1,j)F_k{}^n(i-1,j)x_{Ik}{}^n(i-1,j)$$
$$-\frac{\Delta t}{2\Delta z}q_z{}^{n+1}(i,j+1)[1-c^n(i,j+1)]\sum_k^{NP}\rho_k{}^n(i,j+1)F_k{}^n(i,j+1)x_{Ik}{}^n(i,j+1)$$
$$+\frac{\Delta t}{2\Delta z}q_z{}^{n+1}(i,j-1)[1-c^n(i,j-1)]\sum_k^{NP}\rho_k{}^n(i,j-1)F_k{}^n(i,j-1)x_{Ik}{}^n(i,j-1)$$
$$=w^{n+1}(i,j)[1-c^n(i,j)]\sum_k^{NP} S_k{}^n(i,j)\rho_k{}^n(i,j)z_I{}^{n+1}(i,j)$$

$$z_I{}^{n+1}(1,j)=z_{I,in}$$

$$I=1,2,...NC$$

National Energy Technology Laboratory

626 Cochrans Mill Road
P.O. Box 10940
Pittsburgh, PA 15236-0940

3610 Collins Ferry Road
P.O. Box 880
Morgantown, WV 26507-0880

One West Third Street, Suite 1400
Tulsa, OK 74103-3519

1450 Queen Avenue SW
Albany, OR 97321-2198

2175 University Ave. South
Suite 201
Fairbanks, AK 99709

Visit the NETL website at:
www.netl.doe.gov

Customer Service:
1-800-553-7681